U. S. Department
of Transportation
**Federal Railroad
Administration**

THE AERODYNAMIC EFFECTS OF PASSING TRAINS TO SURROUNDING OBJECTS AND PEOPLE

Office of Research
and Development
Washington, D.C. 20590

Safety of High-Speed
Ground Transportation Systems

DOT/FRA/ORD-09/07

**Final Report
April 2009**

REPORT DOCUMENTATION PAGE

Form Approved
OMB No. 0704-0188

1. AGENCY USE ONLY (Leave blank)	2. REPORT DATE	3. REPORT TYPE AND DATES COVERED
	April 2009	Final Report April 2009

4. TITLE AND SUBTITLE
The Aerodynamic Effects of Passing Trains to Surrounding Objects and People

5. FUNDING NUMBERS
BB049/RR93

6. AUTHOR(S)
Harvey Shui-Hong Lee

7. PERFORMING ORGANIZATION NAME(S) AND ADDRESS(ES)
U.S. Department of Transportation
Research and Special Programs Administration
John A. Volpe National Transportation Systems Center
Cambridge, MA 02142-1093

8. PERFORMING ORGANIZATION REPORT NUMBER
DOT-VNTSC-FRA-04-05

9. SPONSORING/MONITORING AGENCY NAME(S) AND ADDRESS(ES)
U.S. Department of Transportation
Federal Railroad Administration
Office of Research and Development
1200 New Jersey Ave., SE
Washington, D.C. 20590

10. SPONSORING/MONITORING AGENCY REPORT NUMBER
DOT/FRA/ORD/09-07

11. SUPPLEMENTARY NOTES

12a. DISTRIBUTION/AVAILABILITY STATEMENT
This document is available to the public through the National Technical Information Service, Springfield, Virginia 22161.
This document is also available on the FRA website at www.fra.dot.gov

12b. DISTRIBUTION CODE

13. ABSTRACT (Maximum 200 words)
Two safety issues are raised on the aerodynamic effects of a passing train on its surroundings. First, a high-speed train passing other trains on an adjacent track exerts aerodynamic pressure that can affect the structural integrity of window mount and glazing, and the stability of the railroad car being passed. Second, as a high-speed train passes train stations immediately adjacent to the platform without stopping, people and objects on these station platforms are exposed to strong airflow causing debris and objects to be blown about and people to potentially lose their balance. This safety issue also extends to railroad workers on trackside as a high-speed train passes.

The objective of the research was to obtain aerodynamic data on passing trains, and to assess its effects on other trains being passed, as well as on people in proximity to the passing trains. The study entailed both numerical simulation and experimentation. Numerical simulation included both simple single degree-of-freedom dynamics models, and more complex computational fluid dynamics and multi-body simulation models. Experimentation involved full-scale testing of a rail car passed by a high-speed train on an adjacent track, and measurement of train-induced airflow and forces on cylindrical dummies from a passing train.

14. SUBJECT TERMS
high-speed trains, window mount, window glazing, double-stacked containers, station platform, aerodynamic interactions, aerodynamic loads, transient loads, double-stacked well car, induced airflow, slipstream, passing train, aerodynamic effect, railroad and railway aerodynamics, trackside

15. NUMBER OF PAGES
257

16. PRICE CODE

17. SECURITY CLASSIFICATION OF REPORT	18. SECURITY CLASSIFICATION OF THIS PAGE	19. SECURITY CLASSIFICATION OF ABSTRACT	20. LIMITATION OF ABSTRACT
Unclassified	Unclassified	Unclassified	Unlimited

NSN 7540-01-280-5500
Standard Form 298 (Rev. 2-89)
Prescribed by ANSI Std. 239-18
298-102

METRIC/ENGLISH CONVERSION FACTORS

ENGLISH TO METRIC	METRIC TO ENGLISH
LENGTH (APPROXIMATE)	**LENGTH (APPROXIMATE)**
1 inch (in) = 2.5 centimeters (cm)	1 millimeter (mm) = 0.04 inch (in)
1 foot (ft) = 30 centimeters (cm)	1 centimeter (cm) = 0.4 inch (in)
1 yard (yd) = 0.9 meter (m)	1 meter (m) = 3.3 feet (ft)
1 mile (mi) = 1.6 kilometers (km)	1 meter (m) = 1.1 yards (yd)
	1 kilometer (km) = 0.6 mile (mi)
AREA (APPROXIMATE)	**AREA (APPROXIMATE)**
1 square inch (sq in, in^2) = 6.5 square centimeters (cm^2)	1 square centimeter (cm^2) = 0.16 square inch (sq in, in^2)
1 square foot (sq ft, ft^2) = 0.09 square meter (m^2)	1 square meter (m^2) = 1.2 square yards (sq yd, yd^2)
1 square yard (sq yd, yd^2) = 0.8 square meter (m^2)	1 square kilometer (km^2) = 0.4 square mile (sq mi, mi^2)
1 square mile (sq mi, mi^2) = 2.6 square kilometers (km^2)	10,000 square meters (m^2) = 1 hectare (ha) = 2.5 acres
1 acre = 0.4 hectare (he) = 4,000 square meters (m^2)	
MASS - WEIGHT (APPROXIMATE)	**MASS - WEIGHT (APPROXIMATE)**
1 ounce (oz) = 28 grams (gm)	1 gram (gm) = 0.036 ounce (oz)
1 pound (lb) = 0.45 kilogram (kg)	1 kilogram (kg) = 2.2 pounds (lb)
1 short ton = 2,000 pounds (lb) = 0.9 tonne (t)	1 tonne (t) = 1,000 kilograms (kg)
	= 1.1 short tons
VOLUME (APPROXIMATE)	**VOLUME (APPROXIMATE)**
1 teaspoon (tsp) = 5 milliliters (ml)	1 milliliter (ml) = 0.03 fluid ounce (fl oz)
1 tablespoon (tbsp) = 15 milliliters (ml)	1 liter (l) = 2.1 pints (pt)
1 fluid ounce (fl oz) = 30 milliliters (ml)	1 liter (l) = 1.06 quarts (qt)
1 cup (c) = 0.24 liter (l)	1 liter (l) = 0.26 gallon (gal)
1 pint (pt) = 0.47 liter (l)	
1 quart (qt) = 0.96 liter (l)	
1 gallon (gal) = 3.8 liters (l)	
1 cubic foot (cu ft, ft^3) = 0.03 cubic meter (m^3)	1 cubic meter (m^3) = 36 cubic feet (cu ft, ft^3)
1 cubic yard (cu yd, yd^3) = 0.76 cubic meter (m^3)	1 cubic meter (m^3) = 1.3 cubic yards (cu yd, yd^3)
TEMPERATURE (EXACT)	**TEMPERATURE (EXACT)**
[(x-32)(5/9)] □F = y □C	[(9/5) y + 32] □C = x □F

QUICK INCH - CENTIMETER LENGTH CONVERSION

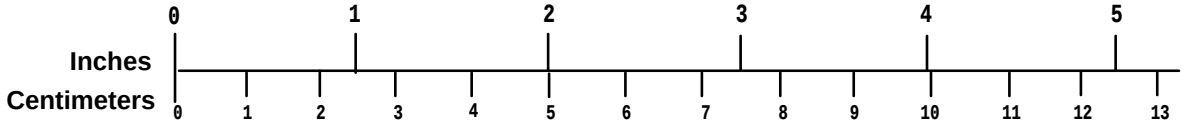

QUICK FAHRENHEIT - CELSIUS TEMPERATURE CONVERSION

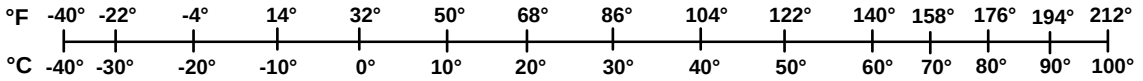

For more exact and or other conversion factors, see NIST Miscellaneous Publication 286, Units of Weights and Measures. Price $2.50 SD Catalog No. C13 10286

Updated 6/17/98

Acknowledgement

The success of this project was due to numerous organizations and individuals including the United States Department of Transportation's (USDOT) Federal Railroad Administration (FRA) and the Volpe National Transportation Systems Center (Volpe), the National Railroad Passenger Corporation (Amtrak), and support contractors. These support contractors include:

(1) Parsons Brinckerhoff Quade and Douglas, Inc. (PB),
(2) Applied Research Associates, Inc. (ARA),
(3) Transportation Technology Center, Inc. (TTCI),
(4) GEOCOMP Corporation,
(5) SYSTRA Consulting, Inc., and
(6) French National Railways (Société Nationale des Chemins de Fer Français or SNCF)

I want to acknowledge the many people from various organizations that participated in this research.

This work was performed as part of the Railroad Systems Safety Program sponsored by the FRA's Office of Research and Development. I would like to thank the following people for their support:

Claire Orth, Division Chief, Equipment and Operating Practices Research Division, Office of Research and Development, FRA.
Tom Tsai, Program Manager, Equipment and Operating Practices Research Division, Office of Research and Development, FRA.

I would like to thank the following colleagues at the Volpe Center:

Robert Dorer, Acting Deputy Director of the Office of Safety and Security, for his extensive support in this research endeavor.
James Lamond, Project Manager of the Railroad Systems Division, and manager of the aerodynamics program, for his steady support throughout this research effort.
Kenny William, Mechanical Engineer of the Structures and Dynamics Division, for his computer programming expertise in processing the massive quantity of data.

The following individuals are acknowledged for their participation in this research:

Samuel Holmes, Principal Engineer at ARA, performed the computational fluid dynamics modeling study and generated the aerodynamic forces on double-stack well cars from a passing train.

Martin Schroeder, Senior Engineer at TTCI, performed the rail dynamics modeling study on the dynamic response of double-stack well cars from the aerodynamic forces of a passing train.

Robert MacNeill, Project Engineer at ARA, performed the full-scale experimental study on the aerodynamic interaction of a double-stack well car with a passing train.

Sam Liao, Senior Professional Associate at PB, provided project management support on the study of aerodynamic effects from trains passing station platforms.

William Kennedy, Vice President at PB, performed the study on train-induced airflow on station platforms.

Martin Hawkes, Project Manager at GEOCOMP Corporation, performed the pitot-static tube airflow measurements and data processing.

Christophe Jehannin, Project Manger at SYSTRA Consulting, Inc., and Jean-Michel Pissot, Direction de l'Ingénierie at SNCF, conducted a test to measure aerodynamic forces on cylindrical dummies from passing trains.

George Binns and David Warner of Amtrak for their support and cooperation in conducting the test along Amtrak's right-of-way.

Thanks should also be extended to the individuals of the test crew for their responses on their experiences to passing trains.

Table of Contents

Part 2

Analysis and Evaluation

List of Figures

List of Tables

Executive Summary

As train speed increases, the train's aerodynamic force on people and objects becomes stronger. This force can have an adverse effect on adjacent trains and equipment, and might jeopardize the safety of people in proximity to the passing train. Consequently, with the inception of high-speed train operation in the United States, a safety evaluation was undertaken by the Federal Railroad Administration (FRA) of the United States Department of Transportation to determine the effects that the aerodynamic force generated by a passing high-speed train have on other trains on an adjacent track, and on people in proximity to a passing train.

Two safety issues are raised on the aerodynamic effects of a passing train on its surroundings. First, a high-speed train passing other trains on an adjacent track exerts aerodynamic pressure that can affect the structural integrity of window mount and glazing, and the stability of the railroad car being passed. Second, as a high-speed train passes train stations immediately adjacent to the platform without stopping, people and objects on these station platforms are exposed to strong airflow causing debris and objects to be blown and people to lose their balance. This safety issue also extends to railroad workers on trackside as a high-speed train passes.

The objective of the research was to obtain aerodynamic data on passing trains, and to assess its effects on other trains being passed, as well as on people in proximity to the passing trains. The study entailed both numerical simulation and experimentation. Numerical simulation included both simple single degree-of-freedom dynamics models, and more complex computational fluid dynamics and multi-body simulation models. Experimentation involved full-scale testing of a rail car passed by a high-speed train on an adjacent track, and measurement of train-induced airflow and forces on cylindrical dummies from a passing train.

Part 1: Digest of Research

The digest of research is a review on the work that has been completed with the details having been described in a number of reports. This includes studies sponsored by FRA since 1995 on the aerodynamic effects from passing trains.

Train Passing Well Car with Double-Stacked Containers

Numerical simulation was performed to compute the response of a double-stack well car from aerodynamic interaction with a passing high-speed passenger train. The results were examined for the potential of derailment and the stability of the containers. The five-unit articulated double-stack well car with empty containers produced strong dynamic response leading to wheel unloading or high lateral wheel force. The lateral to vertical wheel force ratio was much lower reducing the potential of derailment when all the containers were loaded. Results from this study found that the containers should not become dislodged.

A full-scale test was performed to measure the aerodynamic pressure and roll response on a stationary double-stack well car as a high-speed turbine-electric locomotive pulling two passenger cars passes by on an adjacent track. The comparison between computed and measured pressures is generally very good. None of the roll angles were very large, with the maximum zero-to-peak roll angle of 0.312°, producing a maximum change in lateral displacement of 30.1 mm (1.184 in) at the top of the container, when the train passed by at 177 km/h (110 mph).

Passing Train on Window Mount and Glazing

The potential for damage to the window was considered by mathematical modeling of an Acela Express train passing a bi-level Kawasaki passenger car. An Acela Express train traveling at 241 km/h (150 mph) with a headwind of 80 km/h (50 mph) passing a Kawasaki car traveling in the opposite direction at 129 km/h (80 mph), does not appear to have sufficient force to dislodge the window glazing on the passenger car. Sufficient data does not exist to arrive at a conclusion when the Acela Express train overtakes the Kawasaki car.

Airflow Induced by a Passing Train

An Acela Express train and an Amfleet train were modeled to obtain the induced airflow velocity as the train passes a station platform. A numerical simulation of an Acela Express train traveling at 241 km/h (150 mph) and an Amfleet train at 201 km/h (125 mph) induced about the same maximum longitudinal airflow velocities. The Amfleet train produced the strongest airflow from the boundary layer, while the strongest airflow for the Acela Express train came from the wake. The induced airflow from the Acela Express train was lower on a high-level than on a low-level platform.

A full-scale test was conducted using pitot-static tubes to measure airflow velocities induced from a passing Acela Express train, and Amfleet train. Airflow measured from the Acela Express train was higher than from the Amfleet train when they passed by at their operating speeds. The airflow velocity decreases with increased lateral distance from the train, or with increased height from the track. The maximum value of airflow for the Acela Express train occurs usually at the tail of the train, whereas the maximum

value of airflow for the Amfleet train is usually at the head of the train. The main features between test data and results of numerical simulation are generally in good agreement.

Test Measurement of Force on Object from Passing Train

A full-scale test was conducted on a low-level train station platform in Mansfield, Massachusetts to measure the force on two circular cylindrical instrumented dummies (CIDs) from the aerodynamic interaction with a passing train. When the mean force on the CIDs is normalized with respect to the square of the train speed, the Acela Express train produced the lowest force while the Amfleet/AEM-7 train produced the highest force. The Amfleet/AEM-7 train produced an aerodynamic force on the CIDs that is a factor of 2.4 higher than the Acela Express train, and the Amfleet/HHP-8 train is a factor of 1.8 higher than the Acela Express train. When the trains are scaled to the train's maximum nominal operating speed, the Acela Express train passing at a speed of 241 km/h (150 mph) produced a lower force on the CIDs than the passing Amfleet train at the lower speed of 201 km/h (125 mph).

Part 2: Analysis and Evaluation

Studies were conducted by the Volpe National Transportation Systems Center to provide a more comprehensive analysis and evaluation of the results presented in the digest of research.

Numerical Simulation of Rail Car Roll Response to Aerodynamic Loading

A single degree-of-freedom mathematical carbody roll model was created to simulate the dynamic roll response of a rail car from transient aerodynamic force input. This study extended the previous research results by including a broader range of train passing conditions. The responses of carbody roll from the effects of altitude, ambient wind, passing train speed and closing speed, and unbalanced speed on curved track were studied. A comparison of the carbody roll angle for a stationary double-stack well car from aerodynamic force input between simulation and test data is in very good agreement.

Measurements of Airflow and Aerodynamic Load from Full-Scale Test of Passing Train

The airflow measured from pitot-static tubes and forces measured on CIDs from the test at Mansfield, Massachusetts were further processed and analyzed in detail. Based on this data, the aerodynamic effects on people are assessed from the wind speed criteria of Murakami and Deguchi with an indicated minimum distance from a passing train as follows:

Recommended Minimum Distances for People Exposed to the Aerodynamic Effects of a Passing Train

	Minimum Lateral Distance*		
	Distance from Centerline of Nearest Track	Distance from Outer Edge of Nearest Rail	Nominal Distance from Side of Train
Member of Public on Low-Level Passenger Platform	3.12 m (123 in)	2.33 m (92 in)	1.6 m (63 in)
Worker on Trackside at Low-Level Platform Height	2.72 m (107 in)	1.93 m (76 in)	1.2 m (47 in)

*Amfleet/AEM-7 and Amfleet/HHP-8 trains passing at a speed no greater than 201 km/h (125 mph); Acela Express train passing at a speed no greater than 241 km/h (150 mph).

Human Response in Proximity to Passing Train

A single degree-of-freedom mathematical model of a mannequin was created as an instrument to map the stability boundary for a simple standing object that can be applied to evaluate the aerodynamic data produced from a passing train. A method to assess the strength of the airflow data is to relate it to the stability boundaries of the mathematical mannequin. The stability boundaries are interpreted in terms of the Beaufort scale where the effects on people can be assessed. A comparison is made between the effects on people based on the dynamic response of a mathematical mannequin, with the wind speed criteria of Murakami and Deguchi based on wind speed averaged over 3 s. Both methods predict similar effects on people.

1. Introduction

A moving train causes a disturbance to the surrounding air whose effects are insignificant at low train speeds. As train speed increases, the train's aerodynamic force on people and objects becomes stronger, and its effect on people and objects becomes more significant. This force can have an adverse effect on adjacent trains and equipment, and might jeopardize the safety of people in proximity to the passing train. Consequently, with the inception of high-speed train operation in the United States, a safety evaluation was undertaken by the Federal Railroad Administration (FRA) to determine the effects that the aerodynamic force generated by a passing high-speed train has on other trains on an adjacent track, and on people in proximity to a passing train.

In the United States, high-speed passenger trains such as Amtrak's Acela Express trains have been operating in the Northeast Corridor. Figure 1 shows an Acela Express train passing a train station. Two safety issues have been raised on the aerodynamic effects of a passing train on its surroundings. First, a high-speed train passing other trains on an adjacent track will exert aerodynamic pressures on the other trains, with the pressures being strong at high speeds and close track center spacing (the track center distance along parts of the Northeast Corridor is at 3.962 m (13 ft) center distance but as close as 3.658 m (12 ft) at best fit areas). The aerodynamic interactions of a high-speed train passing other trains can have effects on the structures of the trains being passed. The structural integrity of window mounts and glazings, and the stability of the railroad cars being passed may be affected. Second, as a high-speed train passes some train stations immediately adjacent to the platform without stopping, people and objects on these station platforms can be exposed to strong airflow causing debris and objects to be blown and people to lose their balance. This safety issue also extends to railroad workers on the trackside as a high-speed train passes.

Figure 1. Acela Express Train

These two issues, the aerodynamic interaction between passing trains, and the aerodynamic effects of trains passing people on station platforms, have been the focus of research. The research was to obtain aerodynamic data on passing trains, and to assess its effects on other trains being passed, and on people in proximity to the passing trains. This entailed both numerical simulation and experimentation. Numerical simulation included both simple single degree-of-freedom dynamics models, and more complex computational fluid dynamics (CFD) and multi-body simulation models.

Experimentation involved full-scale testing of a rail car passed by a high-speed train on an adjacent track, and measurement of train-induced airflow and forces on cylindrical dummies from a passing train.

This report discusses the research performed by the Volpe National Transportation Systems Center (Volpe) and by organizations contracted for this research, to support the FRA's Railroad Systems Safety program. The scope of this report includes the studies performed since the FRA initiated this research in 1995 to address safety issues related to the aerodynamic effects of high-speed trains, particularly with the commencement of high-speed Acela Express train service in the Northeast Corridor.

This report is organized in two parts. Part 1 provides a digest of research that reviews the work that has been completed, the details having been described in a number of reports. The research review of Part 1 brings together all the studies sponsored by FRA since 1995 on the aerodynamic effects from passing trains. A progress review is presented that includes a description of organizations outside of the United States that are engaged in similar research, and a description of reports produced for FRA. The remainder of Part 1 is a review of the work that has been completed under the FRA program with a summary of results. Part 2 provides an analysis and evaluation with detailed studies that extend the results found in Part 1. In addition to contractor studies, Volpe also conducted studies, which are reported in Part 2. Volpe studies were conducted to provide a more comprehensive analysis of the results in Part 1, and to better understand the aerodynamic interactions, and its effects of a passing train on other trains, and on people. An evaluation is provided of the research along with conclusions and recommendations.

PART 1

DIGEST OF RESEARCH

2. Progress Review

This progress review covers work that was performed in support of the FRA's research that began in 1995 on the aerodynamic effects of high-speed trains as it impacts safety. This research was related to the approaching inception of high-speed passenger train operation in the Northeast Corridor of the United States.

Some of the problems that were addressed in this research are:

- Derailment potential of a double-stack well car and the stability of containers when passed by a high-speed train.
- Strength of window mount and glazing integrity on a passenger car when passed by a high-speed train.
- Safety of people on station platforms when passed by a high-speed train.

Following the assessment based on the literature review, organizations were contracted by Volpe to perform mathematical modeling and experimentation to acquire data on the aerodynamic effects of conventional trains, and on high-speed Acela Express trains, which that were to be operational in the Northeast Corridor.

2.1. Literature Survey and Assessment

The program on the aerodynamic effects of passing trains began with a literature study by Volpe (Lee 1999). The study identified relevant sources of information and data available to assess the aerodynamic effects of a train traveling at high speeds passing another train on an adjacent track, and a train passing a station at high speeds and its effects on people on the station platform.

The following conclusions were drawn from this study:

> The aerodynamic forces exerted on the window glazing during train passage were determined. For trains passing each other at speeds of 150 mph [241 km/h], it is unlikely that these forces will cause the glazing to crack. An assessment of the strength of the glazing attachment will depend on specific, detailed design of the windows.
>
> The aerodynamic forces experienced by a person from pressures and induced airflow of a passing train were determined. For persons situated within 6.6 ft [2 m] from the side of a train passing a station platform at a speed of 150 mph [241 km/h], the effects of pressure and induced airflow are high enough to be a safety issue. The distance of 6.6 ft [2 m] does not represent a safety limit, but it

> does indicate that when people are situated within that distance to a passing train, this can be a safety issue.
>
> When a train is passing a station platform at high speeds, the wake effect of the train with its turbulent fluctuations and buffeting in the air, along with any dust and debris that is blown or propelled, is a serious issue regarding the comfort and safety of people on the platform. (Lee 1999)

From these conclusions, Volpe recommendations included:

> Identify the equipment and fixtures on trains, and on structures along the wayside that are a safety issue when exposed to the aerodynamic effects of pressure and airflow generated from a passing train.
>
> Identify rail cars that are not designed for high-speed operation, particularly cars with large windows, or loosely fitted windows such as those that are designed to be opened. Obtain design information and data on the windows and glazing for these cars to perform a structural integrity assessment on the window glazing to determine if cracking or dislodgement will occur from the aerodynamic pressure acting on the glazing, also factoring in the effects of material fatigue. The assessment should consider the different types of glazing and glazing systems (frames and gaskets) used throughout the industry.
>
> Identify conditions that will impact the magnitude of the data in this study, such as natural wind components, and structures along the track, such as the presence of steep embankments, overpasses, tunnels, and assess their effects on the results.
>
> Confirm the boundaries on passing train speed and distance from the train in terms of human comfort tolerance levels as they impact the safety of people on station platforms. A realistic limiting boundary should include the effects on people when they are exposed to the combined actions of pressure, wind, noise, and blown debris, particularly from the turbulent actions of the wake produced by the passing train. (Lee 1999)

2.2. Rails-with-Trails

Increasing development has occurred of pedestrian pathways constructed on or adjacent to active railroad right-of-way referred to as rails-with-trails (RWT). As RWTs are planned or situated adjacent to high-speed rail lines, the aerodynamic effects from a passing high-speed train can be a safety issue. The research results on the aerodynamic effects from passing trains have been applied to address the safety concern of RWT development (Birk et al 2002; Birk 2003).

Certain considerations that apply to RWT may not be included to a station platform. Different requirements may be recognized in establishing a safe distance between the

track and people on a station platform, and a setback distance (distance measured from centerline of nearest track to edge of paved trail) between the track and a trail. People in RWT can include strollers, people pushing baby carriages, bicyclists, etc. Therefore, different expectations other than safety are considered by people using RWT, which includes comfort and other quality of life factors (noise, startling effects, etc.).

2.3. Compendium of Reports

As part of the research effort, Volpe conducted an assessment based on information obtained from a literature survey, and organizations were contracted by Volpe to study specific facets of the passing train problem. These studies involved mathematical modeling, experimentation, and performing field surveys. The results of this research activity are documented in reports that will be described briefly.

Reference: Liao et al 1999

This study examines the aerodynamic effects that high-speed trains can be expected to have on the safety and comfort of people in and around the Northeast Corridor stations, focusing on the anticipated induced airflow effects on station facilities in the Corridor. This included:

- Numerical modeling of aerodynamic effects from passing trains using the FLUENT™ CFD program.
- Testing to measure the airflow induced by passing trains.
- Visual field survey of selected train stations to obtain information for assessing the impact of Acela Express trains passing the stations at high speeds.

Reference: Lee 1999

This study was to assess the potential hazards created from the aerodynamic effects of passing high-speed trains at speeds of 241 km/h (150 mph). It specifically addresses the hazards to window glazing on passenger trains and to people on station platforms. A literature review was conducted, and the results of that review served as a base for the studies to follow.

Reference: Holmes, Schroeder, and Toma 2000; Holmes and Schroeder 2002

This study examines the potential safety hazards to existing rail traffic operating in the Northeast Corridor from aerodynamic loads generated by the Acela Express high-speed passenger train. It specifically addresses the aerodynamic interaction of a high-speed Acela Express passenger train passing a double-stack well car on an adjacent track. Results were obtained using the Acusolve™ CFD program, and the train dynamics simulation program NUCARS™. Three scenarios were considered:

- Derailment of double-stack well car when passed by an Acela Express train.
- Breaking loose or dislodgement of shipping containers from the double-stack well car when passed by an Acela Express train.
- Breaking or blow-out of windows in a passenger train when passed by an Acela Express train.

Reference: MacNeill, Holmes, and Lee 2002

A full-scale test was performed to measure the aerodynamic pressure and roll angle on a well car with double-stacked containers as a high-speed passenger train passes by on an adjacent track.

Reference: Tsai, Lamond, and Lee 2003

A review of studies conducted by the FRA and the Volpe Center on the aerodynamic effects of trains passing double-stack well cars and station platforms. Initial results are presented on train-induced airflow velocity and forces on cylindrical dummies from trains passing the station platform.

2.4. Information Exchange

Many countries outside of the United States have been conducting research on the aerodynamic effects of passing high-speed trains, including Japan, France, and other European countries.

In Japan, the Railway Technical Research Institute (RTRI) (1998) conducts railway research with aerodynamics being a topic of study as the need arises. The RTRI's Large-Scale Low-Noise Wind tunnel for studying railway aerodynamics was opened in June of 1996 at Maihara-cho in Shiga prefecture. A large belt is used in the wind tunnel to simulate the airflow between the train model and the ground.

In Europe, a research program was formed in January of 1996 called Transient Aerodynamics for Railway System Optimisation (TRANSAERO) to study the problems of transient aerodynamics in railway operations (Gregoire, Eckl, and Malfattti n.d.). This program is a partnership of various institutions, and of three railways (originally together with BR Research) from France, Germany, and Italy: Société Nationale des Chemins de Fer Français (SNCF), Deutsche Bahn A.G. (DB AG), and Ferrovie dello Stato (FS) respectively (Table 1). Some of the problems studied include effects of side-wind gusts on high-speed trains, forces generated from passing of train nose, and generation of pressure waves from train tunnel entry. This was a 3 year program that ended in May of 1999.

Complementing the earlier research from TRANSAERO is a European research project called Railway Aerodynamics of Passing Interactions with Dynamic Effects (RAPIDE). This is a consortium organized as a collaborative research effort by European railway and industrial partners to investigate transient aerodynamic phenomena associated with high-speed trains (RAPIDE 2001). The consortium consists of: AEA Technology Rail, DB AG, SNCF, Bombardier Transportation, FS, Motor Industries Research Association (MIRA), and RUAG Aerospace (Table 1). In this project, it specifically addressed the periodic and oscillatory airflow from the wake of a passing train, and its effects on people and objects on the wayside and on the dynamic and structural behavior of trains.

Table 1. Organizations Performing Research in Railway Aerodynamics

Country	Organization	Resource
Japan	Railway Technical Research Institute (RTRI) Railway research center established in 1986 (includes former Railway Technical Research Institute and Railway Labor Science Institute) to: • develop basic technology and research applications • promote technology transfer to Japan Railways (JR) companies • promote the Maglev (magnetic levitation) system • study safety measures	Capabilities include Large-Scale Low-Noise Wind tunnel.
Great Britain	AEA Technology Rail (Formerly as BR Research) Commercial company that performs research, testing, and consultant service for railway companies.	Capabilities include full-scale site testing, on-site wind tunnel testing, reduced scale tests on moving model rig (MMR), CFD modeling, and subjective pressure comfort tests in transient pressure chamber facility.
Germany	Deutsche Bahn A.G. (DB AG: German Rail) German Rail Transport company.	Research performed by aerodynamics and air conditioning department TZF 102.
France	Société Nationale des Chemins de Fer Français (SNCF: French National Railways) National Rail Transport company.	Capabilities include full-scale site testing, Laser Doppler velocimetry, CFD software (STAR-CD, START, TG-FLO)
Sweden	Bombardier Transportation Railway industry company, acquired Adtranz (ABB Daimler-Benz Transportation) in 2001, that does research, development, design, and manufacturing.	Research performed by NEG2 department.

Continue

Table 1: Organizations Performing Research in Railway Aerodynamics

(Continued)

Country	Organization	Resource
Italy	Trenitalia (FS: Italian Railways) (Formerly Ferrovie dello Stato S.p.A.) Italian National Railway company	Capabilities include surveys of human response, full-scale testing, and model simulation.
United Kingdom	Motor Industries Research Association (MIRA) Provides engineering development and research services to automotive industry.	Capabilities include full-scale wind tunnel, model wind tunnel (up to 40% scale) with moving ground plane, climatic wind tunnel, fluids engineering center, CFD software (EXA Power Flow, Star CD, Fluent, ICEM CFD, Altair Hypermesh, EnSight, Flowmaster, I DEAS).
Switzerland	RUAG Aerospace (Formerly as SF Emmen) Aerospace company that is part of RUAG that does development, manufacturing, assembly, maintenance and upgrade of aircraft, helicopter, drones, missile, C31, and air defense systems.	Performs research in experimental and theoretical aerodynamics by the Aerodynamics and Flight Mechanics Department. Capabilities include three wind tunnels, moving belt facility, CFD, ICEMCFD software for mesh generation, Cray computers at Swiss Federal Institute of Technology (EPFL).

3. Train Passing Well Car with Double-Stacked Containers

An operational hazard that the railroads have known about is the stability of certain railroad cars when exposed to an unbalanced side force due to high wind. For this reason, railroads impose operational restrictions during high wind conditions.[1] In addition to wind, railroad cars are also exposed to unbalanced side forces from aerodynamic pressure produced when being passed by another train on an adjacent track.

An interest exists in the aerodynamic interaction of a passenger train traveling at a high speed passing another train on adjacent track, especially when high speed passenger train service operates at speeds of 241 km/h (150 mph) in mixed traffic with freight trains. Well cars with empty double-stack containers are of particular interest when passed by a high-speed train, because the resultant side force on the containers can be significant due to its great height and large vertical surface area. This aerodynamic side force applied to the light carbody, in addition to any wind that might be present, can lead to the possibility of containers dislodging and falling over, or to an adverse dynamic response of the double-stack well car with a risk of derailment.

The aerodynamic interaction between passing trains and the dynamic train/track response of the train from the transient aerodynamic force input was the subject of study in the European RAPIDE project. The aerodynamic load on the train did not cause significant track force, and the force was found to be within the same range as input from track irregularity (RAPIDE 2001). It was found that the high-speed Inter-City Express 2 (ICE2) train traveling at 350 km/h (217 mph) passing another ICE2 train and a slower train remained within a safe limit from derailment (Minnis and Denti 2001).

A study was conducted to determine the response of a double-stack well car from aerodynamic interaction with a passing high-speed passenger train. Numerical simulation was performed to compute the response of a double-stack well car, and the results were examined for the potential of derailment and the stability of the containers (Holmes, Schroeder, and Toma 2000; Holmes and Schroeder 2002). A full-scale test was performed to measure the aerodynamic loading on a stationary double-stack well car as a train passes on an adjacent track, and the test data was compared with modeling results (MacNeill, Lynch, and Schroeder 2001; MacNeill, Holmes, and Lee 2002).

3.1. Mathematical Modeling of Double-Stack Well Car Aerodynamic Interaction and Response

Computer models were created in this study to simulate a high-speed passenger train passing a freight train with double-stack well cars. The approach was to first compute the aerodynamic pressures on a double-stack well car as the two trains pass each other

[1]Steven E. Forsberg (BNSF Railway). Letter to the author, November 20, 2000.

using the CFD program called Acusolve™ for solving incompressible flow problems. The pressure is integrated over the surface of the double-stack well car to obtain the force and moment. These aerodynamic loads are then used as applied force and moment inputs to the rail car multibody dynamic simulation program NUCARS™ to obtain its dynamic response. In NUCARS™ where the double-stack well cars are modeled, the aerodynamic loads are applied to each double-stack well car sequentially to simulate the effects of being passed by another train. Fifteen cases were evaluated with varying train consist types, speeds, and directions, as well as ambient wind speeds and directions. Some of these were worst-case scenarios that may not necessarily represent normal railroad operating conditions.

Two trains were modeled: an Acela Express passenger train, and a freight train with well cars carrying double-stacked containers (Table 45 and Table 46 of the Appendix). The model of the freight train is a five-unit articulated well car where each connected unit shares the same two-axle truck. In contrast to freight cars connected by independent couplers that transmit principally a longitudinal force between cars, in the articulated well car, the units with shared trucks are joined to transmit forces in longitudinal, lateral, and vertical directions. Consequently, the units in the articulated well car are dynamically coupled to a greater extent than independently coupled freight cars, creating a potential for strong dynamic interaction between the units. At the nonarticulated ends of the unit (the end trucks on the first and fifth unit), the trucks are not shared, so that both axles of the truck are supporting the same unit. This is significant because each axle on those non-shared trucks is more lightly loaded than those on the shared trucks.

In modeling the two trains passing each other, only the pressures generated from the head-end segment or the tail-end segment of the Acela Express train are applied to the double-stack well cars to simulate the passage of the Acela Express train. Therefore, when the Acela Express train meets a double-stack well car, it is modeled with the Acela Express nose passing, but without the passage of the tail end of the Acela Express. In an analogous fashion, to simulate the passage of the tail end of the Acela Express train, the passage of the head end of the Acela Express train is not included. Only two cases were simulated with the passage of the tail end of the Acela Express train.

The dynamic response of the double-stack well car is influenced by the strength and duration of the pressure pulse from the passing train. Factors that affect the strength of the pressure pulse from the passing train include: train speed, train cross-sectional area, lateral clearance between trains, ground clearance, nose geometry, and environmental conditions such as wind and other nearby structures. The duration of the pressure pulse is governed by the closing speed of the two trains, which is determined by the speed of each train, and whether the trains are passing each other in opposite directions, or whether one train is overtaking the other train.

3.1.1. Train/Track Interaction of Double-Stack Well Car

The two passing trains were modeled with a track center distance of 3.7 m (12 ft). The simulation included variations in the speed and direction of each train, and the speed and direction of the wind. A lateral side force is produced on the double-stack well car generated by the aerodynamic pressures of the passing Acela Express train, most significantly by the strong pressure pulse at the nose. This causes an initial push on the double-stack well car away from the Acela Express train and is followed immediately by a pulling force. This results in a roll and yaw moment exerted on each double-stack well car, as the pressure pulse from the passing Acela Express train travels from one end of the container freight train to the other end.

Pressure coefficient from CFD model simulation was computed for the case where an Acela Express train traveling at 241 km/h (150 mph) passes a stationary double-stack well car. The pressure was computed at the center of the stationary double-stack well car, at 1.96 m (77.2 in) from the top of the rail, and at a nominal distance of 0.79 m (31.1 in) between the side of the double-stack well car and the side of the Acela Express train. Figure 2 is a plot of the computed pressure coefficients on the double-stack well car, with the maximum to minimum peaks in pressure coefficients from 0.34 to -0.36, for a maximum peak-to-peak pressure coefficient of $\Delta C_p = -0.70$.

Simulations were performed for three aerodynamic loading conditions on the double-stack well car from a passing train including maximum peak-to-peak difference in lateral force, maximum lateral impulse, and synchronized resonance loading. The speeds of the two passing trains and ambient wind speed were selected to represent some worst-case scenarios. Maximum peak-to-peak difference in aerodynamic force was created when the Acela Express train traveling at the highest speed, and with the greatest headwind, passes the double-stack well car in the opposite direction. This results in a pressure pulse of very short duration exerted on the double-stack well car where the dynamic response is minimal because the short duration of the aerodynamic load is out of its resonance frequency range. When the Acela Express train passes the double-stack well car in the same direction, this leads to either an aerodynamic loading on the well car that creates maximum aerodynamic impulse (maximum product of force and duration), or a load duration that synchronizes with the articulated car resonance mode. These two loading conditions are the ones where the double-stack well car dynamic response exceeds the derailment criteria as defined in the Association of American Railroads (AAR) performance specifications for wheel unloading and wheel/rail lateral to vertical force ratio (L/V).

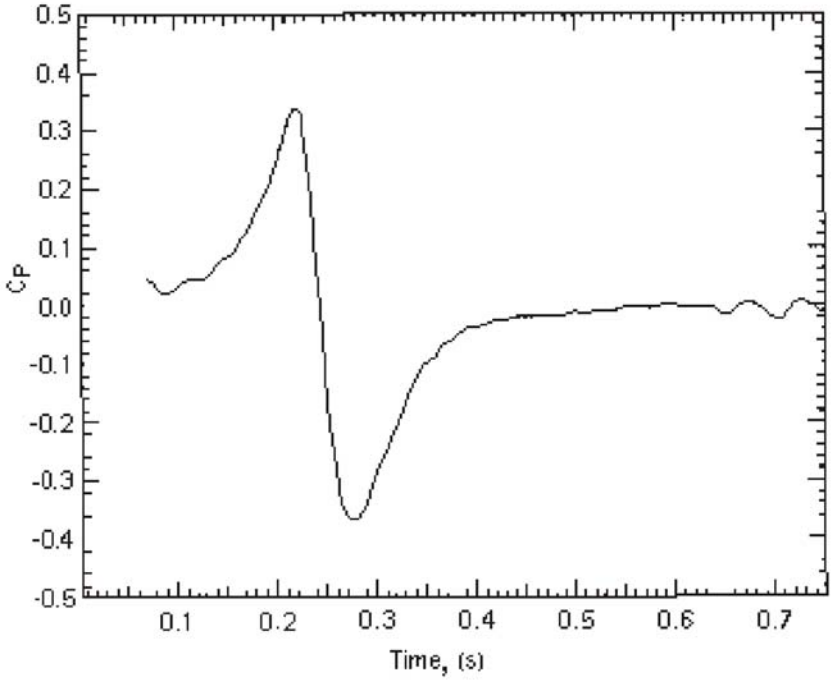

Figure 2. Computed Pressure Coefficient on Double-Stack Well Car from Aerodynamic Interaction with a Passing Acela Express Train

The five-unit articulated double-stack well car with empty containers produced the strongest response when passed by an Acela Express train traveling in the same direction. The lateral aerodynamic loading applied to the double-stack well car did not produce significant carbody roll, but it did produce strong dynamic response leading to wheel unloading or high lateral wheel force. In maximum lateral impulse interaction, the lateral load can produce significant wheel unloading on the empty double-stack well car at the end unit. During interaction with synchronized resonance loading, the lateral aerodynamic loading applied to the double-stack well car produced strong dynamic response in the form of lateral displacement to the wheels. This interaction results in the wheel flanging with high L/V, or large wheel unloading or wheel lift on the wheel opposite the flanging wheel. Five cases are shown with a variety of loading conditions in Table 2 where the five-unit articulated double-stack well car produced either large or total wheel unloading, or with high L/V, initiated by the passing of the Acela Express train. The worst response for the articulated double-stack well car occurs for the nonshared trucks on the first and last units where each axle on those trucks is more lightly loaded than those on the shared trucks. When the Acela Express train passes the articulated double-stack well car with both trains moving in the same direction, the double-stack well car was more likely to be in the frequency range of either the roll or yaw carbody vibration modes, or the lateral resonance modes of the articulated double-stack well car. This operating condition produces the strongest dynamic response to the articulated double-stack well car.

For the cases studied, the greatest potential for derailment on the five-unit articulated double-stack well car was when all the containers are empty, and with the presence of a strong headwind on the Acela Express train or a strong crosswind. The worst response occurred on the non-shared trucks of the first and last cars where each axle on those trucks is more lightly loaded than those on the shared trucks. The conditions improved in a partially loaded configuration, where only the containers at the end units are loaded. With all the containers loaded, vertical wheel load increased and the wheel/rail L/V was much lower, which met performance specification. The only exception was for case 9 (Table 2) when the Acela Express train passed in the opposite direction to the loaded double-stack well car with a crosswind, that significant wheel unloading occurred.

Table 2. Dynamic Response of Five-Unit Articulated Double-Stack Well Car Not Meeting AAR Chapter XI Performance Specifications*

Case	Train Velocity		Wind Velocity***		Response Failing Performance Specification**
	Acela Express Train	Double-Stack Well Car	U_x (Head or Tail Winds on Passing Train)	U_y (Crosswind)	
8	241 km/h (150 mph)	80 km/h (50 mph)	-80 km/h (-50 mph)	0	Maximum Lateral Impulse Coincident Pass with Headwind • low vertical wheel load (E)
9	241 km/h (150 mph)	-80 km/h (-50 mph)	0	-80 km/h (-50 mph)	Opposing Pass with Crosswind • wheel lift (E),(EL) • low vertical wheel load (L) • high L/V (E), (EL)
12	241 km/h (150 mph)	48 km/h (30 mph)	-80 km/h (-50 mph)	0	Synchronized Phased Loading Coincident Pass with Headwind • wheel lift (E) • high L/V (E)
14	241 km/h (150 mph)	80 km/h (50 mph)	-80 km/h (-50 mph)	-80 km/h (-50 mph)	Coincident Pass with Headwind and Crosswind • wheel lift (E) • low vertical wheel load (EL) • high L/V (E), (EL)
15	193 km/h (120 mph)	80 km/h (50 mph)	-80 km/h (-50 mph)	0	Synchronized Phased Loading Coincident Pass with Headwind • wheel lift (E), (EL) • high L/V (E), (EL)

*AAR Chapter XI performance specifications require the wheel force not fall below 10 percent of static wheel load for 50 ms, and the lateral to vertical wheel load not to exceed 1.0 for 50 ms.
**(E): all units empty; (L): all units loaded; (EL): first and last units loaded, intermediate units empty.
***+Ux: tailwind on passing train; +Uy: crosswind pushing double-stack well car away from passing train.

Other results from the simulation are as follows:

- Highest lateral load on the double-stack well car occurs when the passing Acela Express train faces a headwind.
- Speed of the Acela Express train is more important than the speed of the double-stack well car for producing peak loads.

- The duration of the load on the double-stack well car and therefore its response depends on both the speed of the two passing trains and the directions in which they are traveling (passing in opposite directions or in the same direction).

3.1.2. Stability of Container

The stability of the containers is a factor to consider when another train passes a double-stack well car. Well cars can carry containers stacked with one on top of another with the two containers secured to each other by container restraints at each corner. With the container being held in place by its weight and container restraints, it must resist the aerodynamic forces in the longitudinal, lateral, and vertical directions. Critical to stability is the top container, particularly when empty. Results from this study found that the containers should not become dislodged.

3.2. Full-Scale Test of Aerodynamic Loading on Double-Stack Well Car

On August 17, 2001, a full-scale test was performed at FRA's Transportation Technology Center[2] (TTC) in Pueblo, Colorado, to measure the aerodynamic pressure and roll response on a stationary freight car when a train passes by on an adjacent track. The stationary freight car was a well car with empty double-stack containers that were instrumented to measure the aerodynamic pressures applied to the containers, and the roll response of the well car. The passing train consisted of a high-speed turbine-electric locomotive (TEL) pulling two passenger cars. The geometry of the locomotive body is very similar to the Acela Express power car (Table 45 of the Appendix). The test was conducted at an elevation higher than sea level, therefore at a reduced air density, and the force applied to the double-stack well car was lower than if the test was performed at or near sea level. Figure 3 shows the double-stack well car with the TEL train on an adjacent track.

Figure 3. Double-Stack Well Car and TEL Train on Adjacent Track

The test was performed with the high-speed TEL train running from north to south as it passed the stationary double-stack well car on an adjacent track. The track center spacing was 3.658 m (12 ft) with a nominal gap distance between the sides of the containers and the passing train of 0.813 m (32 in). Figure 4 shows the test configuration between the well car and passing train.

[2]TTC is owned by FRA and operated by AAR.

Pressure measurements were obtained on the near side of the container that faced the passing train, and on the far side that faced away from the passing train. On the near side of the containers, there were nine pressure transducer locations (one location had two different types of pressure transducers for comparison purposes for a total of ten pressure transducers on the near side). The pressure transducers were mounted as three rows and three columns. The location of the pressure transducers will be referred to as row position (bottom, middle, and top), and column position (north, middle, and south). Only two pressure transducers were on the far side, which were located on the middle row of the north and south columns. The height of each row of pressure transducers measured from the top of the rail was: bottom row at 2.743 m (108 in), middle row at 4.039 m (159 in), and top row at 5.334 m (210 in). Figure 5 shows the locations of the pressure transducers on the containers.

Another measurement obtained was the carbody roll. String potentiometers were installed on the double-stack well car between the carbody and its truck frame to measure the vertical displacements due to the rocking motion of the well car from the aerodynamic loading. The two string potentiometers were attached on either side of the well car, each positioned 0.930 m (36.625 in) from the car longitudinal centerline. Carbody roll angle was computed from the difference in the vertical displacements relative to the right and left truck frames.

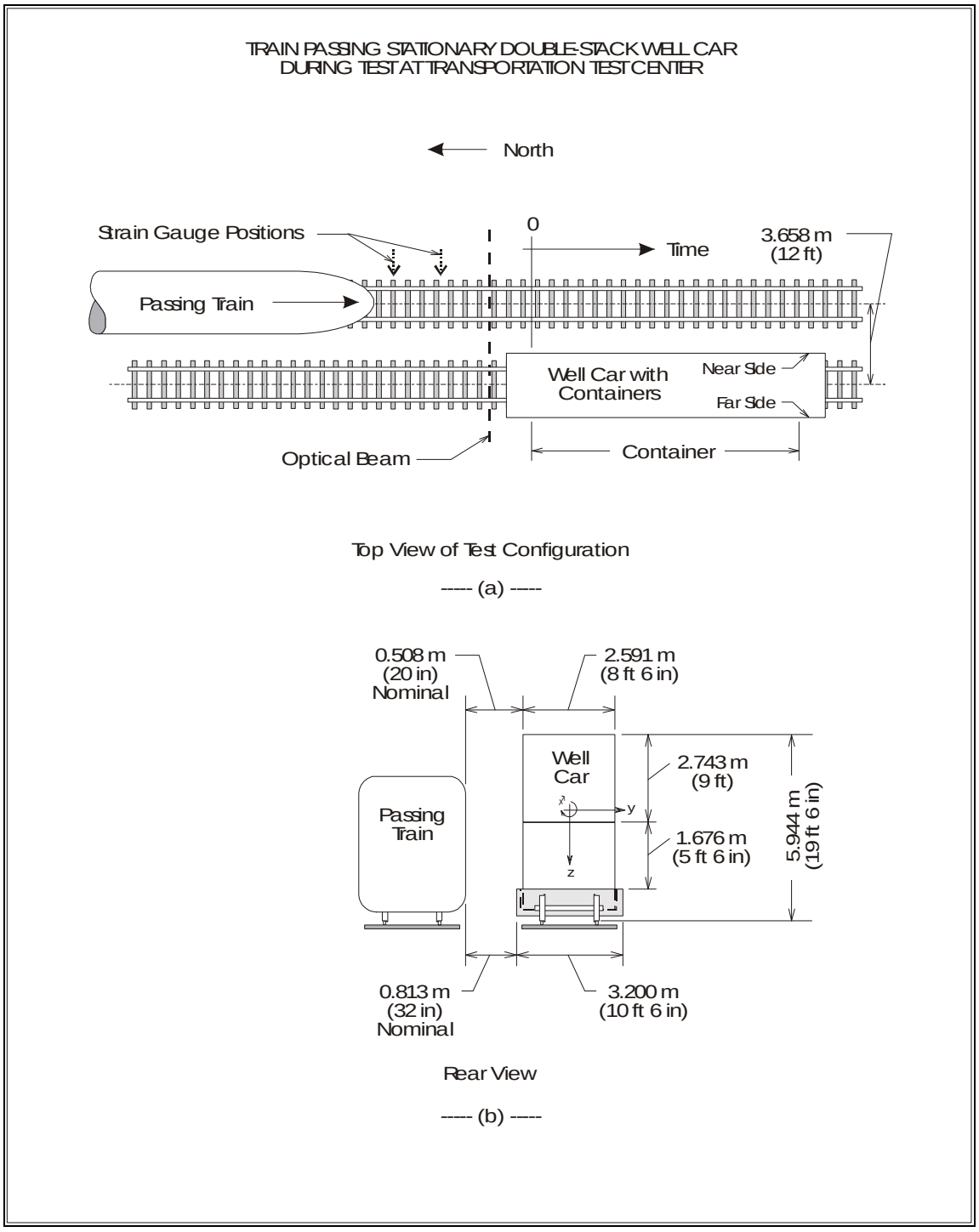

Figure 4. Test Configuration of a Passing Train and a Stationary Double-Stack Well Car

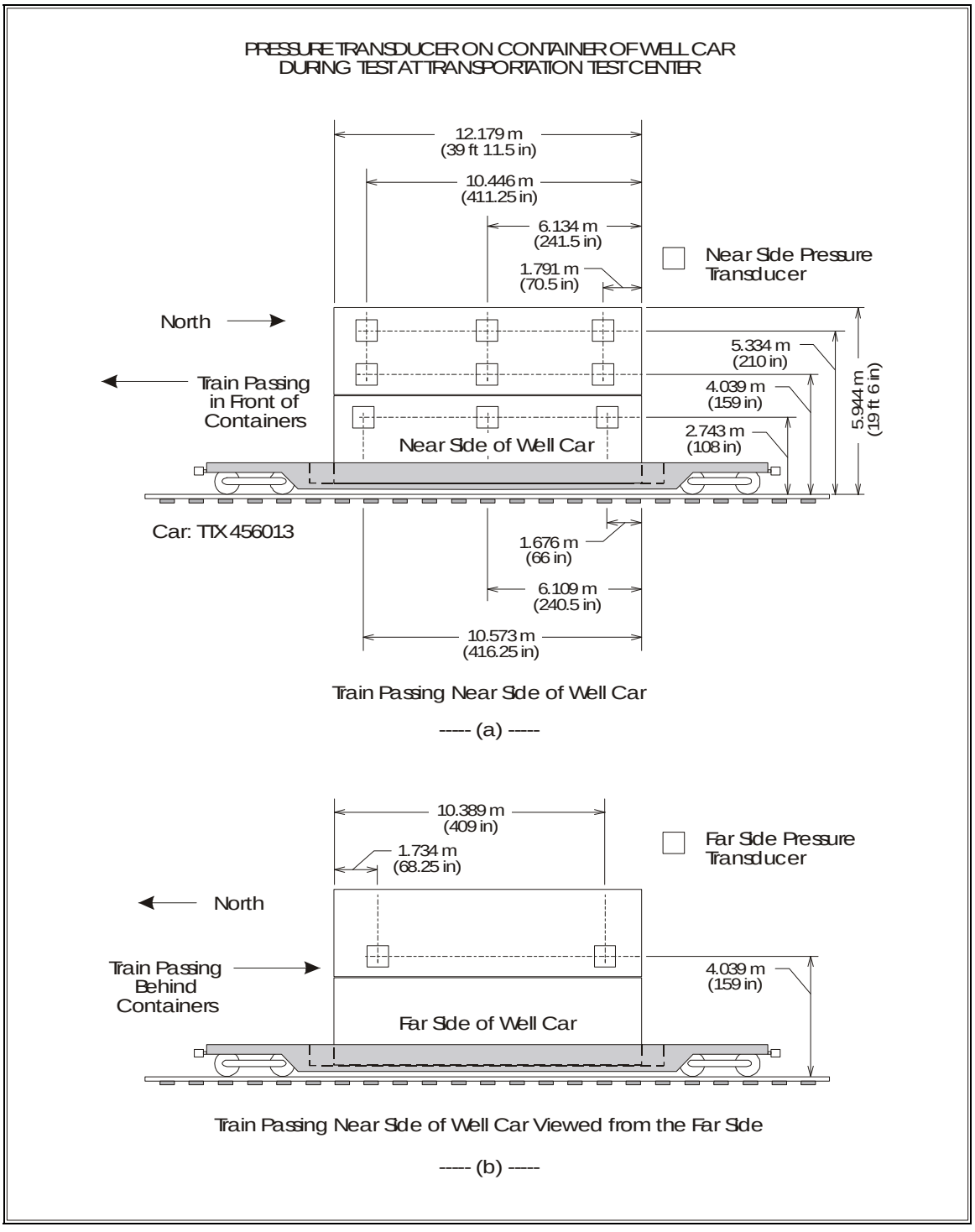

Figure 5. Locations of Pressure Transducers on Containers of a Well Car

3.2.1. Pressure Measurement

The aerodynamic pressures on the double-stack well car were measured for speeds of the passing train ranging from 97 km/h (60 mph) to 209 km/h (130 mph). A maximum peak-to-peak difference in pressures from the passing train was obtained from the measurements for each pressure transducer location, and a difference in pressure coefficients was computed. These maximum pressure changes occurred at the nose of the passing train due to the head perturbation of air around the moving train.

The graph in Figure 6 shows the plots of the maximum peak-to-peak pressure coefficients obtained on the near side at the bottom row of pressure transducers for various passing train speeds. In comparing the peak-to-peak pressure coefficients on the container, little variation occurs in pressure coefficients with passing train speeds from the north column location, which is closest to where the passing train first meets the well car. However, some variability occurs in the pressure coefficients from the middle and south column locations at the lower passing train speeds. At the train speeds that were being tested, compressibility is not expected to be a factor on the pressure coefficients. At the lower speed and reduced Reynolds number, and with the small gap distance between the passing train and the well car being passed, some influence of the viscous boundary layer on the pressure coefficient may occur. Perhaps as the passing train drives the flow downstream along the container side, turbulence may have developed affecting the consistency of the pressure measurements from the middle and south column locations. Despite these variations, when the pressure coefficients are averaged over all speeds of the passing train, the maximum peak-to-peak pressure coefficients for the north and middle columns are both -0.50, while the south column is -0.63.

Also shown plotted in Figure 6 is a single value maximum peak-to-peak pressure coefficient computed from CFD model simulation. The pressure coefficient obtained from the simulation is -0.7, which is higher than the test data. A higher pressure was expected from the model simulation. The pressure coefficient from the simulation was computed at a location that was lower in the container (1.96 m (77 in) from top of the rail) as opposed to the test measurement, which at the lowest position was at 2.74 m (108 in) from the top of the rail.

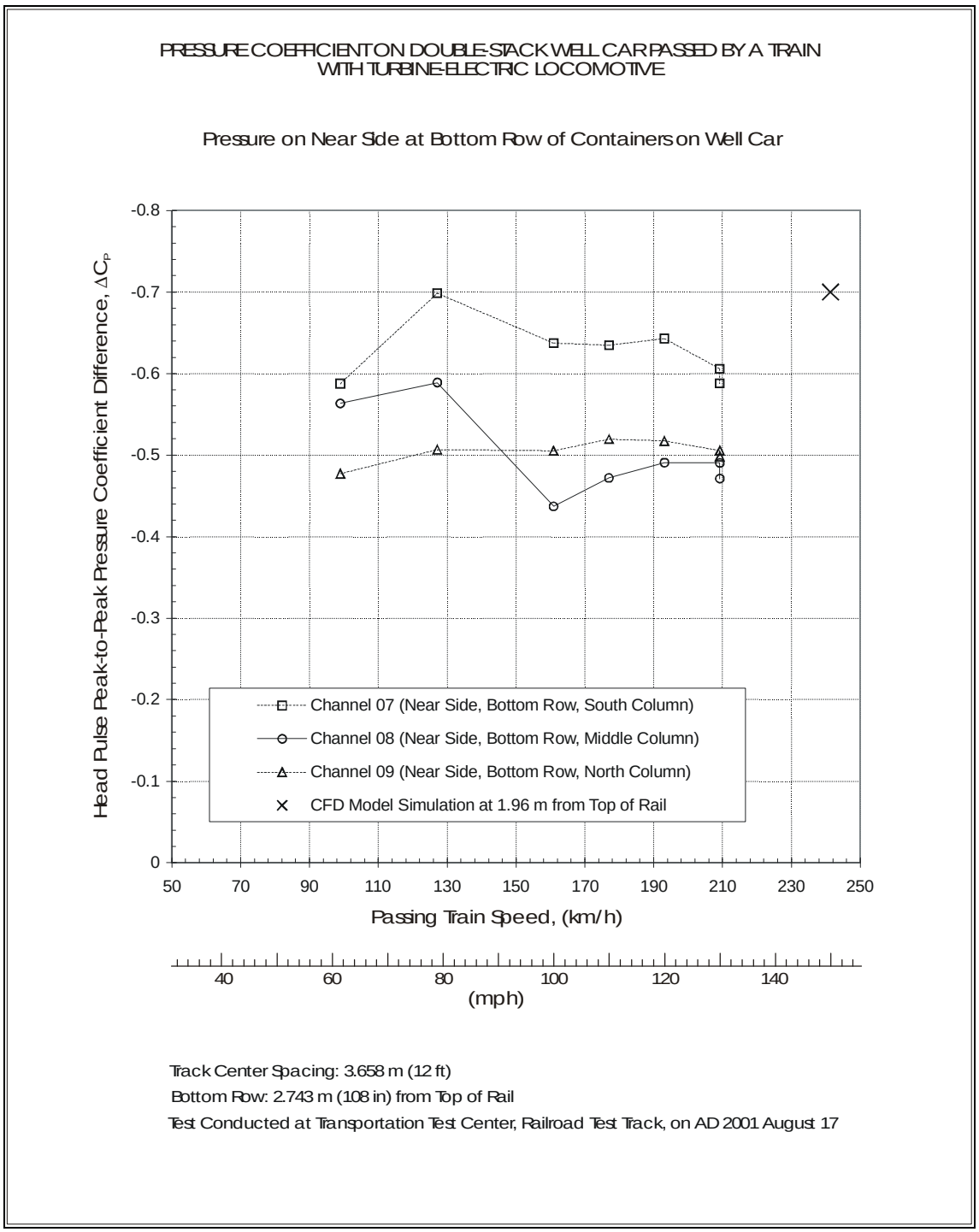

Figure 6. Pressure Coefficients on Near Side at Bottom Row of Double-Stack Well Car

At the next height which corresponds to the middle row, pressures were measured both at the near and far sides of the well car. The maximum peak-to-peak pressure coefficients from the near side at the middle row of the container are shown plotted in Figure 7 for various passing train speeds. Measurements from the pressure transducer at the south end location (channel 4) were not included because of a transducer defect that was discovered after the test. Not much variation occurs in the pressure coefficients with changes in speed; with the average maximum peak-to-peak pressure coefficients very close in value, at -0.45 and -0.46 for the north and middle columns respectively. Figure 8 shows the peak-to-peak pressure coefficients from the far side location, which is very low and varying little with speed, resulting in average maximum peak-to-peak pressure coefficients of -0.050 and -0.037 for the north and south ends respectively.

Finally, Figure 9 shows plots of the maximum peak-to-peak pressure coefficients from the top row of the container for various speeds of the passing train. All the pressure coefficients show a relatively consistent value with the exception of one value from the south column at 99 km/h (61.5 mph). The average maximum peak-to-peak pressure coefficients for the north, middle, and south columns are -0.27, -0.29, and -0.27 respectively. A summary of the averages in peak-to-peak difference in pressure coefficients computed by averaging the pressure coefficients over all the speeds at each location is shown in Table 3.

Table 3. Peak-To-Peak Differences in Pressure Coefficients on a Well Car Averaged over All Speeds of the Passing Train

	Averaged Peak-to-Peak Difference in Pressure Coefficients				
	Near Side of Well Car			Far Side of Well Car	
Distance From Top of Rail	North Column	Middle Column	South Column	North End	South End
2.743 m (108 in)	-0.50	-0.50	-0.63		
4.039 m (159 in)	-0.45	-0.46	xxx	-0.050	-0.037
5.334 m (210 in)	-0.27	-0.29	-0.27		

One of the variables affecting the magnitude of the aerodynamic pressure produced by a passing train is the height from the track. A plot of the average peak-to-peak pressure coefficients at three different heights illustrates this effect as shown in Figure 10. As the height from the track increases toward the top of the train, the average pressure coefficient decreases.

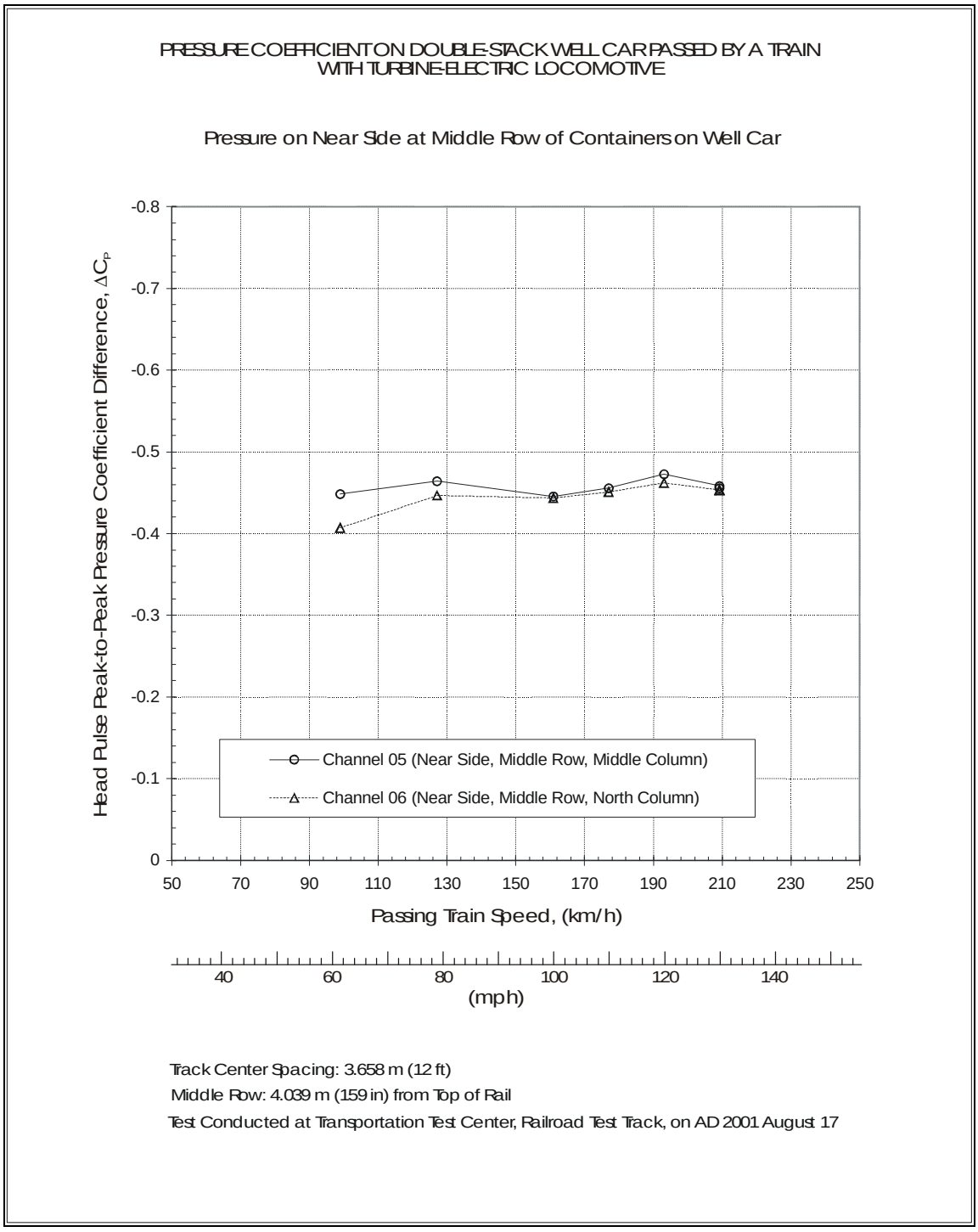

Figure 7. Pressure Coefficients on Near Side at Middle Row of Double-Stack Well Car

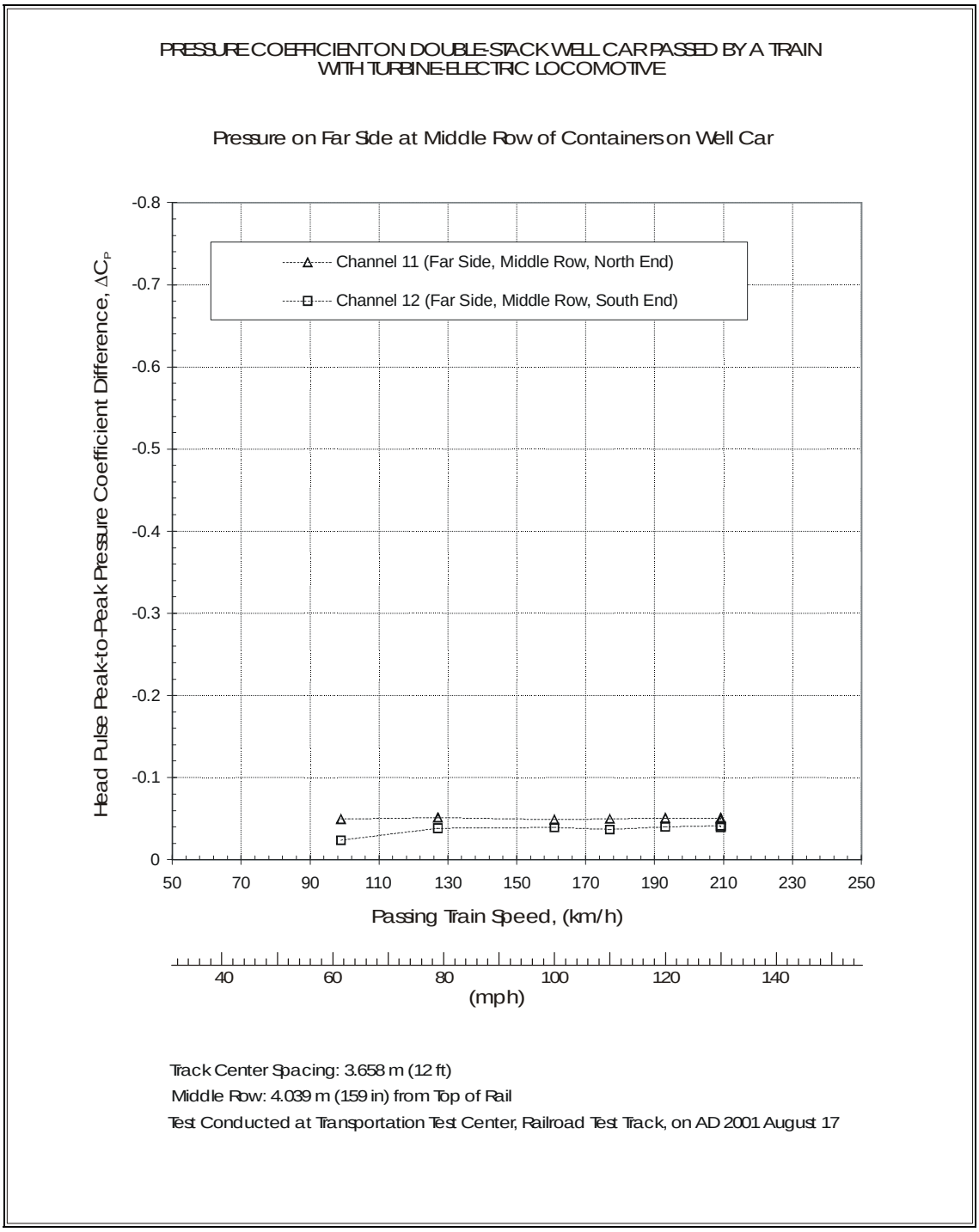

Figure 8. Pressure Coefficients on Far Side at Middle Row of Double-Stack Well Car

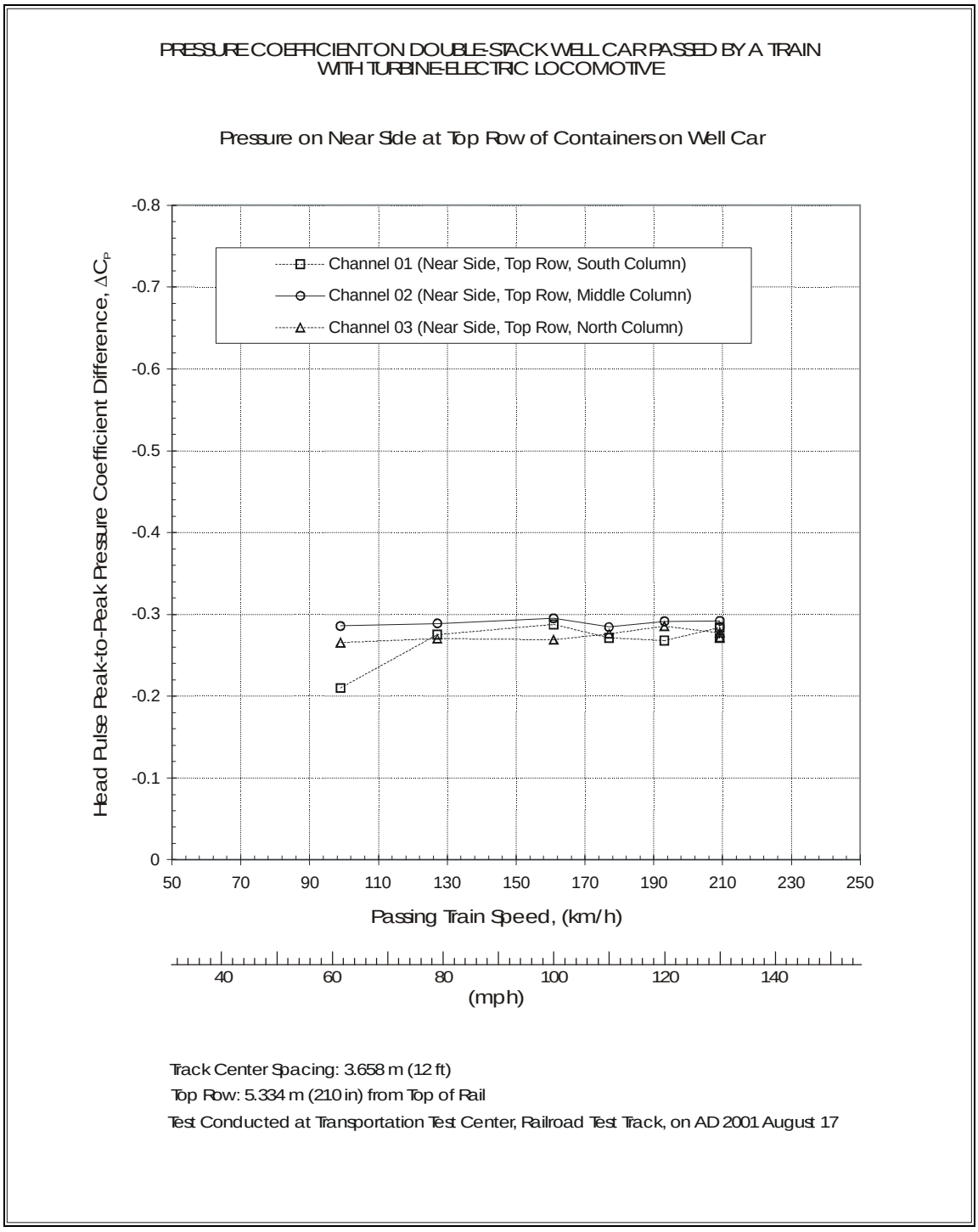

Figure 9. Pressure Coefficients on Near Side at Top Row of Double-Stack Well Car

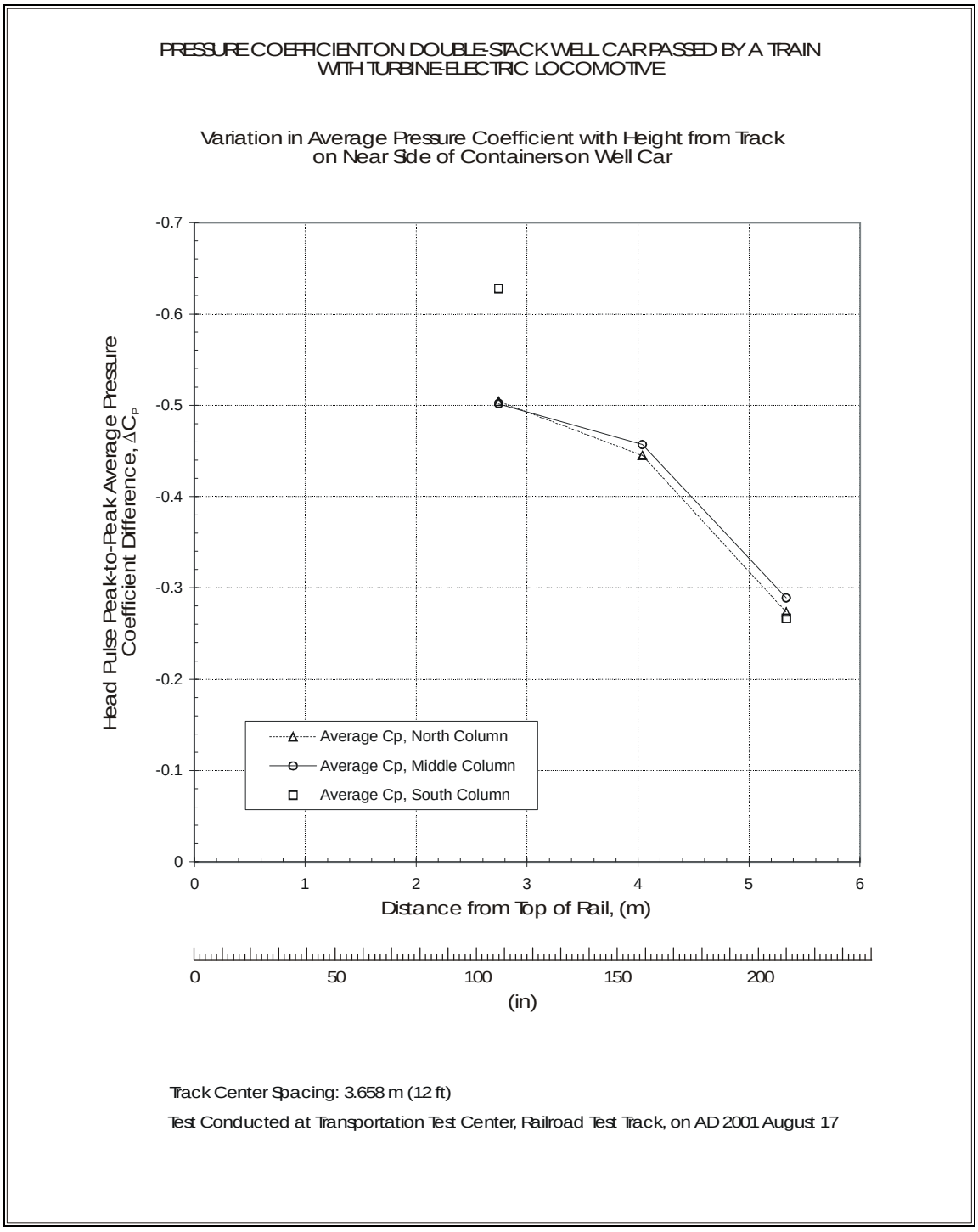

Figure 10. Variation in Pressure Coefficients with Height on Near Side of Double-Stack Well Car

3.2.2. Rail Car Response

The carbody of the double-stack well car rolls in response to the lateral aerodynamic loading from the passing TEL train. The roll angles are small as shown in Table 4, with the maximum zero-to-peak roll angle of 0.312° when the TEL train passed at 177 km/h (110 mph). At this roll angle, it produced a maximum lateral displacement of 30.1 mm (1.184 in) at the top of the container. Since the test was performed at a site with an elevation of 1,400 m (4,600 ft), these roll angles are smaller than would be at sea level where the air density is higher.

Table 4. Maximum Carbody Roll Response of Double-Stack Well Car from a Passing Train

Speed of Passing TEL Train	Maximum Roll Angle of Double-Stack Well Car, Zero-to-Peak (deg)	Maximum Lateral Displacement at top of Container, Zero-to-Peak
97 km/h (60 mph)	0.055	5.26 mm (0.207 in)
129 km/h (80 mph)	-0.117	11.3 mm (0.444 in)
161 km/h (100 mph)	-0.218	21.1 mm (0.829 in)
177 km/h (110 mph)	-0.312 (highest response)	30.1 mm (1.184 in)
193 km/h (120 mph)	-0.281	27.1 mm (1.065 in)
209 km/h (130 mph)	-0.281	27.1 mm (1.065 in)
209 km/h (130 mph)	-0.281	27.1 mm (1.065 in)

3.2.3. Comparison of Test with Numerical Simulation

An objective of the test was to provide data to compare with numerical simulation. As shown plotted in the graph of Figure 6, the value obtained from the model simulation does not correspond to the position of the test measurement. A direct comparison cannot be made, because the height where the pressure was computed from the model is outside the region where the test data was measured. To further compare results, numerical simulation was performed at a speed of 209 km/h (130 mph), which corresponds to one of the speeds in the test. The pressures corresponding to each of the pressure transducer locations were computed against time during the passage of the head of the train where

the maximum peak-to-peak pressures occurred. In comparing these results, the following observations were made (results not shown):

> The agreement between the measured and calculated pressures is generally very good. The peak-to-peak pressure magnitude is very well predicted for most transducer locations….However, the measured data consistently exhibits quicker pressure recovery past the negative pressure peak. This may be due to the lack of a turbulence model in the CFD calculation. (MacNeill, Holmes, and Lee 2002)

4. Effect of Passing Train on Window Mount and Glazing

A high-speed train with its attendant aerodynamic pressure pulse at the nose of the train can exert a brief but strong pressure to structures in proximity to the passing train. The aerodynamic load from the passing train has the potential to damage structures on the train being passed. An emerging problem in the United Kingdom has been on soft-sided swap body[3] wagons where the transient loads from the aerodynamic interactions with passing high-speed trains create the potential for structural damage, especially traveling in tunnels of the Channel Tunnel Rail Link (Gawthorpe 1994; Baker and Sterling 2003). Consequently, and with some damage to internal supports having been reported on swap body wagons with fabric sides, an analytical methodology was developed to simulate the response of the swap body to the aerodynamic interaction and structural loading from a passing train (RAPIDE 2001; Gregoire 2001; Johnson 2001). No aerodynamic pressure limit has been defined from this study, although a pressure limit of 1.44 kPa (0.209 psi) has been the criterion for trains passing each other in open air.

A vulnerable structure on a passenger car is the window where the aerodynamic loading of a passing train can cause the glazing to crack or the window to be dislodged from its mount. This vulnerability was investigated to provide some indication on the potential for damage to the window when two trains pass each other (Holmes and Schroeder 2002). The study consisted of computing the aerodynamic pressures from CFD simulation of two trains passing each other and evaluating the potential for damage to the window using data from glazing impact experiment.

4.1. Glazing Impact Strength

Experiments were conducted on the impact strength for railroad vehicle glazing to develop a new standard for testing (PB 1999). The experiment consisted of a variety of impact objects, glazing specimens, and mounting designs. The glazing specimen was installed in a frame and held in place with a rubber gasket as on the body of a train, and tested as a system. A variety of glazing specimens were tested including glass, glass with anti-spall coating, and polycarbonate.

Although the use of concentrated impact objects to strike the glazing does not relate directly to the distributed aerodynamic pressure loading from passing trains, some of the results from these tests could provide information that is useful in assessing the structural integrity of glazing from aerodynamic interaction as trains pass each other. The impulse that results from the impact object striking the window, and the extent that the glazing can resist impact, can be used as a measure of structure's response under aerodynamic

[3]Swap body is a freight-carrying unit for intermodal transport and optimized to road vehicle dimensions, that was originally not strong enough to be top-lifted or stacked when loaded, but some can now be top-lifted or stacked.

loading, providing that they are impacts of short duations. It was determined from these glazing impact strength tests that a 5.4 kg (12 lbm) ball striking the glazing at a speed of 6.71 m/s (15 mph) did not dislodge the glazing from the window frame. This corresponded to an impulse of 71 N•s (16 lb•s). When an 11 kg (24 lbm) ball struck the glazing at a speed of 6.71 m/s (15 mph), the glazing was dislodged from the window frame. The impulse for this case was 142 N•s (32 lb•s).

4.2. Aerodynamic Pressure Impulse on Glazing

The aerodynamic pressure pulse from the nose of a high-speed train can exert a brief but strong force on the window of another train on an adjacent track. It was estimated that for trains passing each other at a speed of 241 km/h (150 mph), it is unlikely that the aerodynamic force will cause the glazing to crack (Lee 1999). That estimate was based on an extrapolation of results from a test conducted on a particular type of glazing used in railroad cars. An assessment on the strength of the glazing attachment requires further details on the window design and its structural properties.

The dislodging of the glazing from its mount can include a series of events, since it involves a deformation of the rubber gasket and bending of the glazing until the glazing slips out of the gasket, or the gasket slips out of the frame. When the pressure pulse is extremely short, and if certain simplifying assumptions can be made and certain dynamical properties are known, the assessment on the structural integrity of the window can be related to the initial velocity of the glazing generated by the pulse excitation. The impulsive force produces a rapid acceleration of the mass resulting in an almost instant rise in velocity. Therefore, the velocity of the mass being impacted is an indication of the magnitude of the pulse excitation based on the following assumptions:

- The glazing is rigid without any bending and is initially at rest.
- The mass of the rubber gasket is negligible relative to the glazing and its damping is small.
- The pulse duration is short compared to the natural period of the mounted glazing (pulse duration of about one tenth or less of the natural period).

Under these conditions, the effect of the impact on the glazing can be directly related to the mass and impulse (see Appendex for derivation),

$$v(\xi) \approx \frac{1}{m}\int_0^{\xi} F(t)dt$$

where,

$v(\xi)$: velocity of glazing from impulsive force,

m: mass of the glazing,

$\int_0^{\xi} F(t)dt$: impulse from impulsive force F(t).

The potential for damage to the window was considered from results of a simulation for an Acela Express train passing a bilevel Kawasaki passenger car traveling in the opposite and same directions. Assuming that the mass of the glazing from the simulation is the same as the mass of the glazing from the impact strength test, the impulse can serve as a measure of the magnitude of the pulse excitation. The impulses on the window of a Kawasaki passenger car from the aerodynamic pressure of a passing Acela Express train with a headwind of 80 km/h (50 mph) against the Acela Express train was obtained by CFD simulation. When the Acela Express train traveling at 241 km/h (150 mph) passes the Kawasaki car traveling in the opposite direction at 129 km/h (80 mph), an impulse of 62 N•s (14 lb•s) with a duration of 0.011 s is exerted on the window of the Kawasaki car. Therefore, the impulse from the simulation can be assumed to be a safe level since it is less than the impulse from the glazing impact strength test, where the window resisted an impulse of 71 N•s (16 lb•s).

In another case, the Acela Express train is traveling at 241 km/h (150 mph) and overtakes the Kawasaki car traveling at 129 km/h (80 mph), an impulse of 205 N•s (46 lb•s) with a duration of 0.38 s is exerted on the window of the Kawasaki car. In the glazing impact strength test, the glazing was dislodged from the frame when an impulse of 142 N•s (32 lb•s) was applied. While the impulse exerted on the window of the Kawasaki car is 205 N•s (46 lb•s), which is greater than the impulse from the window test where the glazing was dislodged, it may not be meaningful to directly compare impulses in this case. From the information that is available, it is not clear for this case whether or not the glazing will be dislodged. To use only the impulse as a direct comparison, the duration of the applied pressure pulse must be so short that it is treated as a shock impact. If the duration of the pressure pulse is very short (about one tenth of the natural period of oscillation of the window), then a direct comparison of the impulse can be made. A high impulse can also be obtained with a small force but a long duration, in which case, the force applied to the glazing has no damaging effect. Because the duration of the aerodynamic pressure pulse is 0.38 s, to directly compare impulses, the natural period of the window would have to be at least 3.8 s or longer, or a natural frequency no greater than 0.26 Hz. Because of a lack of data on the natural frequency of the window, an estimate cannot be made on the ability of the window to resist the aerodynamic force.

Results from the glazing impact experiment can only provide some indication to the potential damage to the window from aerodynamic pressures. The concentrated load of an object striking glazing does not represent the distributed loading from aerodynamic pressure. There are differences in stress and deformation to the glazing and its supporting structure between these two events.

5. People in Proximity to Passing Train

Circumstances occur where a train traveling at high speeds passes close to people alongside the track (railroad workers on the trackside or people waiting on station platforms). The passing train can produce airflow velocity and changes in static pressure that are destabilizing to people in proximity to the train. Airflow velocity induced by a passing train, particularly the airflow induced from the wake, is considered to be the more serious effect in destabilizing people and objects alongside the track (RAPIDE 2001; Gawthorpe 1978). One simple and obvious approach to reduce these aerodynamic effects is for people to be situated at a sufficient distance away from the passing train. This approach requires information on the strength of the airflow being produced by a passing train, the airflow velocity that could destabilize a person, and whether station platforms as they exist have sufficient area to accommodate the necessary safety zone.

The strength of the airflow velocity produced by passing trains has been the focus of research involving both numerical simulation and experimentation that will be addressed later in this report. To better understand the problem and the analytical and test results, an investigation was conducted that includes:

- A review of the literature on the effects of wind on people, where studies have been performed with application to pedestrians in the vicinity of buildings and built-up environments.

- A survey of conditions that exist in railroad station platforms, centered on stations along the Northeast Corridor of the United States.

- The type of safety measures that exist in the United States and in other countries.

5.1. Effect of Wind on People

The aerodynamic effect felt by a person in proximity to a passing train is primarily in the form of airflow. The turbulent and unsteady airflow induced by the train is a transient event, occurring during the train passage and persisting for a short time afterwards. A relationship is required between wind speed and human response, particularly as it affects physical stability, to evaluate the effects of airflow on a person.

Extensive research has been done on the effects of wind on people, with application to pedestrians in the vicinity of buildings. The data from these studies were to assist architects and planners in their design of tall buildings, where high winds can occur from the presence of these structures. While much of the research on the effects of wind on people was performed to improve the comfort and safety of pedestrians around the outside of buildings, the results from these studies provide a general understanding on a person's response when exposed to a wind force.

Various wind speed criteria have been proposed with some proposed criteria stemming directly from outdoor observations, or from wind tunnel experiments. The Beaufort scale is one of the oldest wind scales relating wind speed to observable effects, which has been expanded over time. Penwarden (1973) presented the expanded Beaufort scale along with some other equivalent wind speed effects. Melbourne and Joubert (1971) observed pedestrians in high wind open-air environments resulting in a proposed wind speed criteria. Hunt, Poulton, and Mumford (1976) based their wind speed criteria on wind tunnel experiments, while Murakami and Deguchi (1981) formed their wind speed criteria on both wind tunnel experiments and outdoor observation. Other wind speed criteria were proposed by: Gandemer (1977); Penwarden and Wise (1975); Lawson and Penwarden (1977).

The effects of wind on people have been observed as pedestrians move about in windy environments. In Australia, people were observed walking in the forecourt of a building exposed to very severe wind conditions (Melbourne and Joubert 1971). People had great difficulty with balance when exposed to wind at gusts up to 20 m/s (45 mph), particularly a gust that caught people sideways. Two girls came down on their hands and knees when the recorded maximum gust velocity was 23 m/s (51 mph), rising from about 12 m/s (27 mph) in 2 to 3 s. Many of those observed were young, with few carrying anything more than a briefcase.

5.1.1. Equivalent Wind Effect

The effect of wind blowing against a person is usually measured in terms of discomfort, difficulty in walking, or loss of balance. To put these descriptors in perspective, wind blowing against a person can be compared to various other activities. Since wind blowing against a person creates a force against the person, the comparison to other activities is based on the same level of force, or expenditure of energy. Penwarden (1973) illustrated these effects in terms of the angle that a person must lean to maintain balance, on the reduction in walking speed, and on an equivalent slope of walking up a hill.

In the first example, the effects of wind blowing against a person can be viewed in terms of the angle a standing person facing against the wind must lean forward to maintain equilibrium. The angle θ that a person must lean forward into the wind can be computed as, $\tan\theta = \frac{\text{Wind Force}}{\text{Body Weight}}$. At a wind speed of 10 m/s (22 mph), the angle that a person must lean against the wind to maintain equilibrium is 5°, while at a Beaufort Wind Force Scale number 7, that lean angle is 10°.

Another example relates walking speed of a person facing against the wind, and the speed of the wind. The energy required for walking at a speed of 1.8 m/s (4 mph) in still air was used as a reference. Next, the walking speed against the wind was computed for a given wind speed based on the same expenditure of energy as walking in still air. Table 5 shows walking speeds when walking against different wind speeds, with a reduction in walking speed as wind speed increases.

Table 5. Walking Speeds Against the Wind Computed Based on the Same Expenditure of Energy as Walking in Still Air (Penwarden 1973)

Wind Speed	Walking Speed
0 m/s	1.8 m/s (4.0 mph)
9 m/s (20 mph)	1.35 m/s (3.0 mph)
14 m/s (31 mph)	0.9 m/s (2.0 mph)
21 m/s (47 mph)	0.45 m/s (1.0 mph)

A final example is the relation between the speed of the wind blowing against a person walking on level ground, and the equivalent slope for a person walking up a hill. This relation was computed based on the same metabolic heat requirements between walking against the wind, and walking up a hill. Table 6 shows the various relative wind speeds (sum of the walking speed and the ground speed of the wind), and walking up the hill with the corresponding slopes. Also shown is the ground speed of the wind if a person was assumed walking at a speed of 1.0 m/s (2.2 mph). In either case, as the wind blowing against a person increases, it is equivalent in energy to walking at up an increasingly steep slope. These examples provide a tangible sense to the description of wind effects when compared to other activities.

Table 6. Wind Speeds Against a Person Walking on Level Ground and Equivalent Slopes for a Person Walking Up a Hill Computed Based on the Same Metabolic Heat Requirement (Penwarden 1973)

Relative Wind Speed (Walking + Headwind)	Wind Speed for Walking Speed of 1.0 m/s (2.2 mph)	Slope
10 m/s (22 mph)	9 (20 mph)	1/20
14 m/s (31 mph)	13 (29 mph)	1/10
16.5 m/s (37 mph)	15.5 (35 mph)	1/7
19.5 m/s (44 mph)	18.5 (41 mph)	1/5
22 m/s (49 mph)	21 (47 mph)	1/4
25 m/s (56 mph)	24 (54 mph)	1/3

5.1.2. Wind Speed Criterion

One of the earliest efforts to characterize the effects of wind as it applies to sailing ships was by Admiral Sir Francis Beaufort, FRS, in 1806. The basis of that scale, known as the Beaufort Wind Force Scale, is still used today. Penwarden (1973) presented an extended

and revised Beaufort scale compiled from various sources for estimating wind speeds on land as shown in Table 7. However, the Beaufort scale does not specify the duration at which the wind speeds are measured,

> In comparing the descriptions with other information it is important to know the time scale involved; whether gusts or long-term average speed are involved. The Beaufort scale is not explicit on this point, but it would seem that the speeds quoted are fairly long-term averages, perhaps over a period of 10 min to one hour. (Penwarden 1973)

The Beaufort scale is a useful indicator on the relationship between wind speed and the expected effect that it could have on a person's ability to perform certain tasks when exposed to that wind. However, it is a scale based on sustained wind speeds, whereas wind induced by a passing train will contain fluctuating or nonsteady components that will be transient in nature:

> While trains passing stations at high speed do not generate sustained winds, the transient induced airflows produced can reach significant velocities, with effects not unlike those described in the Beaufort Scale. Nevertheless, it is important to note that the transient induced airflows may not have as large an effect as a sustained wind of the same velocity. (Liao et al 1999)

A narrative description on the effects of wind on people over some ranges of wind speeds is as follows:

> …discomfort begins at mean wind speed of 5 m/s [11 mph], with hair and clothing flapping and dust and loose paper blowing about. Speeds of 8 to 10 m/s [18 to 22 mph] are unpleasant, with the wind exerting a considerable force on the human body; and speeds of 15 to 20 m/s [34 to 45 mph] or more are likely to be dangerous. (Penwarden and Wise 1975)

Table 7. Effects of Wind in Terms of Beaufort Numbers (Penwarden 1973)

Beaufort Number	Wind Speed		Effect	Source (see bottom of table)
	(m/s)	km/h (mph)		
0, 1	0 – 1.5	0 – 5.4 km/h (0 – 3.4 mph)	• Calm, no noticeable wind.	A, B
2	1.6 – 3.3	5.8 – 11.9 km/h (3.6 – 7.4 mph)	• Wind felt on face.	A
3	3.4 – 5.4	12.2 – 19.4 km/h (7.6 – 12.1 mph)	• Wind extends light flag.	A
			• Hair is disturbed. • Clothing flaps.	B
4	5.5 – 7.9	19.8 – 28.4 km/h (12.3 – 17.7 mph)	• Raises dust, dry soil, and loose paper.	A, C
			• Hair disarranged.	B
5	8.0 – 10.7	28.8 – 38.5 km/h (17.9 – 23.9 mph)	• Force of wind felt on body.	B
			• Drifting snow becomes airborne.	D
			• Limit of agreeable wind on land.	E
6	10.8 – 13.8	38.9 – 49.7 km/h (24.2 – 30.9 mph)	• Umbrellas used with difficulty.	A
			• Hair blown straight. • Difficult to walk steadily. • Wind noise on ears unpleasant.	B
			• Windborne snow above head height (blizzard).	D
7	13.9 – 17.1	50.0 – 61.6 km/h (31.1 – 38.3 mph)	• Inconvenience felt when walking.	A
8	17.2 – 20.7	61.9 – 74.5 km/h (38.5 – 46.3 mph)	• Generally impedes progress.	A
			• Great difficulty with balance in gusts.	F
9	20.8 – 24.4	74.9 – 87.8 km/h (46.6 – 54.6 mph)	• People blown over by gusts.	F

[A]Beaufort land scale.
[B]BRS observations.
[C]Chepil.
[D]Newburg.
[E]Shaw.
[F]Melbourne and Joubert.

Specifying the wind speed for steady wind is straightforward, but when wind speeds are not steady, such as the presence of gust or turbulence, the method of specifying the overall wind speed is less obvious. The wind speed criteria must account for the effects of unsteady conditions. Lawson and Penwarden (1977) described the effect of the

unsteady wind conditions as it relates to the Beaufort scale. It was shown that at a given Beaufort force level, the average wind speed corresponding for that force level increased as averaging time became shorter, and suggested that it is a function of the turbulence intensity. In a case with turbulence intensity of 28 percent, the average wind speed did not change at a given Beaufort force level for averaging durations from 1 hour down to 10 minutes. However, as averaging duration became shorter, the velocity increased at a given Beaufort force level.

Various approaches to establishing wind speed criteria that accounts for fluctuating wind speeds exist. Hunt and Poulton suggest that gusts with durations of 0.1 to 0.5 s are likely to cause the most difficulty with balance (Penwarden 1973). In some cases, wind criteria are based on the frequency of occurrence, where it is unacceptable if induced wind gust velocity is likely to exceed 23 m/s (51 mph) in one year for reasons of safety, and 15 m/s (34 mph) for 1 percent of total time for comfort (Melbourne and Joubert 1971). A similar statement is that the mean hourly wind speed of 5 m/s (11 mph) is the maximum for comfort, and the frequency with which this is exceeded is used as a comfort criterion (Lawson and Penwarden 1977). Another criterion cites wind speeds that include a quantity called the turbulence intensity that accounts for wind turbulence. Gandemer (1977) suggested a criterion based on local mean speed and the corresponding root mean square of the turbulent fluctuation.

Wind tunnel experiments have been conducted to quantify the relation between fluctuating wind speeds and its effects on people. Hunt, Poulton, and Mumford (1976) described wind tunnel experiments and developed quantitative values of wind speeds as it relates to its effects on people. The experiments were performed in a wind tunnel at the National Physical Laboratory in the United Kingdom, which included a gust generator to simulate both steady and turbulent wind. The test subjects were measured for (1) their performance of simple tasks, (2) their steadiness, direction, and the force acting on them while walking, and (3) their subjective assessments of different wind conditions. It was found that, “Our experiments have shown that in gusty winds it is not sufficient to use criteria developed for steady winds and then assume that the effect of a gusty wind is the same as a steady wind with a speed equal to some peak gust” (Hunt, Poulton, and Mumford 1976). The results of these experiments relating the effects of wind on people are summarized in Table 8.

Table 8. Wind Effect on People Categorized by Wind Conditions (Hunt, Poulton, and Mumford 1976)

Wind Condition	Wind Speed, u	Effect on People
Steady Uniform Wind	u < 6 m/s < (13 mph)	For comfort and little effect on performance.
	u < 13-15 m/s < (29-34 mph)	For ease of walking.
	u < 20-30 m/s < (45-67 mph)	For safety of walking.
Non-Uniform Wind Wind speed varies by 70% over a distance less than 2 m (79 in).	u < 9 m/s < (20 mph)	To avoid momentary loss of balance and to be able to walk straight.
	u < 13-20 m/s < (29-45 mph)	For safety (for elderly people, this criterion may be to high).
Gusty Wind u_e : estimated equivalent steady wind speed, $u_e = \overline{u}\left[1 + 3\left(\overline{u}'_{rms}/\overline{u}\right)\right]$ $\overline{u}$: average wind speed. $u'_{rms}/\overline{u}$: turbulence Intensity.*	u_e < 6 m/s < (13 mph)	For comfort and little effect on performance.
	u_e < 9 m/s < (20 mph)	Most performance unaffected.
	u_e < 15 m/s < (34 mph)	Control of walking.
	u_e < 20 m/s < (45 mph)	Safety of walking.

* $u'_{rms} = \sqrt{\left(u'_{Xrms}\right)^2 + \left(u'_{Yrms}\right)^2}$, where u'_{Xrms} and u'_{Yrms} are root mean square turbulent velocity components in the horizontal plane.

In a final study conducted in Japan, Murakami and Deguchi (1981) described experiments both in a wind tunnel and in open air. The wind tunnel experiments were performed at the Japan Automobile Institute where the subjects were exposed to both uniform and nonuniform wind flow. To create nonuniform wind flow, fences were erected to block the wind, but with openings between the fences to produce a rush of wind as the subject walked pass. The experiments had subjects walk on a predetermined path in the wind tunnel at various directions to the wind while carrying various items. Instrument recordings, visual assessment by experimenters, and verbal assessments by subjects were analyzed to determine the wind effects on the subjects. The open-air experiment was conducted at the base of a high-rise building where windy conditions were common. The first part of the open-air experiment had test subjects walk along a predetermined line outside the base of the building where their movements were recorded by a video camera. The results were analyzed based on visual assessments from the experimenters and verbal assessments from the subjects. The second part of the experiment involved analyzing photographs from video recordings to determine the wind effects of over 2,100 pedestrians walking by the base of a building. Acceptance criteria were developed from the results of these experiments as shown in Table 9. The criteria are based on an average wind speed with an averaging duration of 3 s.

Table 9. Acceptance Criteria Based on Tests of Subject in Wind Tunnel and Pedestrians Exposed to Outdoor Wind Averaged over 3 s (Murakami and Deguchi 1981)

Wind Speed (Averaged over 3 s)	Effect on People
Under 5 m/s (11 mph)	No Effect • minor effect on hair and skirt for females
5 – 10 m/s (11 – 22 mph)	Some Effect • footsteps sometimes irregular • hair and skirt considerably disturbed
10 – 15 m/s (22 – 34 mph)	Serious Effect • walking irregular • walking difficult to control • upper body bends windward
Over 15 m/s (34 mph)	Very Serious Effect • dangerous for elderly person • walking impossible to control • body blown sideways or leeward

5.2. Station Survey

A survey was conducted of railroad stations along the Northeast Corridor of the United States to provide the information necessary for assessing the impact of Acela Express trains passing stations at high speeds (Liao et al 1999). The survey was on 57 of the 101 existing stations along the Northeast Corridor between Union Station in Washington, DC, and South Station in Boston, Massachusetts. Stations selected for the survey were those where the Acela Express trains will not stop and at which the current maximum authorized speeds was greater than 161 km/h (100 mph). The survey did not include

stations where the Acela Express trains will stop, or where they will be moving at slow speeds.

The survey of the selected stations involved observing the station surroundings, the general movement of people and trains, and station measurements. The observations were physical presence and condition of platforms and structures, presence and operational state of public address systems, the actions of passengers boarding and disembarking trains, and the period of time between passing and stopping trains. In addition, train movements were observed and experienced from an aerodynamic perspective, and measurements were made of platform dimensions and platform edge safety zone.

Whereas the scope of information obtained in the station surveys was broad, certain information was considered most relevant with respect to aerodynamic effects of passing trains. The physical conditions considered most relevant were platform type (side or island), platform height (high- or low-level), platform dimensions, presence and dimensions of platform-edge safety zones, distance of track for nonexpress-stop trains from platform, presence and condition of platform passenger shelters, presence and legibility of safety signs, presence and type of safety systems, presence and type of platform appurtenances (benches, trash receptacles, billboards, newspaper vending machines, etc.), and the existence of a back wall near the platform.

In addition to the on-site surveys, basic information was collected from Amtrak and other agencies on all 101 stations. The information collected from each station included: station name and location, maximum authorized speeds (MAS) passing each station, name of railroads providing passenger service, ownership of right-of-way, operator responsible for dispatching trains, type of passenger trains stopping at each station, number of stations within each jurisdiction, operator maintaining the stations, presence of safety systems and their accessibility to the disabled, and the station's historical landmark status.

It was found from this survey that the conditions of the stations varied greatly from each other.

5.3. Safety Measure

The strength of the airflow induced by a passing train is dependent on the location relative to the train. Therefore, the lateral distance from the side of the train and the vertical distance from the track, are two significant distances that affect the strength of the airflow experienced by a person in proximity to a passing train. Two dimensions that are established by design but affect the position of a person relative to a passing train are the width of the train and the height of the station platform. The actual or nominal dimensions for trains (AAR 1984) and station platforms (AREMA 1999) are shown in Figure 11.

Safety measures to limit people's exposure to the aerodynamic effects of passing trains vary with railways in different countries. Temple and Johnson (2003) conducted a detailed review of research on airflow effects from passing trains in the United Kingdom and internationally. Baker and Sterling (2003) reviewed recent and current international work and identified specific problems to be addressed relating to train-induced airflow in urban environments.

A common approach practiced by railways in various countries to address the safety of people from the aerodynamic effects of a passing train is to specify a minimum distance from a passing train. Workers are to stay at a certain distance from the track when a train passes, whereas markings are used on station platforms to warn passengers from reaching too close to the edge of the platform. The recommended safe distance from a passing train, as well as the maximum speed of the passing train, varies with railways in different countries as shown in Table 10.

No safety requirements exist in the United States (as of 2005) for people on station platforms as it relates to the aerodynamic effects of passing trains. A survey of stations in the Northeast Corridor has found that,

> Platform-edge safety zones ranged from none, to those denoted by a single yellow stripe, to those well marked and equipped with truncated-dome strips or tiles. In width measured from edge of the platform, the zones ranged from less than [0.61 m] 2 ft to over [1.2 m] 4 ft. Conditions of the markings ranged from very conspicuous to very inconspicuous, due to weathering. (Liao et al 1999)

Amtrak has been installing yellow markings on the edge of station platforms in the Northeast Corridor that are 0.965 m (38 in) wide.

In Britain, British Railway has suggested criteria for exposure to wind speed induced by a passing train to be limited to 11 m/s (25 mph) or a Beaufort scale of 5 for members of the public, and limited to 17 m/s (38 mph) or a Beaufort scale of 7 for railroad workers (Gawthorpe 1972). Their recommended distances from a passing train are as follows:

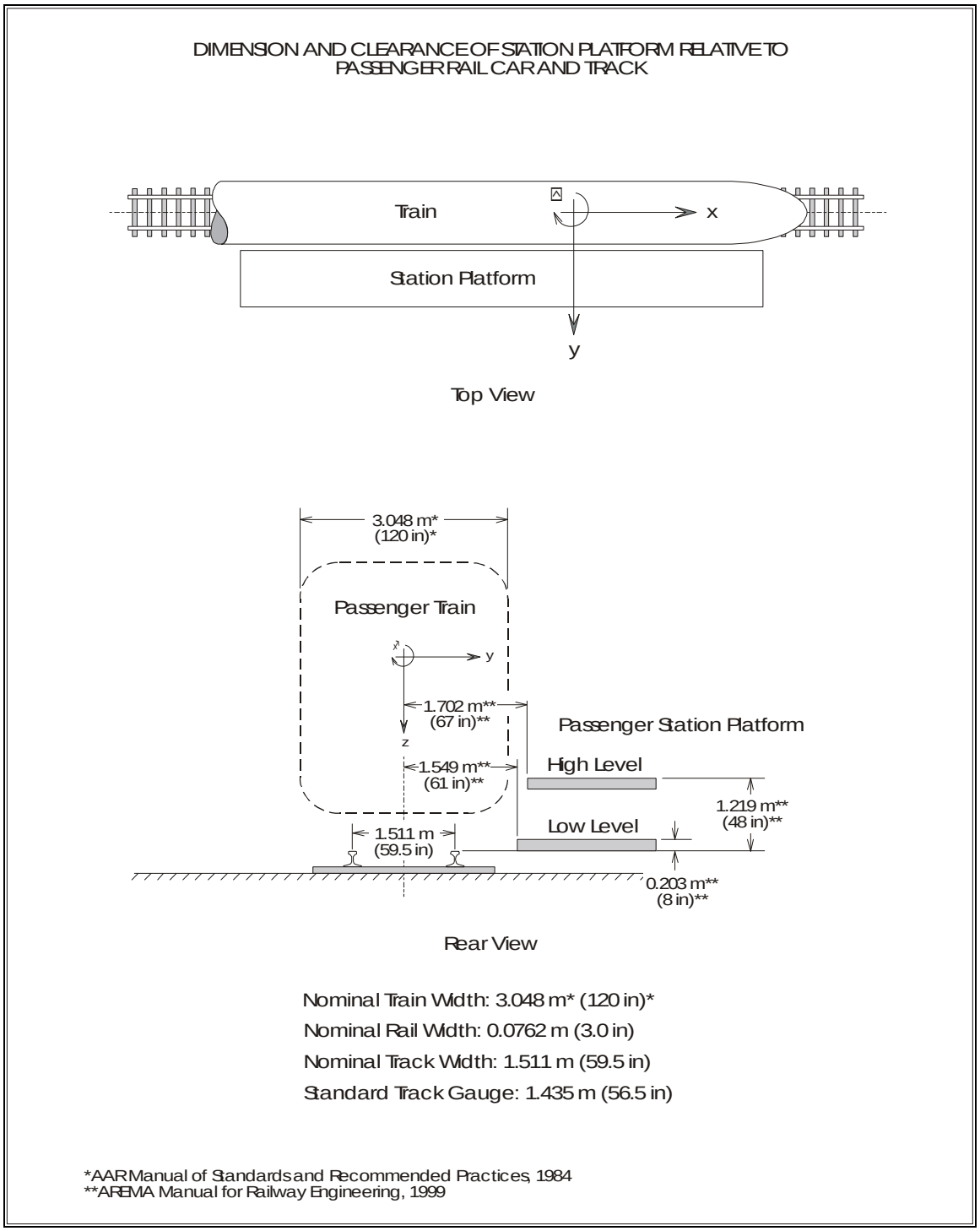

Figure 11. Dimensions and Clearances of Station Platform

Table 10. Recommended Distances from Passing Trains in Various Countries

Country	Railway and Application at Train Speed (V)	Distance to Outer Edge of Nearest Rail	Distance to Edge of Station Platform or to Side of Train
United States		(non recommended)	(non recommended)
Britain	Staff: V ≤ 201 km/h (125 mph).	• 2.0 m (79 in)	
	Public: V ≤ 201 km/h (125 mph).		• 1.5 m (59 in)
France	SNCF worker on classic line: V ≤ 160 km/h (99 mph).	• 1.5 m (59 in)	
	SNCF worker on classic or high-speed line: V > 160 km/h (99 mph).	• 2.0 m (79 in)	
	SNCF public on classic line: V ≤ 160 km/h (99 mph).	• 1.8 m (71 in)	
	SNCF public on classic line: V ≤ 200 km/h (124 mph).	• 2.5 m (98 in)	
Germany	Worker: V ≤ 40 km/h (25 mph).	• 1.10 m (43 in)	
	Worker: V ≤ 300 km/h (186 mph).	• varies up to 2.55 m (100 in)	
	Public: V ≤ 160 km/h (99 mph).		• 1.0 m (39 in)
	Public: V ≤ 200 km/h (124 mph).		• 1.5 m (59 in)
	Public: V ≤ 230 km/h (143 mph).		• 2.2 m (87 in)
China	Employee: V ≤ 160 km/h (99 mph).	• 3.6 m (142 in)	
	Public on existing line: V ≤ 160 km/h (99 mph).		• 1.5 m (59 in)
	Public on new line: V ≤ 160 km/h (99 mph).		• 1.7 m (67 in)
Japan	Public: V ≤ 95 km/h (59 mph).		• 0.8 m (31 in)
	Public: V ≤ 250 km/h (155 mph).		• 2.5 m (98 in)
Russia	Public: V ≤ 200 km/h (124 mph).		• 2.0 m (79 in)

> …trains passing through stations at up to 200 km/h (125 mph), the public are recommended to keep 1.5 m [59 in] from the platform edge; for staff working at the trackside on high-speed routes, a 2 m [79 in] clearance from the nearest running edge should be maintained….
>
> These clearances are largely the result of combined tests involving measurements of the slipstream velocities together with actual subjective assessments. The latter are considered a vital part of the investigation of clearances for people, as the response of the human body to the type of turbulent flows produced by trains is insufficiently understood. Tests have been undertaken in France and Japan with instrumented dummies but it is not clear how the results are related to a maximum allowable gust condition. (Gawthorpe 1978)

A comprehensive long-term development strategy was suggested for improving the railway network in Britain. In planning for an increase in train speed to 225 km/h (140 mph), suggestions were made to upgrade the existing main lines. One of the suggestions relates to the track arrangements at stations:

> In an age when absolute safety has become an obsession in the UK, reinforced with all the vigour of the law, it is inexplicable that speeding trains are still allowed to pass platforms occupied by waiting passengers. All intermediate stations should therefore have a pair of 'through' tracks away from platforms. (Phillips 2000)

In France, no platforms are directly adjacent to a direct line high-speed track. A train that is to stop at a station is routed away from the direct line track onto a siding that runs along the station platform. This off-line track allows at least one track that separates the passing track and the station platform. France based their safety requirement from forces measured on cylindrical dummies, with safety gauged relative to current operations (Temple and Johnson 2003). In the French high-speed train line (Train à Grande Vitesse or TGV), the maximum train speed passing a station platform that is not a direct line high-speed track is 160 km/h (99 mph); while on a classic line, the maximum train speed passing a station platform is 200 km/h (124 mph). No trains are permitted to travel above a speed of 201 km/h (125 mph) when passing people on a station platform.[4,5]

The rules from the SNCF[6] are:

- For workers:
    - On classic lines, the person must be at least 1.5 m (59 in) from the nearest edge of the rail for trains passing by at speeds less than 160 km/h (99 mph).

[4]Tom Tsai (FRA). Trip report to the French National Railroads, December 6–8, 2000.
[5]Marcel Fumey (SNCF). Meeting with the author December 17, 2001.
[6]Laurent Guccia (SNCF). Notes from "Aerodynamic-Aeroacoustics-Aeraulics."

  - On classic or high-speed TGV lines, the person must be at least 2 m (79 in) from the nearest edge of the rail for trains passing by at speeds greater than 160 km/h (99 mph).

- For people on station platforms:

  - On classic lines, the person must be at least 1.8 m (71 in) from the nearest edge of rail for trains passing by at speeds less than 160 km/h (99 mph).

  - On classic lines, the person must be at least 2.5 m (98 in) from the nearest edge of rail for trains passing by at speeds less than 200 km/h (124 mph).

The safe standing distance from a passing train is defined for railways in Germany with safety gauged relative to current operations (Temple and Johnson 2003). Distance for workers on trackside varies according to the train passing speed, ranging from 1.10 m (43 in) for a train passing up to 40 km/h (25 mph) to 2.55 m (100 in) for a train passing up to 300 km/h (186 mph) with the distance measured from the outer edge of the nearest rail. The minimum distances from the edge of the platform for the public are 1.0 m (39 in) for a train passing up to 160 km/h (99 mph), 1.5 m (59 in) for a speed up to 200 km/h (124 mph), and 2.2 m (87 in) for a speed up to 230 km/h (143 mph).

Japan sets its safety distance from a passing train using a limiting airflow velocity of 9 m/s (20 mph) (Tanemoto and Kajiyama 2003). The standard location was set at 0.8 m (31 in) from the platform edge for local trains passing at a maximum speed of 95 km/h (59 mph). This was based on a Beaufort wind scale of 4 to 5, or an airflow velocity of 6 to 9 m/s (13 to 20 mph). A minimum distance was set at 2.5 m (98 in) from the edge of the platform for the high-speed Shinkansen train passing at 250 km/h (155 mph).

Although markings on the edge of the platform are a simple method of warning people from being too close to the track, in some cases, a more elaborate technique is implemented. On the Tokaido Shinkansen railway line in Atami, Japan, the station does not have off-line tracks for nonstop trains where trains pass by at 200 km/h (124 mph) adjacent to the passenger platform.[7] In the Atami station, a protective fence prevents people from wandering too close to the edge of the platform. An attendant is present to operate the gates to allow passengers to pass when a train is stopped at the station.

Railways in China based their recommended safety distance for higher passing train speed from the force measured on a mannequin in a test, and compared it to existing service (Heshou, Dezhao, and Houxiong 1996). A train passing on an existing rail line is limited to a force of 110 N (24.7 lb) on the mannequin, while a new high-speed line is limited to a force of 100 N (22.5 lb). Based on these permissible forces, the recommended distance for employees on the trackside is 3.6 m (142 in) from the outer edge of the nearest rail for a train passing by at a speed of 160 km/h (99 mph). The

[7]John Harding (FRA). Letter to the author, January 24, 2001.

recommended distances from the edge of a station platform for trains passing at 160 km/h (99 mph) is 1.5 m (59 in) for existing lines, and 1.7 m (67 in) for new lines.

Russia sets their safety distance at 2.0 m (79 in) from the edge of the platform for trains passing at 200 km/h (124 mph) (Heshou, Dezhao, and Houxiong 1996).

The separation distance between people and the passing train can be specified from different reference locations. For workers, the distance is generally given relative to the outer edge of the nearest rail, because no platform exists, and therefore no platform edge can be referenced. Where a station platform exists, a convenient reference is the distance to the edge of the platform. Distance from the edge of the platform can be assumed to be approximately the same as to the side of the train. Another reference location is from the track centerline, but this is a less practical location from which to measure for a person on the trackside or platform. The separation distances between people and passing trains as specified by various railways are shown in Table 10.

Certain factors should be considered when comparing distances from a passing train between railroads, especially between railroads from different countries. The reason is that when distances from a passing train are referenced with respect to the edge of the nearest rail or from the edge of the platform, the distance to the side of the train is ambiguous. The distance from the side of the train depends on the train width, platform clearance from the train, and track gauge. These factors affect the actual distance from the side of the train. The ground or platform height relative to the track is also significant as the airflow strength is affected by the height. Even specifying the distance directly from the side of the train is only a nominal distance because the side of a train is not a straight vertical surface from top to bottom. Therefore, these factors must be taken into account when comparing their recommended distances with each other.

6. Airflow Induced by a Passing Train

A moving train produces a disturbance to the surrounding air that induces an airflow, or slipstream,[8] along the train. The train-induced airflow is a complex phenomenon influenced by train speed, train geometry, distance from the train, and ambient wind. The characteristic of the induced airflow in the presence of ambient wind can be described as follows:

> The flow around a train is characterized by strong vorticity on its leeside generated by the shedding of the train boundary layers, by wakes and eddies from the train nose and discontinuities in the train profile. Compounded with this general non-uniformity of flow along the train are the additional unsteady effects due to the continuous variations in the ambient wind meeting the train. This whole unsteady flow field is then given a longitudinal component of motion, relative to a trackside observer, by the viscous action of the train dragging the slipstream along with it. (Gawthorpe 1978)

Consequently, with trains traveling at high speeds passing some train stations without stopping, the airflow from the passing train can affect the safety of people waiting on the platform. An incident reportedly occurred in Ventura, California, where an empty stroller on a train station platform was propelled toward the track, presumably by the airflow induced by the passing train, crushing the stroller under the train's wheels (Freedenberg 2003). Numerous incidents have occurred on station platforms in Britain caused by train-induced airflow that included: a luggage barrow and children's pushchairs being set into motion and hitting the train, and people almost losing their balance from a passing train (Gawthorpe 1994; Johnson, Dalley, and Temple 2002). Passing freight trains have caused most of the incidents in Britain (Temple and Johnson 2003). In addition to station platforms, safety issues have been raised in the United States on the aerodynamic effects from passing trains on people using RWT where shared-use trails (trails for pedestrians and bicyclists) are developed and located adjacent to active rail lines.

Safety concerns exist for people on station platforms as trains pass stations faster and the aerodynamic effects become stronger. The incidents described above illustrate some of the hazards. As a result, a need exists for airflow data to assess its effect on people in proximity to passing trains. Although airflow data are reported in the literature, the results are very much dependent on train geometry and measurement position relative to the train.

[8]According to Professor Christopher Baker of the University of Birmingham in the United Kingdom, the term slipstream is also used to refer to the boundary layer flow around the train, which may or may not include the wake.

Recent studies have been conducted to obtain aerodynamic characteristics specific to current high-speed train designs, and to further understand the airflow around the train. As part of Europe's RAPIDE project, CFD simulation and experiments with full-scale and model tests of 1/25 scale were conducted to measure the airflow velocity induced by a passing German high-speed ICE passenger train (Johnson, Dalley, and Temple 2002; Baker et al 2001). One notable result is the lack of repeatability in the data due to the chaotic nature of the airflow, where there was large variation in airflow velocity at a given location during repeat runs at the same ambient condition and train speed. Therefore, for proper analysis, it is necessary to have sufficient quantity of data on the types of trains that are operating, with data measured from known and consistent positions.

With the high-speed Acela Express train being placed into service in the United States, numerical simulation and full-scale testing were conducted to determine the strength and characteristic of the airflow induced by a train passing a station platform (Liao et al 1999; PB 2000; GEOCOMP 2002; Duffell 2000). Results computed from numerical simulation were compared with test data. Computed and measured airflows from passing high-speed Acela Express and conventional Amfleet trains provided a relative measure of airflow velocity between the two types of trains. By comparing the airflow induced by Acela Express trains with the airflow from the existing operation of Amfleet trains, it provided a gauge for assessing the aerodynamic effects of a passing Acela Express train on people on station platforms. This collection of airflow velocity data measured at various lateral distances from passing trains provided the necessary relation to assess the aerodynamic effects on people from wind speed criteria.

6.1. Mathematical Modeling of Train-Induced Airflow

The FLUENT™ CFD program was used to simulate the airflow induced by a train passing a station platform. An Acela Express train and an Amfleet train were modeled to obtain the induced airflow velocity for low- and high-level platforms, and for various heights from the platform and distances from the passing trains. The train-induced airflow velocity obtained from the CFD was for the longitudinal component along the direction of the passing train.

6.1.1. Acela Trainset

The Acela Express train was modeled as six coaches with two tapered nose power cars (one power car at each end). It was found that the induced airflow from the bow wave and boundary layer effects were not significant, but wake effects are important with the wake from a low level platform being stronger than from a high level platform. The maximum airflow velocities and exposure times at various distances from the side of the passing train are shown in Table 11.

Table 11. Maximum Longitudinal Airflow Velocities and Exposure Times from an Acela Express Train Passing a Low-Level Platform

Train Speed	Distance above Top of Rail	Distance from Side of Train	Airflow Velocity	Exposure Time
177 km/h (110 mph)	0.762 m (2.5 ft)	0.6096 m (2 ft)	17.9 m/s (40 mph)	0.5 to 1 s
177 km/h (110 mph)	0.762 m (2.5 ft)	2.7432 m (9 ft)	11.2 m/s (25 mph)	3 s
177 km/h (110 mph)	1.524 m (5 ft)	1.2192 m (4 ft)	11.2 m/s (25 mph)	2 s
241 km/h (150 mph)	0.762 m (2.5 ft)	0.9144 to 1.8288 m (3 to 6 ft)	17.9 m/s (40 mph)	1 s
241 km/h (150 mph)	0.762 m (2.5 ft)	3.676 m (12 ft)	11.2 m/s (25 mph)	2 to 3 s
241 km/h (150 mph)	1.524 m (5 ft)	2.4384 m (8 ft)	11.2 m/s (25 mph)	2 s

The maximum longitudinal airflow velocities (mean plus maximum fluctuating velocities) that are induced along various areas of the train, the bow wave, boundary layer, and wake, are shown in Table 12 and plotted in Figure 12(a). At a lateral distance closest to the side of the train, the maximum longitudinal airflow velocity is 0.27 of the train speed occurring at the wake, whereas the airflows from the bow wave and boundary layer are lower (Figure 12(a)). Shown with the longitudinal airflow velocity (Table 12) is the corresponding Beaufort number. While some very high velocities are reached, reference to the Beaufort scale must be qualified:

> Mitigating these concerns, however, is that the air velocities have relatively short durations and are transient in nature. Related to this factor, these exposure limits are based to some extent on the Beaufort scale, which was originally developed for sustained wind rather than transient air velocity effects. (Liao et al 1999)

Table 12. Maximum Longitudinal Airflow Velocities at 0.762 m (2.5 ft) above Low-Level Platform Induced by an Acela Express Train Passing at 241 km/h (150 mph)

Distance from Side of Train	Bow Wave Element		Boundary Layer Element		Wake Element	
	Airflow Velocity, U	Beaufort Number	Airflow Velocity, U	Beaufort Number	Airflow Velocity, U	Beaufort Number
0.9144 m (3 ft)	5.8 to 11.2 m/s (13 to 25 mph)	4 to 6	5.8 to 11.2 m/s (13 to 25 mph)	4 to 6	U>17.9 m/s (U>40 mph)	above 8
1.822 m (6 ft)	U<5.8 m/s (U<13 mph)	3	U<5.8 m/s (U<13 mph)	3	11.2 to 17.9 m/s (25 to 40 mph)	6 to 8
2.7432 m (9 ft)	U<5.8 m/s (<13 mph)	3	U<5.8 m/s (U<13 mph)	3	5.8 to 11.2 m/s (13 to 25 mph)	4 to 6
3.6576 m (12 ft)	U<5.8 m/s (U<13 mph)	3	U<5.8 m/s (U<13 mph)	3	5.8 to 11.2 m/s (13 to 25 mph)	4 to 6

6.1.2. Amfleet Train

The second model that was simulated is an Amfleet train that consisted of an AEM-7 bluff nose electric locomotive with six coaches. The maximum airflow velocities that were induced along various areas of the train, the bow wave, boundary layer, and wake, are shown in Table 13 and plotted in Figure 12(b). At the closest lateral distance to the train side, the maximum longitudinal airflow velocity from the boundary layer and wake is 0.32 of the train speed (Figure 12(b)). The bow wave does not reach as high a value, but this is the longitudinal component of airflow, while the lateral component would be expected to be significant for the bow wave as the head of the train pushes the air aside in the lateral direction.

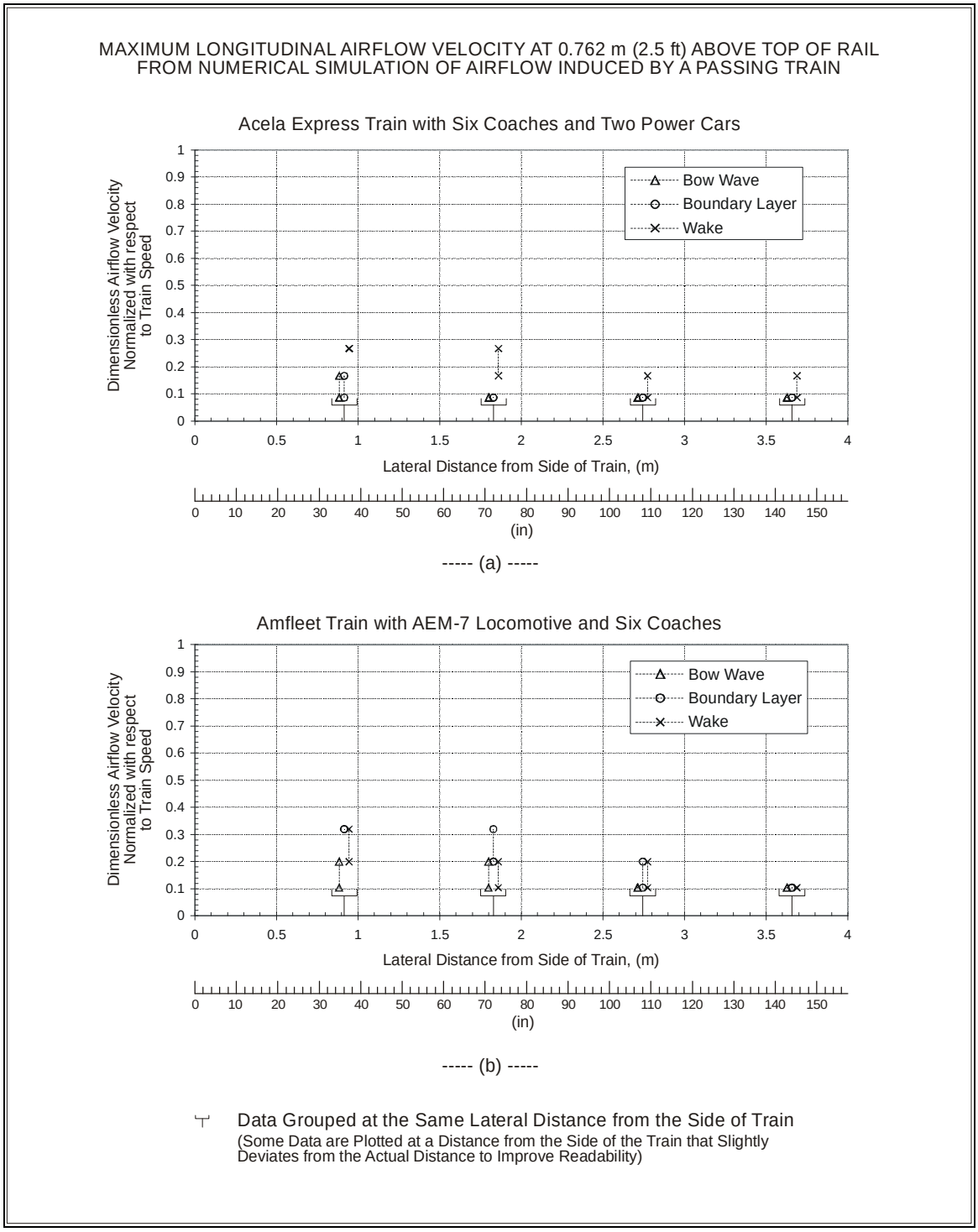

Figure 12. Computed Maximum Airflow Velocities at 0.762 m (2.5 ft) above Top of Rail

Table 13. Maximum Longitudinal Airflow Velocities at 0.762 m (2.5 ft) above Low-Level Platform Induced by an Amfleet Train with AEM-7 Locomotive Passing at 201 km/h (125 mph)

Distance from Side of Train	Bow Wave Element		Boundary Layer Element		Wake Element	
	Airflow Velocity, U	Beaufort Number	Airflow Velocity, U	Beaufort Number	Airflow Velocity, U	Beaufort Number
0.9144 m (3 ft)	5.8 to 11.2 m/s (13 to 25 mph)	4 to 6	U>17.9 m/s (U>40 mph)	above 8	11.2 to 17.9 m/s (25 to 40 mph)	6 to 8
1.822 m (6 ft)	5.8 to 11.2 m/s (13 to 25 mph)	4 to 6	11.2 to 17.9 m/s (25 to 40 mph)	6 to 8	5.8 to 11.2 m/s (13 to 25 mph)	4 to 6
2.7432 m (9 ft)	U<5.8 m/s (U<13 mph)	3	5.8 to 11.2 m/s (13 to 25 mph)	4 to 6	5.8 to 11.2 m/s (13 to 25 mph)	4 to 6
3.6576 m (12 ft)	U<5.8 m/s (U<13 mph)	3	U<5.8 m/s (U<13 mph)	3	U<5.8 m/s (U<13 mph)	3

6.1.3. Comparison of Results

Numerical simulations were performed for an Acela Express train traveling at 241 km/h (150 mph) and an Amfleet at 201 km/h (125 mph). At these operating speeds, both trains induced about the same maximum longitudinal airflow velocities as shown in Table 14, with the Amfleet train producing the strongest airflow from the boundary layer, while the strongest airflow for the Acela Express train was coming from the wake (Table 12 and Table 13). At the furthest distance from the train, the wake from the Acela Express train produced a stronger airflow than the overall airflow from the Amfleet train. Relative to platform height, induced airflow from the Acela Express train was lower on a high-level than on a low-level platform.

A comparison between the results from this CFD model with data reported from the literature indicates some differences:

> …there may be assumptions that limit the absolute predictive accuracy of the CFD models. However, the comparative accuracy of the CFD models has more validity

than the absolute accuracy, e.g., comparison of the relative wind velocities, due to different cars are more valid than absolute values of the calculated velocities themselves. (Liao et al 1999)

Table 14. Maximum Longitudinal Airflow Velocities from Passing Trains at 0.762 m (2.5 ft) above Low-Level Platform

Distance from Side of Train	Acela Express at 241 km/h (150 mph)		Amfleet Train with AEM-7 Locomotive at 201 km/h (125 mph)	
	Airflow Velocity, U	Beaufort Number	Airflow Velocity, U	Beaufort Number
0.9144 m (3 ft)	U>17.9 m/s (U>40 mph)	above 8	U>17.9 m/s (U>40 mph)	above 8
1.822 m (6 ft)	11.2 to 17.9 m/s (25 to 40 mph)	6 to 8	11.2 to 17.9 m/s (25 to 40 mph)	6 to 8
2.7432 m (9 ft)	5.8 to 11.2 m/s (13 to 25 mph)	4 to 6	5.8 to 11.2 m/s (13 to 25 mph)	4 to 6
3.6576 m (12 ft)	5.8 to 11.2 m/s (13 to 25 mph)	4 to 6	U<5.8 m/s (U<13 mph)	3

6.2. Full-Scale Test Measurement of Induced Airflow

Full-scale tests were conducted to measure the airflow induced by a passing train. A series of tests were conducted over a span of time at various locations along the Northeast Corridor route, whose locations were selected based on factors such as speed of passing trains, station configuration, and ease of testing. Airflow velocity was measured by pitot-static tube as illustrated in Figure 13(a), and unless otherwise specified, measurements were for the longitudinal airflow velocity, which was the airflow parallel to the track and flowing in the direction of the passing train (with the pitot tube nose facing the approaching train). In earlier tests, only a single peak airflow velocity value was obtained, whereas later tests used a more sophisticated measurement arrangement in which a time history of the data was recorded during the entire passage of a train.

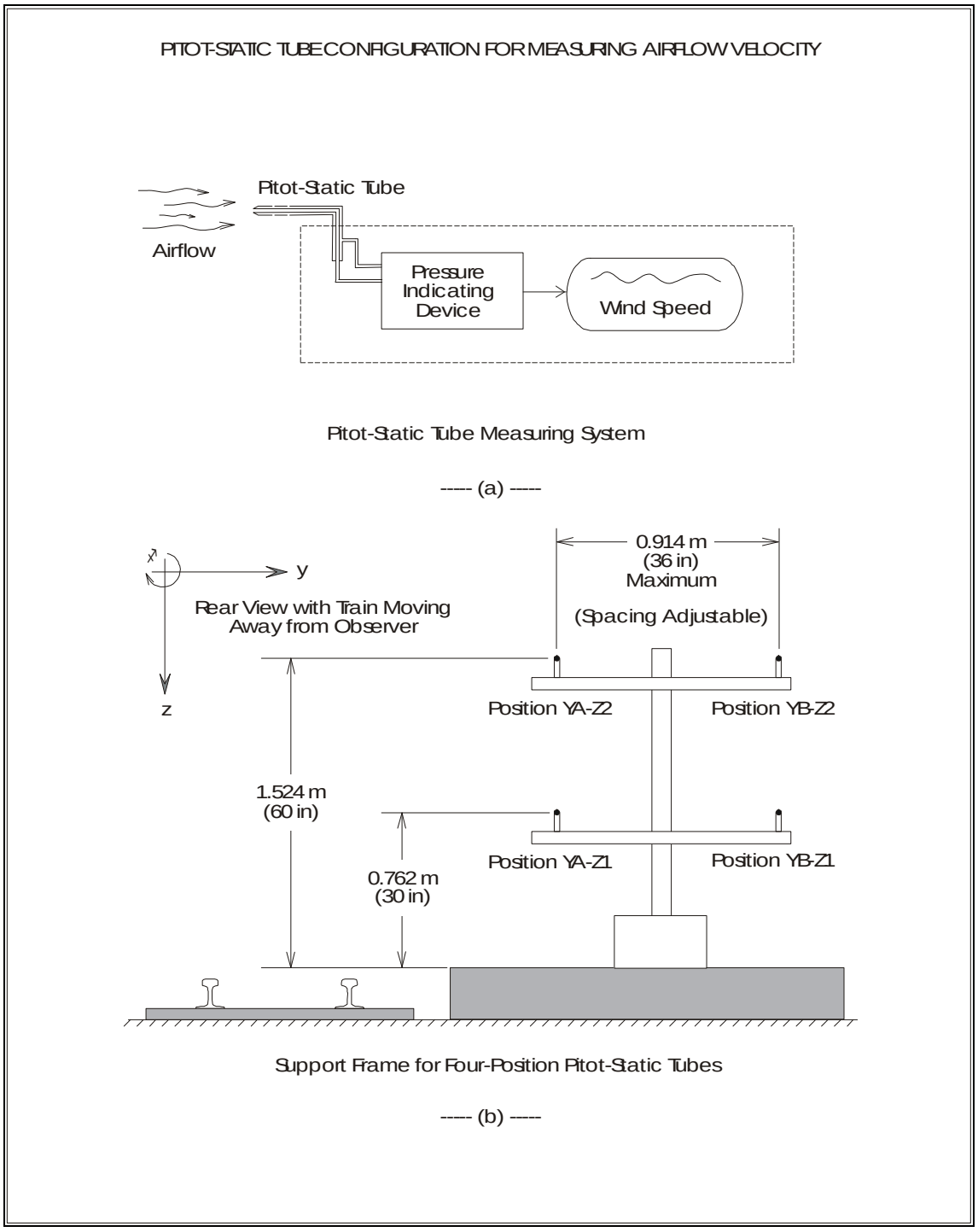

Figure 13. Pitot-Static Tube System for Measuring Airflow Velocity and Support Frame Arrangement

6.2.1. Test of September 1998 in New Jersey and Delaware

The initial test was performed on the train stations at Princeton Junction, New Jersey, and at Newark, Delaware, during September 1998 (Liao et al 1999). The train-induced airflow velocity was measured with a pitot tube positioned parallel to the track at about 1.7 m (5.5 ft) above the platform level, with the pitot tube nose facing the approaching train. Measurements were obtained at high- and low-level platforms.

These measurements demonstrate the effect of position on the strength of the airflow. The airflow velocity, as shown in Table 15, normalized with respect to train speed, decreases with increased lateral distance from the train, or with increased height in the platform. Whereas only longitudinal airflow velocity along the direction of the moving train was measured, a perceived airflow occurred in the lateral direction. Comparison between the full-scale test and CFD results shows some differences with the test results being either within the range or slightly higher than the CFD results.

Table 15. Maximum Longitudinal Airflow Velocities from Passing Amfleet Trains at about 1.7 m (5.5 ft) above Top of Rail from September 1998 Test

Location & Date (Year-Month-Day)	Platform Height	Distance from Side of Train	Train Speed, Vtrain	Airflow Velocity	
				Uair	Uair/Vtrain
Princeton Junction, NJ 1998-09-01	Low	2.74 m (9.0 ft)	201 km/h (125 mph)	27 km/h (17 mph)	0.136
Princeton Junction, NJ 1998-09-08	High	1.68 m (5.5 ft)	177 km/h (110 mph)	16 km/h (10 mph)	0.091
		5.49 m (18 ft)	201 km/h (125 mph)	13 km/h (8 mph)	0.064
Newark, DE 1998-09-17	Low	1.68 m (5.5 ft)	198 km/h (123 mph)	45 km/h (28 mph)	0.23
		5.18 m (17.0 ft)	183 km/h (114 mph)	3 km/h (2 mph)	0.018

6.2.2. Test of February 2000 in Maryland

A second test was performed during February 20 and 21, 2000, on a low-level platform train station in Edgewood, Maryland (Duffell 2000). It was similar to the first test, with a single pitot tube positioned parallel to the track with the pitot tube nose facing the approaching train. The pitot tube was at a distance of about 0.6 m (2 ft) from the edge of the platform and at a height of about 1.5 m (5 ft) above the platform.

Longitudinal airflow velocities were measured for a number of different types of passing trains, including Acela Express, Amfleet, and freight trains. All the passenger trains passed at speeds ranging from 179 to 240 km/h (111 to 149 mph). The Amfleet trains consisted of eight cars pulled by two locomotives. The freight trains were estimated at over 1.6 km (1 mile) long consisting of a mixture of different types of cars pulled by diesel-electric locomotives. In Figure 14 a plot shows the maximum airflow velocity normalized with respect to train speed. The Acela Express train induced the lowest airflow with a mean airflow velocity of 0.25 and a maximum of 0.28 of the train speed. Amfleet trains induced a slightly higher airflow with a mean of 0.33 and a maximum of 0.37. Only two measurements were recorded for the freight train; which passed at a speed of 48 km/h (30 mph) producing a velocity ratio of 0.7. The strong airflow produced by a freight train is consistent to other observations where the aerodynamically rough geometries of the different freight cars induced airflow that is much greater than the smoother profile on a passenger train (Gawthorpe 1978; Temple and Johnson 2003; Johnson, Dalley, and Temple 2002; Andersson, Aronsson, and Pettersson 1994).

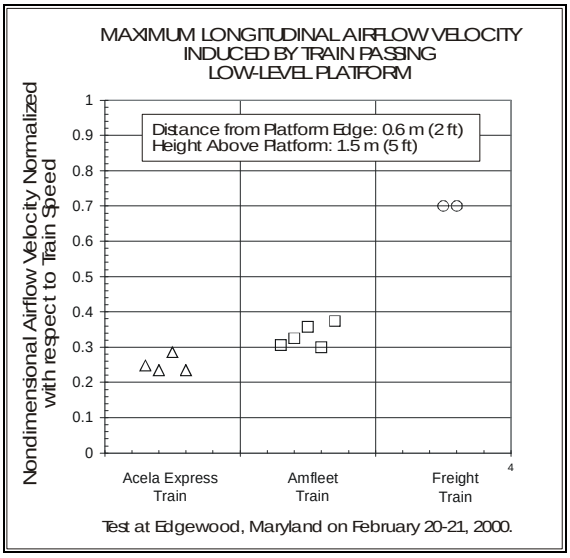

Figure 14. Maximum Airflow Velocities from Passing Trains Measured at Train Station in Maryland

6.2.3. Test of July 2000 in Massachusetts and Rhode Island

In the third July 2000 test series, the measurements were obtained on low-level station platforms at Mansfield and Sharon, Massachusetts, and at Kingston, Rhode Island during July 2000 (PB 2000). The design for this test was more sophisticated than in the previous tests. Simultaneous measurements of longitudinal airflow velocities were obtained from pitot-static tubes at four different positions. Each pitot-static tube was positioned parallel to the track with the pitot-static tube nose facing the approaching train. The measurement was recorded over the duration of the passing train to obtain a velocity-time history of the data. A photoelectric sensor and a light beam that spans across the tracks were used to detect the presence of a train. As a train passes, the light beam is interrupted, therefore providing an indication on the head and tail ends of the train as it passes by the location of the pitot-static tubes.

The four pitot-static tubes were mounted on a frame with two pitot-static tubes on each of the two horizontal arms of the frame as shown in Figure 13(b). This provided measurements at two different lateral distances from the side of the train and at two

different heights. The lateral positions of the two pitot-static tubes on each arm were spaced at a distance of 0.914 m (36 in) relative to each other, with the heights of the lower pitot-static tubes at 0.762 m (30 in) and the upper pitot-static tubes at 1.524 m (60 in) above the platform.

Numerous measurements were made from the passage of Amfleet and Acela Express trains, but because of some test difficulties, only two of the best measurements were selected for detailed analysis as shown in Table 16. The maximum speed of the induced airflow for the Acela Express train traveling at 233 km/h (145 mph) is in most cases slightly lower than the Amfleet train traveling at 154 km/h (96 mph). When the airflow velocity is normalized with respect to train speed, it is apparent that the airflow induced by the Acela Express train is less than the Amfleet train, ranging from 16 to 49 percent less in the strength of the airflow, depending on the location of the measurement.

One of the motivations of the full-scale test was to compare the test data with the results from the CFD simulation. The following observations were made when the results were examined (results not shown):

> …it is seen that the major features of the data and the CFD calculations agree quite well. In particular, it should be noted that the maximum value of airflow for the Acela [Express] occurs usually at the tail of the train, whereas the maximum value of airflow for the Amfleet train is usually at the head of the train, or shortly thereafter, especially for positions closer to the side of the train. This is evident in both the CFD calculations and the measurements. This difference in when the maximum occurs reflects the fact that the Acela [Express] is much more streamlined, whereas the Amfleet engine has a blunt front end that tends to cause more disturbance and tends to push the air ahead of it, causing a more pronounced bow wave effect. (PB 2000)

Table 16. Maximum Longitudinal Airflow Velocities from Passing Trains from July 2000 Test

Location & Date (Year-Month-Day)	Train Type & Train Speed, Vtrain	Lateral Distance from Side of Train	Height above Rail	Airflow Velocity, Uair	Airflow Velocity, Uair/Vtrain
Mansfield, MA 2000-07-07	Amfleet at 154 km/h (96 mph)	0.603 m (23.8 in)	0.914 m (36 in)	116 km/h (72 mph)	0.75
			1.676 m (66 in)	116 km/h (72 mph)	0.75
		1.52 m (59.8 in)	0.914 m (36 in)	88 km/h (55 mph)	0.57
			1.676 m (66 in)	50 km/h (31 mph)	0.32
Kingston, RI 2000-07-19	Acela Express at 233 km/h (145 mph)	0.616 m (24.3 in)	0.914 m (36 in)	114 km/h (71 mph)	0.49
			1.676 m (66 in)	93 km/h (58 mph)	0.40
		1.53 m (60.3 in)	0.914 m (36 in)	68 km/h (42 mph)	0.29
			1.676 m (66 in)	63 km/h (39 mph)	0.27

The results from the measurements listed in Table 16 illustrate the effect of location on the strength of the airflow velocity. Because the pitot-static tubes were located at four corners of the frame, this provided measurements at two different distances from the train and at two different heights. A reduction occurs in maximum airflow velocity from either an increase in lateral distance from the train, or from an increase in height from the track, as shown in Table 17.

Attention will be focused on the measurements from the pitot-static tubes located either at the bottom or the one nearest the train, because these locations will generally have the strongest airflow. An increase in lateral distance from the train by a factor of 2.73 for the bottom measurements reduces the airflow by 40 percent for the passing Acela Express train, and by 24 percent for the Amfleet train. Therefore, increasing the height by a factor of 1.83 for the measurements nearest the train reduces the airflow by 18 percent for the passing Acela Express train, but with no change in the strength of the airflow for the Amfleet train.

All airflow velocities that have been presented are raw data as measured without any additional processing. However, the data contained a high frequency component, which was suspected to be electrical noise (PB 2000). By applying a moving average to the data with a minimum averaging duration of 0.032 s, this acts as a low-pass filter which removes the high frequency noise.

Table 17. Changes in Maximum Induced Longitudinal Airflow Velocities from Changes in Positions

Passing Train	Increase Factor in Lateral Distance	Increase Factor in Height	Reduction in Airflow Velocity
Acela Express	2.73	0	40% (Z1*)
	2.73	0	32% (Z2*)
	0	1.83	18% (YA*)
	0	1.83	7% (YB*)
Amfleet	2.73	0	24% (Z1*)
	2.73	0	57% (Z2*)
	0	1.83	0 (YA*)
	0	1.83	43% (YB*)

*Pitot-static tubes located near (YA) or far (YB) from the train, or at the bottom (Z1) or top (Z2) positions.

In addition to noise removal, there is another purpose of applying an averaging process to the data. The averaging of the data removes the rapid changes and short duration peaks. The results of which can be useful to assessing human response:

> The high frequency components of the airflow, even if they were actual turbulence effects (and not noise in the signal), could likely not be felt or experienced by people. It is unlikely that the human senses can detect rapid changes and short duration peaks. Thus a spike of [113 km/h] 70 mph for less than 0.1 second may not have any practical effect; it would likely be felt as an equivalently lower velocity gust of air….The moving average smoothing technique thus provides an indication of the sustained effects of the airflow as a train passes, over realistic periods (say 0.5 to 2 seconds) that are within the range of human experience. (PB 2000)

To illustrate this effect, a moving average is applied to the data from the bottom pitot-static tube closest to the train. By performing this process on the airflow data from the passing Acela Express train, the maximum induced airflow velocity dropped from a high of 114 km/h (71 mph), with no filtering, to 68 km/h (42 mph), and 64 km/h (40 mph) corresponding to moving average intervals of 1.0 s and 2.0 s respectively. The results suggest that these values "…may reflect the equivalent values of the airflow that could be compared to some extent to such measures as the Beaufort scale, though smoothing at even longer intervals may be appropriate for a direct comparison" (PB 2000).

One of the considerations in applying the moving averages is the effect of averaging duration. Because the disturbance to the surrounding air by a passing train is transient, a very long averaging duration that extends excessively beyond the period of the passing train will approach the condition for the ambient undisturbed air. Also, while smoothing of the data over a certain averaging duration is applicable to human response, a shorter averaging duration is necessary when evaluating the effect of airflow to particles with

low mass. Particles with low mass, and therefore low inertia, can respond much more readily to the rapid changes in the airflow:

> …small particulate matter, such as loose debris, soil particles, snow or ice, on the track or platforms, would respond to higher frequency peak airflow values….In the limit as the particulate mass and density approaches the mass and density of the air (e.g.[,] a mist of rain or snowflakes), the particles may respond at high frequencies to be nearly the same values as the peaks of airflow velocity record. The moving average smoothing technique may thus not [be] as representative of what the buffeting effects of turbulent airflow would be on very small particulate matter. (PB 2000)

6.2.4. Test of September to October 2002 in Massachusetts

In this final test, airflows were measured on a station platform alongside another test where forces were measured from instrumented dummies (Chapter 7 provides information on the instrumented dummies with test configuration related to the airflow measurement) (GEOCOMP 2002). The test was performed on a train station with a low-level platform in Mansfield, Massachusetts, from September 29 to October 3, 2002. Measurements were obtained from three different types of trains as distinguished by its head- and tail-end geometries. In many cases data was obtained for multiple passes of the same type of train. Also, the airflow was measured at various distances from the train and with different orientations of the pitot-static tubes, as shown in Figure 15.

Figure 15. Pitot-Static Tubes for Measuring Longitudinal and Lateral Airflow Velocities Induced by a Passing Train with Cylindrical Instrumented Dummy in the Background

Four pitot-static tubes mounted on a frame at two different heights, and at two different lateral positions or orientations, simultaneously measured the airflow velocities as a velocity-time history data (Figure 13). Except for some reference measurements, each pitot-static tube was either oriented to measure longitudinal (+x) airflow parallel to the track along the direction of the passing train, or oriented to measure lateral (+y) airflow perpendicular to the track away from the passing train, as each pitot-static tube can measure the component flowing in only one direction. These orientations were expected to have the strongest airflow. In some configurations, the pitot-static tubes were oriented

perpendicular to each other to capture the simultaneous longitudinal and lateral components of airflow.

Airflow velocities were measured for six different configurations of the pitot-static tubes. In configuration 1, the pitot-static tubes were arranged with the same alignment to previous tests. With configurations 2, 3, and 4, the pitot-static tubes were placed at the same lateral distance from the track as the axes of the cylindrical dummies. Configurations 5 and 6 were reference measurements to determine the extent of reversed airflow (airflow in the -x and -y directions). The details of each of these configurations are shown in Table 18.

Table 18. Configurations for Airflow Velocity Measurement at Heights Z1=0.866 m (34 in) and Z2=1.628 m (64 in) above Top of Rail

Description	Configuration	Pitot-Static Tube Position*	Lateral Distance (YA or YB) from Side of Train	Direction of Airflow being Measured
Alignment same as July 2000 test with pitot-static tubes parallel to track.	1	YA-Z1 YA-Z2	0.603 m (23.8 in)	• parallel to track • in direction of moving train (+x)
		YB-Z1 YB-Z2	1.442 m (59.8 in)	• parallel to track • in direction of moving train (+x)
YA-Z1 & YA-Z2 aligned with cylinder axes of cylindrical dummies at position 1 with pitot-static tubes parallel to track.	2	YA-Z1 YA-Z2	1.17 m (46.3 in)	• parallel to track • in direction of moving train (+x)
		YB-Z1 YB-Z2	2.09 m (82.3 in)	• parallel to track • in direction of moving train (+x)
YA-Z1 & YA-Z2 aligned with cylinder axes of cylindrical dummies at position 1 with pitot-static tubes parallel & perpendicular to track.	3	YA-Z1 YA-Z2	1.17 m (46.3 in)	• parallel to track • in direction of moving train (+x)
		YB-Z1 YB-Z2	0.933 m (36.8 in)	• perpendicular to track • away from train (+y)
YA-Z1 & YA-Z2 aligned with cylinder axes of cylindrical dummies at position 2 with pitot-static tubes parallel & perpendicular to track.	4	YA-Z1 YA-Z2	1.43 m (56.3 in)	• parallel to track • in direction of moving train (+x)
		YB-Z1 YB-Z2	1.19 m (46.8 in)	• perpendicular to track • away from train (+y)
Reversed airflow measurement with pitot-static tubes parallel & perpendicular to track.	5	YA-Z1 YA-Z2	1.63 m (64.3 in)	• perpendicular to track • toward train (-y)
		YB-Z1 YB-Z2	1.39 m (54.8 in)	• parallel to track • opposite direction of moving train (-x)
YA-Z1 & YA-Z2 aligned with cylinder axes of cylindrical dummies at position 1 for reversed airflow measurement with pitot-static tubes parallel & perpendicular to track.	6	YA-Z1 YA-Z2	0.845 m (33.3 in)	• perpendicular to track • toward train (-y)
		YB-Z1 YB-Z2	0.603 m 23.8 in)	• parallel to track • opposite direction of moving train (-x)

*Pitot-static tubes located near (YA) or far (YB) from the train, or at the bottom (Z1) or top (Z2) positions.

The airflow was measured for six different test configurations of the pitot-static tubes with one or more passes from each of three different types of trains. Table 19 shows the number of train passes for each test configuration for three types of trains: the Acela Express train, and the Amfleet trains with either an AEM-7 or HHP-8 locomotive. The greatest number of airflow measurements was from the Acela Express train, whereas the Amfleet trains generally had only one or two passes for each type of locomotive.

Table 19. Number of Passing Trains

Train Type	Number Passing Trains for each Test Configuration					
	1	2	3	4	5	6
Acela Express Trainset	6	1	6	6	0	1
Amfleet with AEM-7	0	2	2	1	0	1
Amfleet with HHP-8	3	1	2	2	1	0

The results of these measurements are discussed in Part 2 of this report.

7. Measurement of Force on Object from Passing Train

A moving train displaces the air around it and causes a disturbance in the surrounding air that is reflected as a flow field around the train of varying static pressure and flow velocity. When a person is near a passing train, an interaction will occur with the flow field creating a pressure distribution on the person that can result in an unbalanced force. A measurement of airflow velocity captures one component of the disturbance, and while the dynamic pressure from the airflow can be related to a force on a person, yet another method is by a direct measurement of the force on the body.

Forces have been measured using circular cylinders to represent a human body. Horner (1958) indicated that the human body is similar in aerodynamic shape to a circular cylinder with a height to diameter ratio of between 4 and 7. SNCF uses forces measured from instrumented circular cylinders to base their trackside and platform safety distances. However, for the range of airflow velocity of interest, the drag coefficient of a circular cylinder varies by a factor of three, as the airflow occurs in Reynolds numbers that are in the critical regime. The results from these tests indicate that the cylinder responded strongly to static pressure effects, but not to the dynamic wake velocity that is considered significant to the stability of people and objects (RAPIDE 2001).

Because the characteristics of a circular cylinder may not be representative of a human body, tests have been directed to measure the force on a human-shaped mannequin whose geometric and physical properties closely resemble that of a human being. A test was conducted in Sweden to measure forces on simple bodies in the form of a semicircular cylinder that simulated a person standing on a station platform exposed to the wind effects of the following passing trains: Inter-City trains (Swedish express trains), freight trains, and Swedish X2 modern high-speed trains (Andersson, Aronsson, and Pettersson 1994). As part of the European RAPIDE project, a full-scale test was conducted in Germany to measure the forces on instrumented mannequins placed alongside the track as an ICE high-speed train passes (Johnson, Dalley, and Temple 2002; Prevezer 2001). China also performed similar full-scale tests on instrumented mannequins from which the data was used to arrive at recommended trackside and platform safety distances (Heshou, Dezhao, and Houxiong 1996).

Although the circular cylinder may not fully simulate a human body over its full range of airflow velocity, it provides a means of gauging the relative force levels from its aerodynamic interaction with different trains. A circular cylinder's symmetry simplifies the testing, because the response characteristic is the same independent of its orientation. The interaction of fluid flow over a circular cylinder has been extensively studied with an abundance of data available for computation and analysis. Therefore, a test was conducted using instrumented circular cylinders stationed alongside the track to gain a better understanding on the load applied to a body from the aerodynamic interaction with a passing train (SNCF 2002).

7.1. Test Configuration and Instrumentation

In a research program conducted in France by the SNCF, both theoretical and experimental results were obtained on the force that would be experienced by a person in proximity to a passing train (Marty, Coulmy, and Luu 1978). During the early stages of their research, a series of detector pins were placed at various distances from the track. These detector pin were designed to fall at a defined wind speed of 17 m/s (38 mph) generated by a passing train. In the 1970s, SNCF developed a dummy that was instrumented to measure the force from the aerodynamic interaction between the dummy and a passing train. The dummy was designed as a circular cylinder that geometrically represents the trunk of a person and accounts for the muscular reaction time of a human.

Both theoretical calculations and experimental measurements were made to determine the force on the cylindrical object from the induced airflow generated by the head of a passing TGV 001 train. The maximum force measured from the dummy can be related to the airflow velocity from the safety distance found during the test with the detector pins. This establishes the maximum force that is applied to a person (the trunk segment) when situated at a distance from the track where the maximum air velocity is attained.

Using cylindrical dummies similar to those used in France, a full-scale test was conducted by SNCF personnel to measure the forces on the dummies from the aerodynamic interaction with a passing train. The circular cylindrical instrumented dummy (CID) was a SNCF/VR Model 1993 which consisted of a cylinder with a diameter of 0.39 m (15.4 in) and an axial length of 0.92 m (36.2 in) as shown in Figure 16 and illustrated in Figure 17. The cylinder was supported on a post with strain gauges attached to the post to measure the unbalanced force acting on the cylinder along a horizontal plane. Any bending to the post is related to the unbalanced force applied to the cylinder. Data from the CID was measured at 1200 samples per second and was processed through a Bessel second order 15 Hz low-pass digital filter to account for the muscular reaction time of a human being. The resultant force is expressed as two time-varying force components, Fx(t) and Fy(t), with the coordinate frame shown in Figure 18. Relative to an observer facing the same direction of travel as the passing train, the positive longitudinal axis (+x) is in the direction of the facing observer, and the positive lateral axis (+y) is to the right. Zero time occurs when the nose of the train reaches each CID, with time increasing as the train passes.

Figure 16. Cylindrical Instrumented Dummy for Measuring Force from Aerodynamic Interaction with a Passing Train

The test was performed on a low-level train station platform in Mansfield, Massachusetts, from September 29 to October 3, 2002. Two CIDs referred to as CID-4 and CID-5, were placed on the platform (platform height was about 0.1 m (4 in) from the top of the rail) with both CIDs at the same distance away from the track for simultaneous measurements as shown in Figure 19. Forces on the CIDs were measured for two different lateral positions from the track. In the first location, the nominal distance from the side of the train to the axis of the cylindrical body was 1.20 m (47.4 in). At this distance, the nearest surface of the cylinder facing the track was at the edge of the 0.965 m (38 in) wide platform safety line. In the second location, the nominal distance from the side of the train to the axis of the cylindrical body was 1.46 m (57.7 in). This distance corresponded to the safety distance used in France for railroad personnel next to a high-speed track (with TGV trains running faster than 209 km/h (130 mph) and conventional trains running faster than 161 km/h (100 mph)). The lateral distances measured from various locations are shown in Table 20.

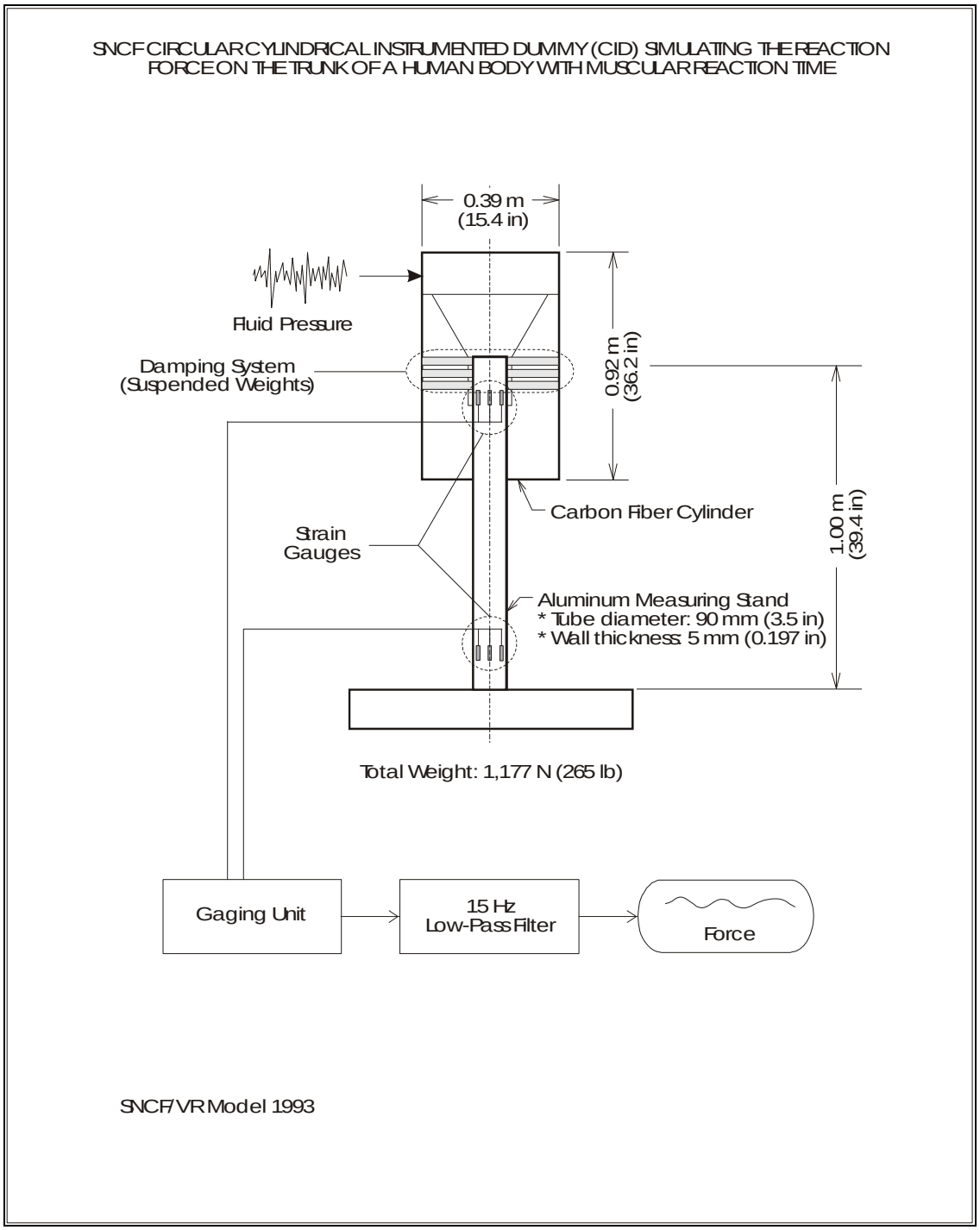

Figure 17. SNCF Circular Cylindrical Instrumented Dummy for Measuring Force from Aerodynamic Interaction with a Passing Train

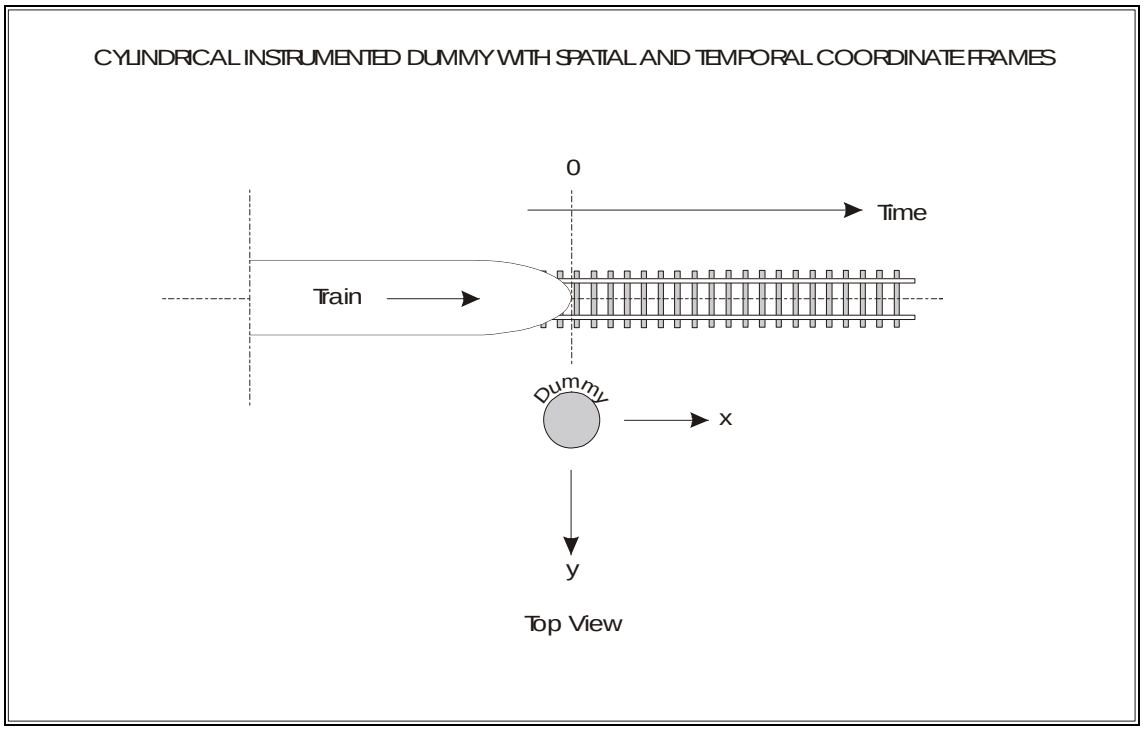

Figure 18. Coordinate Frames for a CID

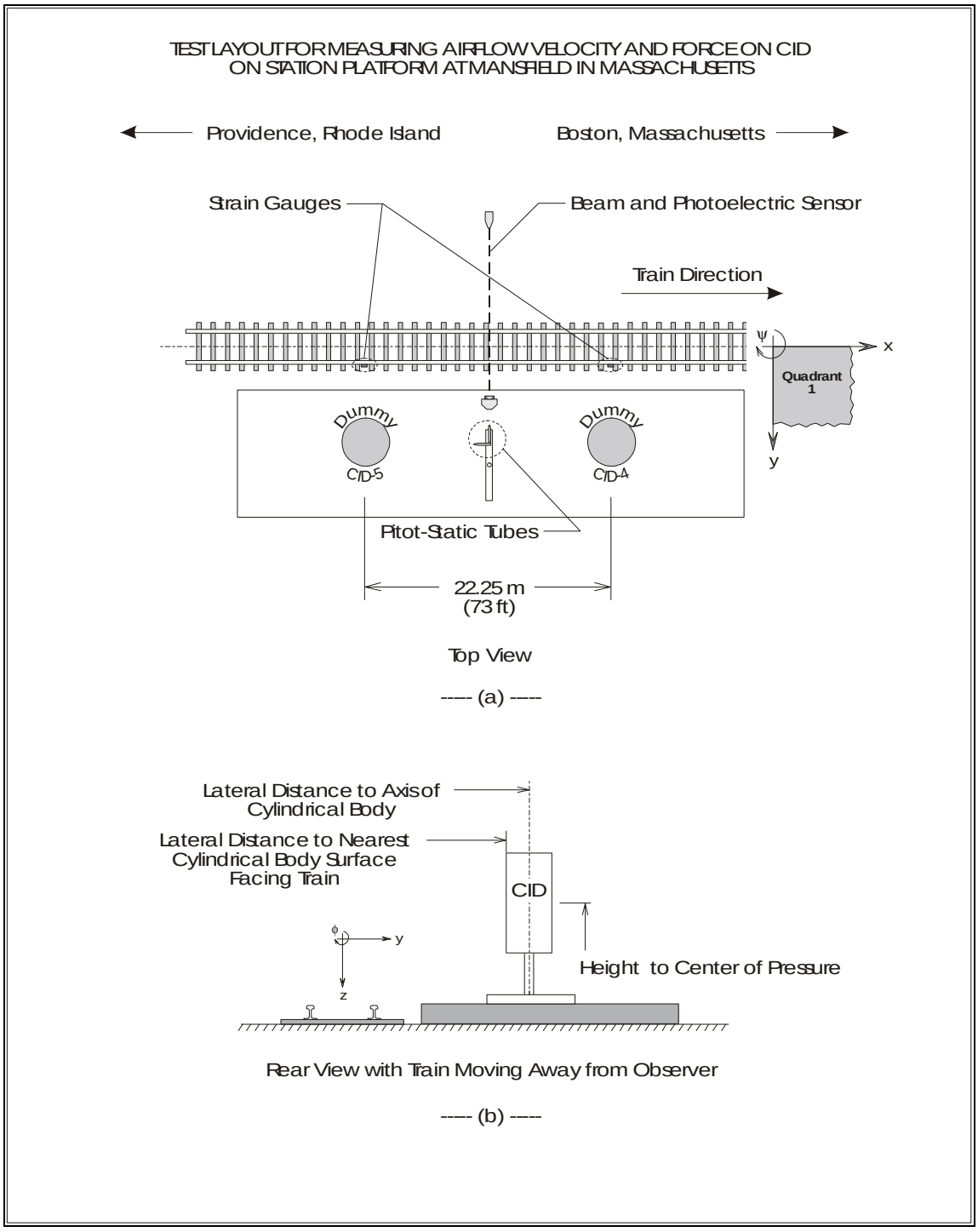

Figure 19. Test Layout on Train Station Platform at Mansfield, Massachusetts Showing (a) Top View and (b) Rear View

Table 20. Positions of CIDs and the Number of Passing Trains Measured

Location	Position 1		Position 2	
	CID-4	CID-5	CID-4	CID-5
Lateral distance (y) from nearest cylindrical body surface to outer edge of nearest rail.	1.74 m (65.50 in)	1.74 m (65.50 in)	2.00 m (78.74 in)	2.00 m (78.74 in)
Nominal lateral distance (y) from axis of cylindrical body to side of train.	1.20 m (47.4 in)	1.20 m (47.4 in)	1.46 m (57.7 in)	1.46 m (57.7 in)
Nominal lateral distance (y) from nearest cylindrical body surface to side of train.	1.01 m (39.8 in)	1.01 m (39.8 in)	1.27 m (49.9 in)	1.27 m (49.9 in)
Height (z) from center of pressure of cylindrical body to top of rail.	1.25 m (49.21 in)	1.24 m (48.82 in)	1.25 m (49.21 in)	1.24 m (48.82 in)
Type of Train	Number of Passing Trains at Position 1		Number of Passing Trains at Position 2	
Acela Express Trainset	14 (28 samples)		12 (24 samples)	
Amfleet Train with AEM-7 Locomotive	8 (16 samples)		9 (18 samples)	
Amfleet Train with HHP-8 Locomotive	7 (14 samples)		3 (6 samples)	

At the location of each cylindrical dummy, strain gauges were installed on the rail to detect the axles of the passing trains. A weather station was present for measuring wind speed, wind direction, air temperature, barometric pressure, and relative humidity. Wind direction is referenced to positive rotation about the z-axis (+z down) with 0° wind direction along (+x), and 90° wind direction along (+y) (Figure 19).

Measurements were made from three different types of trains passing the test site. The significant features that distinguish each type of train are the geometries of the nose and tail with the nose shape generally having the greatest aerodynamic effect. The three types of trains tested that represent the various geometries are:

- High-speed Acela Express trainset with a tapered nose power car at each end (Acela Express train).
- Conventional train with flat end Amfleet cars pulled by bluff nose AEM-7 locomotive (Amfleet/AEM-7 train).
- Conventional train with flat end Amfleet cars pulled by slant nose HHP-8 locomotive (Amfleet/ HHP-8 train).

The geometric profiles for these trains and the number of locomotives and cars for the consist in the test are shown in Figure 20. From the geometric profiles, the Acela Express train represents one end of the geometric spectrum with a tapered nose and tail,

whereas the Amfleet/AEM-7 train represents the other geometric extreme with a bluff nose and flat tail end at the last car. The Amfleet/HHP-8 train is a geometric hybrid with a slant nose and a flat tail end. No trains with the F40PH locomotive were in this test, but this locomotive pulled trains in previous tests.

Many passes of each type of train were measured. To obtain a valid statistical measurement, the test required a minimum of 20 samples (SNCF 2002). Since two CIDs were used, the test required 10 passes for each type of train. Only measurements from the Acela Express train fulfilled the minimum of 20 samples (Table 20). Only six samples were obtained for the Amfleet/HHP-8 train with the CIDs placed at position 2.

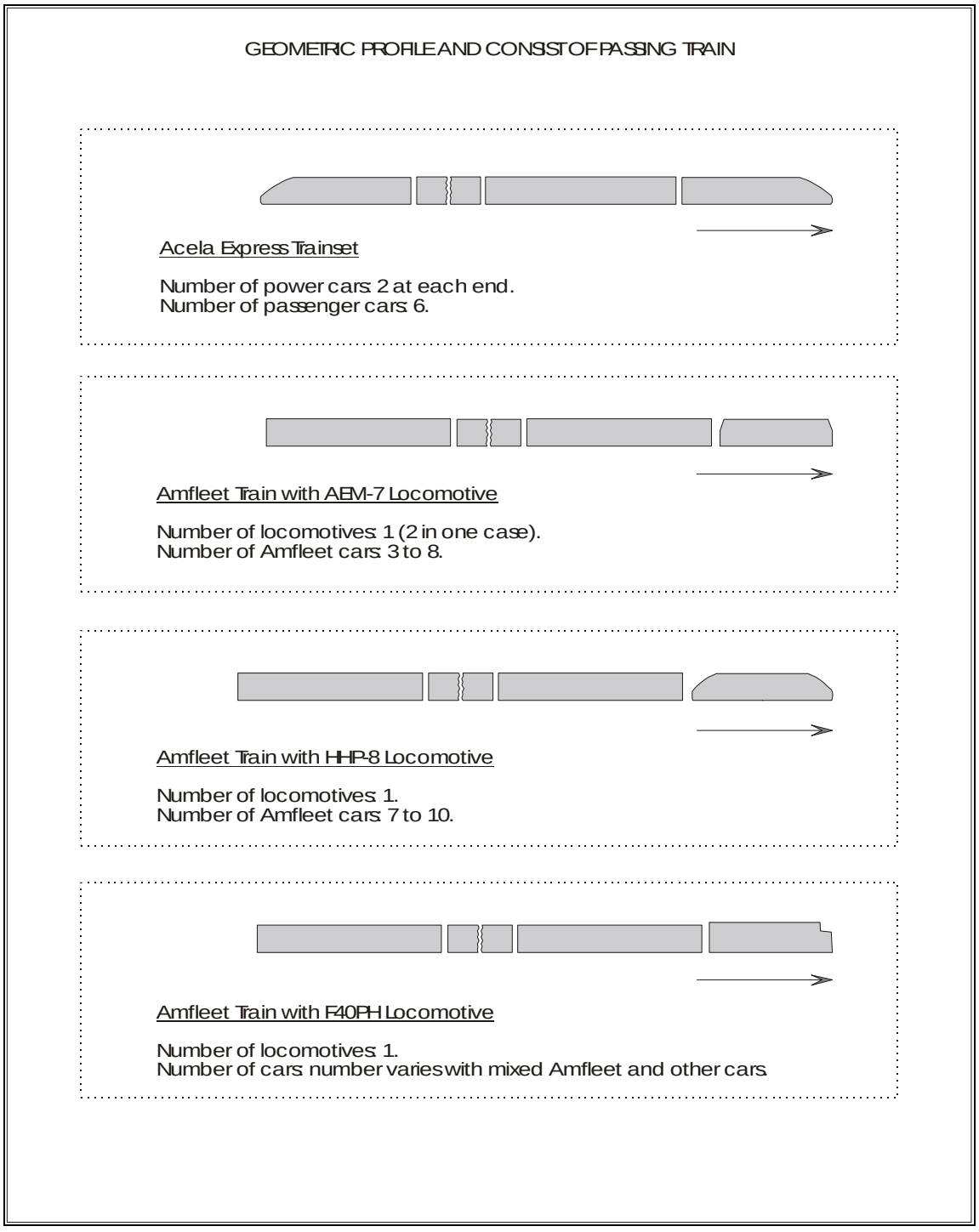

Figure 20. Types of Passing Trains Tested

7.2. Aerodynamic Loading on a Cylindrical Instrumented Dummy

The force measured from each CID was processed to provide a statistical description of the data. First, the raw data representing the force was processed by a digital Bessel second order 15 Hz low-pass filter to account for the muscular response time of a human being as established by SNCF. After the filtering, maximum forces were obtained for various zones along the length of the train.

A train moving through the atmosphere creates peak disturbances to the air in certain defined zones along the length of the train. Generally, these peak changes in static air pressure from the inviscid flow field occur at the head and tail ends of the train, as well as from the gaps between cars or other discontinuities. In addition, regions where airflow velocity from the viscous effects can reach significant levels exist, which are largely influenced by the geometry of the train. Therefore, for purposes of data analysis, the flow field from a passing train is divided into regions of aerodynamic disturbance along the length of the train as shown in Figure 21 and described as follows:

- Head region, from ahead of the nose to the passage of the head of the train,
- Tail region, from the passage behind the head to the tail end of the train including the wake,
- Wake region, from the passage of the tail end behind the base of the train, and
- Train region, the entire flow field surrounding the passing train.

The maximum force from the CID was obtained for each train pass over each flow field. For a given train type and position of the CIDs, the mean and its standard deviations of all the maximum forces are computed for all the train passes. Because trains passed at various speeds, the force on the CID for each train pass is normalized by the square of the train speed from which a drag indicator[9] can be obtained for comparing the aerodynamic force from the different types of trains (SNCF 2002). Train speed is the normalizing parameter because the force on the CID is a drag produced by its interaction with the flow field around the passing train. The drag is proportional to the square of the airflow velocity, and if the assumption is that the airflow velocity on the CID is proportional to the speed of the train, the force on the CID is then proportional to the square of the train speed.

[9]SNCF defines the drag indicator as a force obtained by multiplying the normalized statistical force (mean plus two standard deviation) by the square of the desired train speed for comparing the different types of trains at the desired speed.

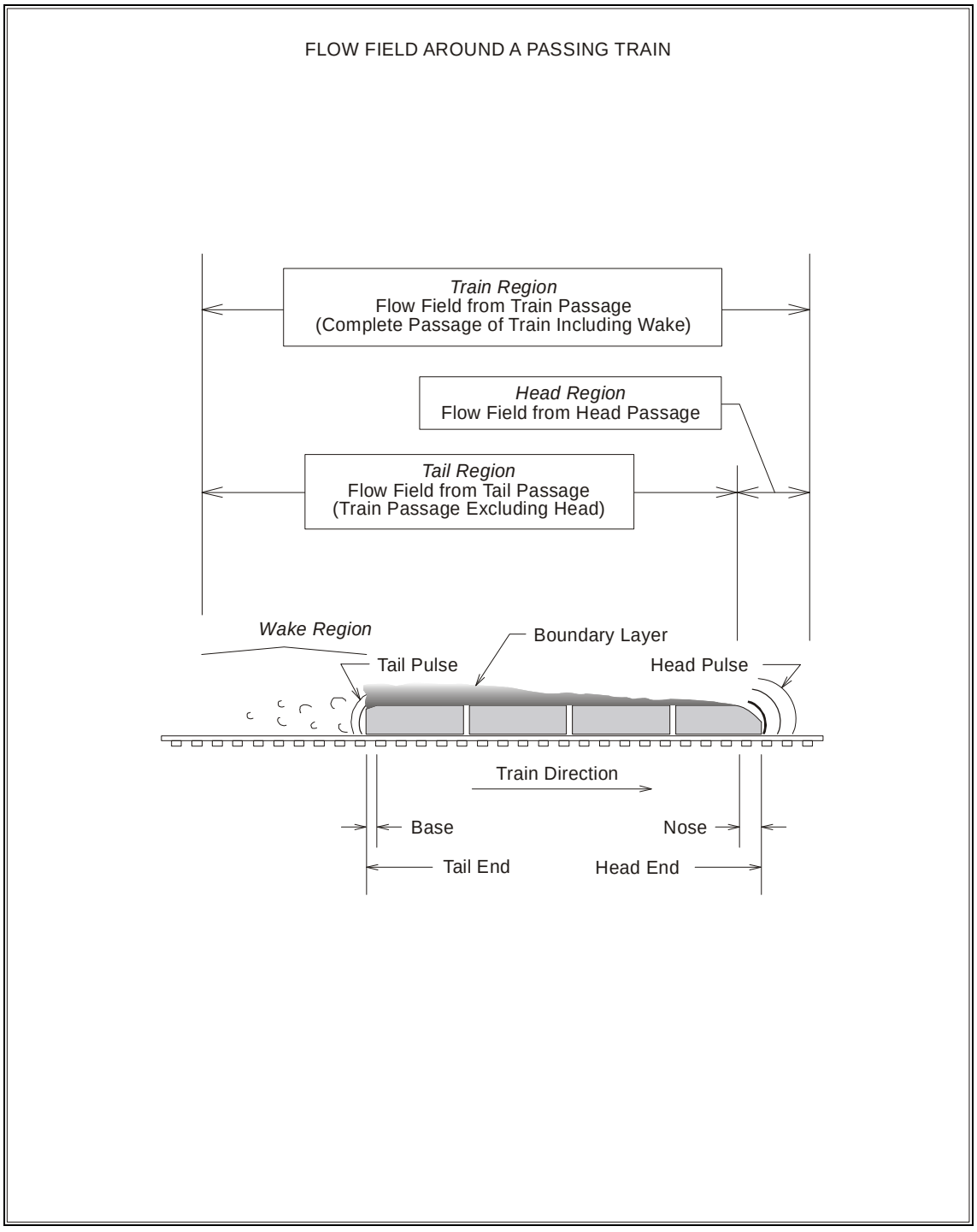

Figure 21. Description of Airflow around a Passing Train

The maximum force per train speed square on the CIDs, with the cylindrical axis at 1.20 m (47.4 in) from the side of the train (position 1), are plotted for each passing train as shown in Figure 22, Figure 23, and Figure 24 for the Acela Express train, Amfleet/AEM-7 train, and Amfleet/HHP-8 train respectively. Each graph is a triptych showing the maximum normalized forces from the passing head and tail of the train for each CID, and the maximum forces from the passage of the entire train from both CIDs. From the first two panels of each graph, the normalized forces on the CID from the head pulse of the Acela Express train and the Amfleet/HHP-8 train are clustered in a narrow range indicating a relatively smooth inviscid flow from the slender nose geometry. This is in contrast to the large scatter in the forces from the head pulse of the AEM-7 locomotive and in the tails of the Acela Express and Amfleet trains. In the last panel of each graph is the maximum normalized force from the passage of the entire train, either from the head or tail, for both CIDs. A horizontal line indicates the mean value of the maximum normalized forces for all the train passes. The Acela Express train produced the lowest mean normalized force whereas the Amfleet/AEM-7 train produced the highest force, and the mean force from the Amfleet/HHP-8 train is between the other two types of trains. When compared with the French TGV train at the same speed and distance away, the head perturbation from the Acela Express train produces a force that is about 15 percent higher (SNCF 2002). The cross sectional area of the Acela Express train is also slightly greater than the TGV train.

The geometry of the train can also influence the location along the train where the maximum force on the CID occurred. Figure 25 shows the plots of the maximum normalized forces on the CIDs and its location of occurrence along the trains. Each dimensionless location is normalized by the length of the passing train, so that the head end of the train is zero, the tail end is one, and locations along the wake of the train will be greater than one. As these plots show, the maximum force for the Acela Express train occurred largely at the wake of the train (Figure 25(a)). This differs from the Amfleet/AEM-7 train where the maximum force was generally from the head of the train (Figure 25(b)), whereas with the HHP-8 locomotive, the maximum force all occurred somewhere between the head and tail ends (Figure 25(c)). None of the Amfleet trains with a flat-tail base create a large wake force.

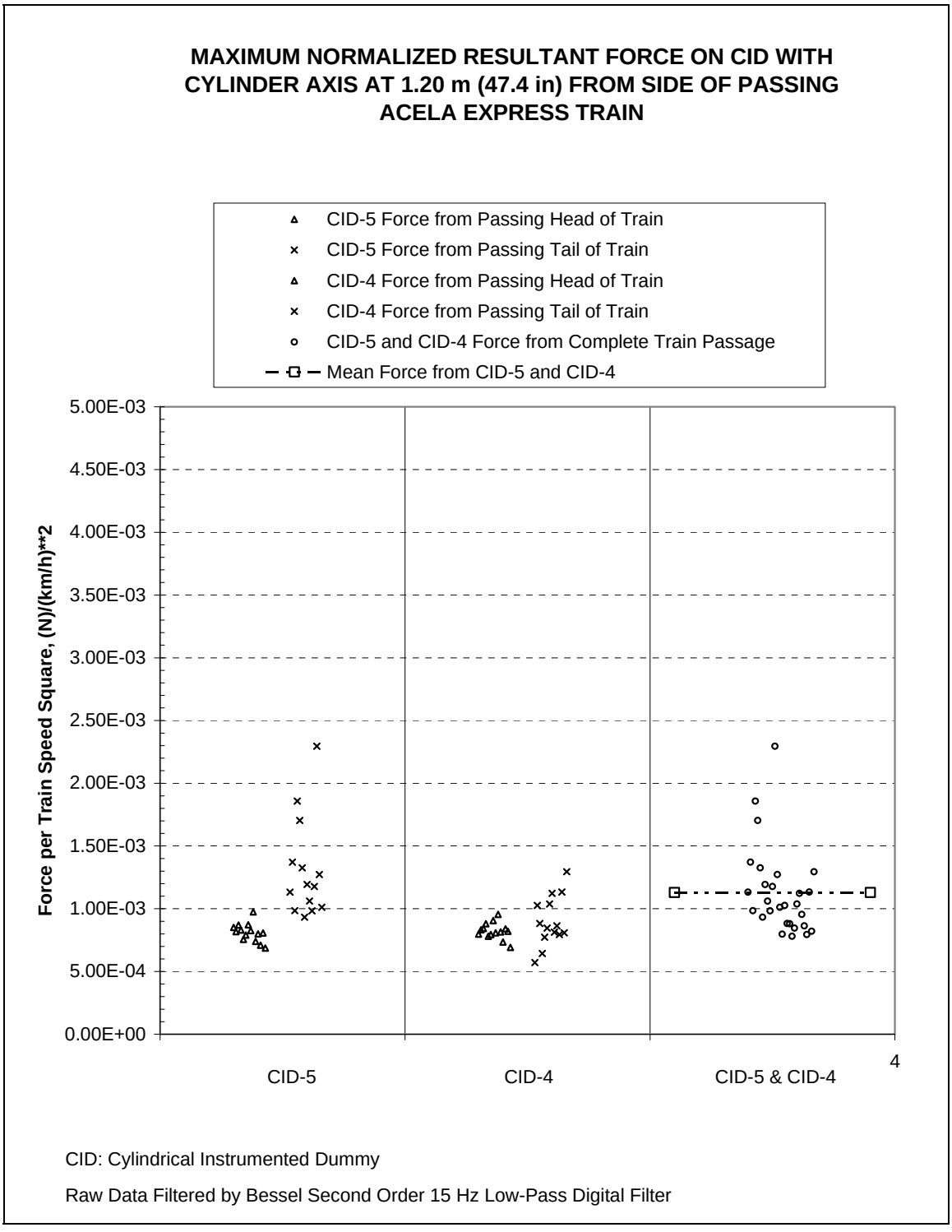

Figure 22. Maximum Forces on CIDs at 1.20 m (47.4 in) from Passing Acela Express Trains

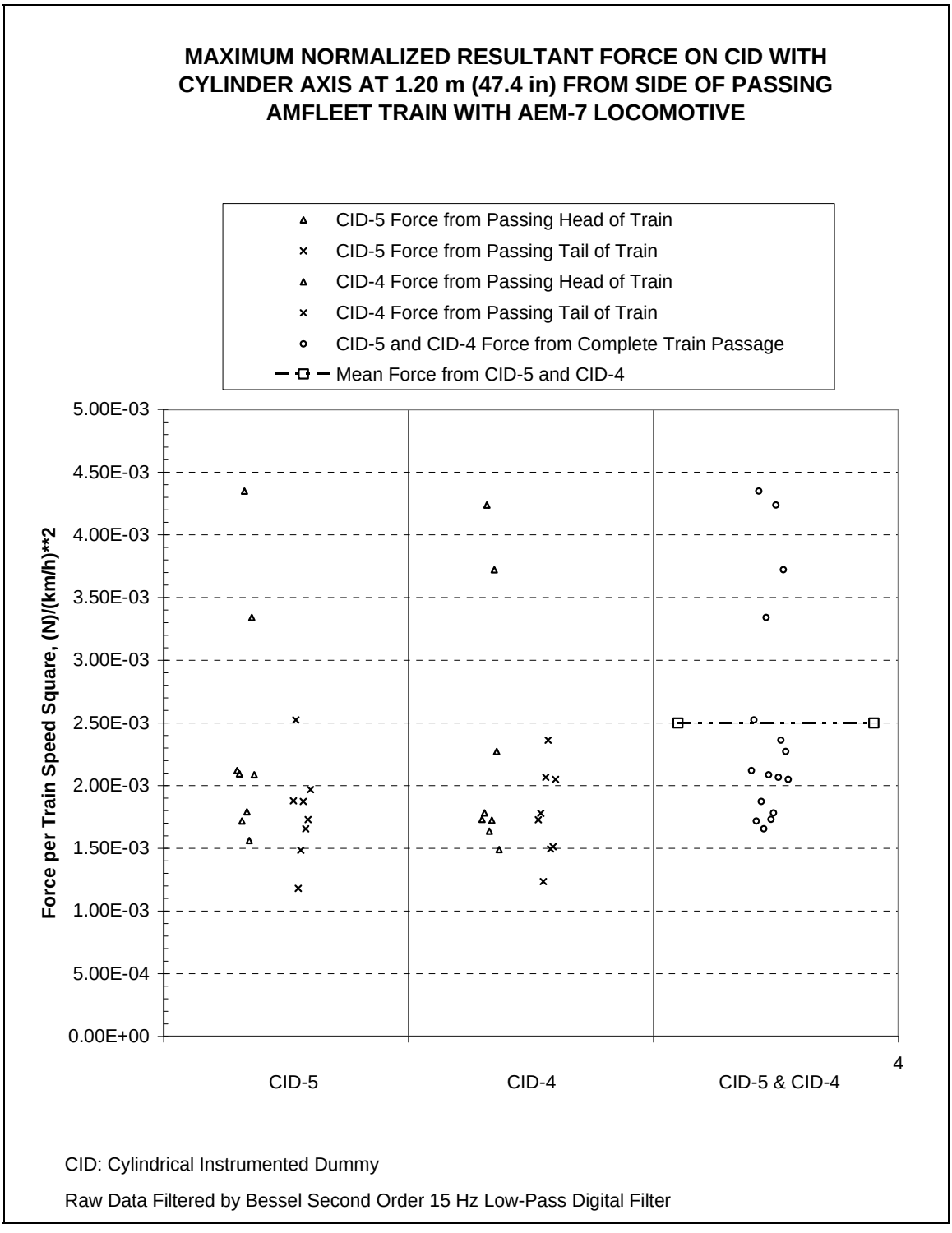

Figure 23. Maximum Forces on CIDs at 1.20 m (47.4 in) from Passing Amfleet Trains with AEM-7 locomotives

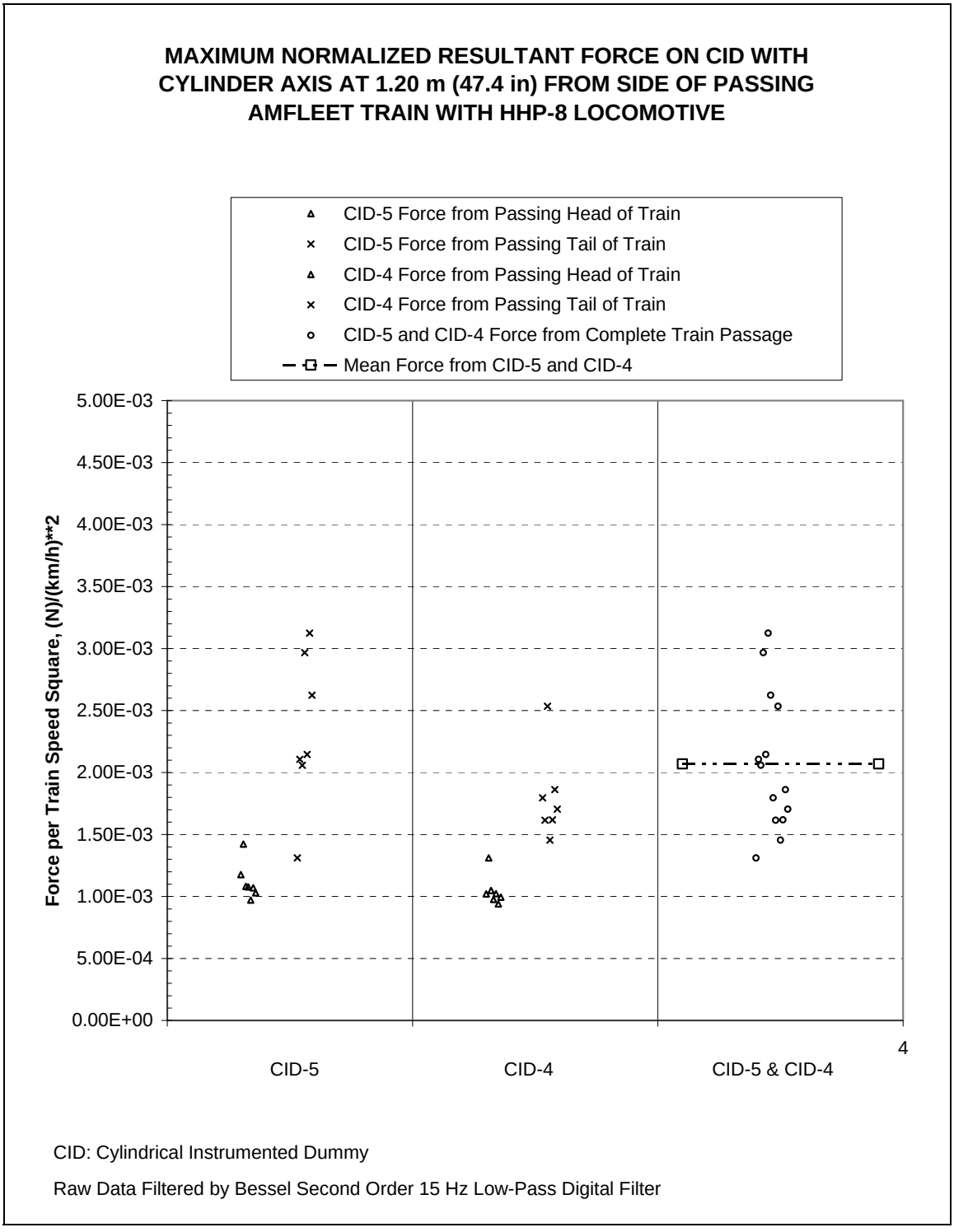

Figure 24. Maximum Forces on CIDs at 1.20 m (47.4 in) from Passing Amfleet Trains with HHP-8 Locomotives

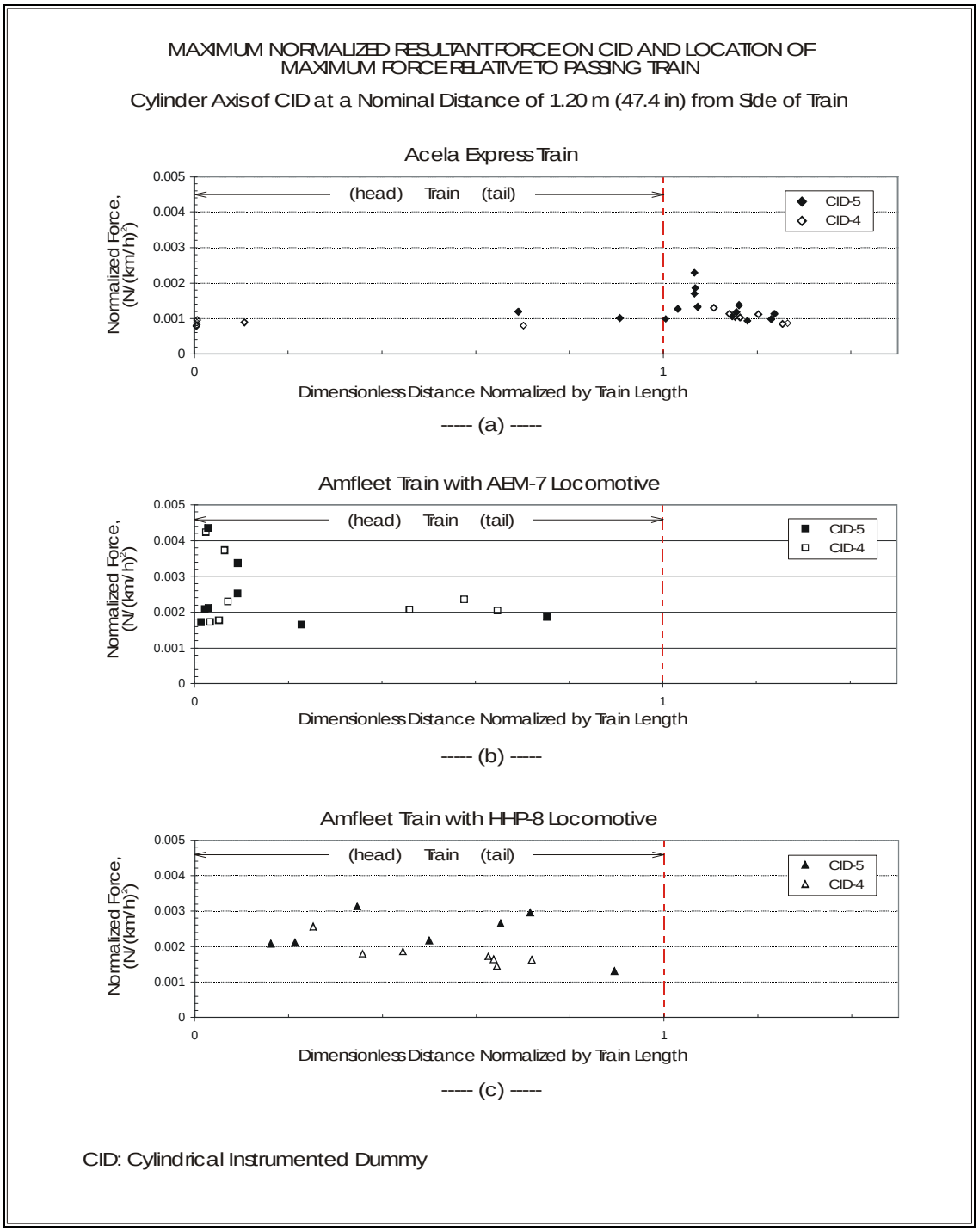

Figure 25. Maximum Forces on CIDs at 1.20 m (47.4 in) from Passing Trains and Locations Along the Passing Trains where Maximum Forces Occurred

These results can be summarized by plotting a bar graph of the mean plus two standard deviations of the maximum normalized forces on the CIDs at various flow fields around the passing trains. Figure 26 shows the plots of the normalized forces comparing the three types of trains along the different flow fields created by the passage of the head, tail, wake, and entire train. Treating each flow field individually (Figure 26(a)), the largest force from the head flow field is from the Amfleet/AEM-7 train, whereas at the wake, it is the Acela Express train that produced the largest force. At the tail flow field, the greatest force is from the Amfleet/HHP-8 train, which occurs before the tail end of the train (Figure 25(c)). These same effects at different flow fields are also shown for each train individually (Figure 26(b)). The maximum force from the Acela Express train is at or near the wake, the maximum force from Amfleet/AEM-7 train is at head flow field, and diminishes toward the wake, whereas the maximum force from Amfleet/HHP-8 train reaches its maximum toward the tail end of the train but before the wake.

Overall, for the passage of the entire train, the Acela Express train produced the lowest normalized force on the CIDs, and the Amfleet/AEM-7 train produced the strongest force. In terms of relative strength with the CID at position 1, the Amfleet/AEM-7 train produced an aerodynamic force on the CIDs that is a factor of 2.4 higher than the Acela Express train, and the Amfleet/HHP-8 train is a factor of 1.8 higher than the Acela Express train. The maximum normalized forces, means, standard deviations, and means plus two standard deviations are all listed in Table 21 for the different trains and flow field regions.

From these results, the geometry of the train, particularly at the head end, has a significant influence on the flow field that is created around the train, and therefore, on the aerodynamic effects to its surroundings. This phenomenon and its relation to the head end geometry can be described as follows:

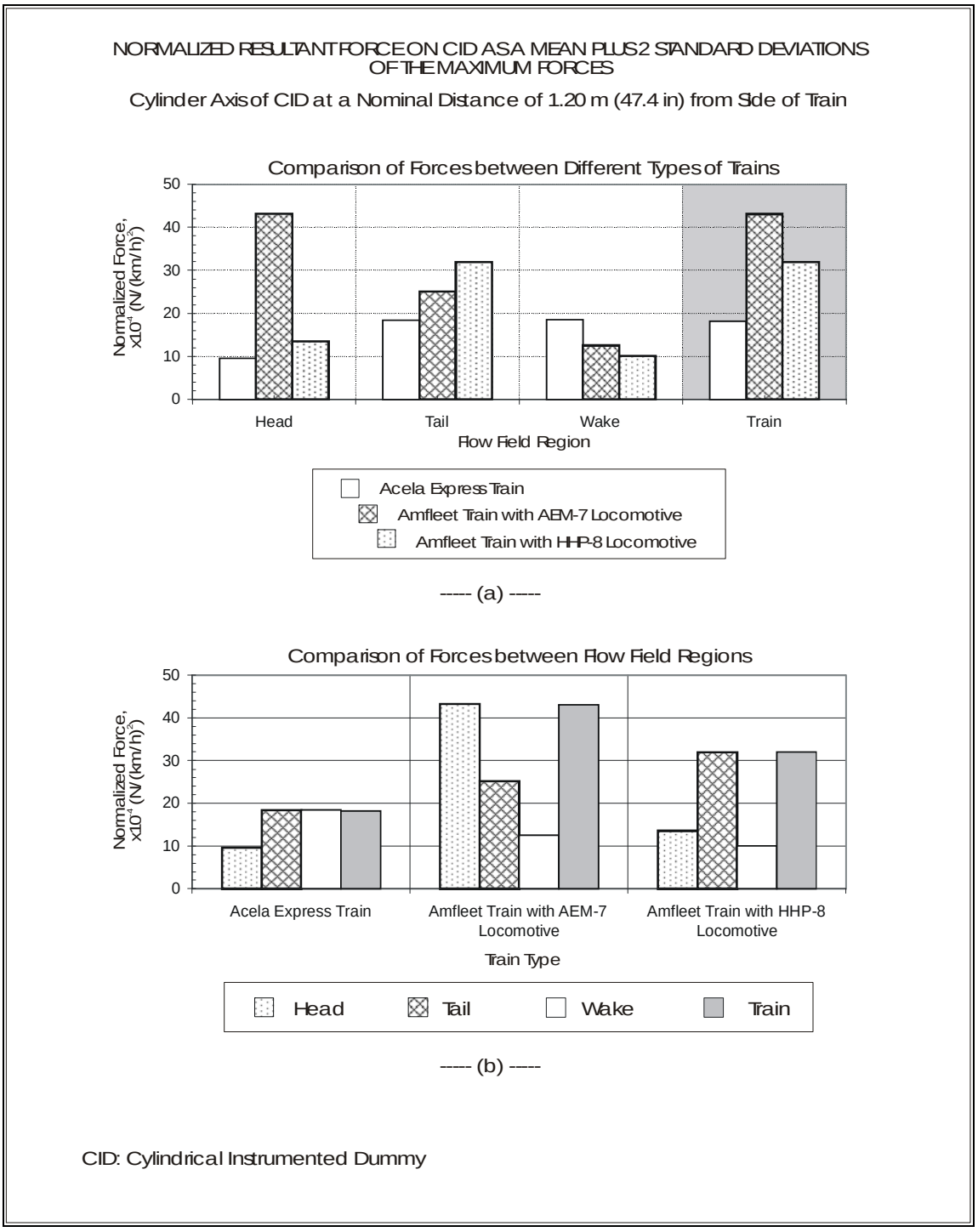

Figure 26. Maximum Forces on CIDs at 1.20 m (47.4 in) from Passing Trains Categorized by Types of Trains and Flow Field Regions

Table 21. Normalized Resultant Forces on CID-4 and CID-5 at Position 1 with Cylindrical Axes at 1.20 m (47.4 in) from Side of Passing Trains

Train Type	Flow Field	Maximum, 10^{-4} $(N/(km/h)^2)$	Mean 10^{-4} $(N/(km/h)^2)$	Standard Deviation 10^{-4} $(N/(km/h)^2)$	Mean + 2 Standard Deviations 10^{-4} $(N/(km/h)^2)$
Acela Express Trainset	Head	9.8	8.2	0.7	9.5
	Tail	22.9	11.0	3.7	18.4
	Wake	22.9	10.7	3.9	18.5
	Train	22.9	11.3	3.5	18.2
Amfleet Train with AEM-7 Locomotive	Head	43.5	23.6	9.8	43.2
	Tail	25.2	17.9	3.6	25.1
	Wake	13.7	8.0	2.3	12.5
	Train	43.5	25.0	9.1	43.1
Amfleet Train with HHP-8 Locomotive	Head	14.2	10.9	1.3	13.5
	Tail	31.3	20.8	5.6	32.0
	Wake	9.8	7.7	1.2	10.1
	Train	31.3	20.8	5.6	32.0

> Firstly, the perturbation to the air caused by the head of the train as it passes is transmitted through the surrounding air for some distance before it dies away….
>
> Although this first phenomenon is an inviscid effect, there may be associated with it, particularly for trains with blunter head shapes, a viscous effect caused by a local separated flow just behind the head, due to the fluid close to surface being unable to negotiate the adverse pressure gradient of the sharp corner around the head. The separation bubble is effectively dragged along with the train and the mean axial velocity of the fluid contained in it is moving at approximately the train speed. Its effect therefore on a stationary body in its path can be significant. In addition, the far-field pressure effects of the head perturbation will be increased due to the enlarged effective train head cross-section caused by the displacement surface representing the separated flow region. However, for well streamlined nose/head shapes, there will be no separated flow region…and these secondary effects will not be present. (Gawthorpe 1972)

The tail end geometry also has its influence on the flow, where a rear-facing power car as in the Acela Express train with its tapered tail end can have the following effect: "For slender-nosed trains, the gust associated with the train nose and the mean level of slipstream speed is much reduced but the gusts in the wake are more pronounced due to

the improved tail-end shapes, which cause a narrower and more concentrated wake" (Gawthorpe 1978).

The relative aerodynamic forces on the CIDs from the different trains are compared, with the mean force plus two standard deviations scaled to the train's maximum nominal operating speed. For trains passing at a speed of 201 km/h (125 mph), the Acela Express train produces a force on the CIDs of 74 N (17 lb), while the Amfleet/AEM-7 train generates a force of 174 N (39 lb). When the Acela Express train is increased to a speed of 241 km/h (150 mph), it produces a force on the CIDs of 106 N (24 lb), which is still a lower force than the force generated from a passing Amfleet train at the lower speed of 201 km/h (125 mph). These results are shown in Table 22.

Table 22. Drag Indicators on CIDs for Trains Passing at Their Nominal Operational Speeds

Train Type	Resultant Force Mean + 2 Standard Deviation			
	Position 1 Cylindrical Axis at 1.20 m (47.4 in) from Side of Train		Position 2 Cylindrical Axis at 1.46 m (57.7 in) from Side of Train	
	201 km/h (125 mph)	241 km/h (150 mph)	201 km/h (125 mph)	241 km/h (150 mph)
Acela Express Trainset	74 N (17 lb)	106 N (24 lb)	63 N (14 lb)	91 N (20 lb)
Amfleet Train with AEM-7 Locomotive	174 N (39 lb)		119 N (27 lb)	
Amfleet Train with HHP-8 Locomotive	129 N (29 lb)		129 N (29 lb)	

The CIDs were also tested at position 2 that was further away from the passing train, with the cylindrical axis at 1.46 m (57.7 in) away from the side of the train. Results for position 2 are shown plotted in Figure 27, Figure 28, Figure 29, and Figure 30 and listed in Table 22 and Table 23. There were only six samples (three train passes) of force measurements from the Amfleet/HHP-8 train (Figure 29), which were insufficient for a valid characterization of this train according to the SNCF criterion (SNCF 2002). The results for this train are listed in Table 22 and Table 23 for completeness, and should not be used for comparison with the other trains. Comparing the relative force level, the Amfleet/AEM-7 train produced an aerodynamic force on the CIDs that is a factor of 1.9 higher than the Acela Express train. An increase in lateral distance from the side of the train by 22 percent reduced the mean force plus 2 standard deviations by 14 percent for the passage of Acela Express train and reduced the force by 32 percent for the Amfleet/AEM-7 train. The trend on the forces for the various flow fields at position 2 is the same as in position 1 (Figure 30) except for a general reduction in the strength of the force.

Table 23. Normalized Resultant Forces on CID-4 and CID-5 at Position 2 with Cylindrical Axes at 1.46 m (57.7 in) from Side of Passing Trains

Train Type	Flow Field	Maximum, 10^{-4} $(N/(km/h)^2)$	Mean 10^{-4} $(N/(km/h)^2)$	Standard Deviation 10^{-4} $(N/(km/h)^2)$	Mean + 2 Standard Deviations 10^{-4} $(N/(km/h)^2)$
Acela Express Trainset	Head	9.8	7.2	1.0	9.2
	Tail	15.8	9.7	3.1	15.9
	Wake	15.8	9.6	3.2	16.1
	Train	15.8	10.1	2.7	15.6
Amfleet Train with AEM-7 Locomotive	Head	31.0	16.7	6.2	29.2
	Tail	22.7	14.1	3.8	21.8
	Wake	9.4	6.5	1.1	8.8
	Train	31.0	17.8	5.8	29.4
Amfleet Train with HHP-8 Locomotive	Head	11.5*	9.4*	1.5*	12.3*
	Tail	27.8*	23.2*	4.4*	32.0*
	Wake	15.8*	9.3*	3.3*	15.9*
	Train	27.8*	23.2*	4.4*	32.0*

*The number of samples was insufficient for a valid characterization of this train according to SNCF criterion but the values were computed and listed for completeness and should not be used for comparison with the other trains.

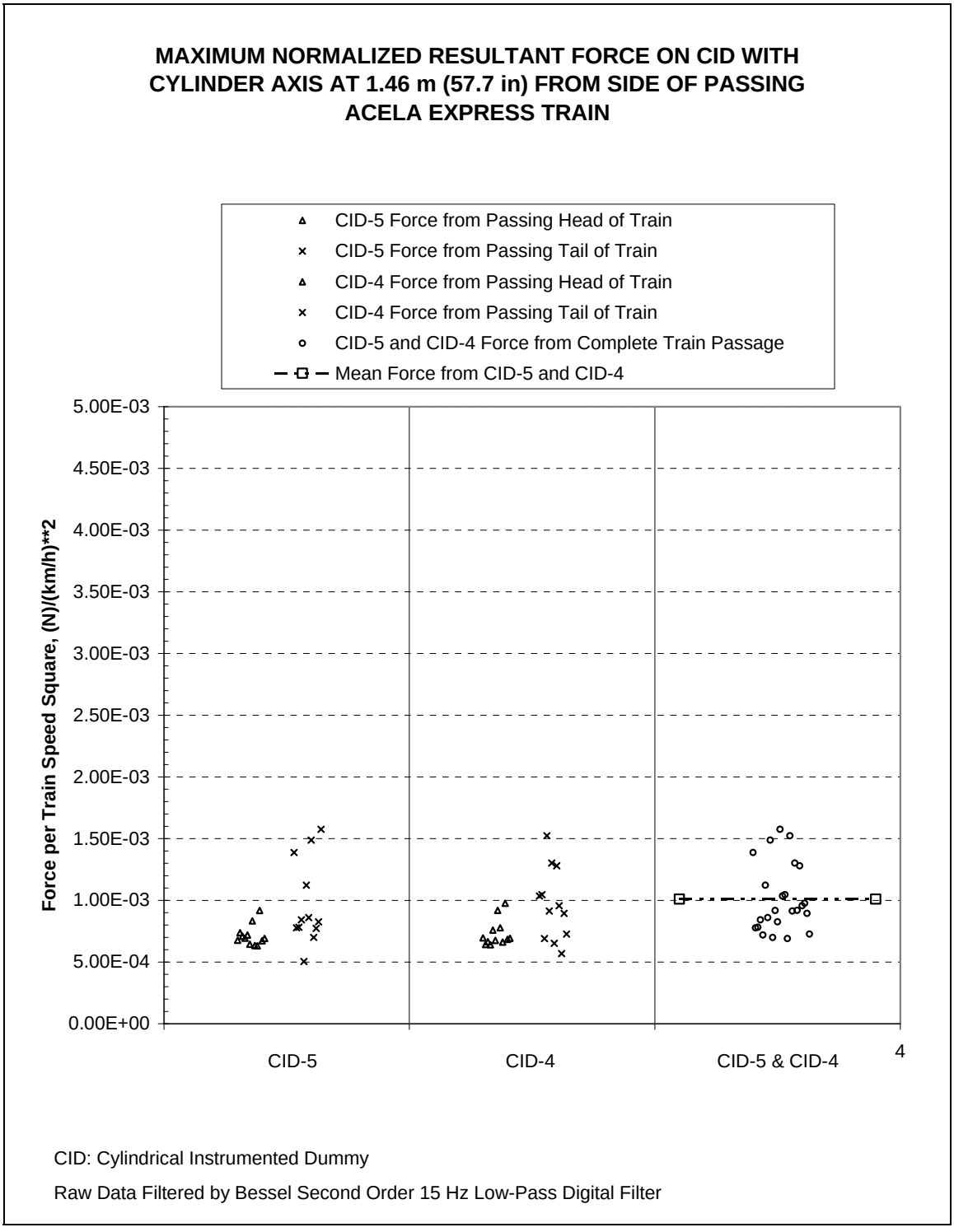

Figure 27. Maximum Forces on CIDs at 1.46 m (57.7 in) from Passing Acela Express Trains

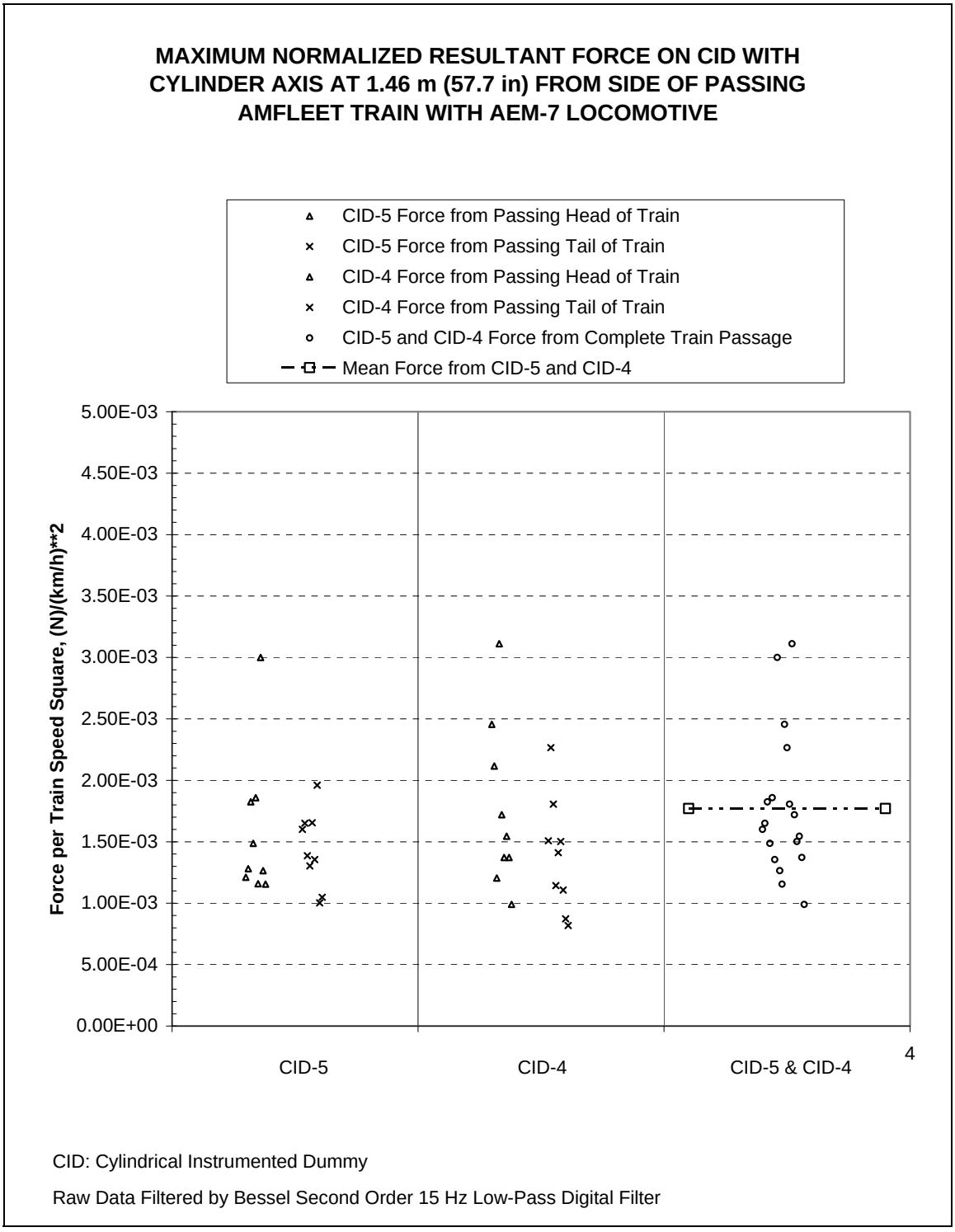

Figure 28. Maximum Forces on CIDs at 1.46 m (57.7 in) from Passing Amfleet Trains with AEM-7 Locomotives

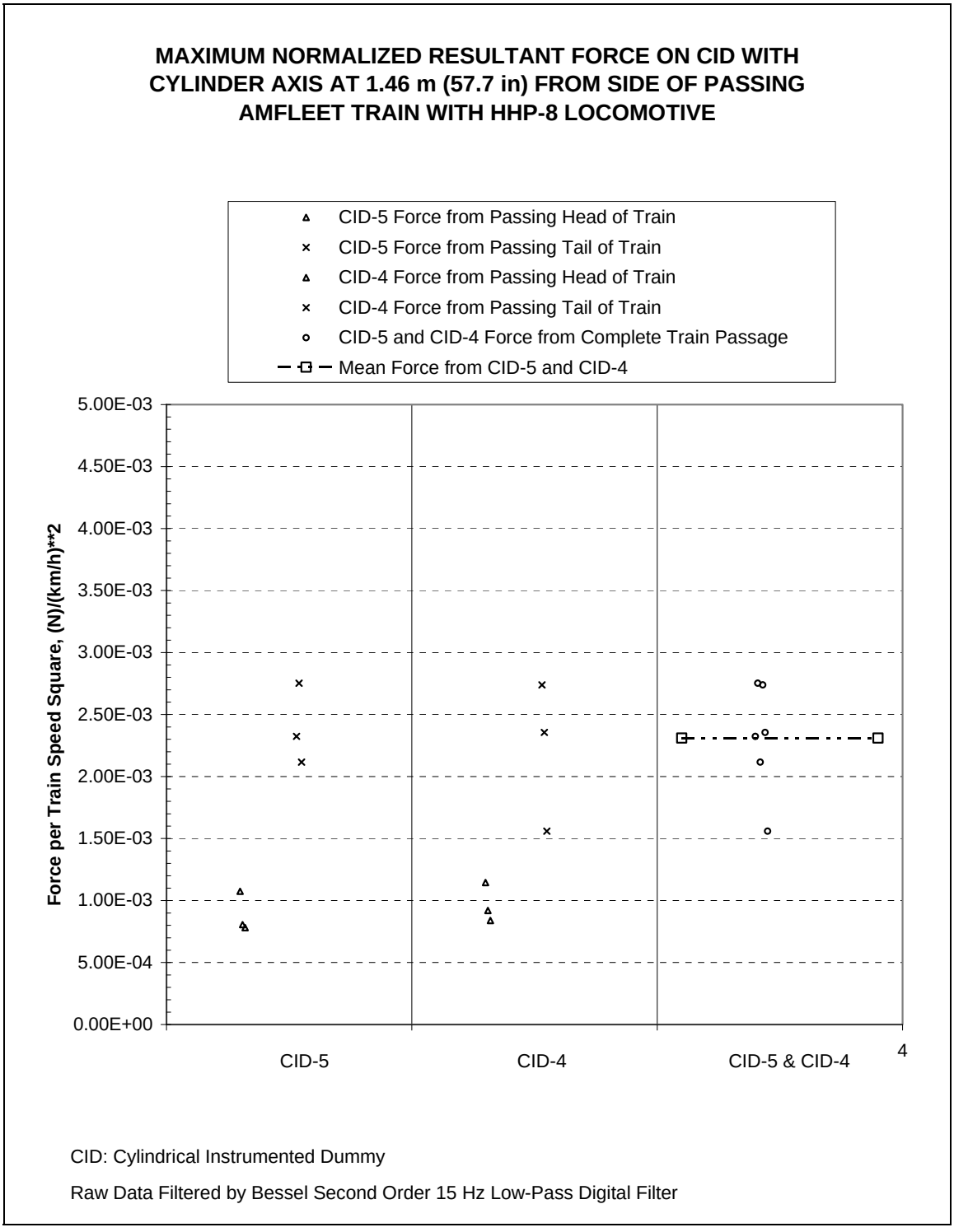

Figure 29. Maximum Forces on CIDs at 1.46 m (57.7 in) from Passing Amfleet Trains with HHP-8 Locomotives

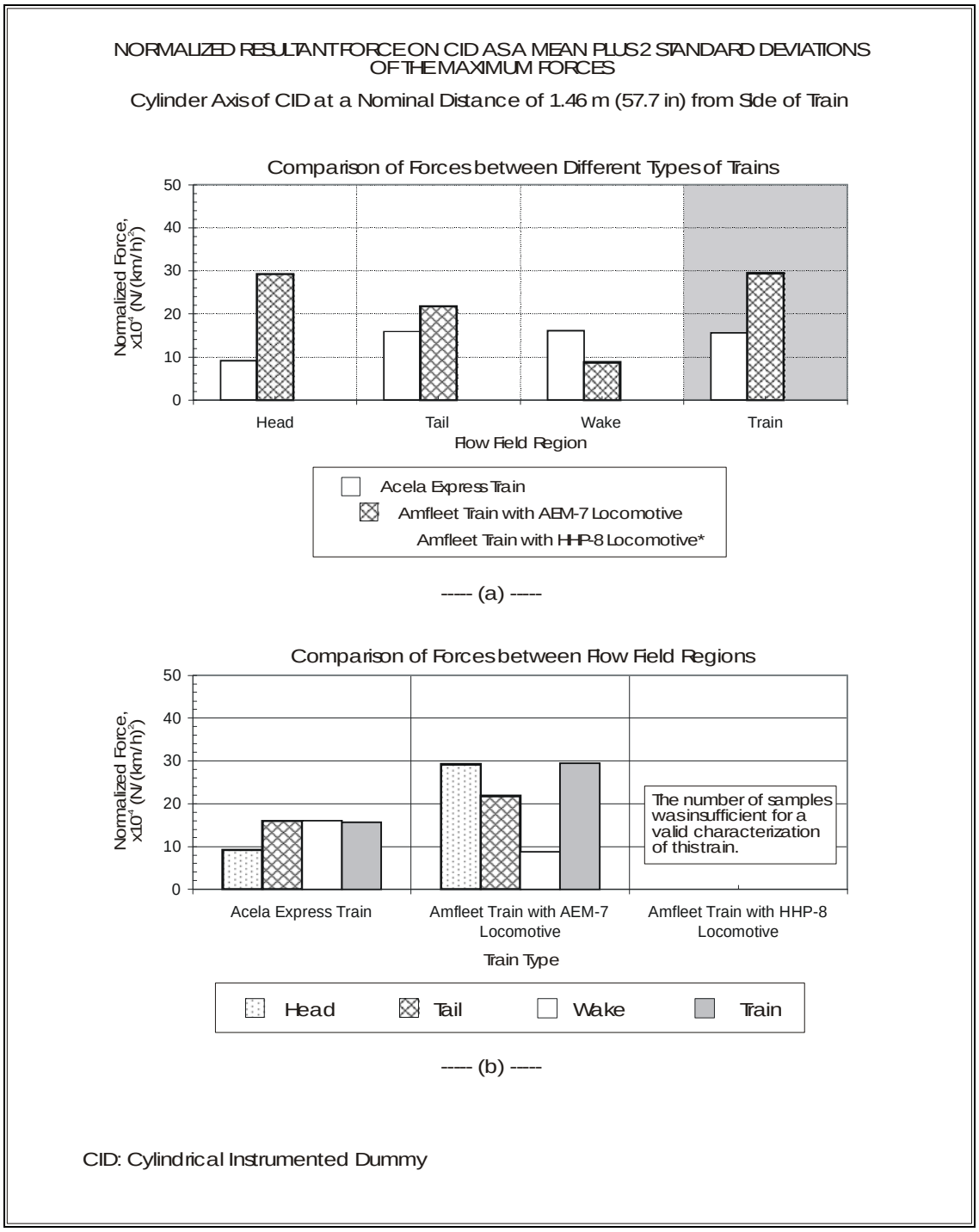

Figure 30. Maximum Forces on CIDs at 1.46 m (57.7 in) from Passing Trains Categorized by Types of Trains Flow Field Regions

Part 2

Analysis and Evaluation

8. Numerical Simulation of Rail Car Roll Response to Aerodynamic Loading

Part 1 of this report described a study to address the issue of dynamic response of a well car carrying empty double-stacked containers from aerodynamic interaction with a passing train. The aerodynamic side force applied to a light carbody can lead to the possibility of containers dislodging and falling over, or to an adverse dynamic response with a risk of derailment. The study involved CFD modeling of a high-speed passenger train passing a double-stack well car on tangent track that included the presence of ambient wind. A multi-body simulation model was used to obtain the dynamic response of the well car. A full-scale test was performed to measure the aerodynamic pressure on the surface of the containers as a high-speed train passes the double-stack well car on an adjacent track to obtain data to compare with modeling results.

This chapter describes a single degree-of-freedom mathematical carbody roll model created to simulate the dynamic roll response of a rail car from transient aerodynamic force input produced by a train passing on an adjacent track. Force input to the double-stack well car was modeled from the aerodynamic pressure variation measured from a full-scale test. The roll response from the model was compared with test data to validate the model. Because the test was conducted at an altitude with a low air density environment, the carbody roll model was used to obtain roll response at sea level, where the force on the double-stack well car would be higher.

The objective of this study was to extend the previous research results by including a broader range of train passing conditions. The responses of carbody roll from the effects of altitude, ambient wind, passing train speed, closing speed, and unbalanced speed on curved track were studied. In the first case, the double-stack well car was modeled traveling at different speeds as another train with different headwinds passes it. A second case was to study the effect on the response of a double-stack well car while negotiating a curved track with excessive cant as another train passes it. The results of this study also demonstrated the capability of using a single degree-of-freedom carbody roll model to predict the roll response of a rail car to aerodynamic interactions with a passing train, and with potential applications to other types of cars and trains.

8.1. Modeling Pressure Variation of a Passing Train

When a train moves through the air, a variation occurs in air pressure produced by the moving train, with the strength and shape of the variations depending on such factors as the speed and geometry of the train in addition to the presence and proximity of surrounding objects. With respect to an observer alongside the track, an increase in aerodynamic pressure occurs immediately before the head of the approaching train. The pressure rises to a positive peak, with the peak corresponding to approximately the nose of the train. As the head of the train passes, the pressure rapidly drops to a negative peak

and rises again to near ambient value. While the train is passing, any perturbations, such as gaps between cars, will produce additional pressure pulses. At the tail end of the train, another pressure pulse is produced, similar to the nose, but with a pressure dropping to a negative peak first and then quickly rising to a positive peak before a gradual recovery to ambient condition. These pressure variations are shown in Figure 31.

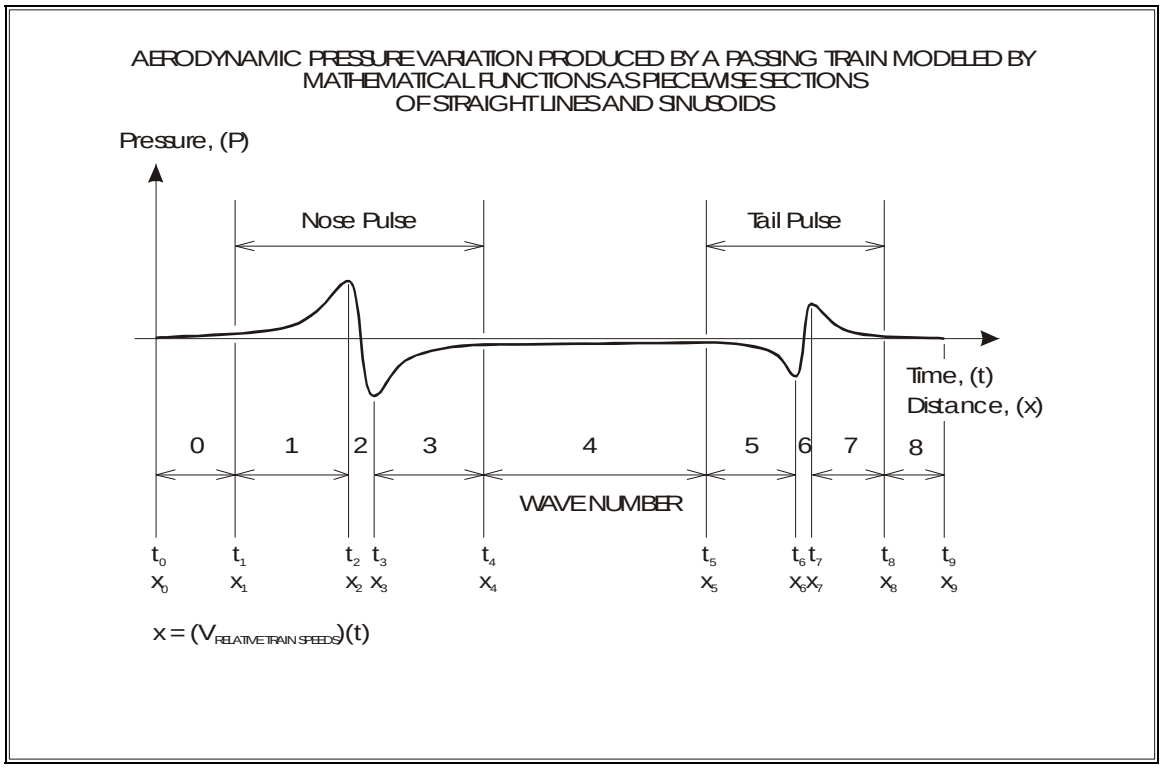

Figure 31. Modeling Aerodynamic Pressure Variation by Mathematical Functions

As the train passes a rail car (a rail car being passed is referred to as the observer car) on an adjacent track, a load is exerted on the observer car from the aerodynamic pressures produced by the passing train. This load creates a lateral force and a roll moment on the observer car as shown in Figure 32. The largest aerodynamic pressure exerted on the observer car appears from the nose and tail of the passing train—with the pressures being highest near the ground—and diminishing toward the top of the train.

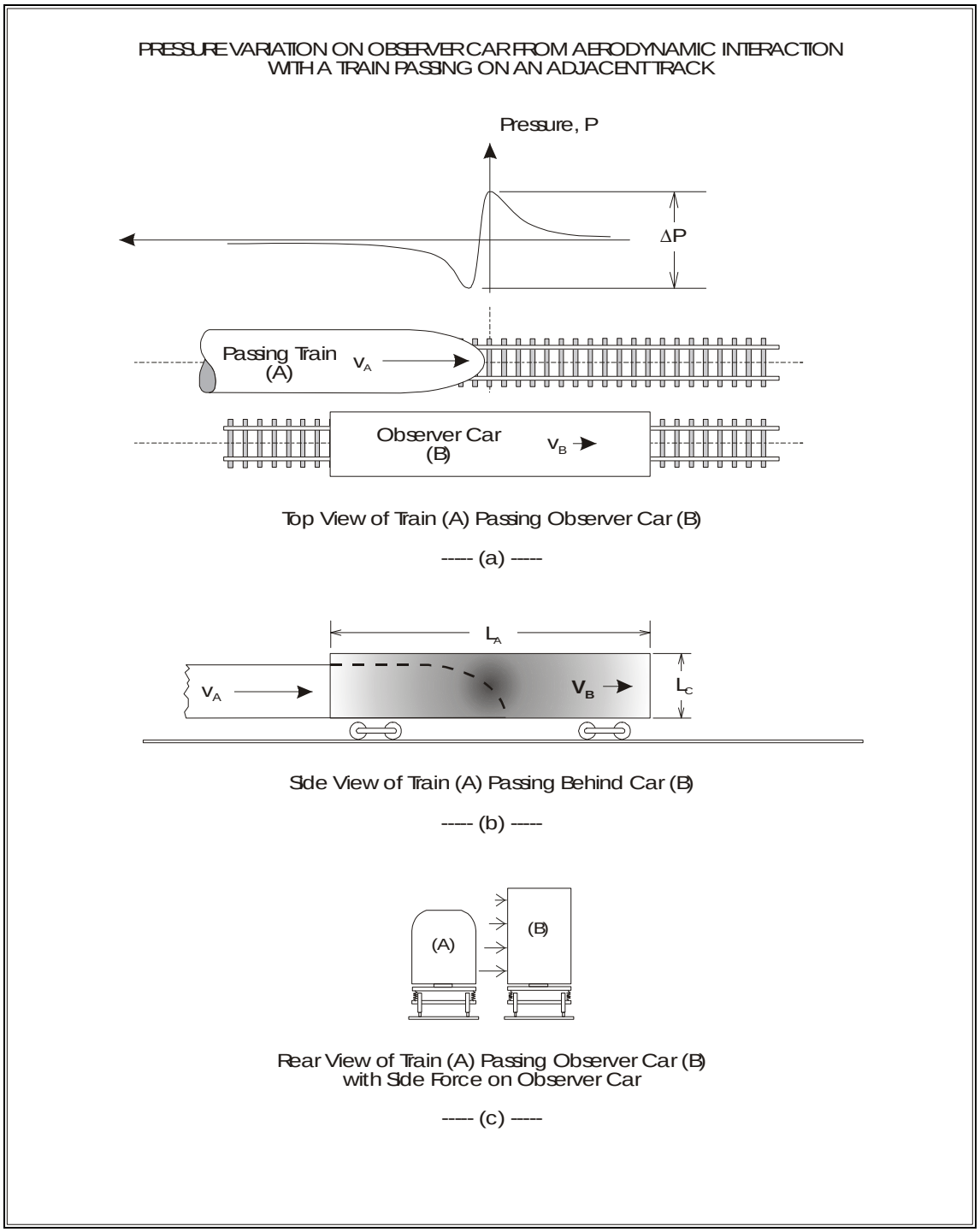

Figure 32. Aerodynamic Interaction Between an Observer Car and a Train Passing on an Adjacent Track

The aerodynamic pressure variations for the entire train were modeled by dividing the variations into nine sections as wave numbers 0 to 8, with each section being modeled as a straight line or sinusoid, as shown in Figure 31. Wave numbers 0, 4, and 8 are modeled as straight lines, and the remaining waves are modeled as sine waves. A detailed description follows for wave number 0, and the nose pressure pulse composed of wave numbers 1, 2, and 3.

Prior to the nose pressure pulse, the pressure variation for wave number 0 is represented by the straight-line equation,

$$x_0 \le x < x_1 \qquad P_0 = P_{x=x_0} + \left(\frac{P_{x=x_1} - P_{x=x_0}}{x_1 - x_0} \right)(x - x_1) \qquad \textbf{Equation 1}$$

The nose and tail pressure pulses are modeled as a series of sinusoidal waves. Since these pressure pulses from the passing train are a significant contribution to the aerodynamic load exerted on the car being passed, it is necessary to have an accurate representation to these pressure variations. Figure 33 shows the aerodynamic nose pressure modeled by a series of three sinusoidal waves as follows:

$$x_1 \le x < x_2 \qquad P_1 = \Delta P_1 + \left[\frac{1}{2}(P_{AO} - \Delta P_1) \right] \left\{ 1 - \cos\left[\frac{2\pi}{\lambda_1}(x - x_1) \right] \right\} \qquad \textbf{Equation 2a}$$

$$x_2 \le x < x_3 \qquad P_2 = \overline{P}_{AB} - \left(\frac{1}{2}\Delta P_{AB} \right) \cos\left[\frac{2\pi x}{\lambda_2}(x - x_2) \right] \qquad \textbf{Equation 2b}$$

$$x_3 \le x < x_4 \qquad P_3 = \Delta P_3 - \left[\frac{1}{2}(\Delta P_3 - P_{BO}) \right] \left\{ 1 - \cos\left[\frac{2\pi}{\lambda_3}\left(x - x_3 + \frac{\lambda_3}{2} \right) \right] \right\} \qquad \textbf{Equation 2c}$$

The peak-to-peak pressure pulse is $\Delta P_{AB} = \frac{1}{2}(P_{BO} - P_{AO})$, and its average value is $\overline{P}_{AB} = \frac{1}{2}(P_{AO} + P_{BO})$. The pressures for wave numbers 4 to 8 can be found in a similar fashion by changing the indices to correspond to that wave number and substituting the values for that particular section.

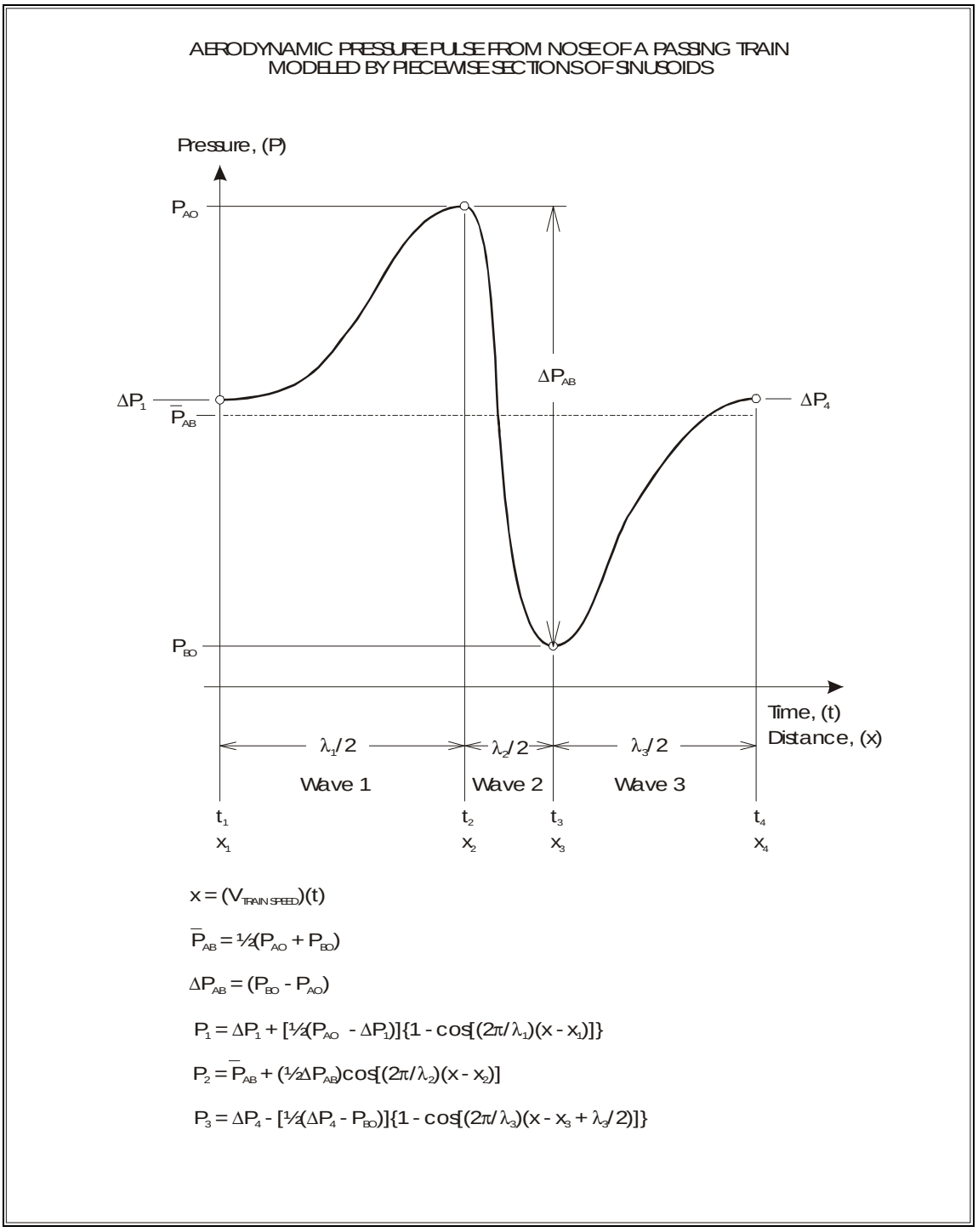

Figure 33. Modeling Aerodynamic Pressure Pulse Produced by Head Perturbation of a Passing Train

When a train passes a flat surface such as a wall besides the track or a rail car on an adjacent track, a force will be exerted on the surface from the aerodynamic pressures of the passing train. The aerodynamic force applied over an area on one side of the surface is, $F = \iint_A p(x,z)dzdx$,

where,

x: longitudinal distance,
z: vertical distance, and
p: aerodynamic pressure.

Assuming that the pressure varies only along the longitudinal (x) direction over the length L_A, but is a uniform average pressure in the vertical (z) direction over the height L_C, the force on the surface is, $F = L_C \int_{L_A} p(x)dx$. This represents the force exerted on only one side of the wall.

Integrating the pressure variations represented by the linear and sinusoidal functions provides the force exerted on only one side of the wall facing the passing train. However, pressure variation measured on the far side of the well car were very small (Table 3 and Figure 8) and therefore, only the pressure variation exerted on the near side of the wall needs to be considered.

From Equation 1 and Equation 2(a to b) for the nose pressure pulse (wave numbers 0, 1, 2, and 3), the forces on the wall are derived as follows:

$$x_0 \le x < x_1 \qquad F_0 = L_C \left\{ \begin{array}{l} \left[P_{x=x_1} - \left(\dfrac{P_{x=x_1} - P_{x=x_0}}{x_1 - x_0} \right) \right] (x - x_1) \\ + \dfrac{1}{2} \left(\dfrac{P_{x=x_1} - P_{x=x_0}}{x_1 - x_0} \right) (x^2 - x_1^2) \end{array} \right\} \qquad \textbf{Equation 3}$$

$$x_1 \le x < x_2 \qquad F_1 = L_C \left\{ \begin{array}{l} \left[\Delta P_1 + \dfrac{1}{2} (P_{AO} - \Delta P_1) \right] (x - x_1) \\ - \left[\left(\dfrac{\lambda_1}{4\pi} \right) (P_{AO} - \Delta P_1) \right] \sin \left[\dfrac{2\pi}{\lambda_1} (x - x_1) \right] \end{array} \right\} \qquad \textbf{Equation 4a}$$

$$x_2 \le x < x_3 \qquad F_2 = L_C\left\{\overline{P}_{AB}(x-x_2)+\left(\frac{\lambda_2}{4\pi}\right)\Delta P_{AB}\sin\left[\frac{2\pi}{\lambda_2}(x-x_2)\right]\right\} \qquad \textbf{Equation 4b}$$

$$x_3 \le x < x_4 \qquad F_3 = L_C\left\{\begin{aligned}&\left[\Delta P_3+\frac{1}{2}(\Delta P_3 - P_{BO})\right](x-x_3)\\&+\left[\left(\frac{\lambda_3}{4\pi}\right)(\Delta P_3 - P_{BO})\right]\sin\left[\frac{2\pi}{\lambda_3}\left(x-x_3+\frac{\lambda_3}{2}\right)\right]\end{aligned}\right\} \qquad \textbf{Equation 4c}$$

Finally, to evaluate the pressure equations requires the values or amplitudes of the pressures at specified points and the range or wavelengths of the pressure variations. The magnitudes of these parameters are obtained either from results of CFD simulation, or from test data.

8.2. Single Degree-of-Freedom Carbody Roll Model

A single degree-of-freedom mathematical model was created to simulate the carbody roll response of the observer car from a transient aerodynamic side force input of a train passing on an adjacent track. The loads applied to the observer car include (1) the aerodynamic pressure variation of the passing train with the effects of ambient wind along the longitudinal direction (head or tail winds) on the passing train, and (2) the unbalanced force on the observer car as it negotiates a curve at unbalanced speed.

8.2.1. Equation of Motion

A freight car consists of a carbody, which is commonly suspended by two trucks. Each truck is composed of a bolster, two side frames, and two wheelsets (two wheels and an axle). The carbody rests on the bolster through the center plate, and the bolster is suspended by springs attached to the left and right side frames. The side frames are supported by the wheelsets. These components are shown in Figure 34(a).

ROLL MOTION OF FREIGHT CAR AND SINGLE DEGREE-OF-FREEDOM MODEL OF CAR-BODY ROLL

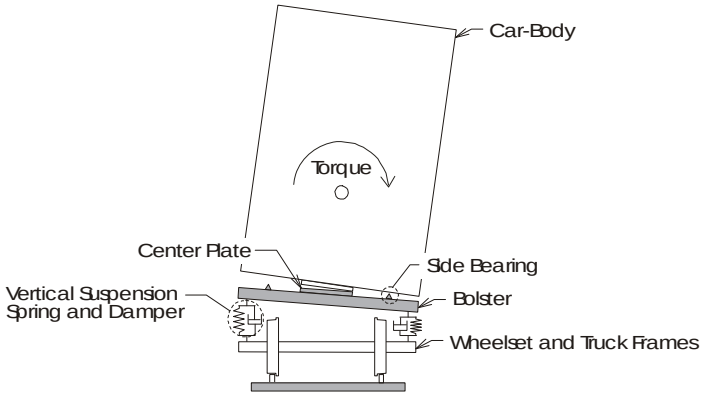

Freight Car Roll Motion with Bolster Deflecting Suspension Springs and Car-Body Lifting off the Center Plate

----- (a) -----

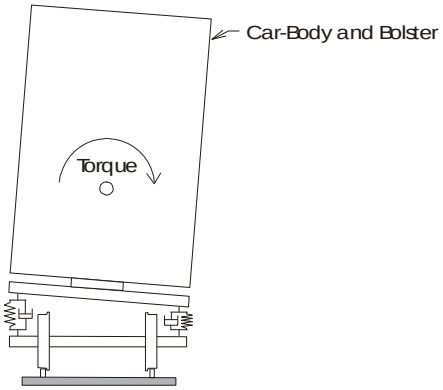

Single Degree-of-Freedom Car-Body Roll Model with Car-Body and Bolster Rolling together as a Single Body on the Suspension Springs

----- (b) -----

Figure 34. Freight Car and Single Degree-of-Freedom Model

The roll motion of a freight car is highly nonlinear during large roll angles. The roll moment is computed by applying a pure torque to the carbody (Figure 34(a)), as shown by the moment/roll angle plot in Figure 35(a). At small roll angles, the carbody and bolster roll as a unit deflecting the springs where it is relatively linear. At larger roll angles, the center plate has only partial contact with the carbody as the carbody rolls pivoting about the edge of the center plate. For even larger roll motion, the carbody completely lifts off the center plate and pivots about the side bearing.

The significance of the carbody roll as it relates to the potential for derailment can be seen from the wheel loading. Carbody roll during static equilibrium redistributes the reaction forces at the wheel/rail contacts so that the reaction force on one wheel increases, while the reaction force on the other wheel decreases. Figure 35(b) shows the plots of the wheel loads on the unloading wheel for three different cases of applied torque. A pure torque applied to the carbody will not cause any wheel lift, with the minimum wheel load at 4.7 percent. However, a lateral force producing the equivalent applied torque either at the center-of-mass or at the center-of-pressure will cause the wheel to lose contact with the rail at about 0.85 deg. While these wheel loads are for static equilibrium, and do not account for the dynamic response, the wheel load to an initial lateral aerodynamic load to the carbody can be approximated from the static loading.

The single degree-of-freedom mathematical model consists of a single mass that represents the carbody and bolster, with both always rolling as a unit (Figure 34(b)). It is suspended by a single set of linear springs and viscous dampers on each side. Figure 36(a) shows the lateral forces acting on the model that consist of aerodynamic force and inertia forces from track superelevation and curvature. The free body diagram of the model with the suspension forces and the forces acting at the center-of-mass and center-of-pressure are shown in Figure 36(b). The roll moment for the linear single degree-of-freedom model is shown in Figure 35(a), where the roll moment is valid until it reaches a carbody roll angle of about 0.3°. Therefore, when this roll angle is exceeded in the simulation, the results should be regarded as qualitative trends.

Another parameter included in this model is ambient wind that is either a headwind or tailwind to the passing train. The wind speed is an additive or subtractive component to the airflow velocity relative to the passing train. The assumption is that the end effects of the observer car do not disrupt the airflow as if the passing train is running along side an infinitely long smooth wall as shown in Figure 37.

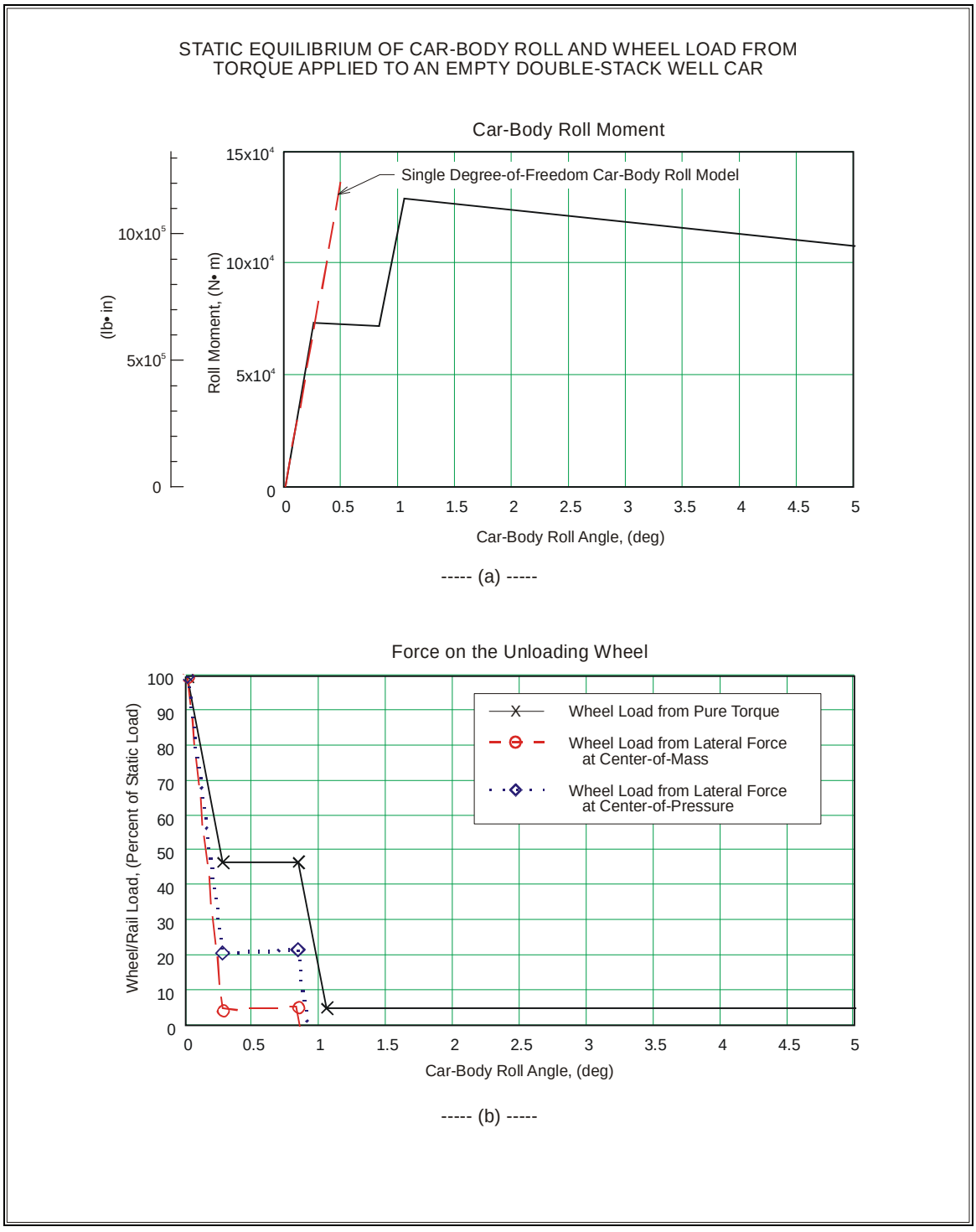

Figure 35. Moment and Wheel Load of Carbody Roll at Equilibrium

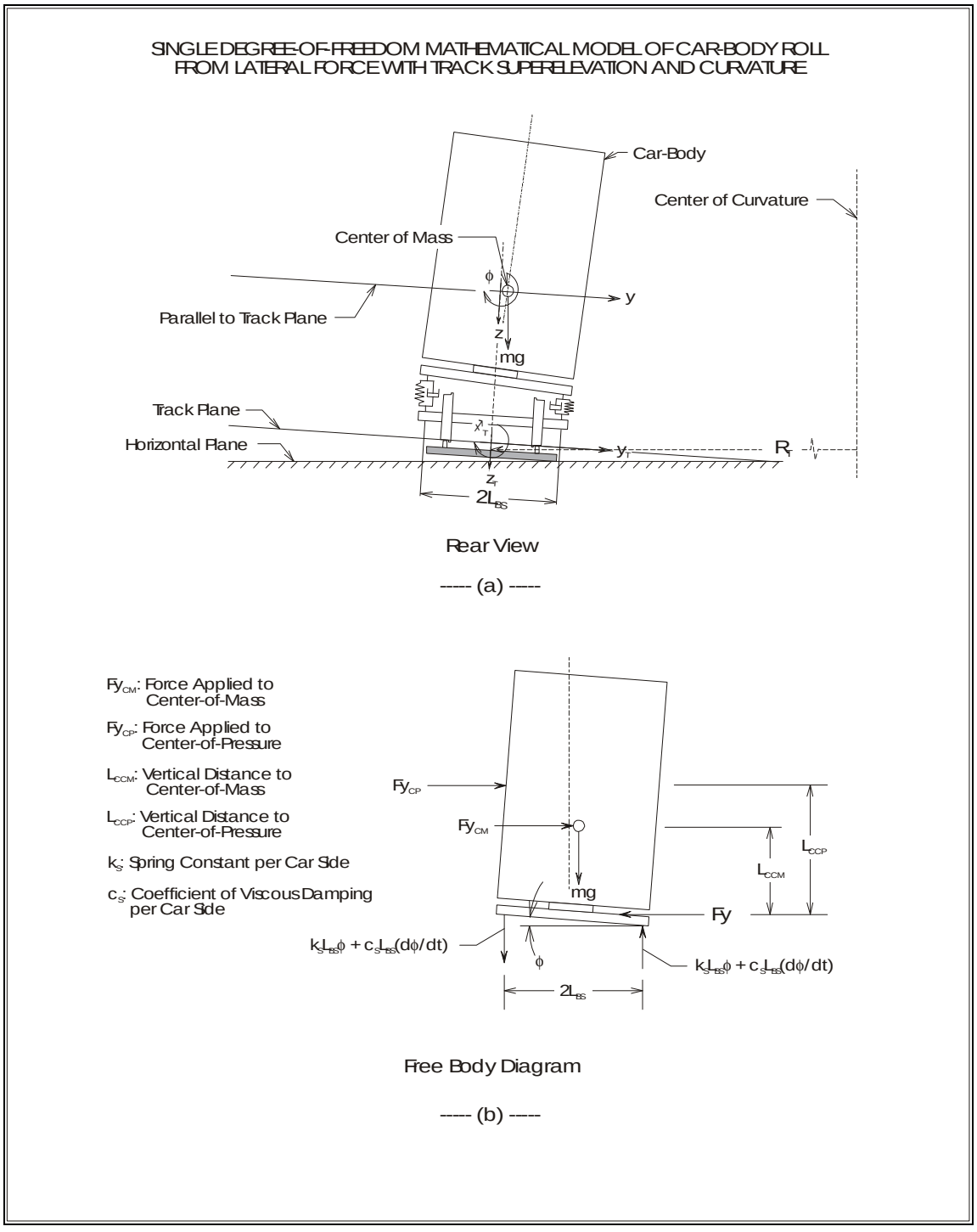

Figure 36. Single Degree-of-Freedom Mathematical Model for Carbody Roll

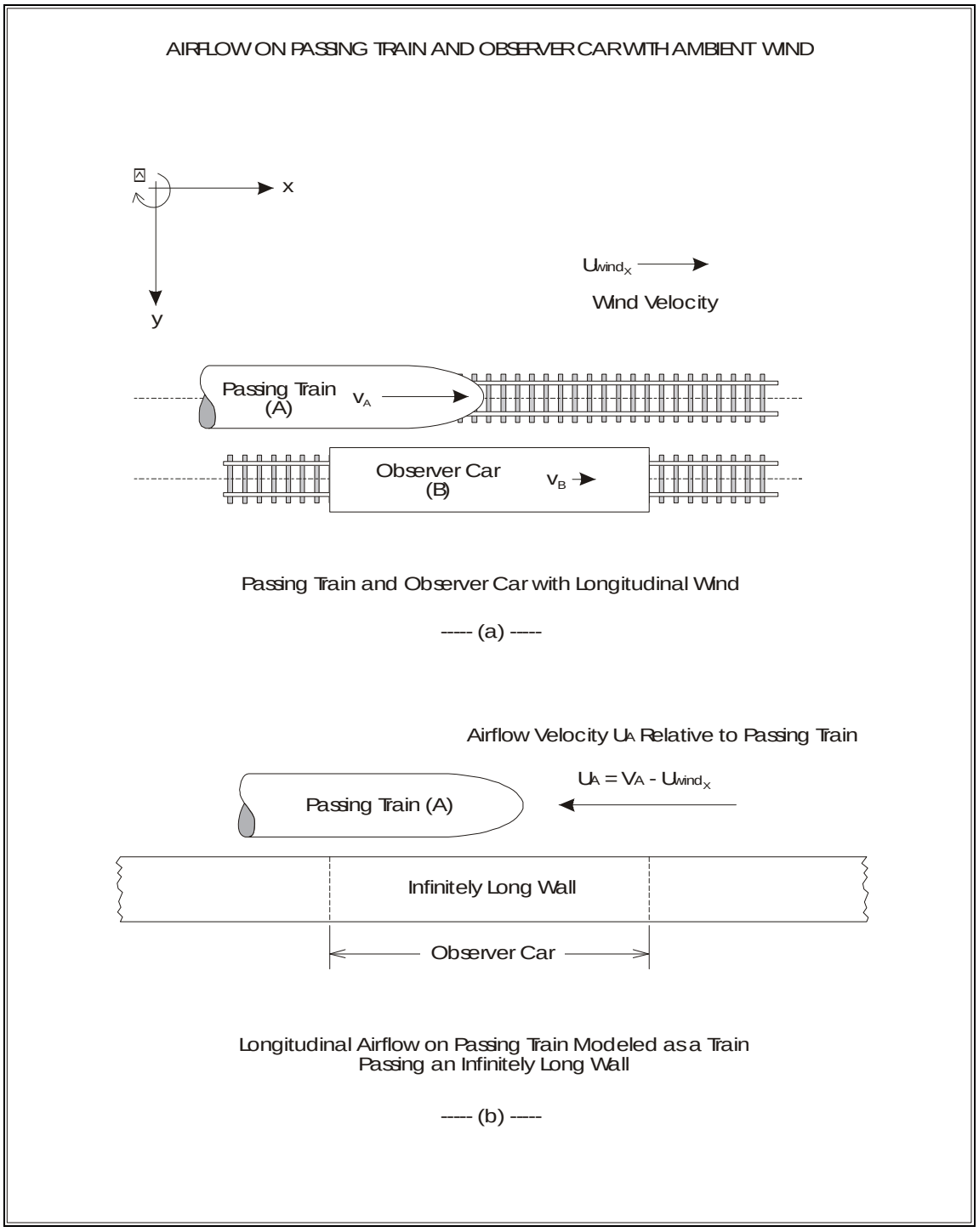

Figure 37. Modeling Airflow Relative to a Passing Train

By summing moments about the roll axis at the base of the truck bolster, and assuming small roll angles, the equation of motion for the single degree-of-freedom model is:

$$\frac{d^2\phi}{dt^2} + \left(\frac{2c_S L_{BS}^2}{I_{XXCB}}\right)\frac{d\phi}{dt} + \left(\frac{2k_S L_{BS}^2}{I_{XXCB}}\right)\phi = \frac{F_{YCM}(t)L_{CCM}}{I_{XXCB}} + \frac{F_{YCP}(t)L_{CCP}}{I_{XXCB}} \qquad \textbf{Equation 5a}$$

or in terms of damping ratio ζ, and natural frequency ω_n (Thomson 1988):

$$\frac{d^2\phi}{dt^2} + (2\zeta\omega_n)\frac{d\phi}{dt} + (\omega_n^2)\phi = \frac{L_{CCM}F_{YCM}(t)}{I_{XXCB}} + \frac{L_{CCP}F_{YCP}(t)}{I_{XXCB}} \qquad \textbf{Equation 5b}$$

where,

$$2\zeta\omega_n = \frac{2c_S L_{BS}^2}{I_{XXCB}}$$

$$\omega_n^2 = \frac{2k_S L_{BS}^2}{I_{XXCB}}$$

The differential equation was solved numerically using a state transition method.

Two lateral forces are applied to the car. One of the forces, $Fy_{CP}(t)$, is from the aerodynamic pressures of a train passing on adjacent track and acting at the center of pressure of the observer car. The other is the unbalanced force, $Fy_{CM}(t)$, which acts at the center of mass and occurs during curve negotiation when the observer car is not running at balanced speed, either due to excessive track superelevation (cant excess), or an insufficient track superelevation (cant deficiency). In this simulation, it was assumed the observer car was negotiating a track with constant curvature and superelevation in a steady-state condition, and therefore the unbalanced force, Fy_{CM}, did not vary with time.

8.2.2. Model Parameter

The parameters for the simulation were to be the same as those in the test that was conducted at TTC and described in Part 1 of this report. This included duplicating the values for the physical properties of the observer car, and the aerodynamic pressure from the passing train. In that test, the observer car was a stationary well car carrying empty double-stacked containers, which was passed by a high-speed passenger train pulled by a TEL locomotive.

The physical properties of the car were modeled to represent the car in the test, which included reproducing its mass, inertia, dimensions, and values for stiffness and damping of the suspension elements. The dimensions for a double-stack well car are shown in Figure 38. The double-stack well car was suspended by three-piece freight trucks with nonlinear elements in the suspension such as clearances, stops, sliding friction, and different regions of roll motion (rolling about the truck springs, or rocking about the center plate and side bearings). However, the model consists of linear springs and viscous dampers for the suspension elements, which is a good approximation for small roll angles where the roll motion of carbody is from the deflection of the spring groups that are relatively linear. Values of the parameters were obtained from the literature (Holmes and Schroeder 2002; Przybylinski and Anderson 1980; R.E.R. 1997), except the damping ratio for the roll mode of the carbody, which was measured from the roll response in the test (Figure 88, Table 47, and Table 48 in the Appendix). Specifications for a freight truck with a 70-ton capacity were assumed because information on the freight truck used in the test was not available, and the carbody roll response from this truck compares best with the test data. Values of the parameters for the model are shown in Table 24.

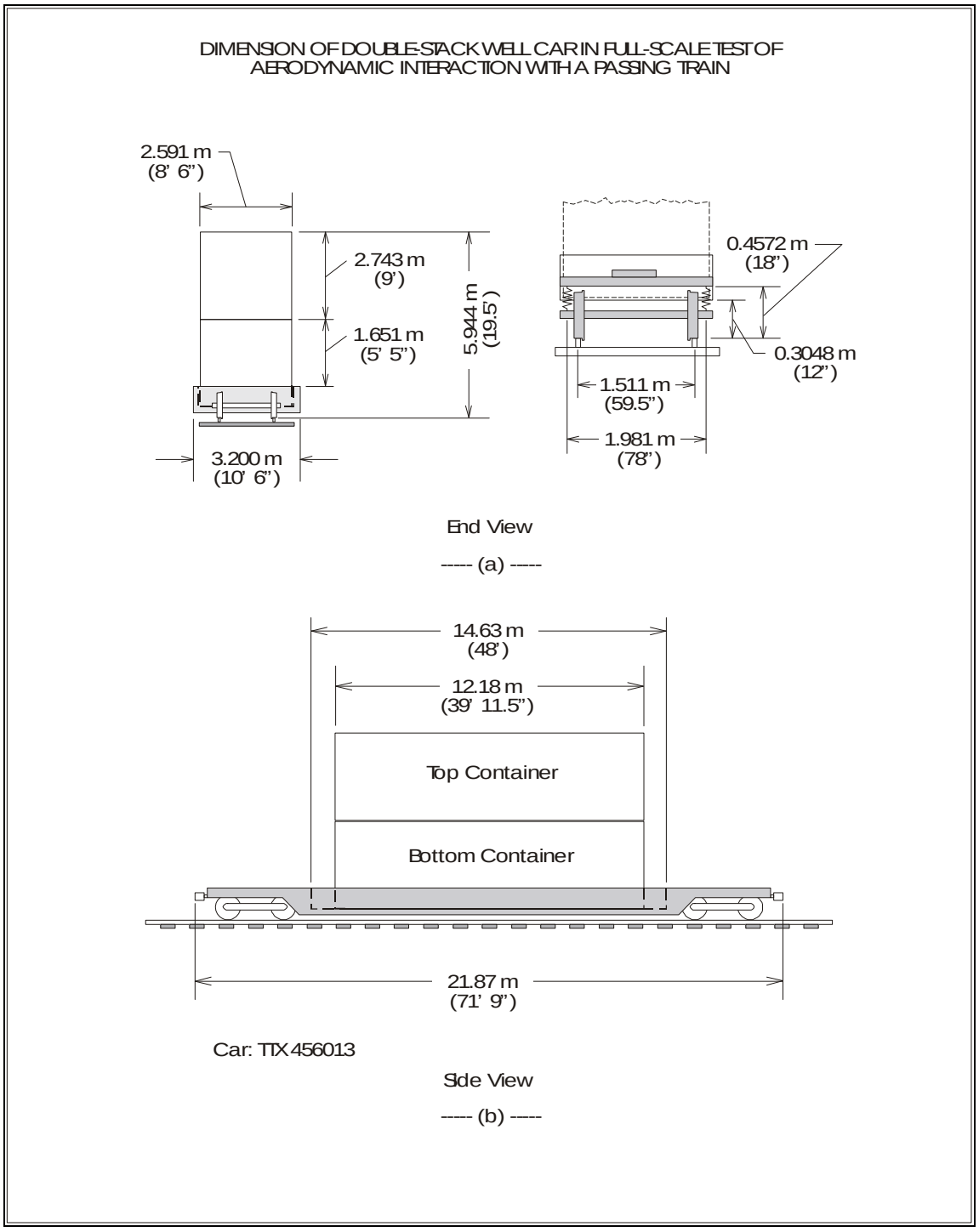

Figure 38. Dimensions of a Double-Stack Well Car

Table 24. Physical Properties of a Well Car with Double-Stacked Containers

Description	Symbol	Value
Mass of Carbody (with Empty Containers)	m_{CB}	21,420 kg (122.3 lb•sec^2/in)
Mass of a 70-Ton 3-Piece Freight Car Truck	m_T	3,695 kg (21.1 lb•sec^2/in)
Mass of a Wheelset (Axle and 2 Wheels)	m_W	981 kg (5.6 lb•sec^2/in)
Roll Moment of Inertia of Carbody about Center of Mass (with Empty Containers)	I_{XXCB}	110,000 kg•m^2 (970,000 lb•in•sec^2)
Spring Constant per Truck (same as per Car Side for Two Trucks)	k_S	8.252x10^6 N/m (47,130 lb/in)
Half Width between Suspension Springs	L_{BS}	0.991 m (39 in)
Height of Car Center of Mass	(From Top of Rail)	1.81 m (71.3 in)
	L_{CCM} (From Top of Spring)	1.35 m (53.3 in)
Height of Car Center of Pressure	(From Top of Rail)	2.68 m (105 in)
	L_{CCP} (From Top of Spring)	2.22 m (87.4 in)
Damping Ratio for Carbody Roll	□	0.03
Diameter of Center Plate		0.356 m (14 in)
Lateral Distance of Side Bearing from Center of Car		0.635 m (25 in)
Diameter of Wheel		0.838 m (33 in)
Vertical Clearance of Side Bearing		6.35 mm (0.25 in)

The second test condition reproduced for the model was aerodynamic pressure, which provides the input force to the car. The pressure waves for the model are in the forms of linear and sinusoidal shapes, and were adjusted to match the pressure variations measured from the test. While the actual pressure exerted on the side of the car is a distributed load that varies both longitudinally and vertically, the pressure only varied longitudinally in the model and remained uniform in the vertical direction. Therefore, the distributed aerodynamic load in the vertical direction is reduced to a single force acting at the center of pressure on the side of the car.

The pressure variation was measured from the test of a TEL passenger train passing a double-stacked well car. The maximum and minimum peak pressures and its wavelengths of the various wave sections can be fitted based on the test data. Expressing the pressure variation from a passing train in terms of pressure coefficient, the results between the modeled and test measurement are compared as shown in Figure 39. Accurate modeling of the pressure pulses is important at the nose and tail, because it is these pressure pulses that provide the significant loading to the car being passed. Figure 40 shows in greater detail a comparison of the nose and tail pressure pulses between the model results and test data, where the model achieved a very good fit. The pressure variation on the far side of the well car is assumed to be at ambient condition. As the test data indicate, the changes in pressure on the well car at the far side of the passing train are small compared to the changes in pressure at near side of the car.

8.2.3. Comparison of Simulation with Full-Scale Test

The roll response of the stationary well car with empty double-stack containers was computed from the single degree-of-freedom roll model for a speed of 177 km/h (110 mph). A comparison of the time history in the response of the carbody roll angles between simulation and test data is in very good agreement, as shown in Figure 41. The maximum zero-to-peak roll angle from the model is computed to be 0.301°, while the maximum zero-to-peak roll angle measured from the test is 0.312°. Based on the roll response from the test, the natural frequency in roll is about 1.6 Hz, and the damping ratio is about 0.03. The roll natural frequency computed from the car parameters is 1.64 Hz, which agrees with the measured value. A skewing can be observed in the test data, where the roll motion of the carbody initially oscillates with the average roll angle centering about zero, but it gradually drifts to a negative average roll angle (Figure 88 in the Appendix). Thus, an apparent divergence exists between the computed roll angles and those from test data because of the skewing effect in the test data with increasing time.

The maximum roll angles of the double-stack well car from model simulation and test are compared for the entire tested speed range of the passing train. An excellent agreement exists between the roll angles obtained from simulation and measured from the test, as shown in Figure 42. The simulation result predicts the maximum roll angle as it reaches a peak at about 177 km/h (110 mph), and drops above that speed, as in the test data. The simulation shows the maximum roll angle increasing again above a train passing speed of 209 km/h (130 mph), which is beyond the speed range of the test, and therefore no test data are available.

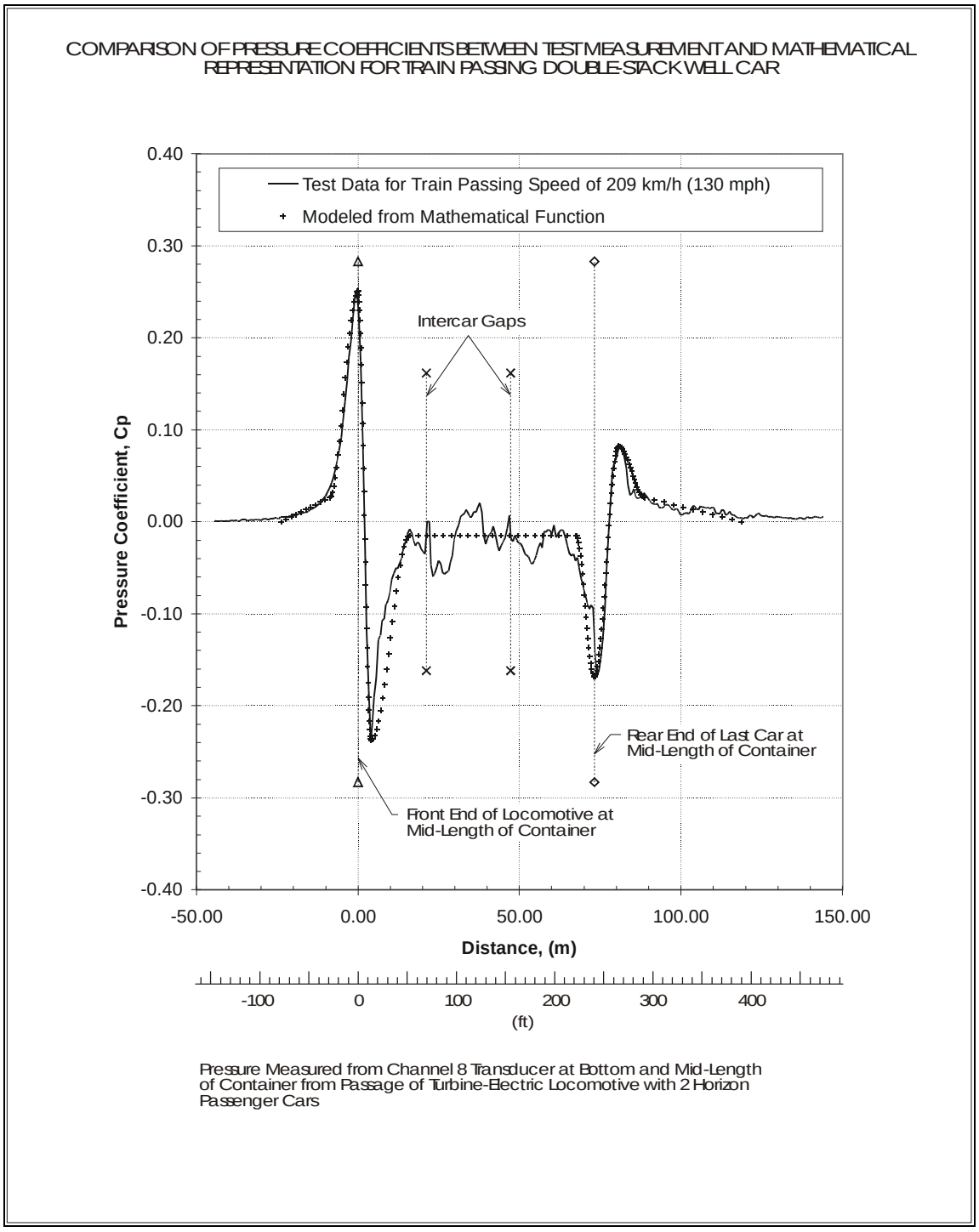

Figure 39. Pressure Coefficients from Test Measurement and Modeled from Piecewise Mathematical Functions

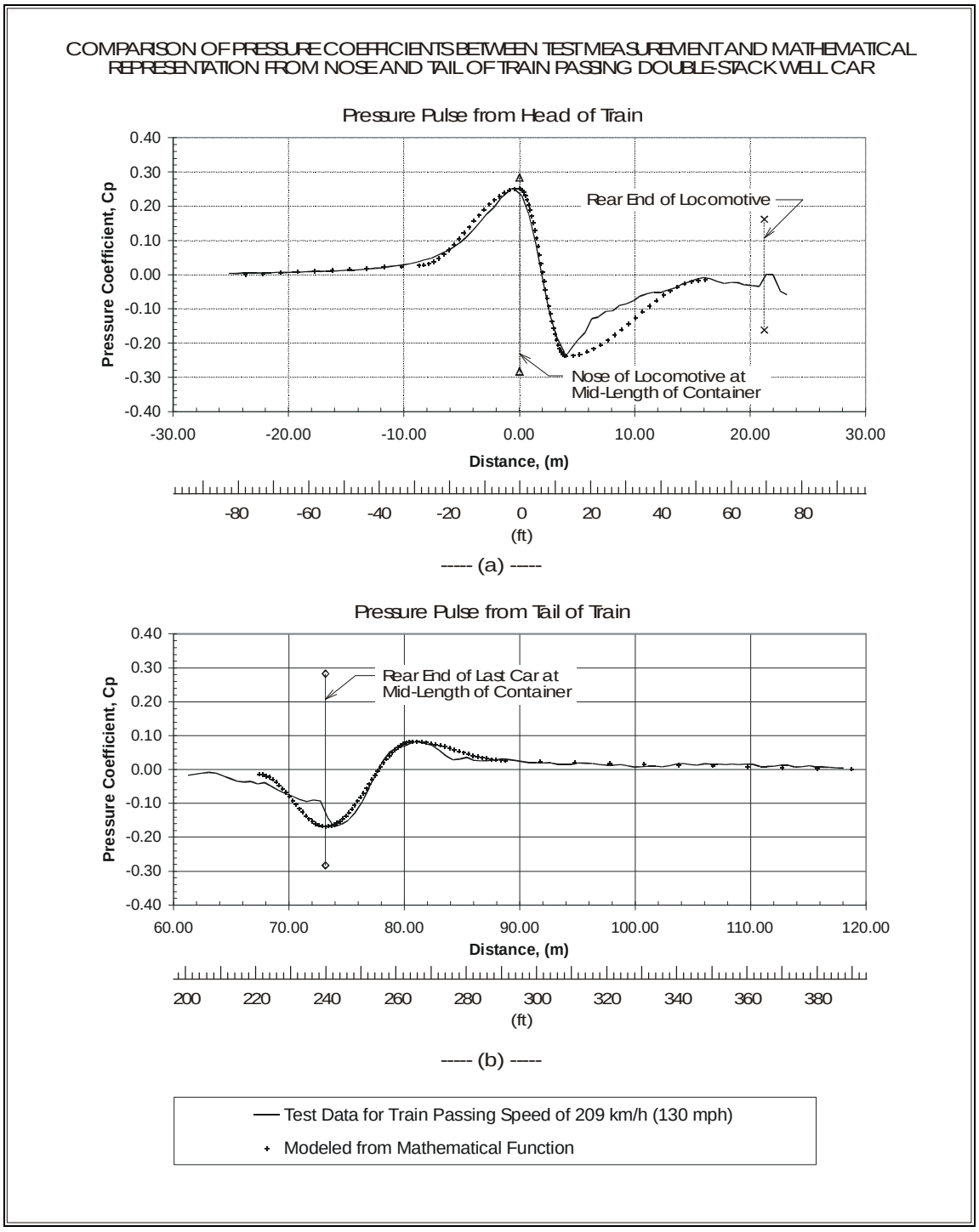

Figure 40. Pressure Coefficients from Test Measurement and Modeled from Piecewise Mathematical Functions of Pressure Pulses from the Nose and Tail of a Passing Train

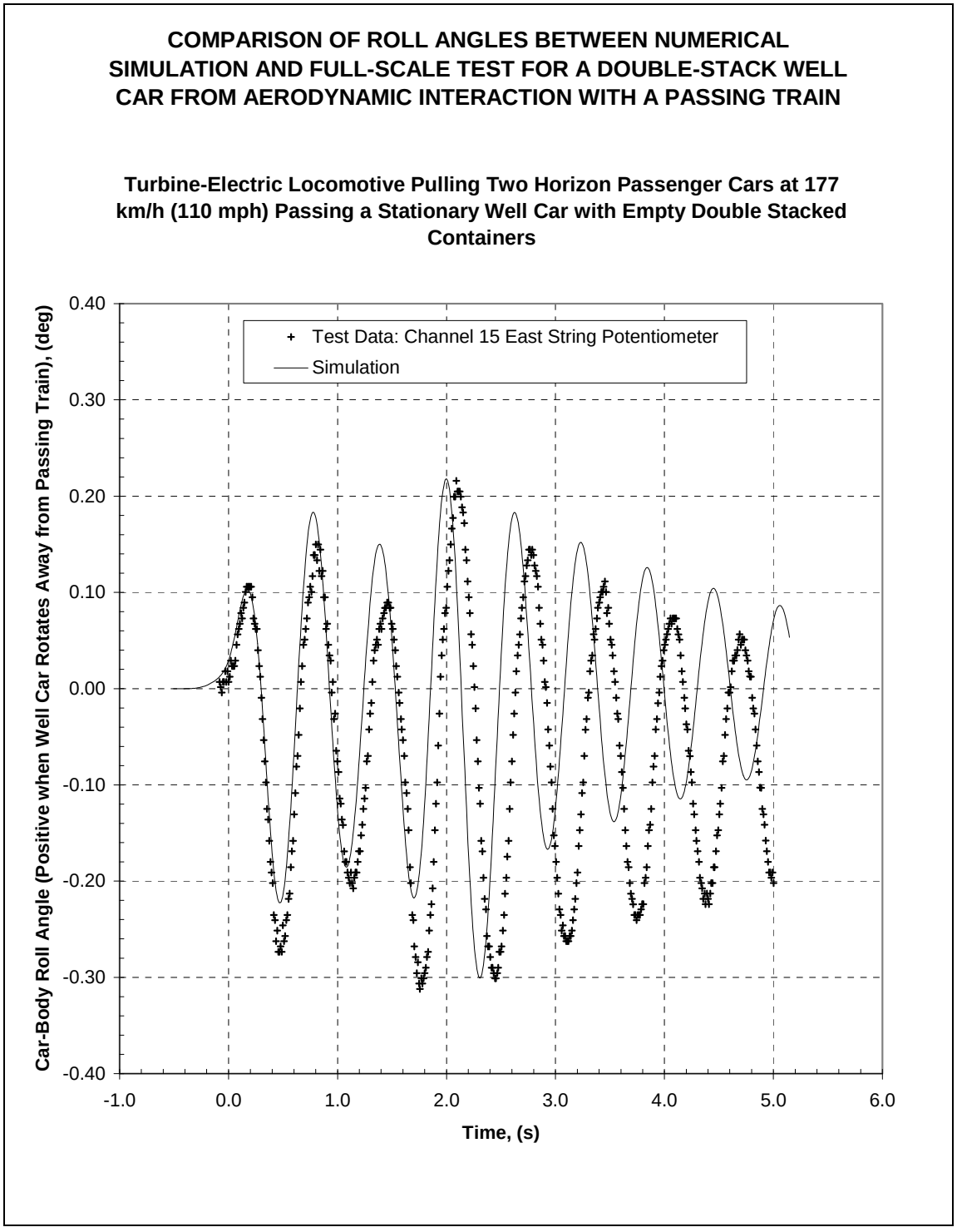

Figure 41. Time History Roll Response of a Double-Stack Well Car from Numerical Simulation and Full-Scale Test

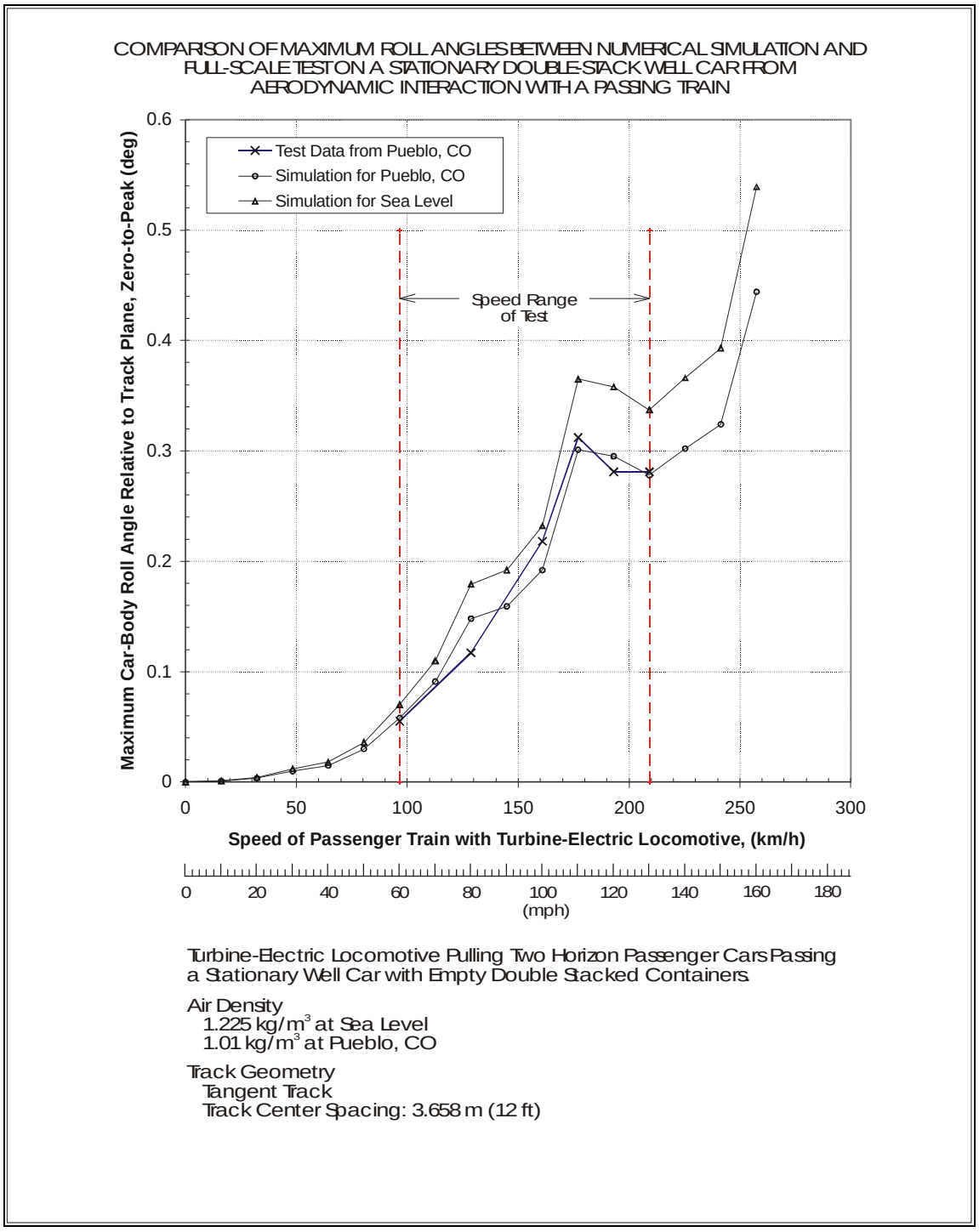

Figure 42. Maximum Carbody Roll Angles of a Double-Stack Well Car from Numerical Simulation and Full-Scale Test

The previous results compared model simulation with a full-scale test for conditions at Pueblo, Colorado, where the altitude is significantly above sea level. The simulation was repeated to determine the roll response of the double-stack well car at sea level since the air density would be noticeably higher. Carbody roll angles for air density at sea level were computed and are plotted along with those for Pueblo (Figure 42), where the maximum carbody roll angle at sea level is higher than for Pueblo, but the trend is otherwise similar.
`

Two factors influence the roll response of the double-stack well car, which are related to the speed of the passing train. As the passing train increases in speed, the aerodynamic pressure around the train increases as the square of its velocity, resulting in a higher force applied to the double-stack well car, and therefore a greater roll response. The second factor is the relation between the passing train speed and the natural frequency of the carbody roll. A pressure pulse that sweeps by at a speed that matches the carbody roll natural frequency can amplify the carbody response. Besides the frequency content of the pressure pulse, a period exists between the passage of the head pulse and the arrival of the tail pulse. If the tail pulse arrives to produce a net force on the double-stack well car that is in phase with the carbody roll motion, the carbody roll angle is further amplified. This phenomenon is shown in Figure 43, where the lateral aerodynamic force of the passing train and the roll response of the double-stack well car are plotted for the case of a train passing at a speed of 177 km/h (110 mph). The roll response of the double-stack well car is further magnified from the passage of the tail pulse. If the passing train is long, the roll motion of the double-stack well car can decay sufficiently, so that the passage of the tail pulse will have a lesser effect.

These results demonstrate that the simple single degree-of-freedom roll model can provide good predictions of carbody roll from transient aerodynamic force input produced by a passing train. Besides the roll motion to the carbody, a dynamic vehicle/track interaction occurs as a result of the aerodynamic force applied to the double-stack well car. The time-varying aerodynamic pressure sweeping along the side of the double-stack well car produces both roll and yaw moments to the car. The roll moment about the longitudinal axis at the track plane (from the top of the rail), and the yaw moment about the vertical axis at the center of the car, applied to the stationary double-stack well car from a train passing at a speed of 177 km/h (110 mph), are shown plotted in Figure 44. Although roll is the only degree-of-freedom in the carbody roll model, the aerodynamic force along with the computed roll and yaw moments complete the forcing inputs to a more complex multi-body simulation model for dynamic response from vehicle/track interaction.

NUMERICAL SIMULATION OF ROLL RESPONSE FOR A STATIONARY DOUBLE-STACK WELL CAR FROM AERODYNAMIC INTERACTION WITH A TRAIN PASSING AT 177 km/h (110 mph)

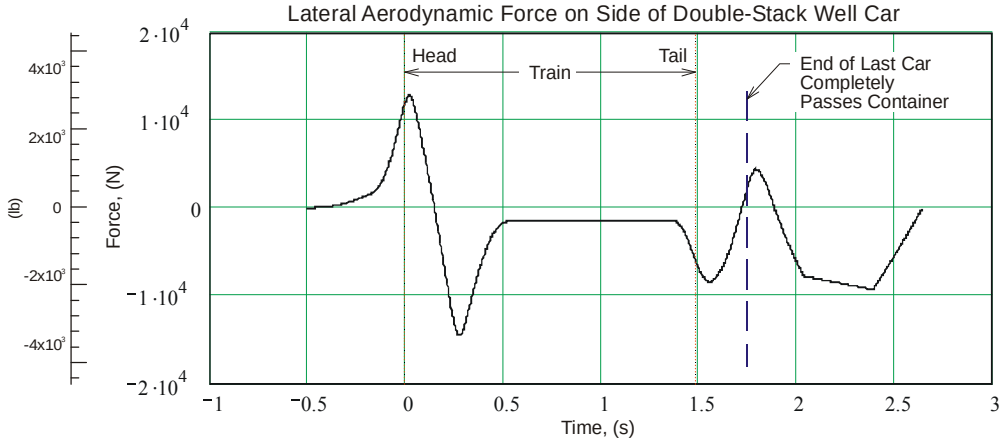

----- (a) -----

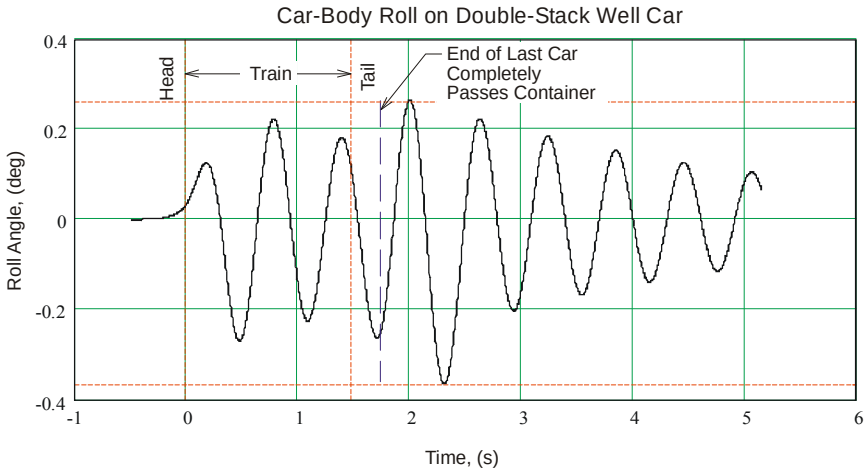

----- (b) -----

Turbine-Electric Locomotive Pulling Two Horizon Passenger Cars Passing a Stationary Well Car with Empty Double Stacked Containers.

Track Center Spacing: 3.658 m (12 ft)

Air Density: 1.225 kg/m^3 (Sea Level)

Figure 43. Time Histories of Applied Force and Roll Response of a Double-Stack Well Car

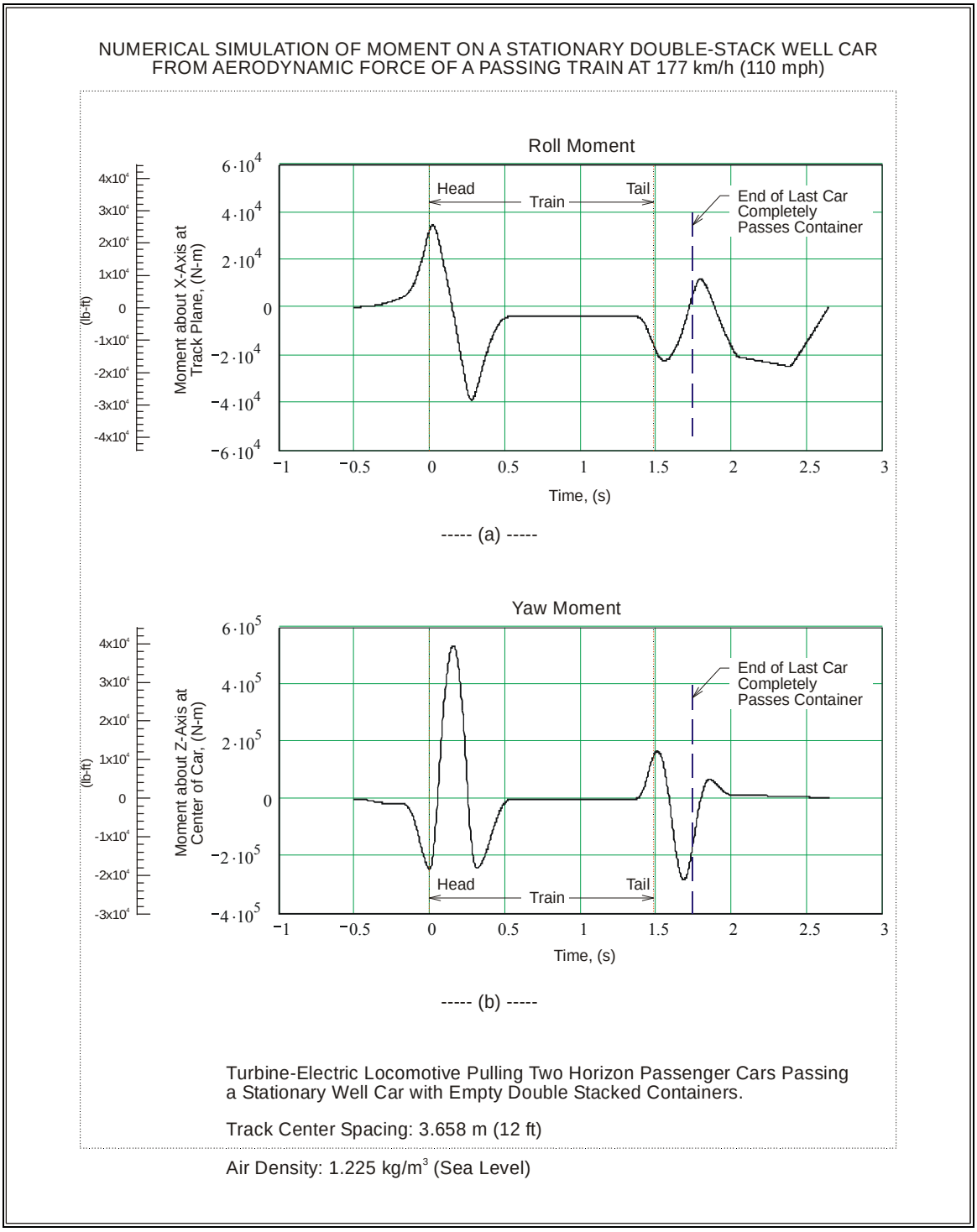

Figure 44. Time Histories of Applied Moments to a Double-Stack Well Car

8.3. Simulation Results with Headwind and on Curved Track

A parametric study of roll response was conducted for a well car with empty double-stacked containers as a TEL train with two passenger cars passes by on an adjacent track (consist in this simulation corresponds to the consist in the full scale test (see Section 3.2)). Simulations were performed using the single degree-of-freedom carbody roll model for the following conditions: (1) a double-stack well car traveling over a range of speeds being passed by a train traveling against various headwind speeds, and (2) a double-stack well car traveling over a range of speeds on a curved track being passed by a train on the inside and outside tracks of the curve. The double-stack well car traveled over a speed range both in the same and in opposite directions to the passing train.

8.3.1. Train Passing with Headwind

The strength of the aerodynamic pressure generated by the passing train is dependent on the speed of the airflow relative to the train. With a headwind, the airflow velocity relative to the passing train is the speed of the headwind added to the speed of the train. The roll response for the observer car was for passing train encounters in the same and opposite directions with the observer car traveling over a speed range of 0 to 129 km/h (0 to 80 mph) in both directions passed by a train traveling in one direction at 241 km/h (150 mph) with and without headwind. Four headwind speeds were included in the simulation from 24 km/h (15 mph) to 80 km/h (50 mph).

Maximum carbody roll angles were obtained for the observer car traveling at various speeds passed by a train against various headwind speeds. The roll angle on the observer car is lowest when the passing train has no headwind, with higher roll angle as the passing train encounters higher headwind, as shown in Figure 45. The speeds of the passing train and observer car simulated in this study produced a relative, or closing speed ranging from 370 km/h (230 mph) to 113 km/h (70 mph). For any given ambient wind speed, the trend of the observer car response is a relatively consistent increase in roll angle, as the relative speeds between the observer car and passing train decrease (or with the observer car traveling at 129 km/h (80 mph) in the opposite direction to the passing train, to 129 km/h (80 mph) in the same direction as the passing train). At a decreasing closing speed, the aerodynamic pressure pulse from the passing train sweeps by the observer car approaching that of its roll natural frequency. As the observer car increases in speed opposite to the passing train direction, the pressure pulse sweeps by increasingly beyond its roll natural frequency and resulting in a reduced roll angle.

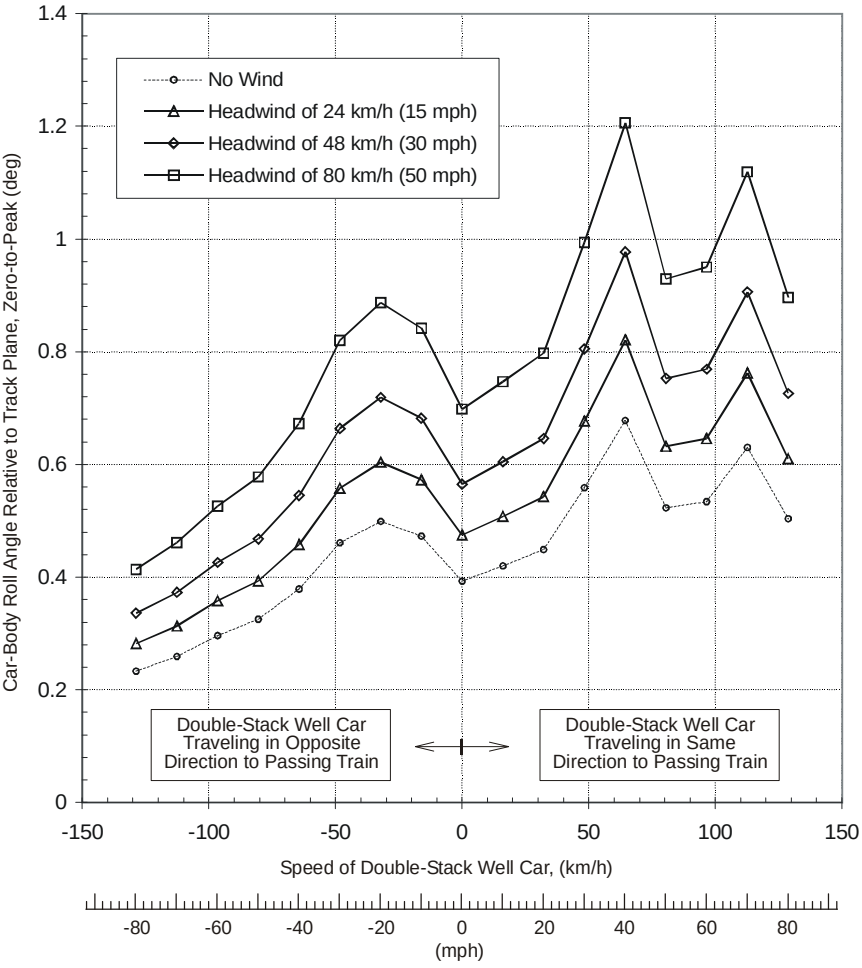

Figure 45. Maximum Roll Angles of a Double-Stack Well Car when Passed by a Train with Headwind

Another characteristic, when the train passes the observer car, is periodic peaks in the maximum roll angles of the observer car at certain relative speeds (Figure 45). This occurs when the observer car is traveling at speeds of 64.4 km/h (40 mph) and 113 km/h (70 mph) in the same direction as the passing train, and when the observer car is traveling at 32.2 km/h (20 mph) in the opposite direction to the passing train. In each of these speeds, the observer car reaches its highest roll angle following the passage of the last car of the passing train. The roll motion of the observer car from the initial pressure pulse is further amplified when the tail pulse arrives to produce a net force on the observer car that is in phase with the carbody roll motion. This corresponds to relative speeds between the passing train and observer car of 177 km/h (110 mph), 129 km/h (80 mph), and 274 km/h (170 mph).

When the passing train overtakes the observer car, the peak maximum roll angle on the observer car traveling at 64.4 km/h (40 mph) is greater than the peak maximum roll angle when traveling at 113 km/h (70 mph). As the closing speed between the observer car and passing train continues to be reduced, the pressure pulse will sweep along the observer car further away from its roll natural frequency. Moreover, it takes the passing train a longer time to pass a faster moving observer car traveling in the same direction, resulting in a longer time lapse between the arrival of the nose and tail pressure pulses from the passing train. In that extra time, the observer car rolls an extra cycle with a further decay in roll motion. Therefore, a lower peak roll angle is attained on the observer car since it has a reduced roll angle when it encounters the tail pressure pulse of the passing train.

8.3.2. Train Passing on Curved Track

When a rail car is traveling on curved track at balanced speed, no net lateral force occurs on the rail car from negotiating the curve, and the response of the car from a passing train is similar to traveling on tangent track. However, when it is negotiating a curve at a speed that is not balanced, a net lateral force acts on the rail car. If it is traveling below the balanced speed, or at a cant excess, the net lateral force applied to the car is inward toward the center of the curve (toward the inside of the curve). If the car is traveling above the balanced speed, or at a cant deficiency, the net lateral force applied to the car is outward away from the center of the curve (toward the outside of the curve). The relationship between train speed and unbalanced track cant is shown in Figure 46 for a track with a 1 deg curve and a 152 mm (6.0 in) superelevation. Balanced speed occurs when the cant unbalance is zero, which for a 1-degree curve is at a speed of 150 km/h (93 mph).

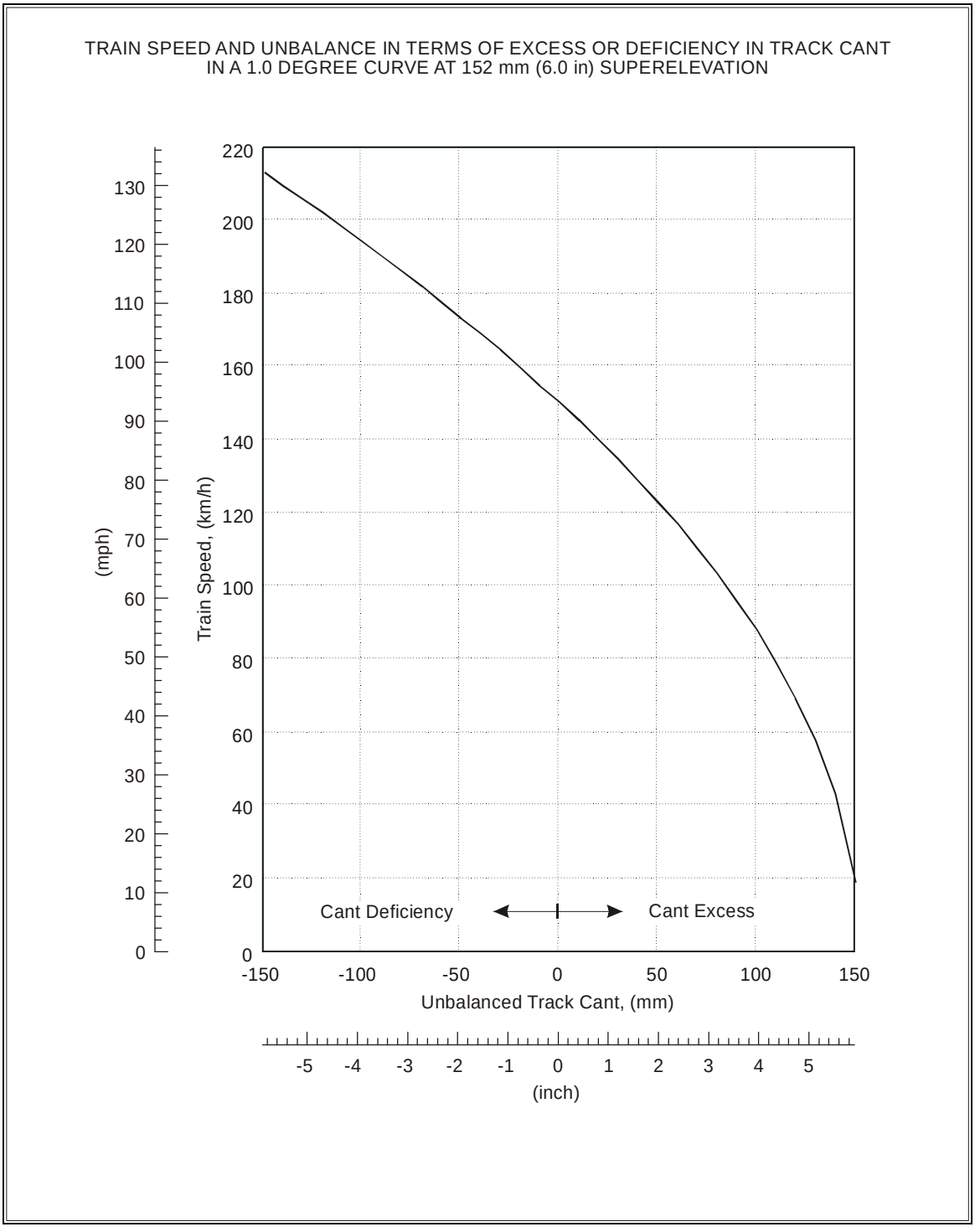

Figure 46. Train Speed and Unbalanced Track Cant

A simulation was performed with the observer car traveling at various below balanced speeds (cant excess) on a 1-degree curve with a 152 mm (6.0 in) superelevation while a train passes on an adjacent track. The observer car traveled over a speed range of 0 to 129 km/h (0 to 80 mph) in both directions, while the passing train traveled at 184 km/h (114.5 mph) in one direction, providing for passing train encounters in the same and opposite directions. The train passed the observer car on an adjacent track that is on the inside, and on the outside tracks of the curve. The observer car responds to the aerodynamic force of the passing train with a roll motion oscillating toward the inside and outside of the curve as shown plotted in Figure 47. Highest maximum roll angle is when the observer car rolls toward the inside of the curve, which is especially noticeable with high cant excess (stationary car). This is the case whether the train is passing the observer car on the inside or outside of the curved tracks.

Also shown in the Figure 47 is a plot of the maximum roll angle due only to the lateral force from unbalanced speed with no trains passing. Because the observer car is traveling below balanced speed, a bias exists in the roll angle where the carbody is rolled toward the inside curve. This additional constant bias in the roll angle contributes to the perturbed roll angle of the observer car to be greater toward the inside of the curve than toward the outside. As the car increases toward the balanced speed, the roll angle becomes smaller and approaches zero, and will roll toward the outside curve as it traverses the curve above the balanced speed (not shown in the graph).

The maximum roll angle of the observer car is dependent on if a train passes it on an adjacent track that is on the inside or outside curve. The observer car traveling at below balanced speed produces a greater maximum roll angle of oscillation when it is passed by a train on the inside than on the outside of the curved track as shown plotted in Figure 48 (carbody roll angle measured relative to steady-state carbody roll as zero reference). The reason is that these two passing situations are not equivalent when the observer car is traveling at an unbalanced speed, where a constant bias occurs in the roll angle. The initial pressure pulse from the passing train is always a positive to negative pressure, producing a push and then a pull on the observer car. When the train is passing the observer car on the outside curve, it first pushes the car toward the inside of the curve; while when passing the observer car on the inside curve, it first pushes the car to the outside of the curve. However, as the observer car approaches balanced speed, the roll angles become the same whether the passing train on the adjacent track is on the inside or outside of the curve. When the carbody roll angle is measured as a deviation from its steady-state roll, a train passing the observer car on the inside curve produces the same maximum carbody roll angle as a train passing the observer car on tangent track (Figure 48).

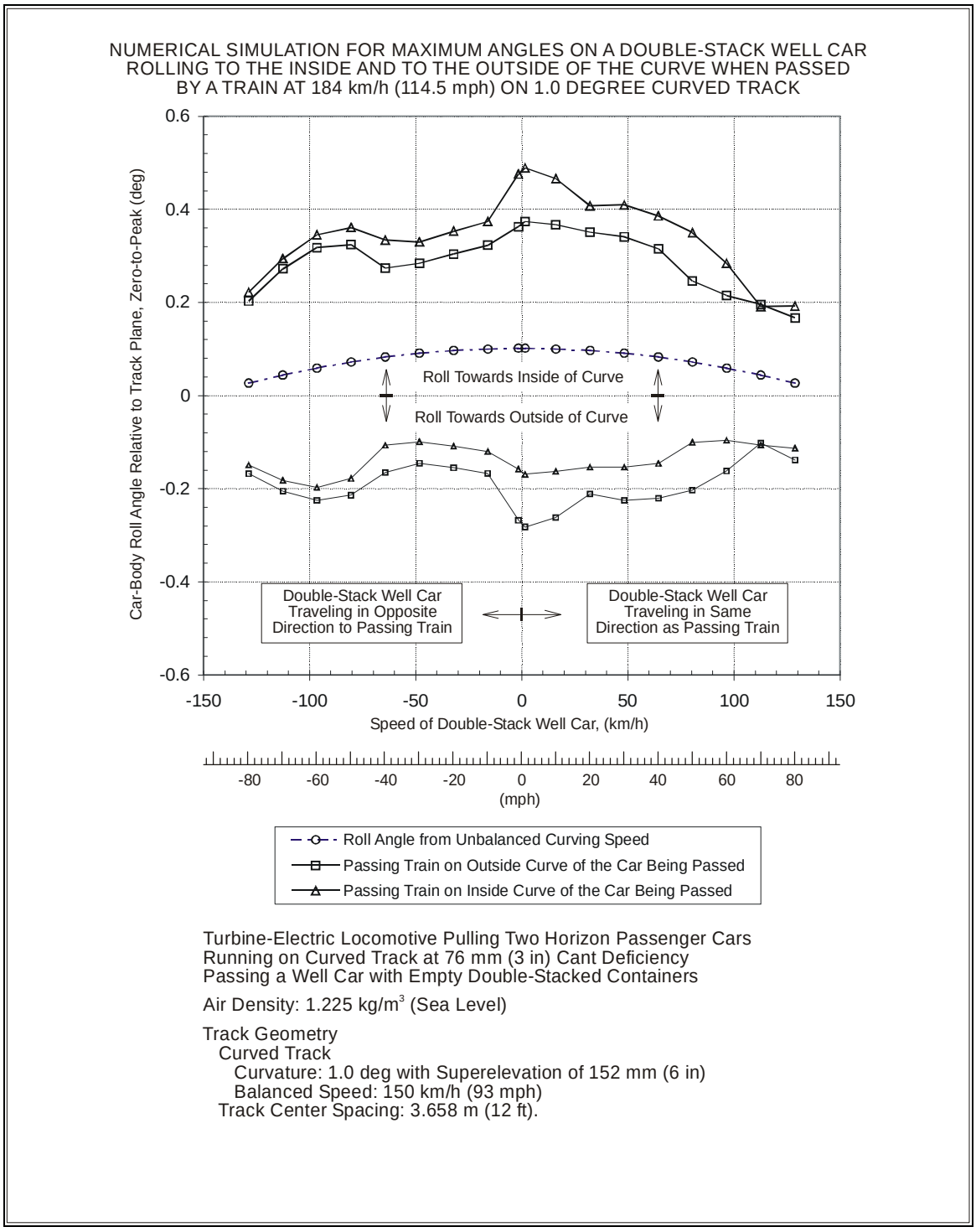

Figure 47. Maximum Roll Angles to the Inside and to the Outside of the Curve for a Double-Stack Well Car Passed by a Train on Curved Track

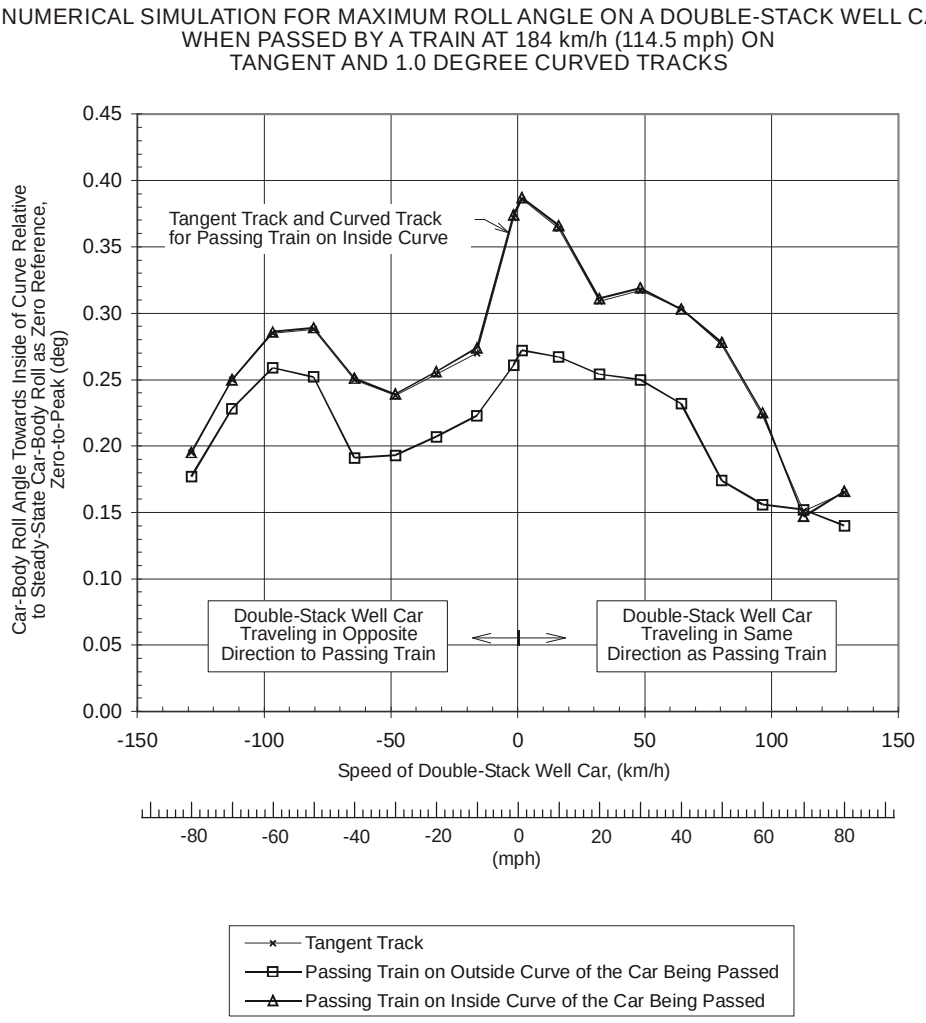

Turbine-Electric Locomotive Pulling Two Horizon Passenger Cars Running on Tangent Track and Curved Track at 76 mm (3 in) Cant Deficiency Passing a Well Car with Empty Double-Stacked Containers

Air Density: 1.225 kg/m^3 (Sea Level)

Track Geometry
- Tangent Track
- Curved Track
  - Curvature: 1.0 deg with Superelevation of 152 mm (6 in)
  - Balanced Speed: 150 km/h (93 mph)
- Track Center Spacing: 3.658 m (12 ft).

Figure 48. Maximum Roll Angles of a Double-Stack Well Car Passed by a Train on Tangent and Curved Tracks

9. Measurements of Airflow and Aerodynamic Load from Full-Scale Test of Passing Train

Part 1 of this report presented a digest on the mathematical and full-scale test results of the effects to people and objects alongside the track from the airflow and aerodynamic pressure created by a passing train. In this chapter, the data obtained from the test conducted in Mansfield, Massachusetts from September to October of 2002, is further processed and analyzed in detail. In that test, airflow velocities were measured using pitot-static tubes, and forces were measured on CIDs. Also, some of the airflow velocity data from previous tests are included in the analysis.

Two methods were used to characterize the aerodynamic effects of passing trains with the purpose of assessing safety of people alongside the track. One method was to measure the airflow velocity, which characterized the fluid property in the flow field surrounding the passing train. The drag on a body can then be computed from the airflow velocity. This measurement is significant because the airflow velocity induced by a passing train is considered to be the more serious effect in destabilizing people and objects (RAPIDE 2001; Gawthorpe 1978). The second method was to directly measure the force on a cylindrical object situated beside a passing train. This method measures the effect on an object instead of the property of the fluid. The airflow velocity measured by a pitot-static tube, and the load on the cylindrical object, represent two different methods of arriving at the force on an object.

In this chapter, the aerodynamic data are processed and analyzed, and then applied to relate the distance from a passing train with the strength of airflow. First, the airflow velocity and force on the CID are analyzed to characterize the aerodynamic signatures associated with the different trains. Also, the force measured on the CID is compared with computed drag on other bodies. Next, a relationship is established between induced airflow velocity and lateral distance from the train. Finally, the aerodynamic effects on people are assessed from wind speed criteria with an indicated minimum distance from a passing train.

9.1. Processing Test Data

Data were measured as time histories of airflow velocities from pitot-static tubes and of forces on the CIDs. One of the processing procedures involves filtering out certain frequencies in the data, which in almost all cases was performed to remove noise in the signal. However, the filtering process was also performed so that the data conforms to proper conditions for analysis. Another processing involves computing drag on a cylinder from airflow velocity. Because the drag coefficient for a cylinder varies with Reynolds number, a mathematical function is required to be derived for the drag coefficient. The other processing procedure includes extracting maximum values in the data and obtaining statistical quantities.

9.1.1. Time History of Aerodynamic Data

The geometry of the train, particularly the head end, has a strong influence on the aerodynamic effect as the train passes by. Aerodynamic data was obtained from passing trains of different head and tail end geometries. These trains consisted of four train styles with distinctive geometric appearance, which are:

- Acela Express trainset,
- Amfleet train with AEM-7 locomotive,
- Amfleet train with HHP-8 locomotive, and
- Amfleet train with F40PH locomotive.

An example of the aerodynamic data is presented as time history plots for each of these trains except the Amfleet/F40PH train. The time history data includes airflow velocities measured from pitot-static tubes and the force on one of the two CIDs. Only one of the train passes from each of the three styles of trains is included as an example. Table 25 describes the example cases.

Table 25. Example Cases in Time History Plots

Train	Speed	Length*	Designation
Acela Express	239 km/h (149 mph)	202 m (663 ft) 1L+6C +1L	B02J01-1012
Amfleet with AEM-7 Locomotive	184 km/h (114 mph)	224 m (735 ft) 1L+8C	B02J01-1825
Amfleet with HHP-8 Locomotive	201 km/h (125 mph)	228 m (748 ft) 1L+8C	B02J01-1101

* L: locomotive or power car; C: passenger car

The data of the time history plots are measurements from the CID at the location closest to the track, and from pitot-static tubes that are placed to correspond with the cylinder axis of the CID. Data, from the lower or in some cases the average value from data that is measured from the top and bottom pitot-static tubes, are plotted. The positions of the pitot-static tubes and CID for the example plots are shown in Table 26.

Table 26. Positions of Pitot-Static Tube and CID in Example Time History Plots

Measurement	Nominal Lateral Distance from Side of Train	Nominal Vertical Distance from Top of Rail
Pitot-Static Tube	1.17 m (46 in)	0.97 m (38 in)
Pitot-Static Tube for Computing Cylinder Force*	1.17 m (46 in)	1.25 m (49 in)
CID-5	1.20 m (47 in) Cylinder Axis	1.24 m (49 in) Center of Pressure

* Airflow velocity was averaged from values measured at two other heights.

9.1.2. Airflow Velocity from Pitot-Static Tube

Time histories of airflow velocities were measured from four pitot-static tubes at two different heights and at various lateral distances from the train (Figure 13 and Table 18). In configurations 1 and 2, the pitot-static tubes were oriented to measure longitudinal airflow (+x airflow in the direction of the passing train) for two different lateral distances from the passing train. In configurations 3 and 4, pitot-static tubes were oriented perpendicular to each other, and at the same two nominal lateral distances from the track as the cylindrical axes of the CIDs. These orientations of the pitot-static tubes measured the airflow velocities on the horizontal plane along two directions to obtain simultaneous measurements of the longitudinal (+x) and lateral airflow (+y airflow in the direction away from the side of the train) velocity components. A single quadrant resultant airflow velocity is computed as a vector sum from the two perpendicular components in the positive longitudinal and positive lateral directions (any negative velocity was set to zero), and is referred to as the quadrant 1 resultant airflow velocity (coordinate axes shown in Figure 19).

One significant source of error in these measurements is in the misalignment of the pitot-static tube with the direction of airflow. The misalignment error depends on the nose shape of the pitot tube (Ower and Pankhurst 1977). With the hemispherical nose pitot tube that was used, the manufacturer specifies that it has low sensitivity to misalignment, and gives accurate reading even when the tube is misaligned up to 15°. However, airflow velocity from a passing train can be from any direction, although the expected flow is primarily on a horizontal plane and longitudinal in the direction of the passing train. It was also assumed that some significant lateral airflow component occurs away from the side of the train. In these conditions, the pitot-static tube can be greatly misaligned because the airflow can be in any direction along the horizontal plane, with a significant flow between 0 to 90° (0-degree positive longitudinal and 90-degree positive lateral). No

single orientation of the pitot tube can measure the airflow over its full range of flow directions.

To obtain the two orthogonal components of airflow velocities, two pitot-static tubes were placed perpendicular to each other to measure the airflow in the positive longitudinal and lateral directions. However, a significant error can exist in computing the resultant airflow as the vector sum of the two components. A correct resultant airflow velocity from a vector sum of its components requires that the velocity due to misalignment error varies according to the cosine of the misalignment angle (or that the differential pressure from the pitot-static tube vary according to the cosine square of the misalignment angle). However, the error of misalignment does not vary according to these relationships (Figure 89 in the Appendix) (Ower and Pankhurst 1977; Devenport 2001). When the airflow is at 45 deg, the error is estimated to be 17 percent. If the airflow is primarily along the longitudinal direction, and if the lateral airflow component is small relative to the longitudinal component, then the impact of this error is not expected to be significant.

Two pitot-static tubes at one location were arranged perpendicular to each other to measure horizontal airflow along the two directions. Because each pitot tube can only measure airflow in one direction, no reverse airflow (flow away from the pitot tube orifice) was measured at any one time. Therefore, any airflow that was parallel to the track flowing opposite to the direction of train travel, and perpendicular to the track flowing toward the train, was not included in computing the resultant velocity. Some test cases were performed where the pitot-static tubes were place facing the opposite direction to its normal orientation to determine the extent of reverse airflow. A noticeable reverse flow was found, particularly in the lateral direction back toward the direction of the track.

When two pitot-static tubes were placed perpendicular to each other, the pitot-static tube in the lateral orientation was at least 0.241 m (9.5 in) closer to the track than the nominal distance. The reason is that due to mounting limitation on the support rack, it was difficult to position the two pitot-static tubes to measure the airflow at exactly the same position. Therefore, the two pitot-static tubes measured airflow that was at a distance of 0.341 m (13.4 in) from each other. The nominal distance was always referenced to the location of the pitot-static tube in the longitudinal orientation to be consistent with reference to other measurements.

Airflow data were measured at various lateral distances from the train. In some cases, the pitot-static tubes were configured to measure simultaneous airflows at two different lateral positions. Generally, that was not the case, and the airflows measured at different lateral distances were from different passing trains.

9.1.3. Data Filtering

The forces measured from the CIDs have been processed by a Bessel second order 15 Hz low-pass digital filter to account for the muscular-response time of a human being. Airflow velocity data measured from the pitot-static tube was processed either by a moving average or a Bessel filtering depending on the application of the data. All airflow data that was not treated to Bessel filtering was processed by a moving average filtering with a minimum of 0.032 s duration window to remove the 60 Hz noise that was present in the data. Airflow velocity data that was used to compute the cylinder force was processed by a Bessel second order 15 Hz low-pass digital filter to maintain consistency when comparing with forces measured from the CIDs.

9.1.4. Force on a Circular Cylinder

The force on the CID is created by the pressure distribution around the cylindrical body from its aerodynamic interaction with a passing train. The unbalanced force along the horizontal plane of the CID can be computed from the airflow velocity and the drag coefficient for a cylinder. The drag is computed from the drag coefficient measured for airflow to an isolated cylinder, which does not account for the effect of static pressure variation around the cylinder due to the presence of a passing train. The drag on an object is computed as,

$$F_D = \left(\frac{1}{2}\rho_\infty v_\infty^2\right) C_D A_P \qquad \textbf{Equation 6}$$

where,

- ρ_∞: free stream density
- v_∞: free stream flow velocity
- C_D: drag coefficient
- A_P: projected area

The drag on a circular cylinder situated with its axis perpendicular to the airflow, with $A_P = D_C L_C$, is computed as,

$$F_{D-cyl} = \frac{1}{2}\rho_\infty v_\infty^2 D_C L_C C_D(\mathrm{Re}) \qquad \textbf{Equation 7}$$

where,

- D_C: diameter of the cylinder
- L_C: Axial Length of the cylinder

Re: Reynolds number

The drag coefficient $C_D(Re)$ for a circular cylinder is a function of the Reynolds number, and airflow over a cylinder can occur in different flow regimes depending on the Reynolds number. The CID consists of a cylindrical body that is smooth and rigid and similar to a two-dimensional circular cylinder (cylinder of infinite or very long axial length) where drag coefficient data has been measured (Figure 85(a) in the Appendix). If the cylinder dimensions, fluid density, and viscosity remain constant, then the drag coefficient for the cylinder depends only on the speed of the air flowing toward the cylinder (Table 44 in the Appendix). The Reynolds number and airflow velocity where the flow regime changes for the CID are shown in Table 27 (Schlichting and Gersten 2000). Much of the train-induced airflow velocities to the CID are at the critical Reynolds number.

Table 27. Drag Coefficients for a Two-Dimensional Circular Cylinder and Corresponding Airflow Velocity for the CID

Reynolds number	Drag Coefficient	Airflow Velocity CID*
300 to $1x10^5$ subcritical regime	≈1.2	0.011 to 3.7m/s (0.025 to 8.4 mph)
$1x10^5$ to $1x10^6$ critical regime	0.2 to 1.2	3.7 to 37 m/s (8.4 to 84 mph)
$1x10^6$ to $3.5x10^6$ critical regime	0.2 to 0.5	37 to 131 m/s (84 to 293 mph)

*Standard atmosphere at sea level

When a cylinder has a short axial length, the flow that is induced around the side edges to the rear of the cylinder will contribute to a reduction in drag coefficient from that of a two-dimensional body (Horner 1958). The flow over a short cylinder must be treated as flow over a three-dimensional body. For a short cylinder, the drag coefficient will be reduced from a two-dimensional body by a factor $\left(\frac{C_D}{C_{D2}}\right)$, where C_D is the drag coefficient for a cylinder that is a three-dimensional body, and C_{D2} is the drag coefficient for a cylinder that is a two-dimensional body.

An indication on the character of the flow can be obtained from the aspect ratio, or the ratio of the span (axial length) to the diameter of the cylinder (Figure 85(b) in the Appendix). Studies have found that for the same profile shape, the drag coefficient for a two-dimensional shape is higher than for a three-dimensional shape by a factor of about

1.8 (McCormick 1979). For the CID, the span is L_C=0.92 m (36.22 in), the diameter is D_C=0.39 m (15.35 in), and aspect ratio $AR_C=L_C/D_C$ is AR_C=2.36. With an aspect ratio of approximately 5 or less, the drag coefficient is nearly constant at a value corresponding to a three-dimensional shape (Horner 1958; McCormick 1979). Therefore, the drag for the CID can be corrected for three-dimensional effects as approximately $\left(\frac{C_D}{C_{D2}}\right) = 0.56$.

The drag coefficient for a circular cylinder varies with Reynolds number, particularly when the Reynolds numbers are very low and at high Reynolds numbers over the critical flow regime. Application of the drag equation for the CID (Equation 7) requires a functional relationship between the drag coefficient and Reynolds number. A series of piecewise linear functions for the drag coefficient of a circular cylinder were fitted to the data over the Reynolds numbers of interest (Table 43, Figure 86, and Figure 87 in the Appendix).

9.2. Characterization of Airflow

Airflows induced by passing trains are characterized for three different types of trains as distinguished by their nose and tail base geometries. Frequently, the maximum airflow velocity is required. Therefore, the relative strength between longitudinal and lateral airflow components is compared to determine if a measurement of the longitudinal airflow component alone is sufficient to obtain the maximum airflow velocity of the passing train.

9.2.1. Time History Examples

The example plots illustrate the characteristic aerodynamic signature of these different trains and the influence of train geometry on the signature. Some of the significant characteristics are the trends in the aerodynamic signature along the positions of the passing train, and the magnitudes of the head and tail perturbations, and the wake, relative to the total trace. The local variations in aerodynamic signature from any one of these example time history plots are not expected to be the same as other examples of the same type of train because of the random nature of the turbulent airflow. Measurements from the different types of trains were generally at different train speeds so any comparison of magnitudes in the data between trains must account for the speed difference.

The relative magnitudes between the longitudinal and lateral airflow velocity components are compared for the three different trains (Figure 49(a), Figure 50(a), and Figure 51(a)). Generally, the lateral airflow velocity component is very small relative to the longitudinal component. The exception is at the head of the train where the lateral airflow velocity component is higher than the longitudinal component, and is especially strong for the Amfleet train with the bluff nose AEM-7 locomotive (Figure 50(a)). However, the

signature and magnitude of the resultant airflow at quadrant 1 (Figure 49(b), Figure 50(b), and Figure 51(b)) appeared almost identical to the longitudinal component except for the higher resultant airflow at the head end, especially for the Amfleet/AEM-7 train (Figure 50(b)).

Each of the three trains, with its different nose and tail base geometries, produced a distinctive time history signature for the resultant airflow at quadrant 1. The Acela Express train with its tapered nose produced a weak head perturbation, with the resultant airflow gradually increasing in strength toward the tail end of the train (Figure 49(b)). The airflow velocity is highest near the tail end, continues to be strong after the last power car with its rearward facing tapered nose has passed and is only slowly reduced far into the wake. The Amfleet/AEM-7 train produced a very different airflow signature (Figure 50(b)). Its bluff nose locomotive creates a strong initial gust, with the airflow reaching a high level immediately behind the head of the train, and remains high along the length of the train. A drop in airflow does occur toward the flat-tail base with a weak airflow at the wake. The Amfleet/HHP-8 train with its slant nose and flat-tail base produced an airflow signature similar to the other two types of geometries. Its slant nose is similar to the Acela Express. It is reflected by a similar signature (Figure 51(b)), except for a more rapid decrease in airflow at the tail end, similar to the signature of the Amfleet/AEM-7 train that also has a flat tail base. These results illustrate the influence of train geometry on airflow signature, especially the nose and tail-base geometries.

The strength of the airflow is derived mainly in the longitudinal component. The lateral airflow component does not appear to contribute significantly to the resultant airflow, except in the case of a bluff nose head end where a very strong lateral gust is encountered. These results are limited to the longitudinal airflow in the direction of the passing train and to the lateral airflow away from the side of the train, where these airflow directions were expected to be the strongest.

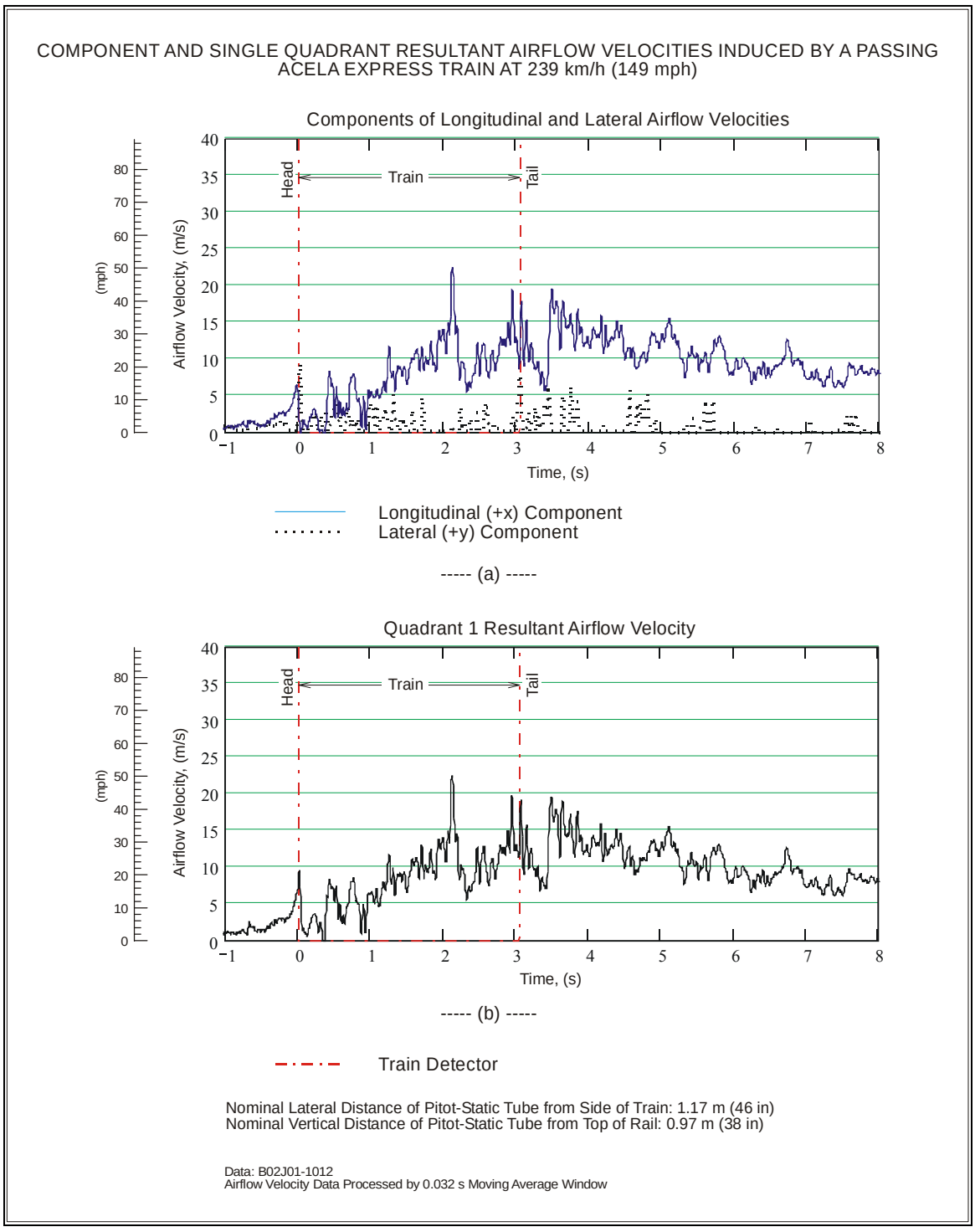

Figure 49. Time Histories of Airflow Velocities Measured from Pitot-Static Tubes for a Passing Acela Express Train

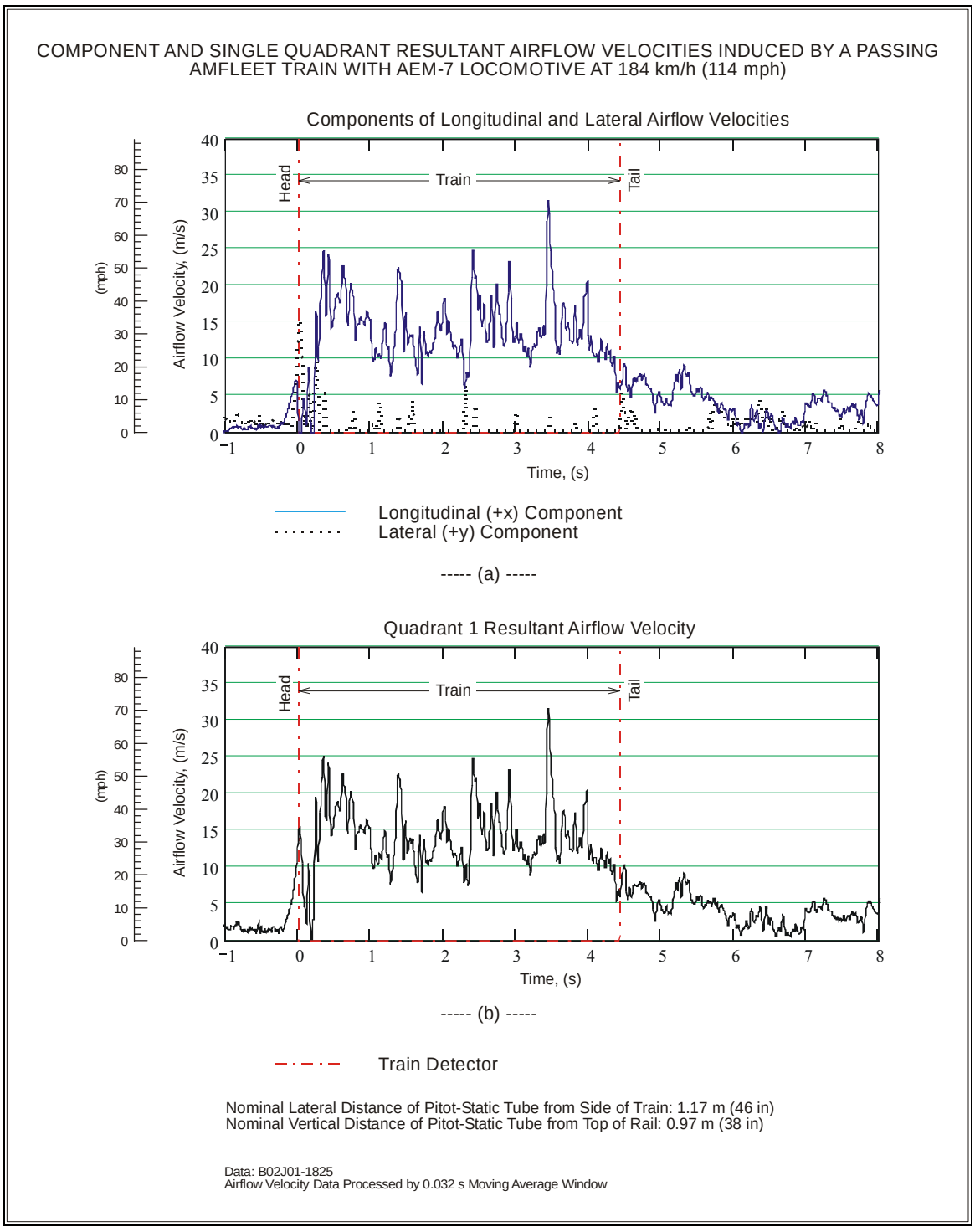

Figure 50. Time Histories of Airflow Velocities Measured from Pitot-Static Tubes for a Passing Amfleet Train with AEM-7 Locomotive

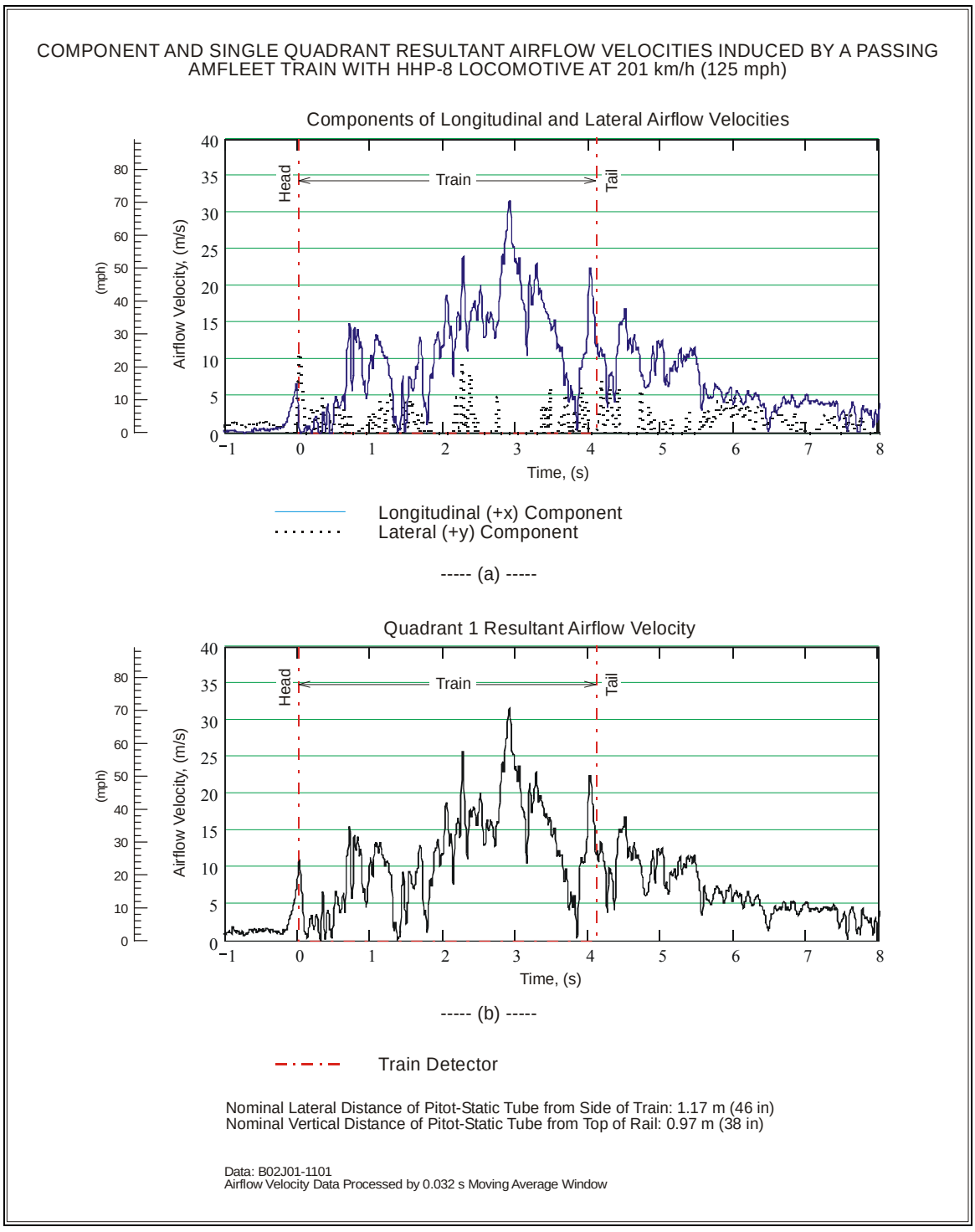

Figure 51. Time Histories of Airflow Velocities Measured from Pitot-Static Tubes for a Passing Amfleet Train with HHP-8 Locomotive

9.2.2. Airflow Strength and Distance

Both lateral distance from the train and height above the track are factors affecting the strength of the airflow. The maximum airflow velocities at two heights for the three different types of train are shown plotted in Figure 52, Figure 53, and Figure 54. If both the longitudinal and lateral airflow velocities were measured, then the maximum longitudinal and the resultant airflows at quadrant 1 were plotted on the same graph for comparison. This comparison shows that the maximum resultant airflow velocity over the entire length of the passing train is not noticeably greater than the maximum longitudinal component.

The airflow velocity measured at the same location from different passes of the same type of trains is not very repeatable, as evident by the considerable scatter in the data. This is consistent with observation from other studies on the lack of repeatability in the data due to the chaotic nature of the airflow (Johnson, Dalley, and Temple 2002). However, the trend in the data is a reduction in airflow velocity at increased distance from the train or at increased height from the track. The influence of train geometry is apparent with the Acela Express train inducing a lower airflow velocity than the Amfleet trains with either locomotive. These results are summarized in Table 28.

Table 28. Ranges of Airflow Velocities Induced by Different Trains for all Lateral Positions

Train	Range of Airflow Velocity as Percent of Train Speed	
	Height above Top of Rail	
	0.97 m (38 in)	1.73 m (68 in)
Acela Express	24 to 49%	18 to 41%
Amfleet with AEM-7	32 to 62%	20 to 39%
Amfleet with HHP-8	46 to 65%	27 to 60%

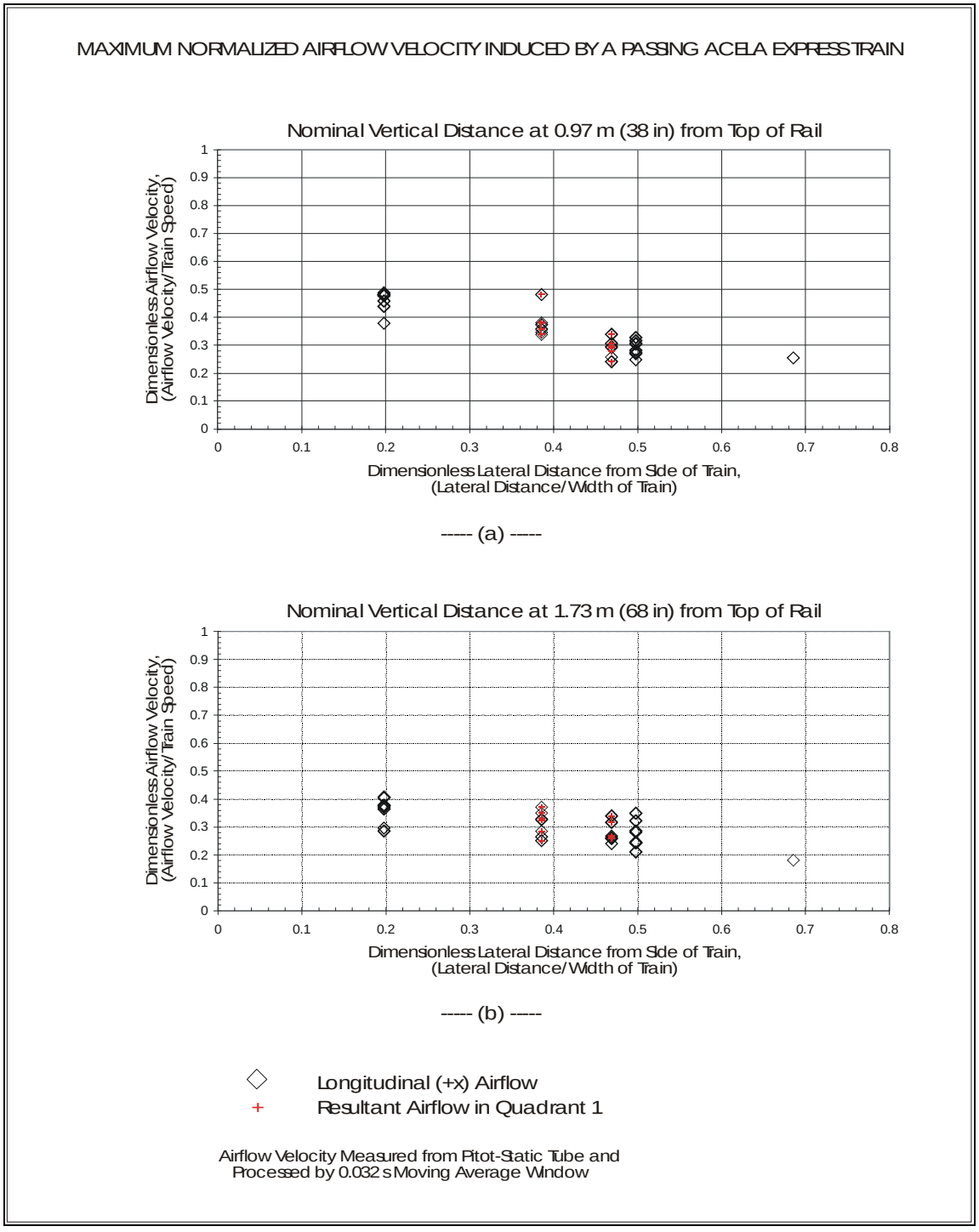

Figure 52. Maximum Airflow Velocities from Passing Acela Express Trains

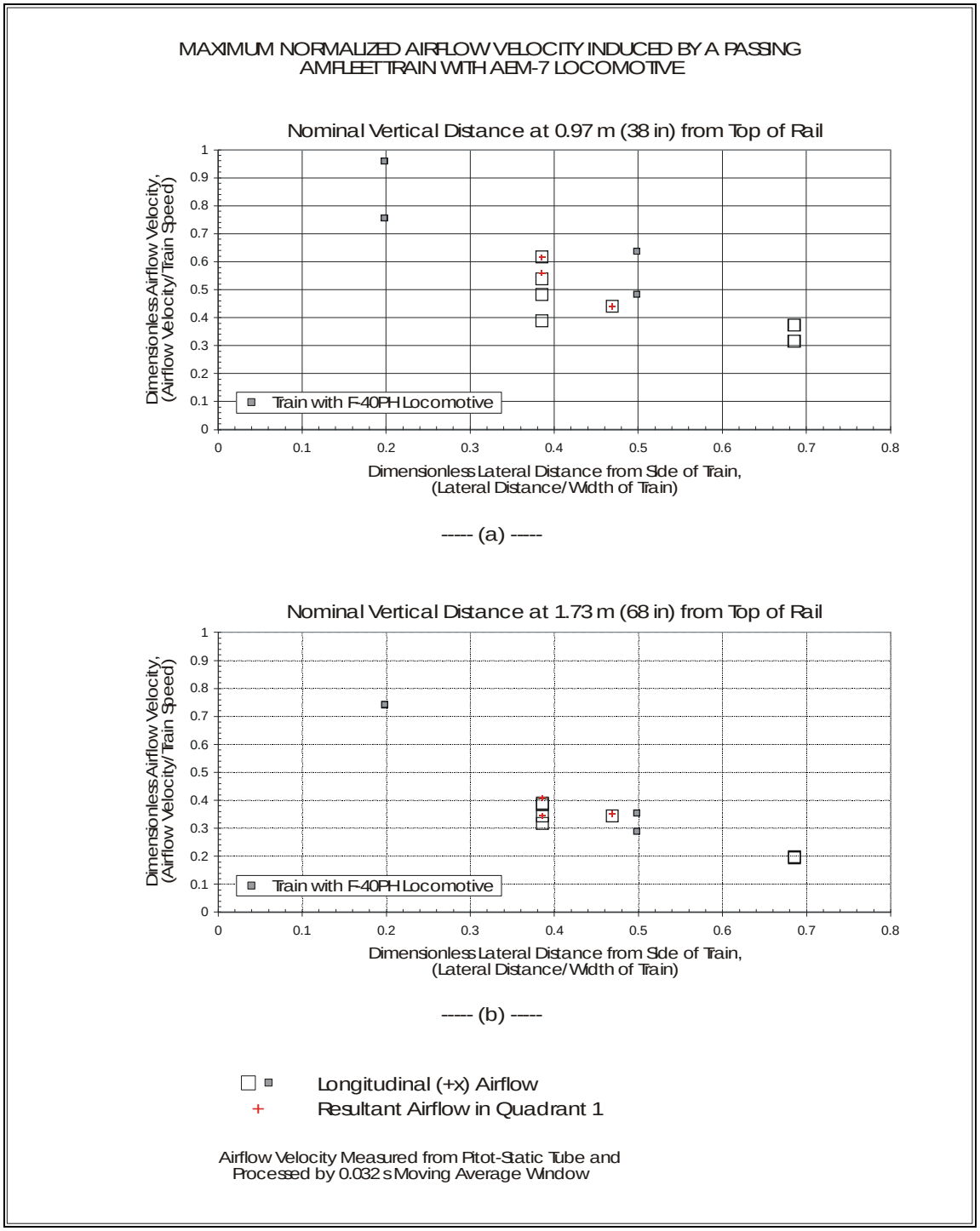

Figure 53. Maximum Airflow Velocities from Passing Amfleet Trains with AEM-7 Locomotives

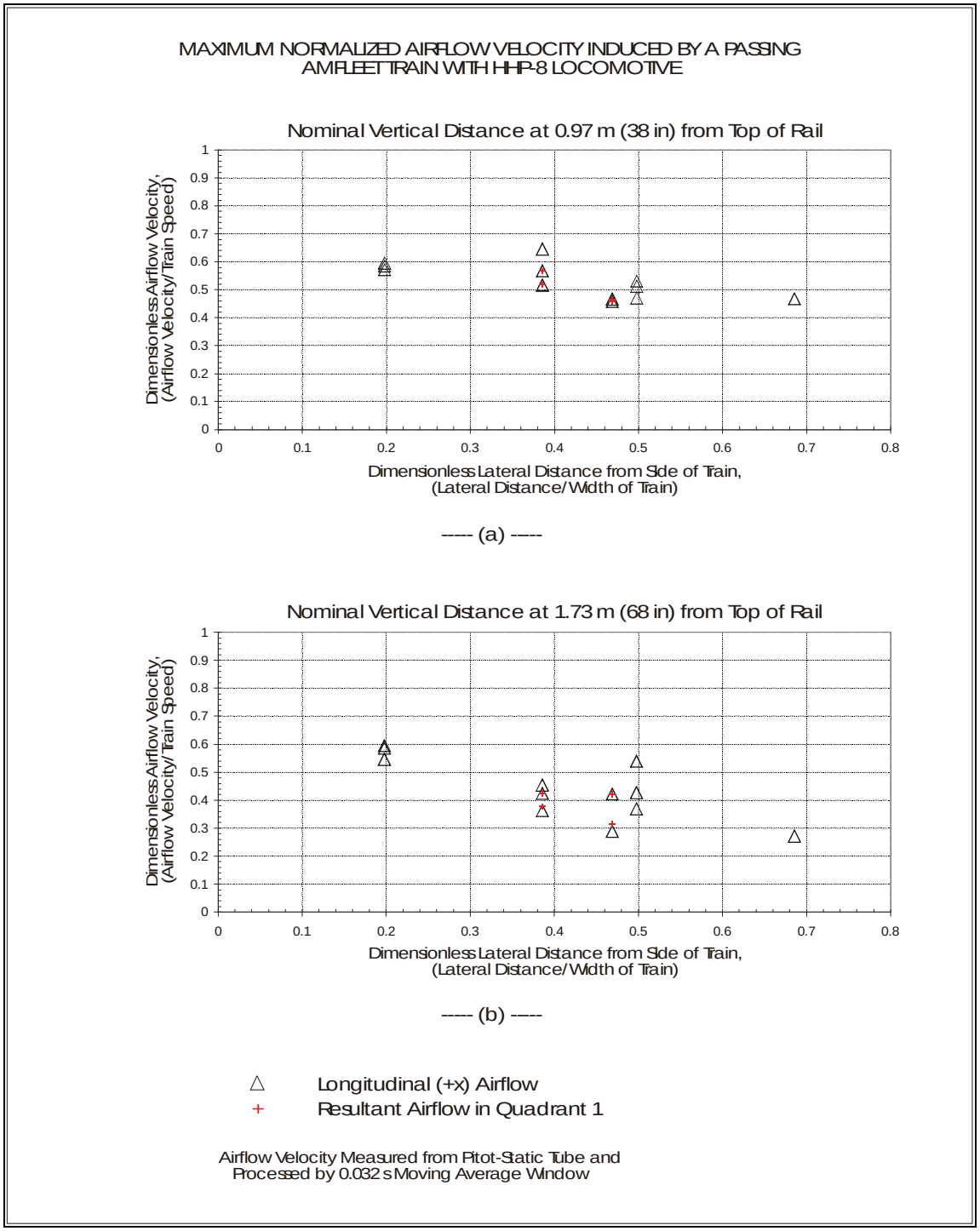

Figure 54. Maximum Airflow Velocities from Passing Amfleet Trains with HHP-8 Locomotives

9.3. Force on a Body

Another method to characterize the effect of aerodynamic interaction with a passing train is to measure the force on a cylindrical body alongside the track. Examples of forces on CID-5 as time history plots are illustrated for the three types of trains. Drag on a circular cylinder was also computed from airflow velocity data and compared with the force measured directly on the CID. Also, the drag was computed for a body with the same projected area as the cylinder but with constant drag coefficient. This provides an estimate on the extent that the force from a circular cylinder can represent the drag on a human body.

The forces applied to the CID in the longitudinal and lateral directions share certain similar characteristics between the different trains as shown in Figure 55(a), Figure 56(a), and Figure 57(a). As the head of the train passes, the longitudinal component of force pushes the CID in the same direction as the passing train and is immediately followed by a pull in the reverse direction. After the head of the train passes and for the remainder of the passing train, the CID is primarily being pushed in the same direction as the passing train. In the lateral direction, the force initially pushes the CID away from the train immediately followed by a pull toward the train, as the head of the train passes by. Afterwards, the CID is pushed and pulled oscillating about zero for the remaining train passage.

Whereas certain characteristics in the force are similar to all the passing trains tested, distinctive signatures between the different trains also exist. This is illustrated by the resultant forces on the CID shown in Figure 55(b), Figure 56(b), and Figure 57(b). For the passing Acela Express train, the force on the CID increases to a peak toward the tail of the train and remains high beyond the tail end, only slowly decreasing further into the wake. This is in contrast to the force on the CID from the passage of the Amfleet/AEM-7 train where the force rises immediately from the head of the train, and remains at a high level until at the tail end where it decreases, then dropping to a very small level at the wake. The signature of the force on the CID from the Amfleet/HHP-8 train has similarities with both of the other two trains. The force increases from the head toward the tail, begins to drop before the tail end, and generates a very low force at the wake. In all these trains, very prominent peak forces occur, especially at the head end and toward the tail end, with the highest peak force produced at the tail end by the tapered base Acela Express train (rearward-facing tapered nose) and at the head end by the bluff nose AEM-7 locomotive.

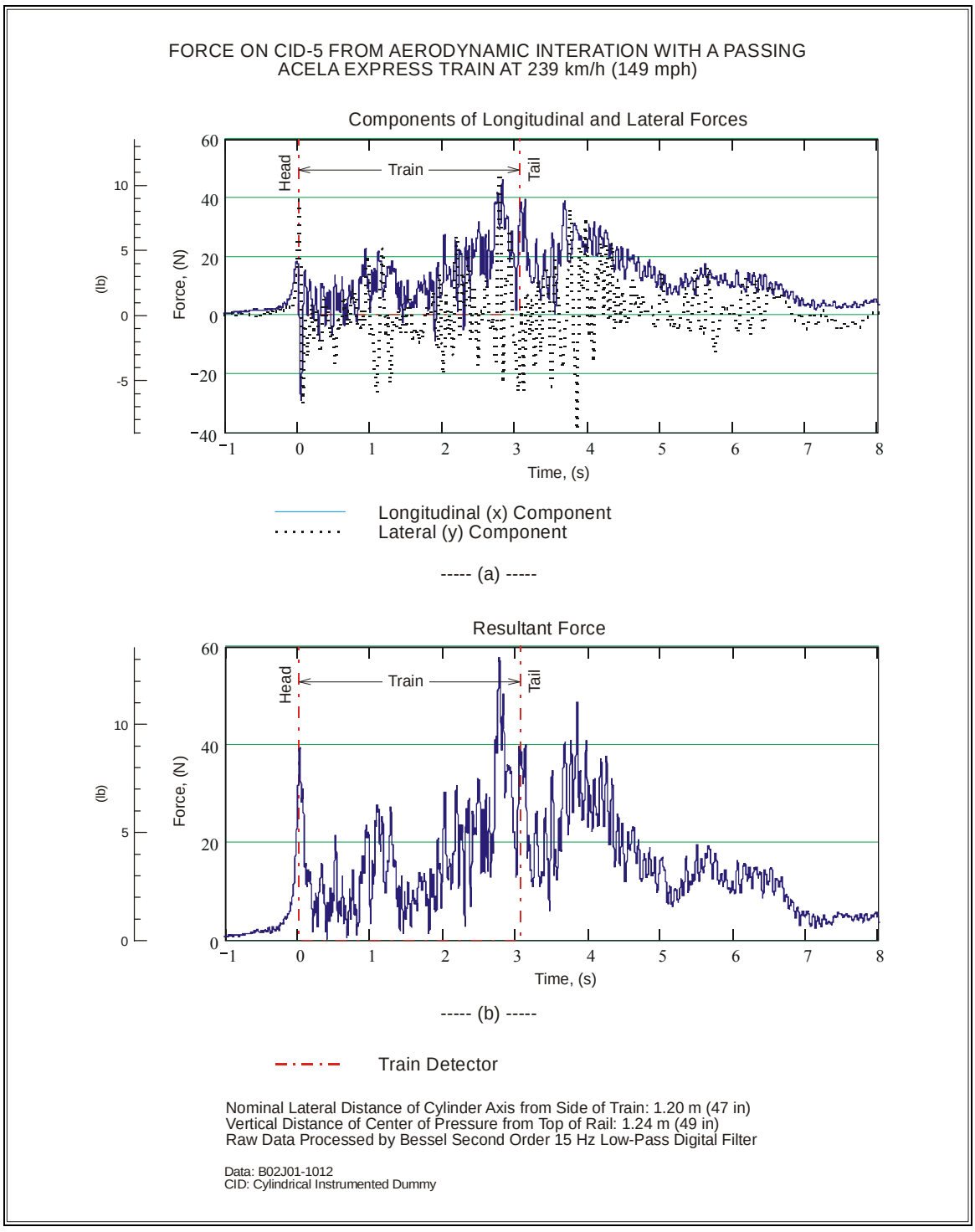

Figure 55. Time Histories of Forces on a CID from a Passing Acela Express Train

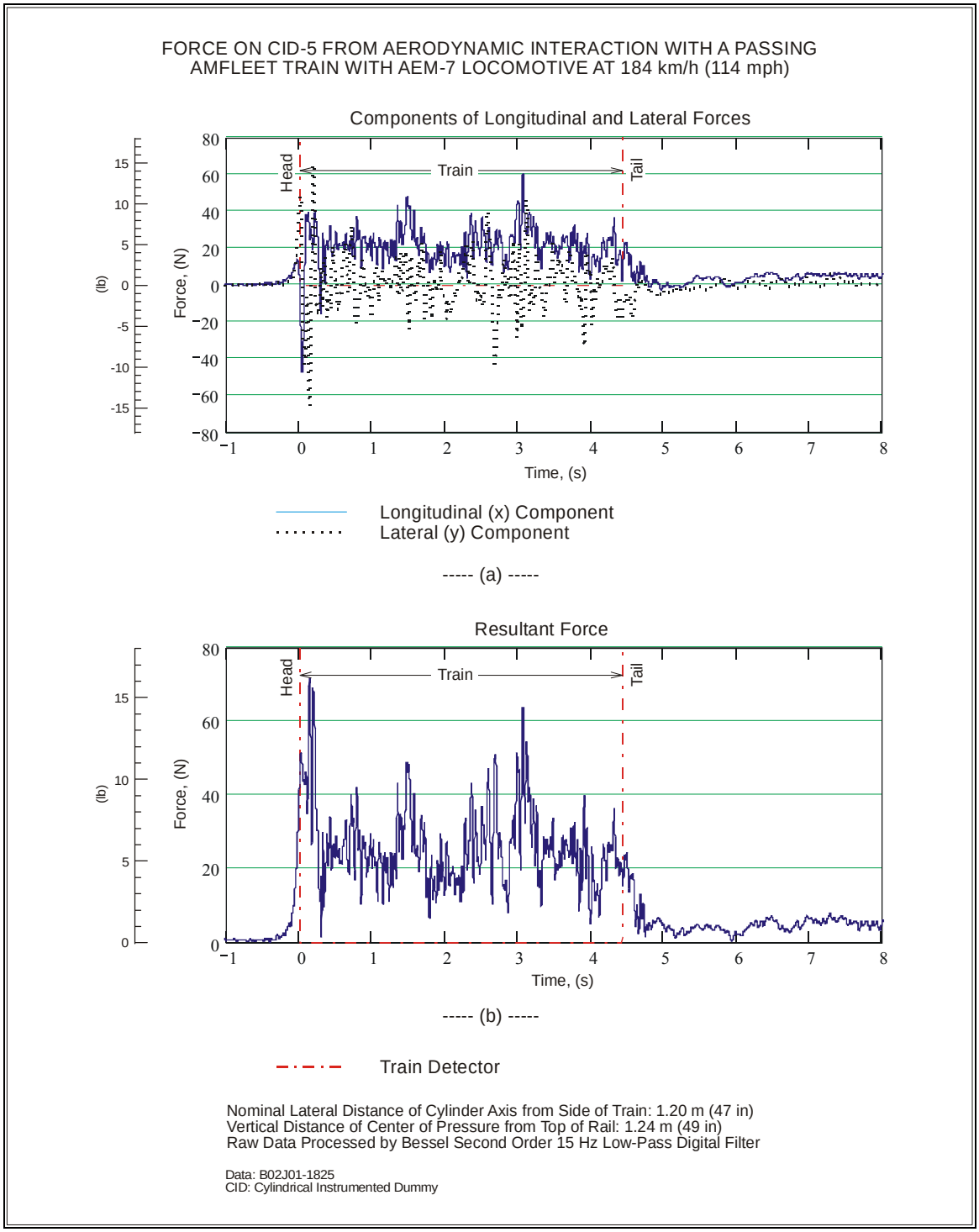

Figure 56. Time Histories of Forces on a CID from a Passing Amfleet Train with AEM-7 Locomotive

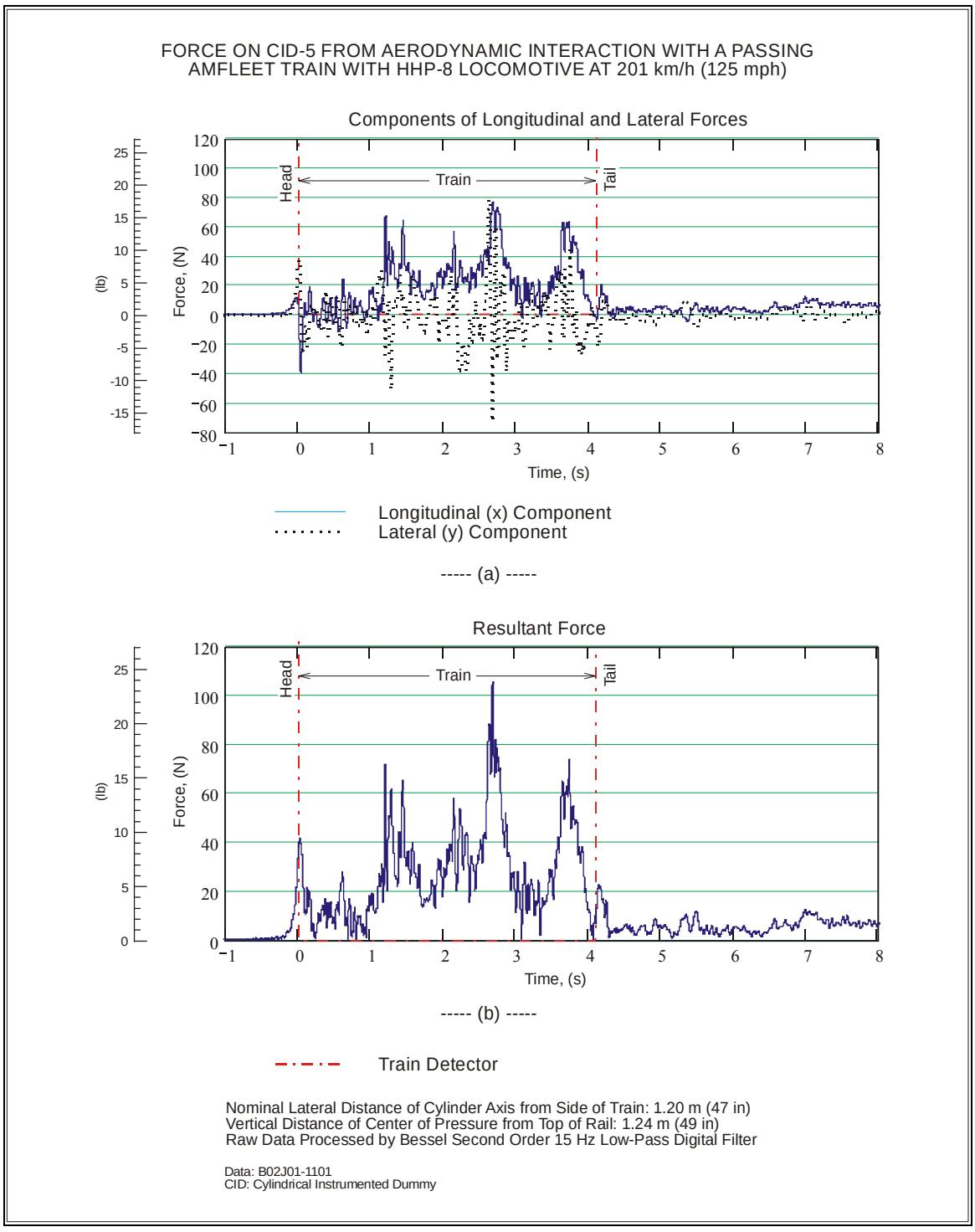

Figure 57. Time Histories of Forces on a CID from a Passing Amfleet Train with HHP-8 Locomotive

The force measured on the CID is compared with the computed drag on a circular cylinder with the same dimensions as the CID. The drag on a cylinder was computed from the resultant airflow velocity at quadrant 1 with the airflow velocity measured at the same nominal location as the CID. To make corresponding comparisons between the measured force on the CID and the drag computed on a cylinder, both are processed by a Bessel second order 15 Hz low-pass filter, and only the resultant force from the CID that belongs to quadrant 1 was retained. The force measured from the CID and the drag computed on a cylinder are shown plotted in Figure 58(a), Figure 59(a), and Figure 60(a) for the three types of trains. The CID-measured force is higher in magnitude and frequency and with greater peak-to-peak fluctuations, than from the computed cylinder drag. Next, the forces were processed by a 1 s moving average window to filter out the lower frequencies, which provided a clearer trend as shown in Figure 58(b), Figure 59(b), and Figure 60(b). These results show the CID force is generally higher than the computed cylinder drag. Although in some locations, mostly in the wake region, the computed cylinder drag does exceed the CID force.

The CID was designed to be representative of the trunk of a human being. Below the critical Reynolds number, the drag coefficient on a circular cylinder is about the same as for a human body, which is about 1.2 based on projected frontal area. Once the critical Reynolds number is reached, the drag coefficient is reduced to about 0.3, and the drag on a circular cylinder may not be a good representation of a human body. To determine this effect, the force measured from the CID is compared to the drag computed for a body with the same projected area as the CID but with a constant drag coefficient of 1.1, which is more representative of a human body. The body with a constant drag coefficient will be referred to as a flat body, and approximates the drag on a human trunk (scaled to the size of the CID) assuming that the drag coefficient on a human body remains constant over the range of Reynolds numbers.

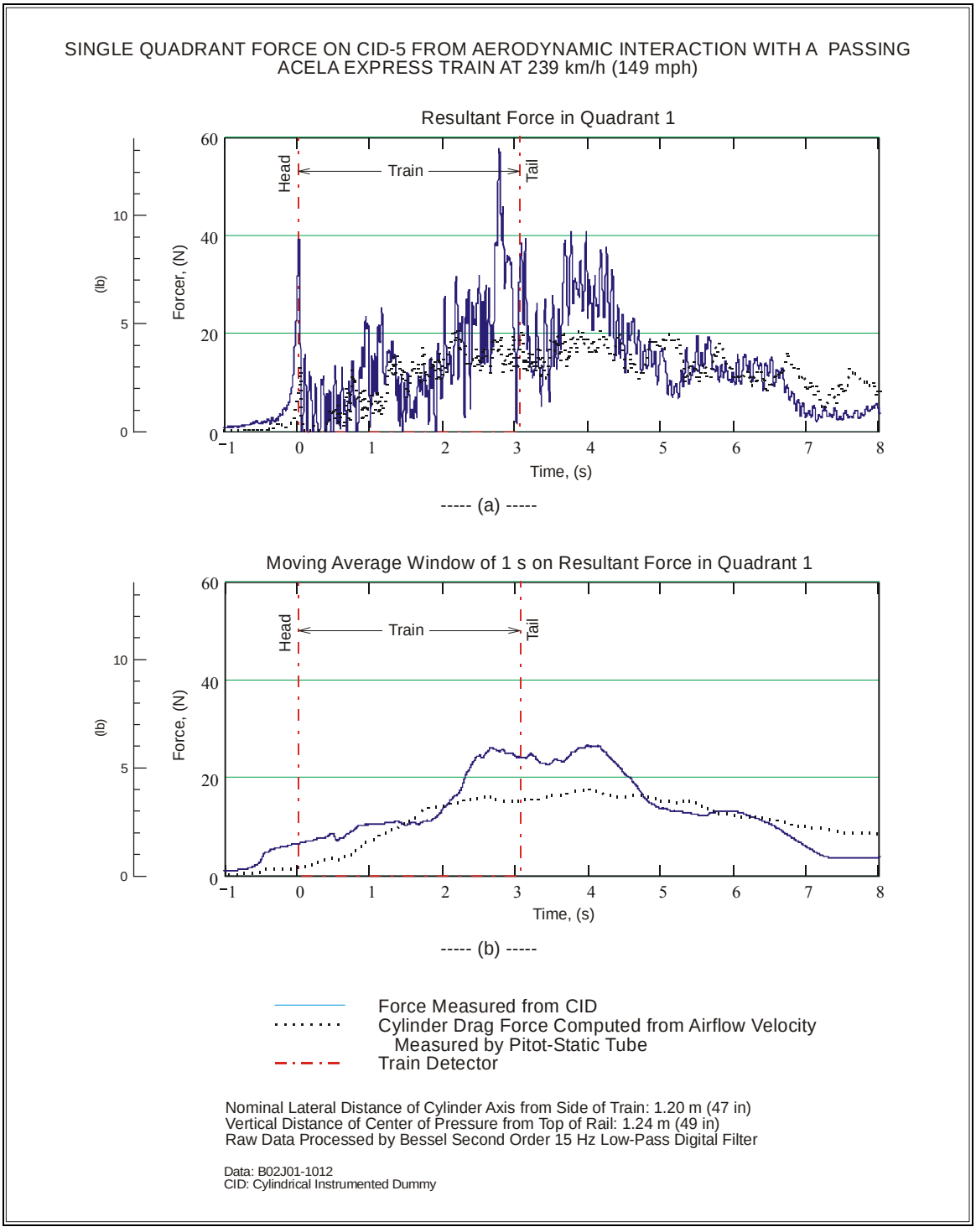

Figure 58. Time Histories of Single Quadrant Forces Measured on a CID and Computed from Airflow Velocity from a Passing Acela Express Train

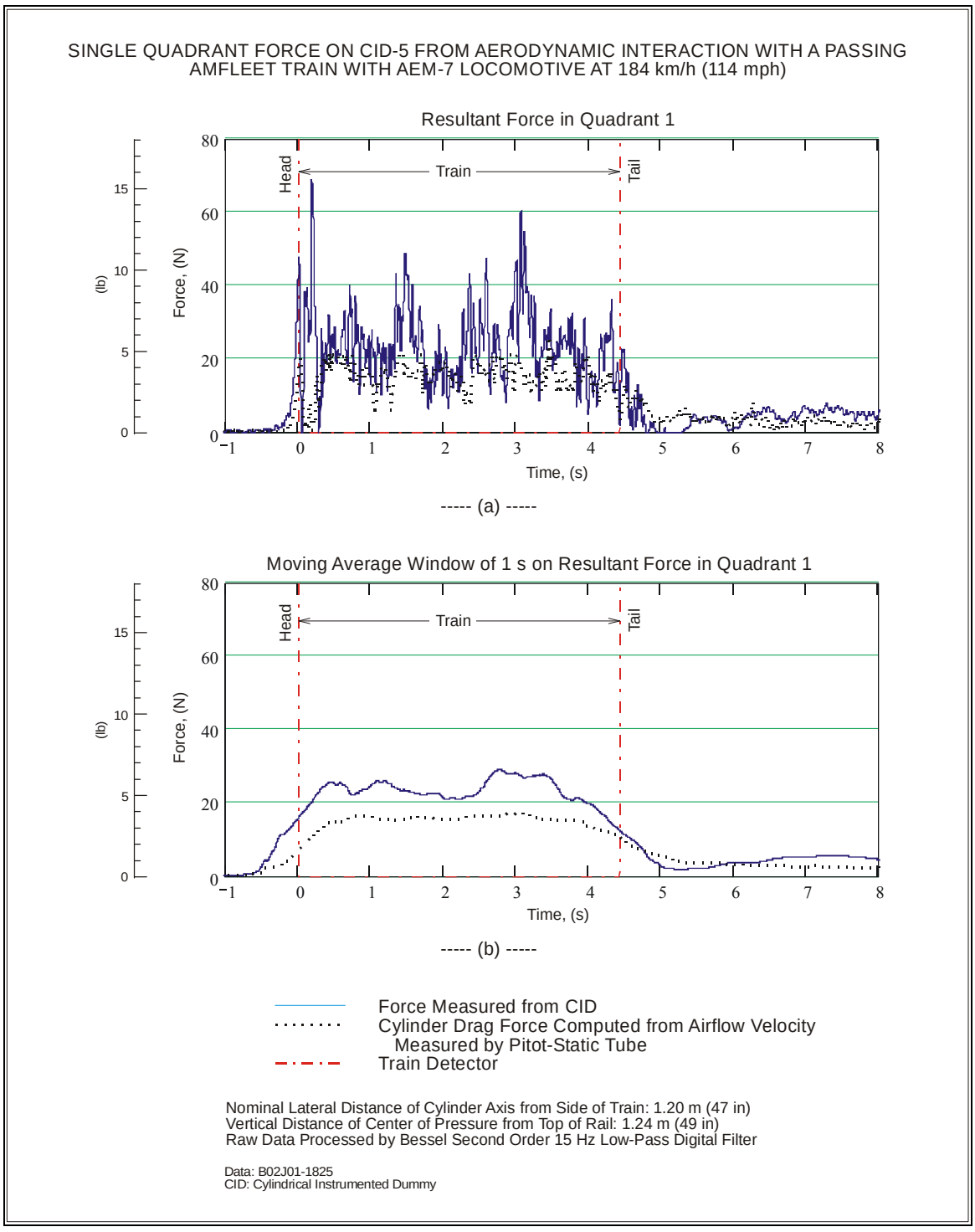

Figure 59. Time Histories of Single Quadrant Forces Measured on a CID and Computed from Airflow Velocity from a Passing Amfleet Train with AEM-7 Locomotive

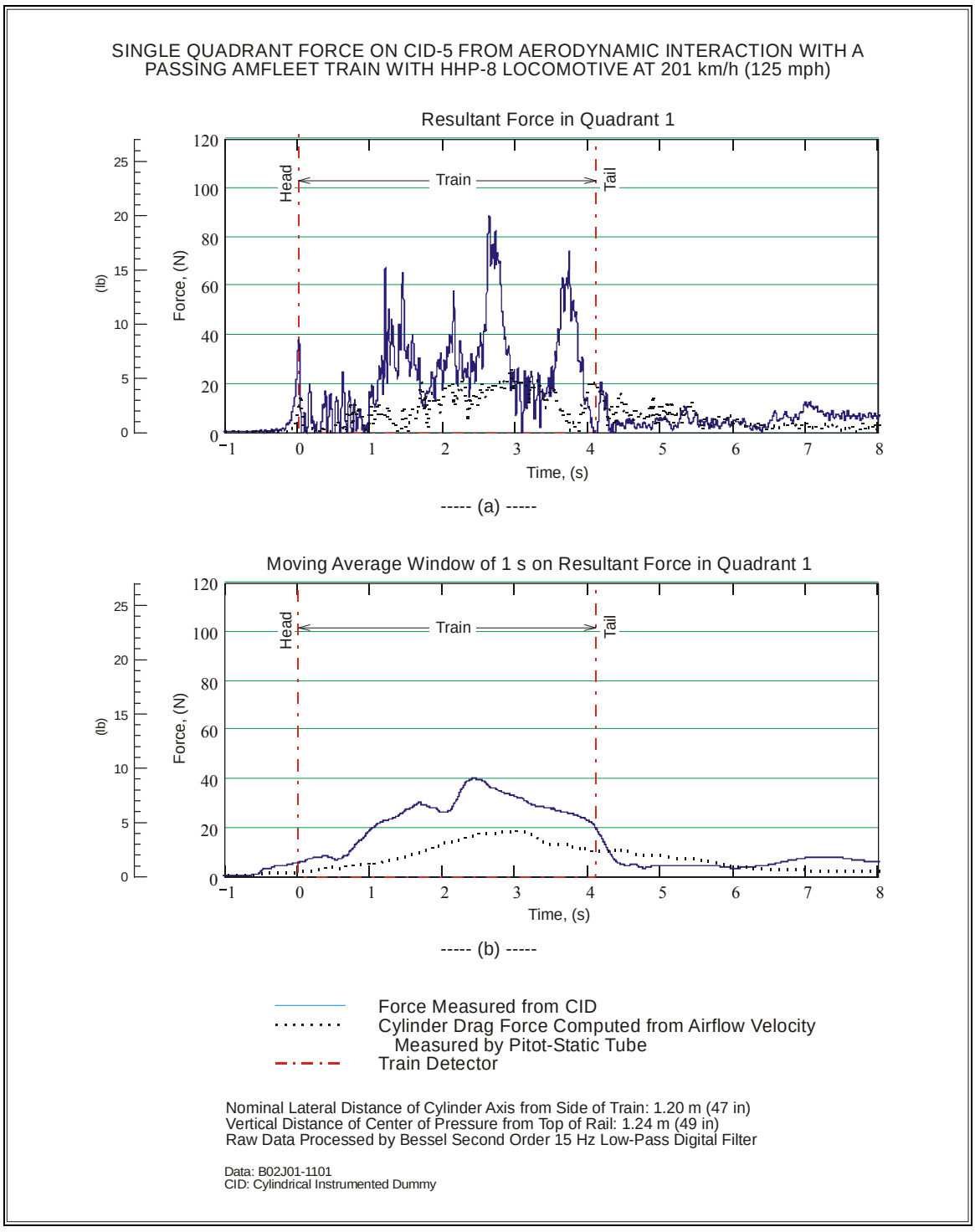

Figure 60. Time Histories of Single Quadrant Forces Measured on a CID and Computed from Airflow Velocity from a Passing Amfleet Train with HHP-8 Locomotive

The single quadrant force measured from the CID is compared with the drag on a flat-body computed from measured airflow velocity. For the three types of passing trains, the computed drag on the flat-body is in general considerably higher than those computed for a circular cylinder, and is also generally higher than the force measured from the CID (Figure 61(a), Figure 62(a), and Figure 63(a)). Next, the forces were processed by a 1 s moving average window to remove the higher frequencies to better view the trend as shown in Figure 61(b), Figure 62(b), and Figure 63(b). Although the flat-body drag is generally higher than the measured CID force along the length of the train, forces from both bodies diminished to about the same level in the wake region for the Amfleet/AEM-7 train. However, the flat-body drag remains consistently higher than the CID force in the wake region of the Acela Express train. This is likely due to the high airflow velocity in the wake of the Acela Express train, which is at the critical Reynolds number for a circular cylinder where the variable drag coefficient remains low. Therefore, the circular cylinder produces a lower drag on the CID than on a flat body where the drag was computed with a constant higher drag coefficient. Finally, the flat-body drag and CID force from the Amfleet/HHP-8 train share similar characteristics with the other two trains.

These results are consistent with those from the RAPIDE study, which states that,

> Comparison between and instrumented cylinder and an instrumented mannequin showed extremely different results, both in magnitude of response and in response to different slipstream events.
>
> …a cylinder is not a very good representation for a person. Its drag coefficient varies by a factor of three over the wind speed range of interest…Its symmetry about the vertical axis generates a larger pressure differential between the front and back surfaces than does that of the more elliptical cylinder-shape of a human. This causes a larger difference in force due to the train pressure field….
>
> …The cylinder that was tested only responded strongly to the static pressure effects of the train passing. It did not react significantly to the dynamic wake velocity….The results suggest that it is effectively measuring a pressure phenomenon. (RAPIDE 2001)

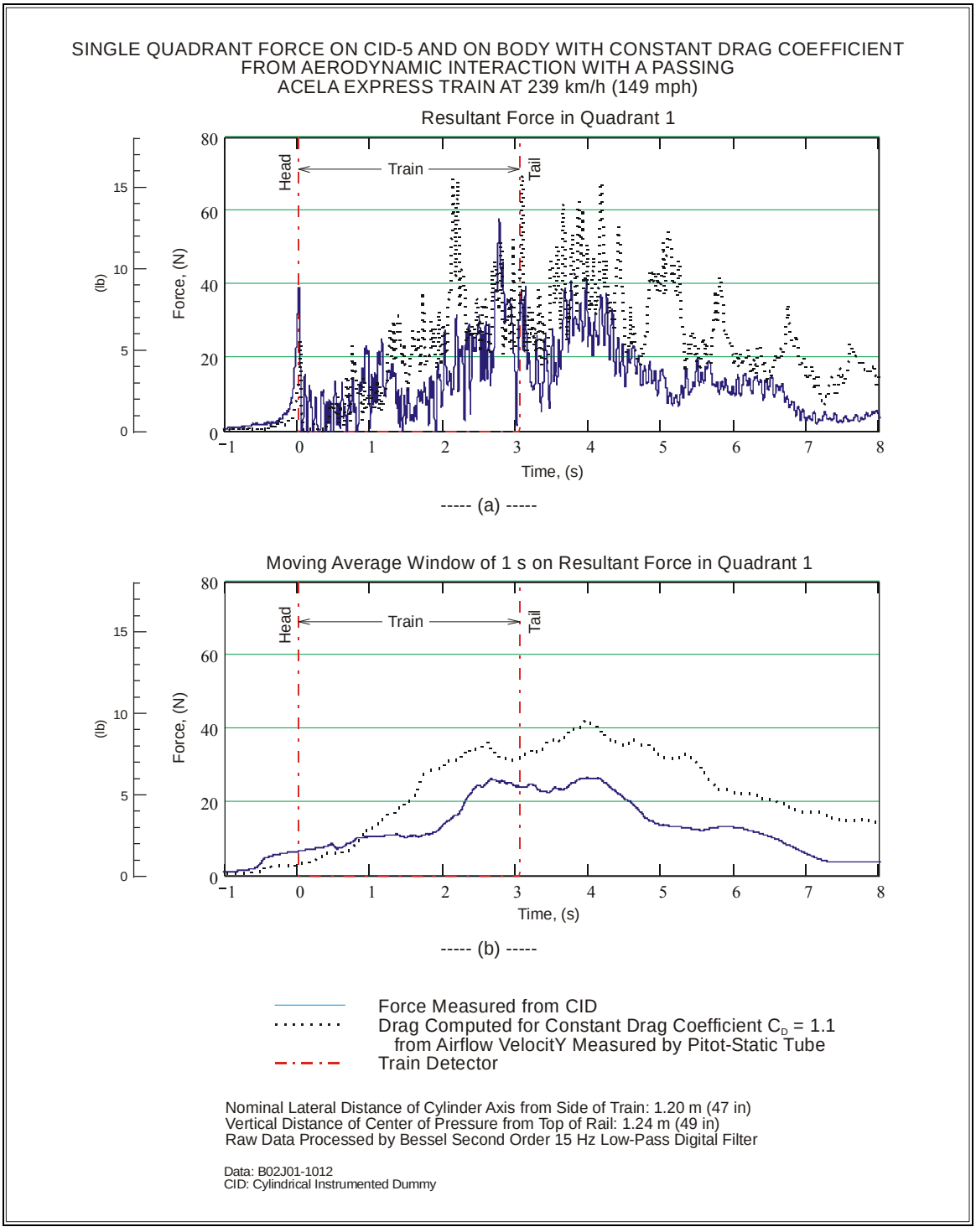

Figure 61. Time Histories of Single Quadrant Forces Measured on a CID and Computed with Constant Drag Coefficient from a Passing Acela Express Train

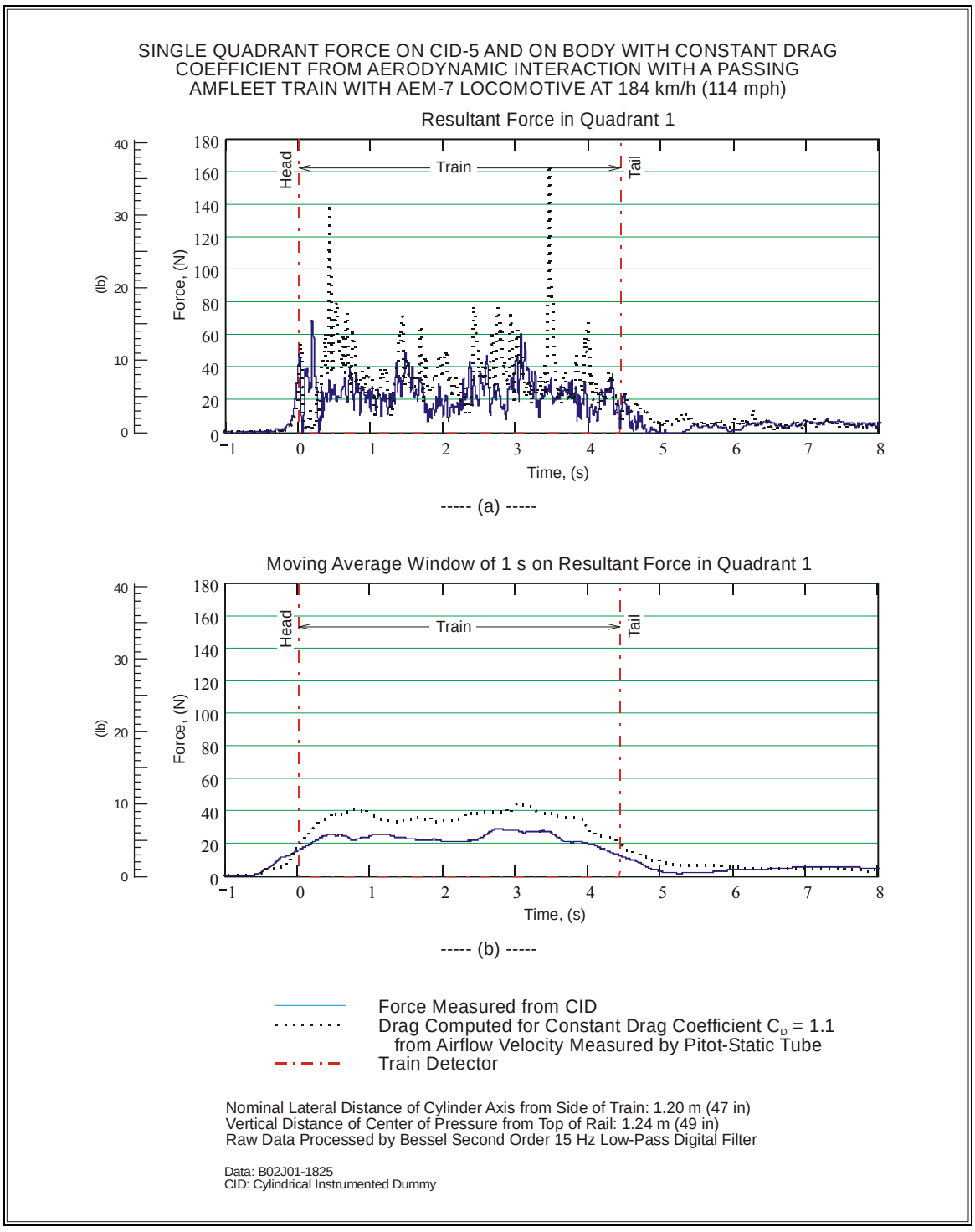

Figure 62. Time Histories of Single Quadrant Forces Measured on a CID and Computed with Constant Drag Coefficient from a Passing Amfleet Train with AEM-7 Locomotive

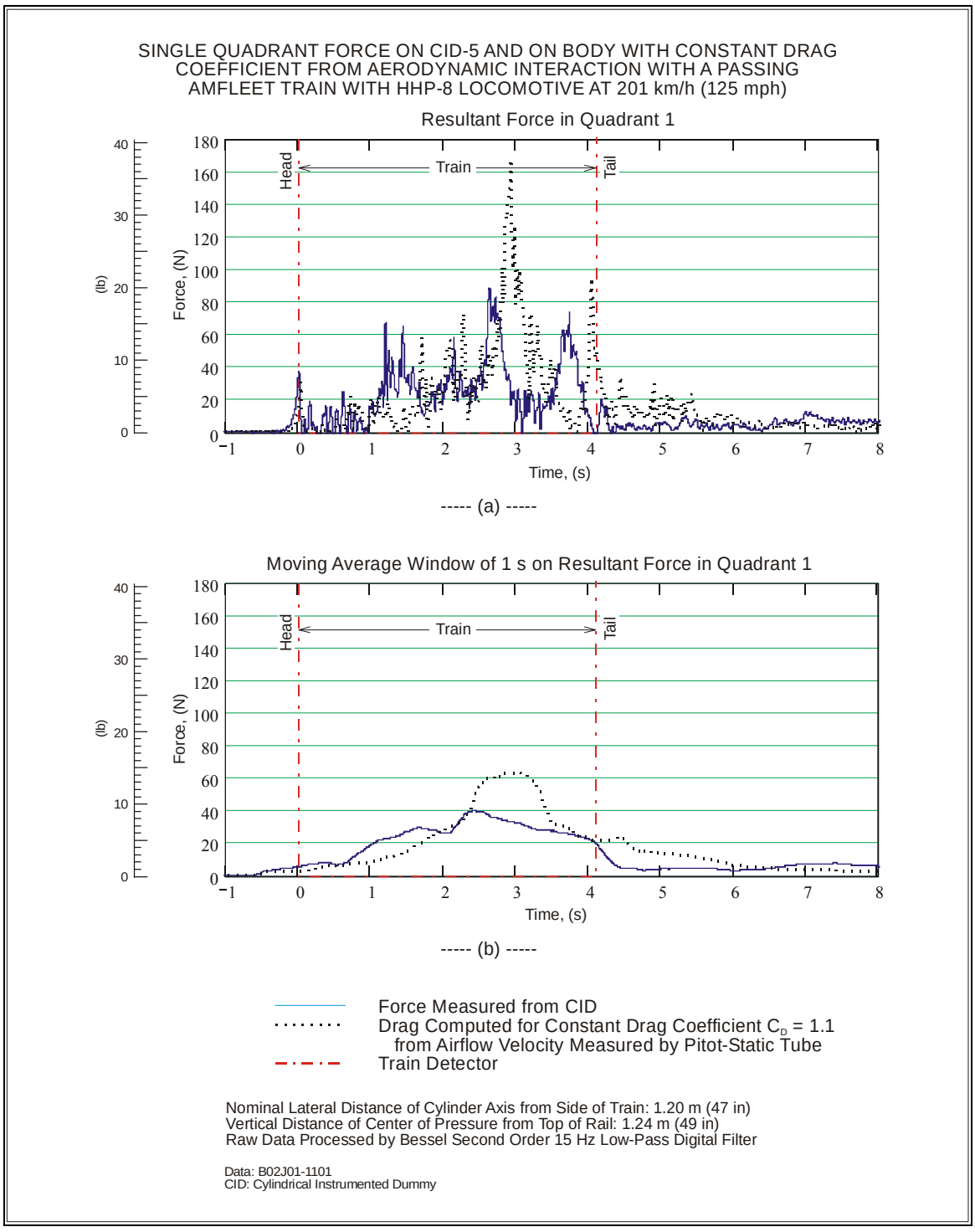

Figure 63. Time Histories of Single Quadrant Forces Measured on a CID and Computed with Constant Drag Coefficient from a Passing Amfleet Train with HHP-8 Locomotive

Although differences exist in relative magnitudes between the drag computed on a circular cylinder from the train-induced airflow velocity and the force measured on a CID from its aerodynamic interaction with the passing train, the general trend is the same. The time history signatures from airflow velocity and CID force for the different passing trains are similar. Both types of measurements indicate that the dominant airflow and force on the cylinder is primarily the longitudinal component in the direction of the passing train.

9.4. Human Exposure Limit to Train-Induced Airflow Referenced to Wind Speed Criterion

Airflow velocity referenced directly to a wind speed criterion is one approach to determine the aerodynamic effects of a passing train on people alongside the track. Another method based on the effects of airflow velocity on the stability of a mathematical mannequin will be discussed in the next chapter. In this section, wind speed criteria obtained from two different processes were applied to determine their suitability for evaluating the effect of train-induced airflow velocity on people.

9.4.1. Example Time History of Formulated Wind Speed

Airflow generated from a passing train is both transient and highly turbulent, and this factor must be considered in comparing the airflow velocity with any criterion relating wind speed to its effect on people. Two different wind speed criteria that were discussed in Part 1 were applied to the airflow induced by a passing train. One of the criteria that accounts for gusty wind was proposed by Hunt, Poulton, and Mumford (1976). They calculated an estimated equivalent steady wind speed for gusty wind conditions based on both an average wind speed and its turbulence intensity (Table 8). The duration window over which the average and fluctuating values are computed must be large enough to average the fluctuations effectively, but small compared to the time during which significant variations occur in the average value (Whitaker 1968). The turbulent fluctuation was computed as a deviation from a mean airflow velocity that was averaged over a 30 m (98 ft) averaging window. The other criteria were by Murakami and Deguchi(1981), which are based on the wind speed averaged over a 3 s averaging window (Table 9).

The two different wind speed criteria are applied to the three example types of trains and their results are compared (Figure 64(a), Figure 65(a), and Figure 66(a)). All the data were scaled so that the time and airflow velocity for the Acela Express train corresponds to a train speed of 241 km/h (150 mph). In the case of the Amfleet train, the data was scaled to correspond to a train speed of 201 km/h (125 mph). Two of the curves were processed from moving averages with averaging windows of 0.032 s and 3 s, while the third curve was computed from Hunt's formulation on the equivalent steady airflow velocity for gusty conditions. The airflow velocity processed from the moving average window of 0.032 s serves as the baseline for the raw data. The maximum airflow velocities for these three processes and the three different trains are shown in Table 29. Hunt's criteria predict that the airflow velocity for all three trains in these examples exceed the safe walking speed of 20 m/s (45 mph). By applying the Murakami and Deguchi criteria, both the Acela Express and the Amfleet/HHP-8 train induced airflow velocities between 10 to 15 m/s (22 to 34 mph) in which walking is difficult to control. The airflow velocity induced by the Amfleet/AEM-7 train is over 15 m/s (34 mph), which makes walking impossible to control.

Table 29. Maximum Train-Induced Airflow Velocities Derived from Different Processes

Train	Scaled Train Speed	Airflow Velocity		
		Moving Average Window of 0.032 s	Equivalent Steady Wind for Gusty Conditions*	Moving Average Window of 3 s**
Acela Express train (B02J01-1012)	241 km/h (150 mph)	22.6 m/s (51 mph)	23.7 m/s (53 mph)	12.5 m/s (28 mph)
Amfleet train with AEM-7 locomotive (B02J01-1825)	201 km/h (125 mph)	34.5 m/s (77 mph)	31.7 m/s (71 mph)	16.2 m/s (36 mph)
Amfleet train with HHP-8 locomotive (B02J01-1101)	201 km/h (125 mph)	31.6 m/s (71 mph)	35.3 m/s (79 mph)	14.5 m/s (32 mph)

*Formulation of equivalent airflow velocity for wind speed criteria of Hunt, Poulton, and Mumford.
**Average airflow velocity over 3 s for wind speed criteria of Murakami and Deguchi.

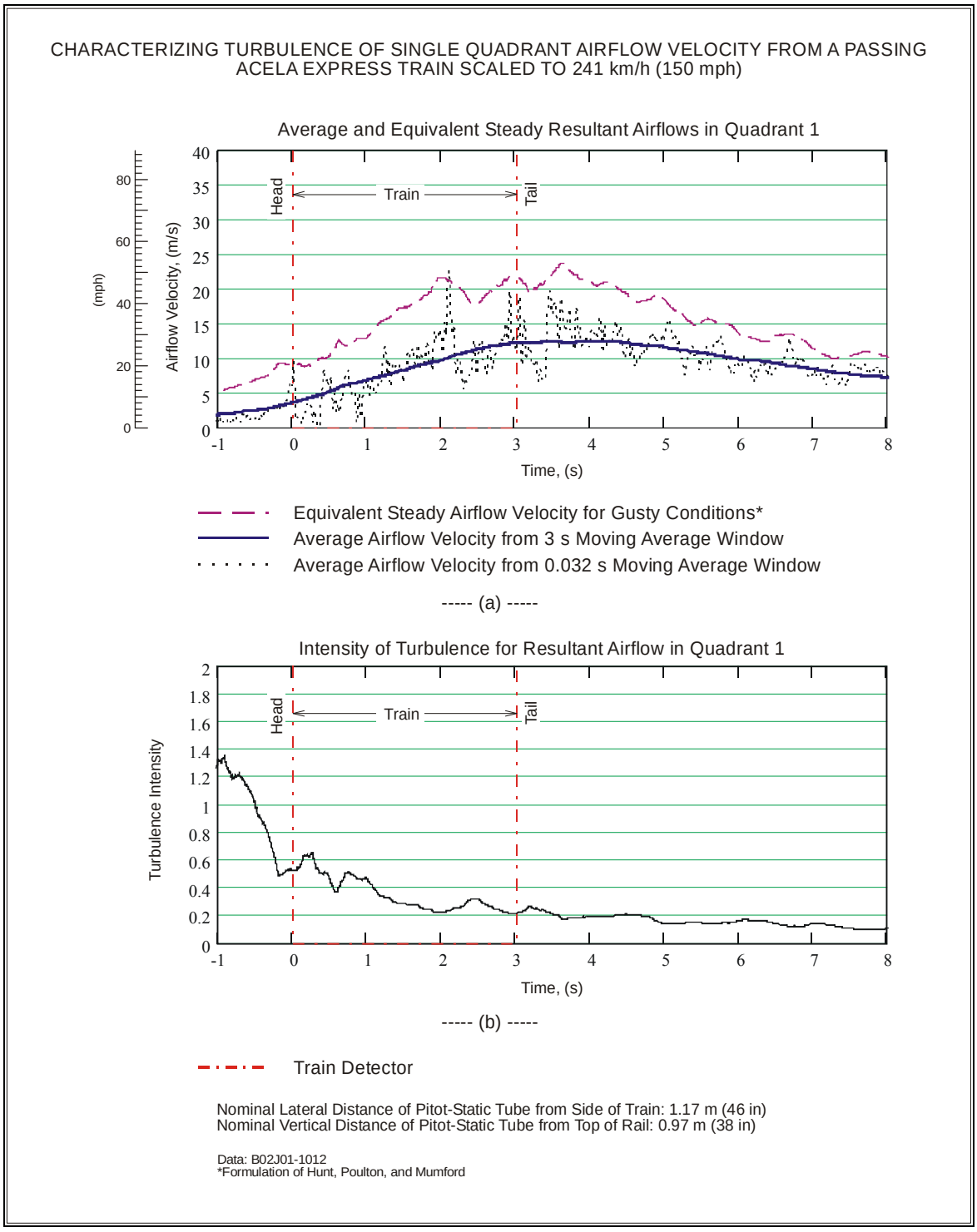

Figure 64. Time Histories of Single Quadrant Airflows Characterizing Turbulence from a Passing Acela Express Train

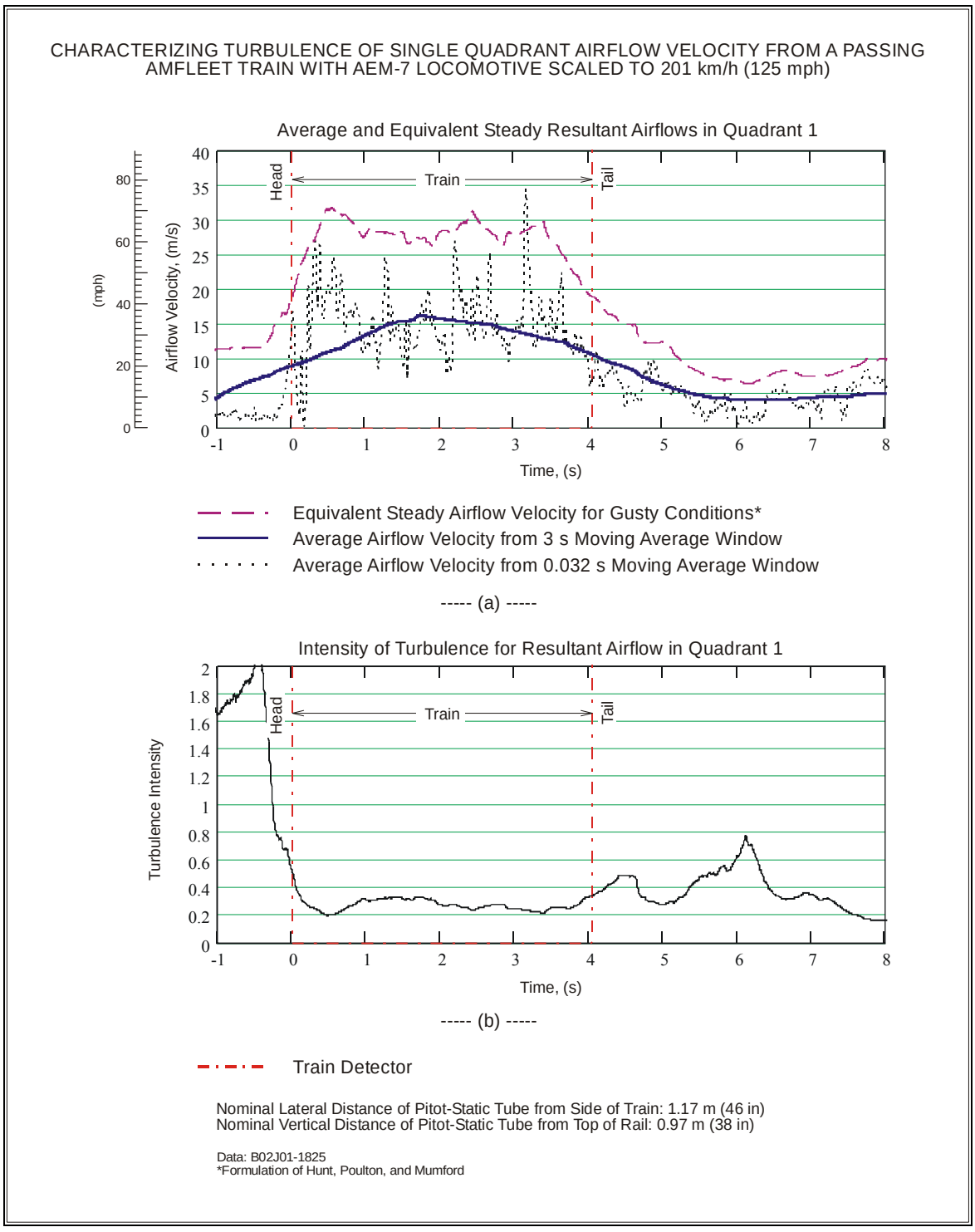

Figure 65. Time Histories of Single Quadrant Airflows Characterizing Turbulence from a Passing Amfleet Train with AEM-7 Locomotive

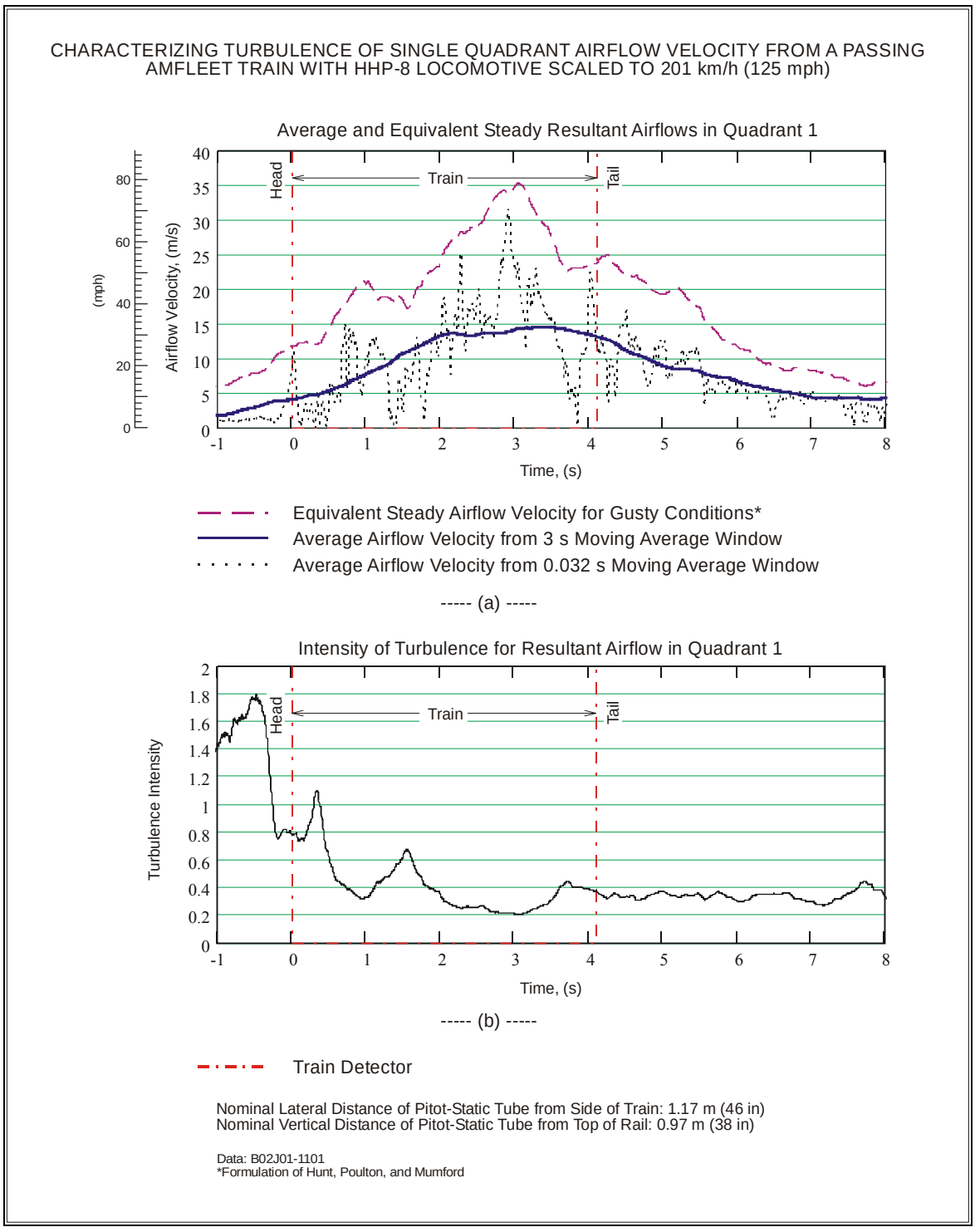

Figure 66. Time Histories of Single Quadrant Airflows Characterizing Turbulence from a Passing Amfleet Train with HHP-8 Locomotive

Whether the equivalent steady wind for gusty conditions computed from Hunt's formulation can be properly related to the airflow induced from a passing train remains uncertain. The equivalent steady wind is related to the turbulence intensity, which is about 0.14 (about the same amount of energy as in the natural wind) for airflow that was generated by the wind tunnel during their experiment (Hunt, Poulton, and Mumford 1976). However, the transient nature of airflow and the high turbulent fluctuation induced from a passing train can result in high turbulence intensity, especially at the nose region where the average airflow velocity is small (Figure 64(b), Figure 65(b), and Figure 66(b)). It is difficult to select a duration window sufficiently long enough to average the fluctuations effectively, but still small compared to the time during which significant variations occur in the average value. This is especially true near the head and tail ends of the train where rapid changes in average airflow velocities occur.

9.4.2. Minimum Distance from Passing Train

A relation between maximum longitudinal airflow velocity and lateral distance from the passing train was established from the data that was measured for the different types of passing trains. The maximum airflow velocity was computed from a 3 s moving average window, and scaled so that the airflow velocity for the Acela Express train corresponded to a train speed of 241 km/h (150 mph) and 201 km/h (125 mph) for the Amfleet train. The maximum airflow velocity is plotted from a 3 s moving average window at various lateral distances from a passing train at a nominal vertical distance of 0.97 m (38 in) from the top of the rail (Figure 67). A great deal of scatter occurs in the maximum airflow velocity because of the turbulent nature of the airflow as well as the varying types of trains. Plotted next is the maximum airflow velocity at a nominal height of 1.73 m (68 in) from the top of the rail where the induced airflow velocity is reduced at the increased height (Figure 68).

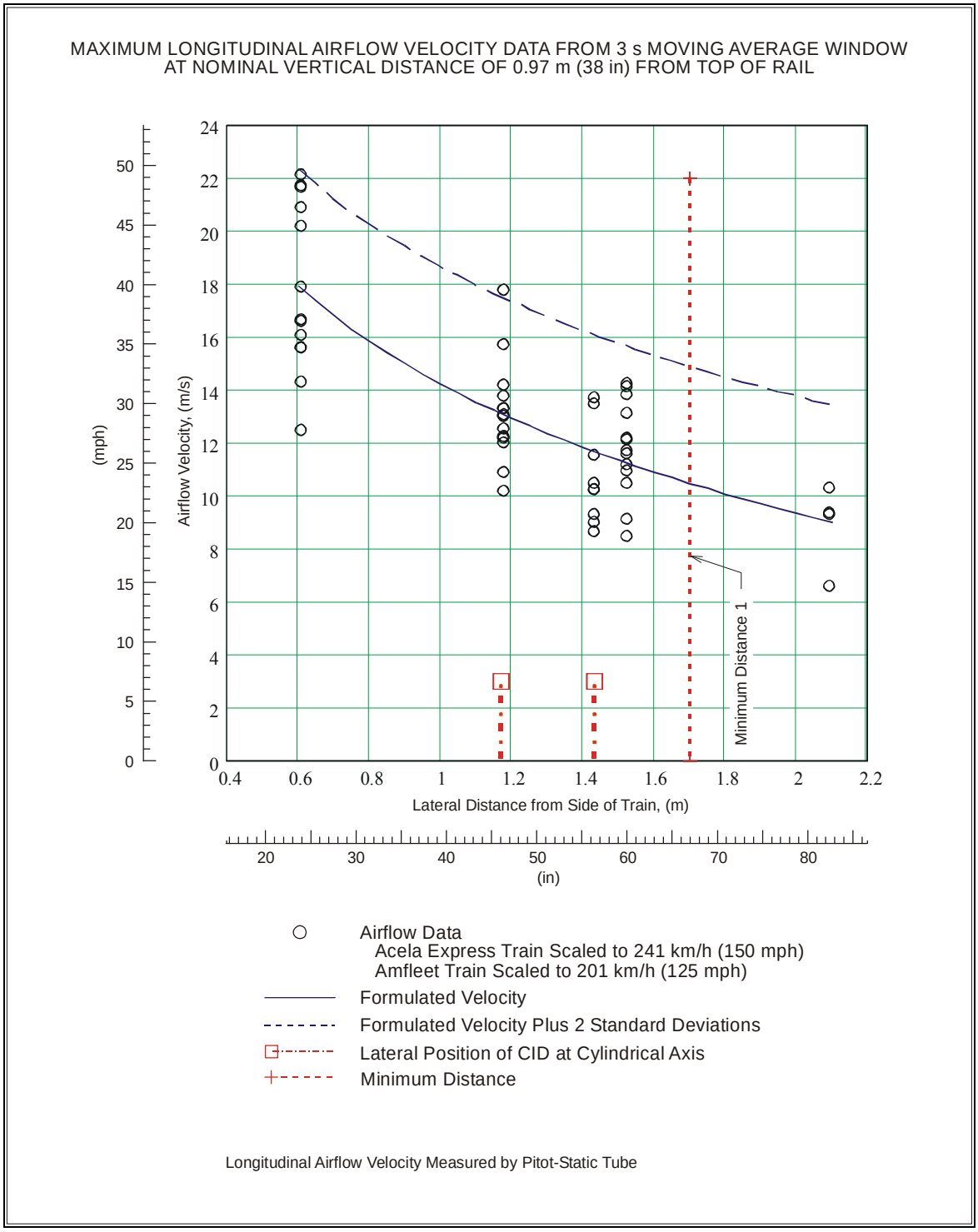

Figure 67. Train-Induced Airflow Velocity Data Measured at 0.97 m (38 in) above Top of Rail with Formulated Velocity Curves

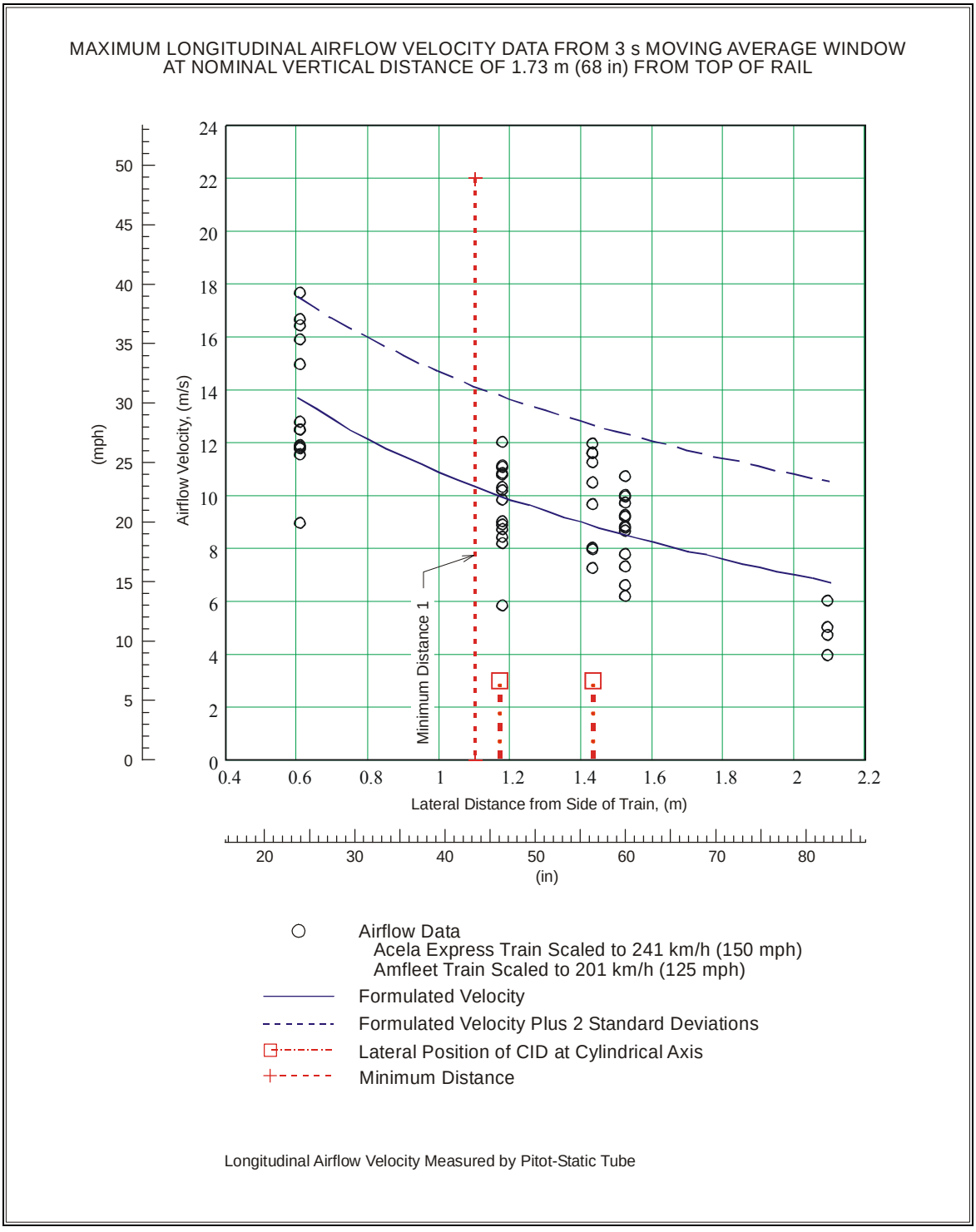

Figure 68. Train-Induced Airflow Velocity Data Measured at 1.73 m (68 in) above Top of Rail with Formulated Velocity Curves

A curve was fitted to the data by regression as a power function to obtain a continuous empirical relation between airflow velocity and lateral distance as follows,

$$\widetilde{u}_{\max-3s} = \left(A_O y_{train}^{k}\right) + U_O \qquad \textbf{Equation 8}$$

where,

$\widetilde{u}_{\max-3s}$: is formulated longitudinal airflow velocity.
y_{train}: is the lateral distance from side of a train.

The function for the formulated longitudinal airflow velocity, $\widetilde{u}_{\max-3s}$, represents the best fit to the maximum airflow velocity obtained from a 3 s moving average window as a function of lateral distance from the side of a train. Table 30 shows the values for the constants of the function that were computed by minimizing the error between the function and the data measured at the two heights of 0.97 m (38 in) and 1.73 m (68 in) from the top of the rail. These constants are valid for the data between the limits of lateral distances from the side of train of 0.60 m (24 in) and 2.1 m (83 in). This curve for the formulated velocity along with the curve for the formulated velocity plus 2 standard deviations are plotted with the measured airflow data (Figure 67 and Figure 68).

Table 30. Constants to the Formulated Velocity Regression Power Curve Fitted to Data for the Maximum Longitudinal Airflow Velocity over a 3 s Moving Average Window

$\widetilde{u}_{\max-3s} = \left(A_O y_{train}^{k}\right) + U_O$ m/s			
Nominal Height above Top of Rail	A_O	k	U_O
0.97 m (38 in)	1.952×10^{2}	-3.661×10^{-2}	-1.810×10^{2}
1.35 m (53)	1.065×10^{6}	-5.978×10^{-6}	-1.065×10^{6}
1.73 m (68)	1.155×10^{6}	-4.835×10^{-6}	-1.155×10^{6}

With the relation between lateral distance from the train and airflow velocity established, its effect on people can be estimated from the wind speed criteria of Murakami and Deguchi (1981). The effect is based on the wind speed averaged over 3 s. The effect of airflow on people is described at the two lateral positions corresponding to the locations of the CIDs. These two positions are indicated in Figure 67 and Figure 68 at nominal lateral distances of 1.17 m (46 in) and 1.43 m (56 in) from the side of the train. The formulated velocity plus 2 standard deviations corresponding to the two locations of the CIDs and at two heights of 0.97 m (38 in) and 1.73 m (68 in) are shown in Table 31. While the airflow velocity is lower at the CID location further away from the train, the magnitudes of the airflow velocities at both lateral locations are described relative to its effect on people as: walking can be impossible to control for airflow close to the ground, and walking can be difficult to control for airflow further from the ground.

Table 31. Formulated Longitudinal Airflow Velocities from 3 s Moving Average Window Corresponding to CID Positions

Nominal Height from Top of Rail	Nominal Distance from Side of Train	Airflow Velocity, $\tilde{u}_{\max-3s} + 2\sigma$
0.97 m (38 in)	1.17 m (46 in)	17.5 m/s (39 mph)
	1.43 m (56 in)	16.1 m/s (36 mph)
1.35 m (53 in)	1.17 m* (46 in)*	15.1 m/s* (34 mph)*
	1.43 m* (56 in)*	13.8 m/s* (31 mph)*
1.73 m (68 in)	1.17 m (46 in)	13.8 m/s (31 mph)
	1.43 m (56 in)	12.7 m/s (28 mph)

*Interpolated values.

The lateral distance from the train set by the limits of airflow velocity also depends on the height at which the airflow is referenced since the airflow velocity varies with height from the ground. If the airflow velocity is limited to 10 to 15 m/s (22 to 34 mph) where walking is difficult to control, based on airflow that is 0.97 m (38 in) above the top of the rail, this would require a distance of about 1.7 m (67 in) from the side of the train (Figure 67). If the requirement is based on airflow 1.73 m (68 in) above the top of the rail, the lateral distance is reduced to about 1.1 m (43 in) from the side of the train (Figure 68). These lateral distances are referred to as minimum distance 1.

People vary in height and shape, which affect their center of pressures. Furthermore, the height of the platform on which the person is standing can vary. Therefore, the center of pressure relative to the track can vary. Given these variations, a nominal height of 1.35 m (53 in) from the top of the rail is selected as the vertical location that is representative of the strength in the airflow that is experienced by an adult standing on a low-level passenger platform. This height references the airflow velocity that is slightly above the center of pressure of the human body for an average adult male when the person is standing on a low-level station platform that is at a height designed according to specification. This representative intermediate height also corresponds to the nominal location of the center of pressure of the CID.

Airflow velocity at 1.35 m (53 in) from top of the rail is estimated by linear interpolation from the airflow data measured at 0.97 m (38 in) and at 1.73 m (68 in) from the top of the rail (the interpolated airflow is also the average airflow since it is at the midpoint of the two measured values). The interpolated maximum airflow velocity at a nominal height of 1.35 m (53 in) from the top of the rail is shown plotted in Figure 69 along with the curve fitted to this data with new constants for the formulated velocity (Table 30). At this middle height, the magnitude of the airflow velocity at the lateral location of the CID closest to the train is described relative to its effect on people as walking can be impossible to control. Airflow velocity, occurring at the lateral location of the CID and further away from the train, has the effect on people described as "walking can be difficult to control."

Two minimum lateral distances from a passing train are indicated from two ranges of airflow velocities. In the first minimum distance (minimum distance 1), the exposure of airflow velocity is limited to a range of 10 to 15 m/s (22 to 34 mph), which is described relative to its effect on people as walking is irregular and difficult to control. This requirement is met at a nominal minimum distance of 1.2 m (47 in) from the side of a passing train. At this distance, the formulated velocity and the formulated velocity plus two standard deviations are both within the specified limiting airflow velocity range. A second minimum distance (minimum distance 2) is to limit the exposure of airflow velocity such that the formulated velocity is below 10 m/s (22 mph), which is described relative to its effect on people as walking with footsteps that are sometimes irregular. This requirement is met at a nominal minimum distance of 1.6 m (63 in) from the side of a passing train. At this distance, the formulated velocity is below 10 m/s (22 mph), while the formulated velocity plus two standard deviations is between 10 and 15 m/s (22 and 34 mph). These two minimum distances are shown in the graph of Figure 69. The results of all the minimum distances are summarized in Table 32.

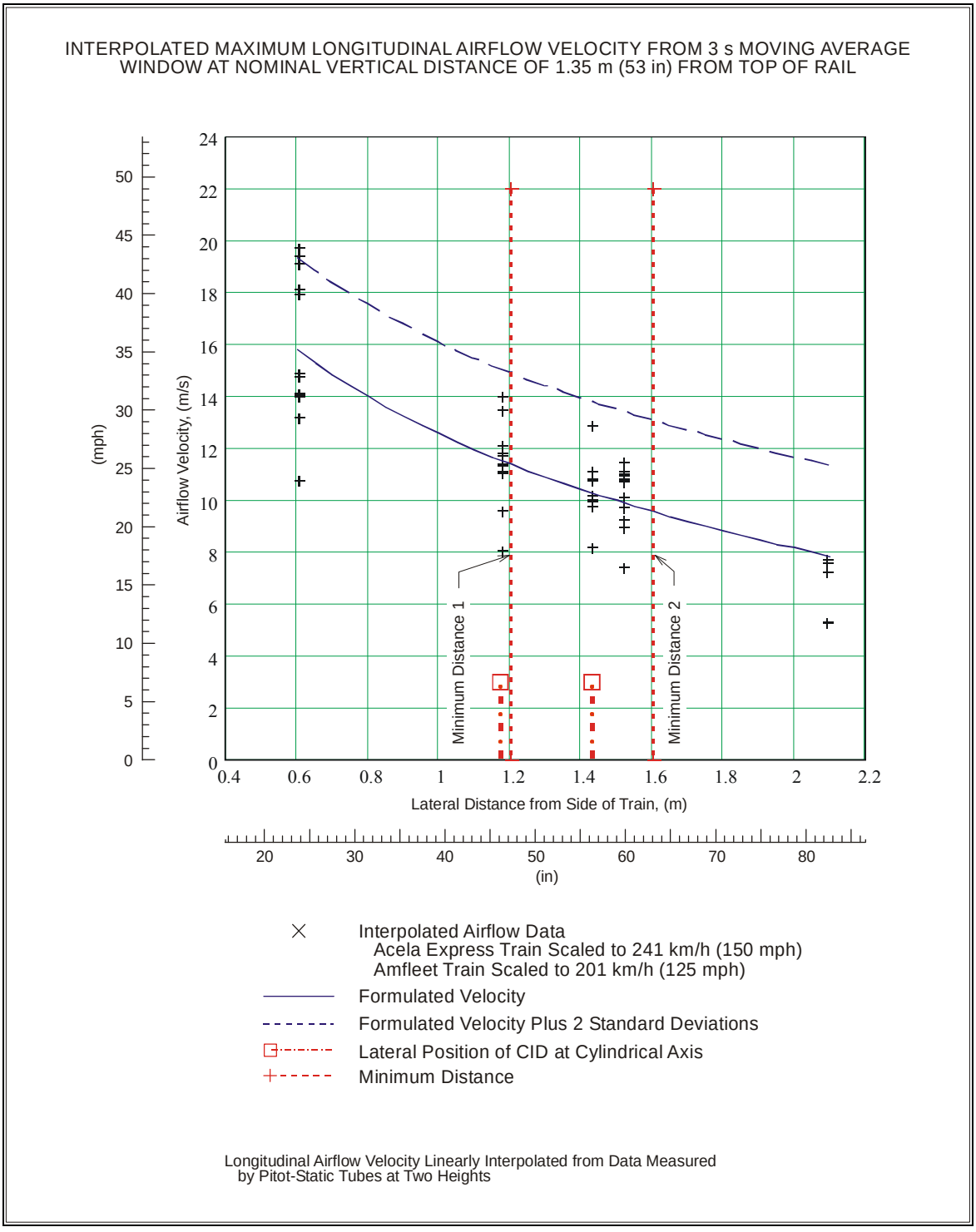

Figure 69. Interpolated Train-Induced Airflow Velocity Data at 1.35 m (53 in) above Top of Rail with Formulated Velocity Curves

Table 32. Minimum Distances from a Passing Train for a Person Exposed to Train-Induced Airflow Velocity

Nominal Height from Top of Rail	Location Number	Lateral Distance		Airflow Velocity	
		Distance from Outer Edge of Nearest Rail	Nominal Distance from Side of Train	$\tilde{u}_{\max-3s}$	$\tilde{u}_{\max-3s} + 2\sigma$
0.97 m (38 in)	Minimum Distance 1	2.43 m (96 in)	1.7 m (67 in)	10.5 m/s (23 mph)	14.9 m/s (33 mph)
1.35 m (53 in)	Minimum Distance 1	1.93 m (76 in)	1.2 m (47 in)	11.4 m/s (26 mph)	14.9 m/s (33 mph)
	Minimum Distance 2	2.33 m (92 in)	1.6 m (63 in)	9.5 m/s (21 mph)	13.1 m/s (29 mph)
1.73 m (68 in)	Minimum Distance 1	1.83 m (72 in)	1.1 m (43 in)	10.3 m/s (23 mph)	14.1 m/s (32 mph)

No airflow was measured at a height corresponding to an adult standing on a high level platform. The greatest height that was measured is 1.73 m (68 in) from the top of the rail. This is above the high level platform of 1.219 m (48 in) from the top of the rail, but below the center of pressure of an average adult standing on a high level platform. An estimate for a minimum lateral distance for a high level platform can be indicated from the airflow data measured at the greatest height (Figure 68) and limiting the exposure to a formulated velocity below 10 m/s (22 mph), and the formulated velocity plus two standard deviations below 15 m/s (34 mph). A minimum distance that satisfies this requirement is 1.2 m (47 in) from the side of the train. This estimate does not take into account the effect that the presence of the high level platform would have on the measurement of the airflow.

10. Human Response in Proximity to Passing Train

A person in proximity to a train passing at high speeds will experience a force from the aerodynamic effects of the train's passage. The person can respond both physically and psychologically to this event. There is the physical sensation of a force on the person's body, which the person can sense as a loss of balance if the force is of substantial magnitude. A passing train, because of its mass, size, noise, and speed, can also evoke a psychological response from a person. From a safety standpoint, the aerodynamic effects of a passing train should not cause a person to fall, be drawn closer toward the train, or create an unsafe condition such as being struck by propelling debris. The subjective experience will also be considered to provide a comprehensive picture of this human experience.

Human response to an external force on the body is complex, particularly when muscular action is involved. Many variables exist such as people of different heights, size, weight, physical strength, and psychological states. Different people can respond differently to the same event. The same person can respond differently to the same event at different times, depending on their attentiveness at the moment. Finally, added to the complexity of human response is the unsteady nature of the transient turbulent airflow induced by the passing train.

Although a complete human response to an external force is complicated, predictions can be made for a short time interval where the human body initially acts as a rigid body. Prevezer (2001), and Johnson, Dulley, and Temple (2002) described a mathematical model base on mechanical action to simulate human response from the application of a short duration force. A single degree-of-freedom mechanical human response model was used to predict human response for a period of about 0.35 s after application of force. The force applied to the body was a superposition of a mean wind speed and a sinusoidal pulse. A time-stepping solution was used to determine when the model would fall over from rotation. The mechanical model is appropriate only within about 0.35 s from the application of a sudden force. After time, subjective response is assumed to take place, and human response cannot be predicted mechanically.

A mannequin can be a useful tool in assessing the effects of wind on people if its dynamic response can be related to the long-established Beaufort scale. A simple single degree-of-freedom model can serve to illustrate the methodology, whose principle is similar to the previous use of detector pins that falls at a defined wind speed. The dynamic response of the mannequin may provide insight on the effects that wind force of varying magnitude and duration have on stability, particularly from a single strong gust over a short duration. Therefore, the mannequin model, when used in conjunction with the wind speed criteria of Murakami and Deguchi, can complement each other to provide a more adequate assessment on the effects of wind on human stability.

A mathematical model of a mannequin was created as an instrument to map the stability boundary for a simple standing object that can be applied to evaluate the aerodynamic data produced from a passing train. The mannequin stability model is a rigid body with dimensions and mass based on a human body. Impulsive force is applied to the body at various durations from which a relationship can be obtained between magnitude of impulsive force and duration of applied force to satisfy a given state of stability. The mannequin stability model is not intended to replicate the complex behavioral response of a human being, but it is a rigid inanimate object with the size and shape of a person. As such, it will provide a metric for the measured data that is valid for this rigid mannequin.

10.1. Property of Human Body

The stability boundaries will be developed for a mannequin based on properties for a human. Geometric and dynamic properties required to model a human include the mass, moment of inertia, center of mass, center of pressure, projected area, and drag coefficient. Some of these values were obtained from reference sources, whereas others had to be computed or estimated. Table 33 shows the weights, heights, and center of masses for a small, average, and large person (Diffrient, Tilley, and Bardagjy 1974).

Table 33. Properties of Nude Human Bodies (Diffrient, Tilley, and Bardagjy 1974)

Property	Gender	Size (Percentile)		
		Small (2.5)	Average (50)	Large (97.5)
Weight	Male	68.5 kg (151 lb)	78 kg (172 lb)	87.1 kg (192 lb)
	Female	60.3 kg (133 lb)	65.8kg (145 lb)	71.2 kg (157 lb)
Height	Male	1.615 m (63.6 in)	1.748 m (68.8 in)	1.880 m (74 in)
	Female	1.491 m (58.7 in)	1.615 m (63.6 in)	1.74 m (68.5 in)
Center of Mass	Male	0.879 m (34.6 in)	0.963 m (37.9 in)	1.046 m (41.2 in)
	Female			

The two properties of a human body that affect the wind force experienced by a person are the body's drag coefficient and the projected area. Penwarden, Grigg, and Rayment (1976) described a wind tunnel experiment that measured the wind drag on people, from which drag coefficients, and the relationship of their projected area to total surface area were obtained. The measurements were performed for a wide range of people wearing

different types of clothing. Each person's weight and height were measured, and grouped according to the type of clothes that were worn. Once the ratio of a person's projected areas to total surface areas is established, the projected areas can be estimated from the formula of DuBois and DuBois (1916a, 1916b), which relates a person's total body surface area to weight and height as follows (converted to present system of units (Penwarden, Grigg, and Rayment 1976)):

$$A_{Du} = 0.0769 \times (mg)^{0.425} x(L_h)^{0.725},$$

where,

A_{Du}: total body surface area, (m),
mg: weight, (N), and,
L_h: height, (m),

The results for a human body's projected area to total surface area ratios and its drag coefficient with various types of clothing are shown in Table 34. Hill (1928) reported a wind tunnel test using an unclothed scaled model to measure the air resistance of a man. A drag coefficient was computed from the test data to be 0.98 for a nude man in the erect position facing the wind (Penwarden, Grigg, and Rayment 1976). These drag coefficients are all in the range determined by Horner (1958). The drag coefficients for a standing person are between 1.0 and 1.3, and 5 to 10 percent less without clothing.

Table 34 Human Body Drag Characterization from Wind Tunnel Measurement at a Wind Speed of 8.5 m/s (19 mph) (Penwarden, Grigg, and Rayment 1976)

Category	Frontal Area Ratio, A_f/A_{Du}	Side Area Ratio, A_s/A_{Du}	Frontal Drag Coefficient, C_{Df}	Side Drag Coefficient, C_{Ds}
Skirt with shirt, sweater or buttoned jacket.	0.30	0.21	1.08	0.95
Skirt with shirt, sweater or buttoned jacket, carrying bag or clothing.	0.32	0.23		
Skirt with coat or open jacket.				
Trousers with shirt, sweater or buttoned jacket.	0.32	0.22	1.17	1.01
Trousers with shirt, sweater or buttoned jacket, carrying bag or clothing.	0.35	0.23		
Trousers with buttoned coat.	0.35	0.24		
Trousers with open coat.	0.36	0.24		
Trousers with jacket held open.	0.34	0.22	1.23	1.06
Trousers with flapping coat or carrying clothes.	0.35	0.26	1.33	1.12

Finally, the moment of inertia and the location of the center of pressure were computed from a rigid geometric model (no movable joints) representing the human body. The human body was modeled by a series of geometric shapes that were superimposed over the outline of the human body (Figure 90 in the Appendix). Next, a series of geometric solids were used to approximate the human body as shown in Figure 70. Each human body segment was modeled by: (1) an ellipsoid for the head (head included the neck), (2) a frustum for the shoulder, (3) elliptical cylinders for the trunk, upper arms, forearms, thighs, and legs, and (4) rectangular prisms for the hands and feet. In modeling the body segments, each geometric solid was assumed to be of uniform density. When the center of mass of a body segment was not located at the geometric center, the total mass of that segment was redistributed by an addition of a point mass at one end of the geometric segment to produce the proper center of mass location. The moment of inertia, center of pressure, and projected area were computed for each geometric segment from which the moment of inertia and the location of the center of pressure for the human body were determined (Table 49 and Figure 91 in the Appendix).

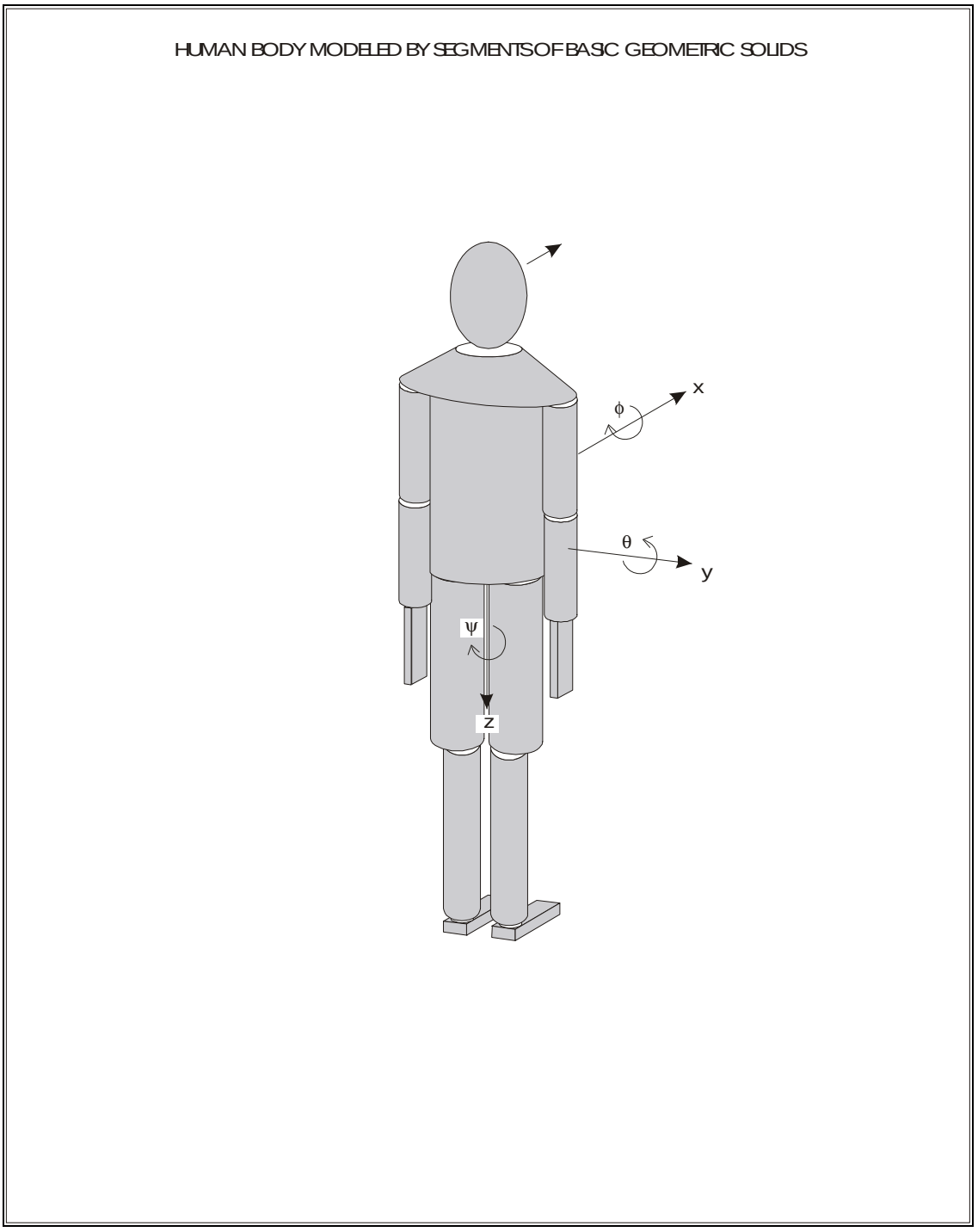

Figure 70. Human Body Modeled as Geometric Solids

The stability boundaries were developed from a mannequin based on the specifications for an average 50 percentile adult male. Table 35 lists the value of the parameters for the mannequin. The stability of the mathematical mannequin from wind force is determined for a frontal facing projected area. Whereas a person is least stable when pushed sideways, wind blowing against the front of a person and being pushed backwards is expected to create the most instability given the greater frontal area being presented to the wind (Temple and Johnson 2003). The computed center-of-pressure can be compared with the dummy used in the experiment conducted by China Academy of Railway Sciences, which had a center of pressure that was 51 percent of the dummy height (Heshou, Dezhao, and Houxiong 1996). The height to the top of the head of a 50 percentile male is 1.748 m (68.8 in), and the computed center of pressure for the mathematical mannequin is 0.894 m (35.2 in), which is 51 percent of its height—the same relative height as the physical dummy.

Table 35. Properties of the Mannequin for Simulation Based on an Average 50 Percentile Adult Male Wearing Light Clothing

Property	Value
Mass (Diffrient, Tilley, and Bardagjy 1974)	78 kg [0.445 (lb•s^2)/(in)]
Pitch Moment of Inertia about Bottom of Feet	82.1 N•m•s^2 (727 lb•in•s^2)
Height to Center of Mass (Diffrient, Tilley, and Bardagjy 1974)	0.963 m (37.9 in)
Height to Center of Pressure	0.894 m (35.2 in)
Frontal Area (DuBois Formula)	0.628 m^2 (973 in^2)
Frontal Drag Coefficient	1.1

10.2. Destabilizing Force to Human Body from Horizontal Acceleration

A critical threshold value needed to interpret the measured train-induced airflow data is the relationship between a person's stability, the force applied to a person, and the duration of that force. Two types of studies provide insight to this question. One type of study is the stability of people when exposed to the force of wind. The results of these studies were discussed previously on the effect of wind on people. The other study discussed is the measurements of stability on people that are in a standing position, and undergoing control levels of horizontal accelerations.

An experience that is common to many people is the attempt to maintain balance while standing on a train or bus during acceleration or braking. Hirshfeld (1932) conducted an experiment to determine the best form of acceleration curve for rapid starting of a streetcar that would attain the maximum acceleration and cause the least discomfort to standing passengers. The test apparatus was a movable platform where test subjects stood. Sensors on the platform detected when the weight of the person shifted due to tipping or loss of equilibrium. The person stood with their feet 0.254 m (10 in) apart with the heel of one foot 0.203 m (8 in) behind the heel of the other foot. Any loss of contact between a foot and the ground was considered a loss of balance. The tests were performed for different rates of acceleration, different acceleration curves (linear or parabolic acceleration, and dips in acceleration), and different standing configurations (facing forward, backward, sideways, and holding on to straps).

Of the tests conducted, the method that is of interest is the steep rise starting method where a very high rate of acceleration of 3.048 m/s^3 (10 ft/s^3) is applied, and the equilibrium performance of the test subjects was measured. The performance of the test subjects as measured by the average acceleration attained while maintaining equilibrium is shown in Table 36. Almost everyone in this test could maintain balance at acceleration below 0.305 m/s^2 (1 ft/s^2), but nobody was able to do so at acceleration of 1.067 m/s^2 (3.5 ft/s^2) or higher. In these tests, the acceleration level was obtained within 1 s, and the acceleration was maintained within the physical limits of the length of the platform track. The time it took for balance to be lost was not a consideration in these tests, and therefore, not specified.

Table 36. Equilibrium Distribution of Standing Subjects Facing Forward for Rate of Change of Acceleration of 3.048 m/s^3 (10 ft/s^3) (Hirshfeld 1932)

Average Acceleration Attained	Acceleration, Number of Gravity (g)*	Percentage of Test in which Equilibrium was Maintained
---	---	100
0.305 m/s^2 (1 ft/s^2)	0.031	98
0.457 m/s^2 (1.5 ft/s^2)	0.047	87
0.610 m/s^2 (2.0 ft/s^2)	0.062	56
0.762 m/s^2 (2.5 ft/s^2)	0.078	25
0.914 m/s^2 (3.0 ft/s^2)	0.093	11
1.067 m/s^2 (3.5 ft/s^2)	0.11	0

*Number of gravities were computed for this report by dividing the average acceleration attained by the acceleration of gravity.

Three of the results arrived by Hirshfeld (1932) from this experiment relating to human response are:

- The ability to withstand acceleration force in standing position does not appear to be influenced to any marked extent by age, sex, occupation, size, or build.
- An individual varies in his ability to maintain equilibrium, which could be affected by his physical and mental condition.
- Performances vary with different individuals for the same conditions.

10.3. Modeling Mannequin Stability

When the airflow velocity is relatively steady, or an unsteady airflow velocity is averaged over an extended period of time, the Beaufort wind force scale can be used to relate wind speed with its effects on a person. However, when a significant gust occurs over a short duration, a strong wind force could be imparted to the person. This effect cannot be adequately captured by use of the Beaufort wind force scale, which relies on an extended averaging duration. Therefore, a mannequin stability model was used as an analytical tool to map the stability boundary from an applied force of both short and long durations, and to relate these results to the Beaufort scale.

10.3.1. Defining Stability Boundary

A mathematical mannequin model was used to develop the stability boundary that relates an applied external force to the duration of applied force. In modeling mannequin stability, the assumption is that the body only undergoes rotation as shown in Figure 71 for the various states of stability. When a force, $F_{CP}(t)$, is applied to the mannequin at the center of pressure, the mannequin remains stationary until the moment from the applied force balances the moment due to its weight. The moment that is reached at this balancing condition will be referred to as the breakout moment. Although the applied force is below the breakout moment of the mannequin, the mannequin will remain stationary and be statically stable (Figure 71(a)). Once a force of sufficient magnitude is applied to the mannequin to exceed the breakout moment, the body will rotate, and depending on the strength and duration of the applied force, the body will either be dynamically stable and return to its initial position, or continue to rotate and become dynamically unstable and fall over (Figure 71(b)). A state exists such that the application and then the release of a force will cause the mannequin to rotate, and then the mannequin comes to rest when it's center of mass is immediately above the pivot point, or point of center-of-rotation (Figure 71(c)). This position is statically unstable and will be referred to as the statically unstable equilibrium (SUE) point. Any greater force or duration of applied force will cause the mannequin to continue to rotate and fall; any less force or duration of applied force will return the mannequin to a stable standing position. The stability boundary for the mannequin is the relationship between the magnitude and duration of applied force for the mannequin to reach the SUE point.

The stability boundary for the mannequin will be developed for an applied force with waveforms that are representative of gust profiles that are present during train passages. A velocity variation that can be loosely identified as an isolated single pulse is referred to as a gust, while a fluctuating airflow velocity that is continuous, such as a series of individual gusts, is spoken of as turbulence (Hoblit 1988). Gust profiles for aircraft design application were originally modeled as a sharp-edge gust but have evolved to the current one-minus-cosine pulse (Hoblit 1988). The stability boundaries for the mannequin were developed for three different gust profiles: sharp-edge profile (or square wave), a half sine wave, and a one-minus-cosine wave (or versine wave). These three gust profiles are shown in Figure 72. For each gust profile, a stability boundary was computed for various time durations.

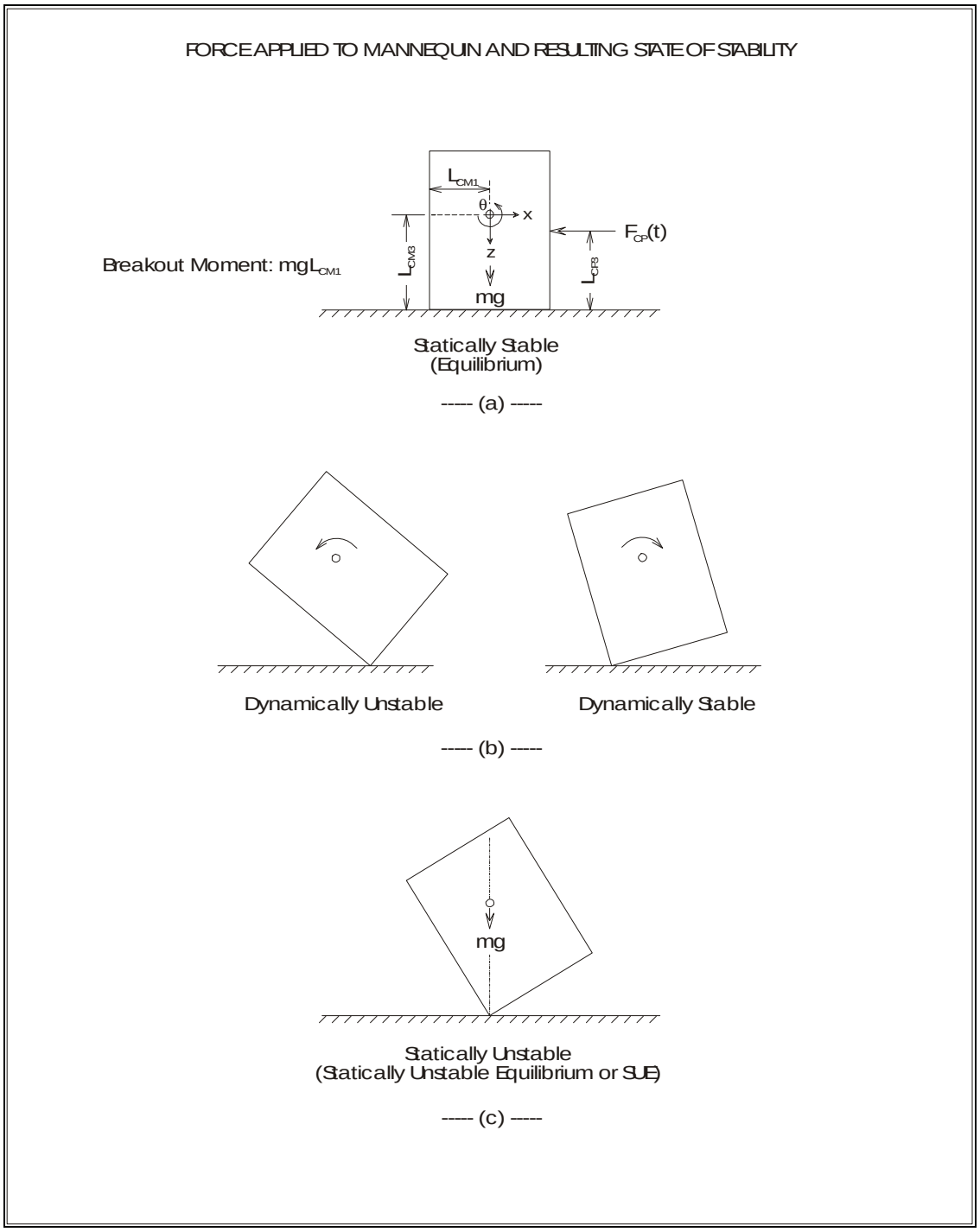

Figure 71. States of Stability for a Mannequin

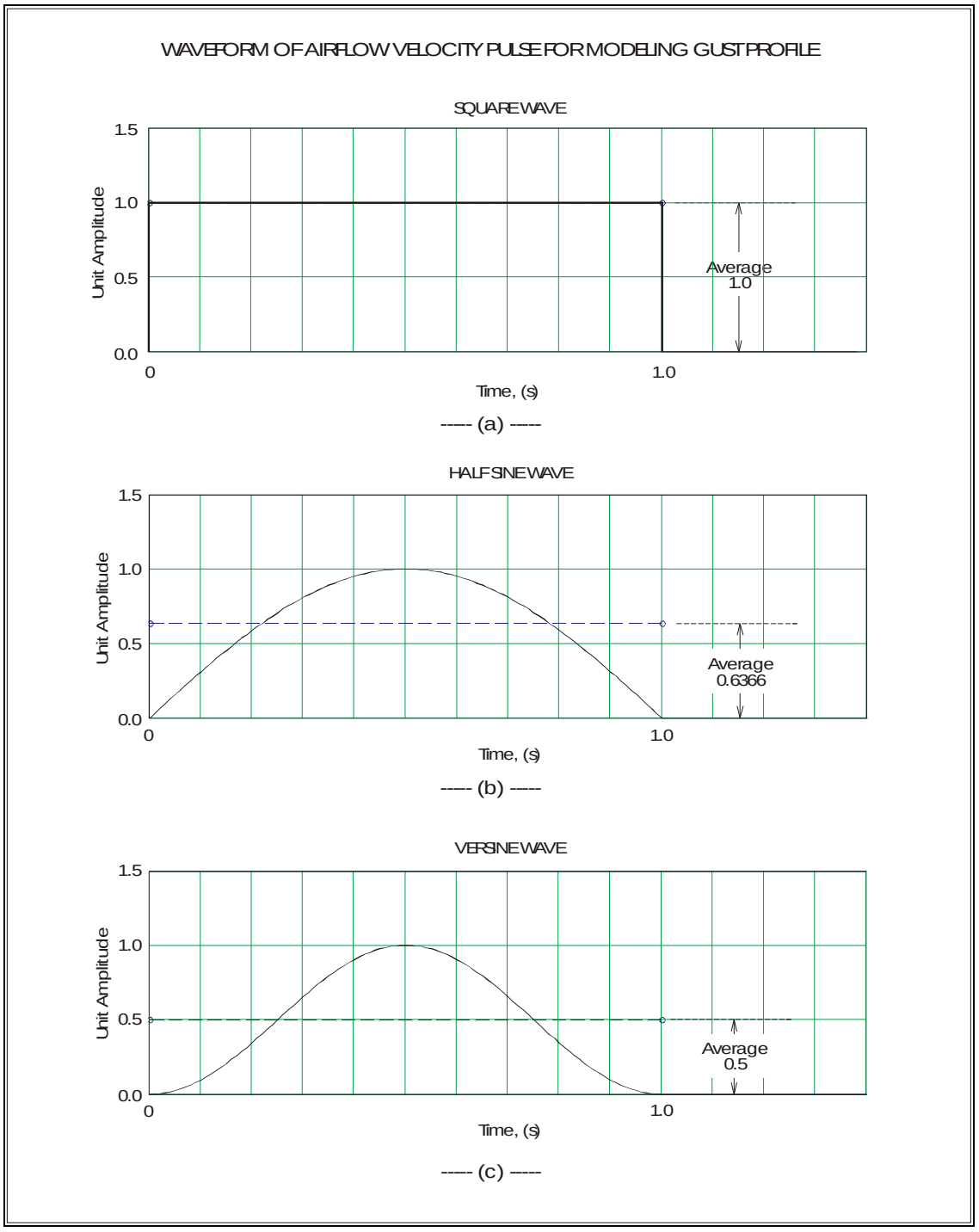

Figure 72. Waveforms for Modeling a Gust Profile

10.3.2. Relating Airflow to Mannequin Stability

Once the stability boundaries are developed, they can be applied to determine the stability of the mannequin to the airflow induced by a passing train. However, the transient aerodynamic effect created by a passing train is an unsteady fluctuating airflow, and this stochastic phenomenon cannot be described by a simple waveform. In contrast, the stability boundaries will be based on simple well-defined gust profiles. Therefore, the approach was to use the mean as the statistical quantity that relates the stability boundaries with the airflow data. The premise is that the average values of the gust profiles can be a good description of the airflow data when they are averaged over a range of averaging duration windows.

If it is assumed that the destabilizing force acting on the mannequin is due to the dynamic pressure of the airflow, then the force on the mannequin is the aerodynamic drag, $F_D = \frac{1}{2}\rho u^2(t) C_D A_P$. The airflow velocity u(t) can be expressed as $u(t) = U_O f_S(t)$, where U_O is the amplitude of the gust, and $f_S(t)$ is a shape function, which is a time varying waveform of unit amplitude that represents the gust profile. Letting the amplitude of the drag be F_O, where $F_O = \left(\frac{1}{2}\rho C_D A_P\right) U_O^2$, the drag can be expressed as an amplitude and a time-varying component, $F_D = F_O f_S{}^2(t)$.

In developing the stability boundary, for each gust profile that is applied to the mannequin over a given period of time, there will be a force amplitude and a corresponding airflow velocity amplitude that will cause the mannequin to reach a SUE point. The average airflow velocity, or the root mean square of the drag, forms the stability boundary. On the basis of a unit amplitude of each gust profile (Figure 72), the means and root-mean-squares are shown in Table 37.

Table 37. Mean and Root-Mean-Square for Waveforms of Unit Amplitude

Unit Amplitude Waveform	Mean	Root Mean Square
Square	1	1
Half Sine	$\frac{2}{\pi} \approx 0.6366$	$\frac{\sqrt{2}}{2} \approx 0.7071$
Versine	0.5	$\sqrt{\frac{3}{8}} \approx 0.6124$

To relate the airflow data to the stability boundaries, the average airflow velocities are computed from the airflow data at various averaging durations over the entire flow disturbance created by the passing train. From this moving average, the maximum airflow velocity is obtained for each averaging duration. The duration of the moving average is considered to correspond to the duration of the gust force that acts on the mannequin. These average airflow velocities are plotted on the same graph as the plots

of the stability boundaries to determine the effects of the airflow data on the stability of the mannequin. The averaging technique is applied to relate the two sets of results, the airflow velocity data from a passing train, and the stability boundaries derived from numerical simulation on a mannequin, to a common measurement.

Simplifications and assumptions exist in this procedure. First is that averages are not unique, because different sets of numbers produce the same average value. Therefore, the waveforms applied to the mannequin are assumed to approximate the waveform of the airflow data. Secondly, the response of the mannequin is from a single isolated airflow velocity pulse, and not from a continuous airflow stream that occurs during train passage.

10.3.3. Rotational Load Factor for Inertia and Drag

The force on a person standing on a platform undergoing acceleration differs from the force of air pressure. These differences must be taken into account when comparisons are made between data from a moving platform and those from the effects of wind. The unbalance that a person senses standing on an accelerated platform is due to the inertia of the body as the force acts horizontally at the feet. This inertial reaction, or body force, can be considered to act at the center of mass of the body. The force on a body from air pressure is a surface force, which acts on the surface of the body and can be considered to act at the center of pressure of the body. For a human body, which is composed of many movable segments with flexible body surface, the type of force and its point of application are significant, in terms of sensation and injury, and its dynamic response. However, for a rigid inanimate object, no difference in response between the effect of inertia and aerodynamic drag exists, except for the point at which the force acts.

An index will be defined to relate the wind force acting on a body, with the inertia of an accelerated platform. The response of the mathematical mannequin to drag is modeled as a pure rotation. Because the body is responding to the moment produced by the drag, the drag acting at the center of pressure of the body can be replaced by an effective force acting at the center of mass that produce the same moment. A rotational load factor, n_α, will be defined as the ratio of the effective force acting at the center of mass to the weight of the body. The rotational load factor is a dimensionless quantity and is interpreted as the ratio of the effective acceleration on the body to the acceleration of gravity, or as the number of gravities (g). Using this definition of rotational load factor, a force applied to the body causing pure rotation can be compared to the force from ground acceleration.

10.3.4. Stance

The ability of the mannequin to resist rotation from an external force depends on the stance, or the distance of the moment arm from the center of mass to the center of rotation. This distance on the mannequin (Figure 71), L_{CM1}, is analogous to the positions of the feet on a standing person, and corresponds to approximately half the distance

between the front and rear feet. The stance distance for the mannequin is determined by the breakout moment that the mannequin is to resist, which is,

$$L_{CM1} = L_{CP3}\left(\frac{F_{CPbo}}{mg}\right) \qquad \textbf{Equation 9}$$

where F_{CPbo} is the breakout force applied at the center of pressure that causes a state of impending rotation on the mannequin.

The ability of the mannequin to resist rotation depends on the stance, and a stability boundary occurs for each stance distance. Corresponding to each stance is a breakout moment produced by the wind force acting at the center of pressure of the mannequin. Each stability boundary is identified by the rotational breakout load factor at the center of mass, which is computed as,

$$n_{\alpha bo} = \left(\frac{F_{CPbo}}{mg}\right)\left(\frac{L_{CP3}}{L_{CM3}}\right) \qquad \textbf{Equation 10}$$

The stance distances, forces, and moments of the mannequin for various values of rotational load factor at breakout are shown in Table 38. A breakout rotational load factor of 0.05 g, which is produced by an airflow velocity of 9.86 m/s (22.1 mph), was selected as the lower limit of destabilizing force applied to the mannequin for computing the stability boundary. This value corresponded to a small percentage of people losing their balance in the Hirshfield (1932) test (Table 36), and where there is only a minimal effect of wind speed on a person (Table 7, Table 8, and Table 9). The largest destabilizing force applied to the mannequin is a breakout rotational load factor of 0.25 g, which is equivalent to an airflow velocity of 22.1 m/s (49.3 mph). This is at or above the wind speed limit considered to be safe for walking.

The purpose of the mannequin stability model is to provide an analytical tool to evaluate the aerodynamic effects of a passing train on people. A method to interpret the breakout load in terms of its effect on people is to relate it to the Beaufort scale. The rotational load factor at breakout is based on a steady uniform force applied to the center of mass of the mathematical mannequin. Corresponding to the rotational load factor is an equivalent steady uniform airflow velocity acting at the center of pressure of the mannequin. The Beaufort scale can now be applied since the airflow velocity at breakout is steady and uniform. Table 38 shows the Beaufort number associated with each of the equivalent steady uniform airflow velocity.

Table 38. Stance Distances and Dynamic Values of a Mannequin at Rotational Breakout

Rotational Breakout Load Factor, n_{bo}	Stance Distance, L_{CM1}	Breakout Force, F_{CPbo}	Breakout Moment	Airflow Velocity at Breakout	Beaufort Number
0.05	48.2 mm (1.90 in)	41.2 N (9.26 lb)	36.8 N•m (326 lb•in)	9.86 m/s (22.1mph)	5
0.10	96.3 mm (3.79 in)	82.4 N (18.5 lb)	73.7 N•m (652 lb•in)	13.9 m/s (31.2 mph)	7
0.15	144 mm (5.67 in)	124 N (27.9 lb)	110 N•m (973 lb•in)	17.1 m/s (38.2 mph)	7
0.20	193 mm (7.60 in)	165 N (37.1 lb)	147 N•m (1300 lb•in)	19.7 m/s (44.1 mph)	8
0.25	241 mm (9.49 in)	206 N (46.3 lb)	184 N•m (1628 lb•in)	22.1 m/s (49.3 mph)	9

10.4. Single Degree-of-Freedom Mannequin Stability Model

A mathematical model of a mannequin with a single degree-of-freedom was developed to establish the stability boundary from the response to an airflow velocity pulse. It is assumed that sufficient friction occurs at the feet of the mannequin so that a horizontal force applied to the body will cause it to rotate, but not to slide.

10.4.1. Equation of Motion

The mannequin is modeled as a rigid body with an applied force representing the wind drag as shown in Figure 73. The dynamics of the standing object subject to an applied force F(t) acting at the center of pressure can be determined from the equations of motion.

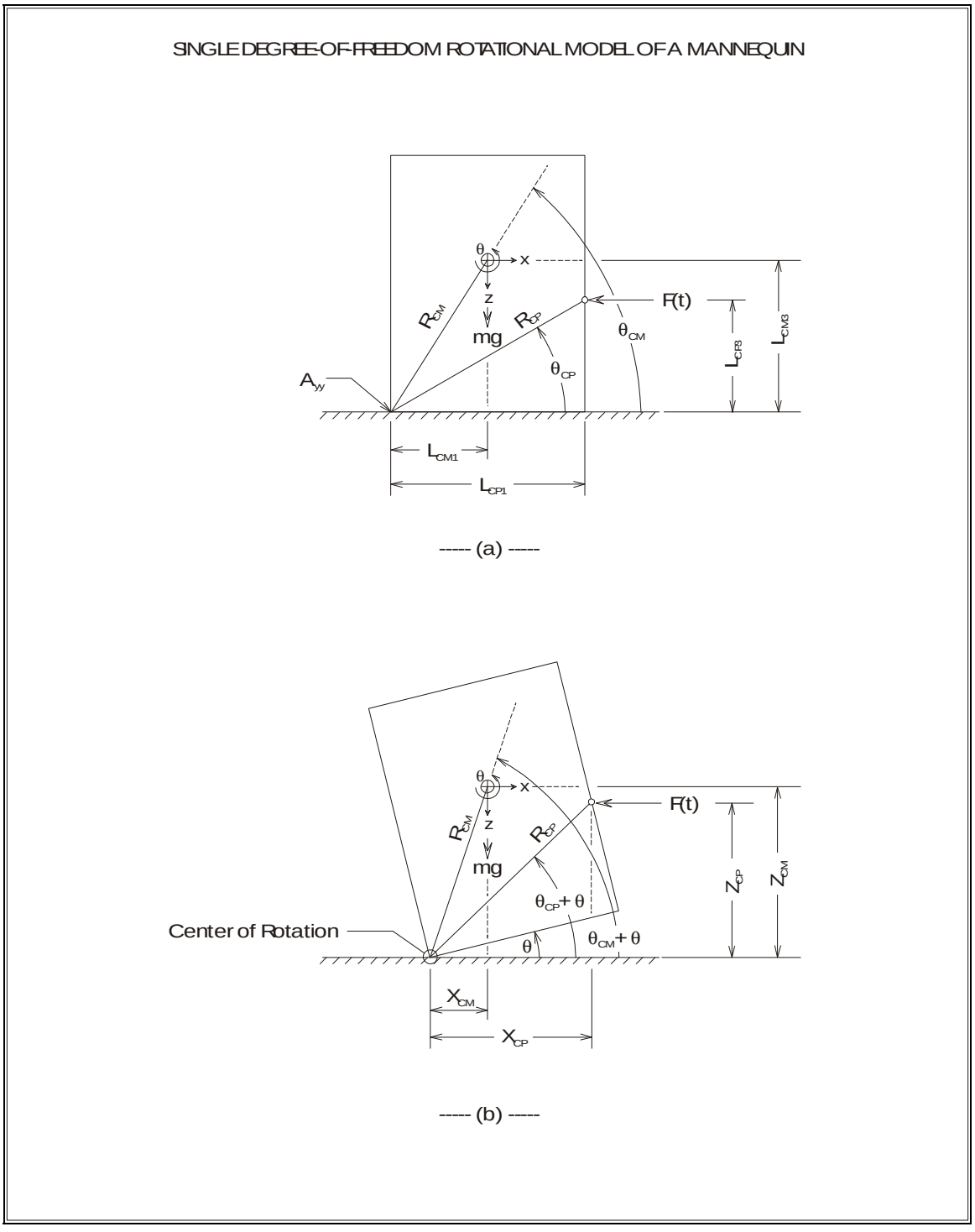

Figure 73. Mathematical Model of a Mannequin

Summing the moments about the center of rotation Ayy, $\sum M_{Ayy} = I_{Ayy}\frac{d^2\theta}{dt^2}$, the equation of motion is,

$$F(t)\left[L_{CP3}\cos\theta + L_{CP1}\sin\theta\right] - mg\left[L_{CM1}\cos\theta - L_{CM3}\sin\theta\right] = I_{Ayy}\frac{d^2\theta}{dt^2} \qquad \textbf{Equation 11}$$

The height to the center of pressure is,

$$z_{CP} = L_{CP3}\cos\theta + L_{CP1}\sin\theta \qquad \textbf{Equation 12}$$

The angle at the SUE point is,

$\theta_{SUE} = \frac{\pi}{2} - \theta_{CM}$, or

$$\theta_{SUE} = \tan^{-1}\left(\frac{L_{CM1}}{L_{CM3}}\right) \qquad \textbf{Equation 13}$$

Generally, the stance distance is small compared to the height of the center-of-pressure, and therefore, (L_{CP1}/ L_{CP3}) is small, $\frac{L_{CP1}}{L_{CP3}} << 1$, θ_{SUE} will be small, and the change in height of the center of pressure, z_{CP}, will be small. Because the equation is applied up to the SUE point, the angle, θ, will be small, $\sin\theta \approx \theta$, $\cos\theta \approx 1$, and the height in the center of pressure can be approximated as,

$$z_{CP} = L_{CP3}\cos\theta\left[1 + \left(\frac{L_{CP1}}{L_{CP3}}\right)\tan\theta\right]$$
$$\approx L_{CP3}\left[1 + \left(\frac{L_{CP1}}{L_{CP3}}\right)\theta\right]$$

The equation of motion for small angle is,

$$\frac{d^2\theta}{dt^2} - \frac{1}{I_{Ayy}}\left\{\left[L_{CP3}F(t)\left(\frac{L_{CP1}}{L_{CP3}}\right) + mgL_{CM3} \right]\right\}\theta = \frac{1}{I_{Ayy}}\left[L_{CP3}F(t) - mgL_{CM1}\right]$$

Equation 14

If it is assumed that the height of the center of pressure does not change with rotation, the equation of motion can be further simplified as follows:

$$\frac{d^2\theta}{dt^2} - \left(\frac{mgL_{CM3}}{I_{Ayy}}\right)\theta = \frac{1}{I_{Ayy}}\left[L_{CP3}F(t) - mgL_{CM1}\right]$$

Equation 15

The applied force F(t) depends on the waveform of the airflow velocity pulse, period T_p, and frequency Ω. The equations of motion for the three waveforms are as follows:

Square Wave Airflow Velocity Pulse

$$\frac{d^2\theta}{dt^2} - \left[\frac{1}{I_{Ayy}}\left(L_{CP1}F_O + mgL_{CM3}\right)\right]\theta = \left[\frac{1}{I_{Ayy}}\left(L_{CP3}F_O - mgL_{CM1}\right)\right]$$

Equation 15a

$$F(t) = F_O \quad \text{for} \quad 0 < t < T_P$$

Half Sine Wave Airflow Velocity Pulse

$$\frac{d^2\theta}{dt^2} - \left(\frac{mgL_{CM3}}{I_{Ayy}}\right)\theta = \left(\frac{1}{I_{Ayy}}\right)\left[L_{CP3}F_O\left(\sin^2\Omega t\right) - mgL_{CM1}\right]$$

Equation 15b

$$F(t) = F_O\left(\sin\Omega t\right)^2 \quad \text{for} \quad 0 < t < \left(T_P/2\right)$$

$$\textit{where} \quad T_P = 2\pi/\Omega$$

Versine Wave Airflow Velocity Pulse

$$\frac{d^2\theta}{dt^2} - \left(\frac{mgL_{CM3}}{I_{Ayy}}\right)\theta = \left(\frac{1}{I_{Ayy}}\right)\left[\left(\frac{L_{CP3}F_O}{4}\right)(1-\cos\Omega t)^2 - mgL_{CM1}\right]$$

Equation 15c

$$F(t) = F_O\left[\frac{1}{2}(1-\cos\Omega t)\right]^2 \quad \text{for} \quad 0 < t < T_P$$

$$\text{where} \quad T_P = 2\pi/\Omega$$

10.4.2. Stability Boundary

A series of stability boundaries were established for a mannequin based on properties for a frontal facing average 50 percentile adult male wearing light clothing. The stability boundary was computed by solving a set of simultaneous equations to determine the amplitude of the drag corresponding to the airflow velocity pulse for a given time duration that the pulse is applied to the mannequin. The solution must satisfy the equation of motion, the SUE point, and other constraints. Once the force amplitude was found, the velocity amplitude, and the average force and velocity were computed.

In addition to the stability boundary, the time history response of the mannequin was also computed. The equation of motion for the mannequin in its simplified form (Equation 15) is a linear differential equation with constant coefficients, which can be determined exactly for the general solution. Once the required force amplitude was determined for a given pulse duration, the angular acceleration, velocity, and displacement responses of the mannequin can be computed.

A case will be illustrated with an airflow velocity pulse of 1 s duration applied to the mannequin for a rotational breakout load factor of 0.05 g. The angle at the SUE point for this stance on the mannequin is 2.86 deg. A square wave airflow velocity pulse was applied to the mannequin. The applied force and the corresponding moment are shown in Figure 74. The resultant positive moment on the mannequin increases with time to destabilize the mannequin, and immediately drops to a negative value pulling the mannequin back once the applied force is released. The angular displacement and velocity in response to the applied force are shown in Figure 75. The angular displacement approaches the SUE angle as the angular velocity approaches zero. The maximum angular velocity is reached when the applied force is released.

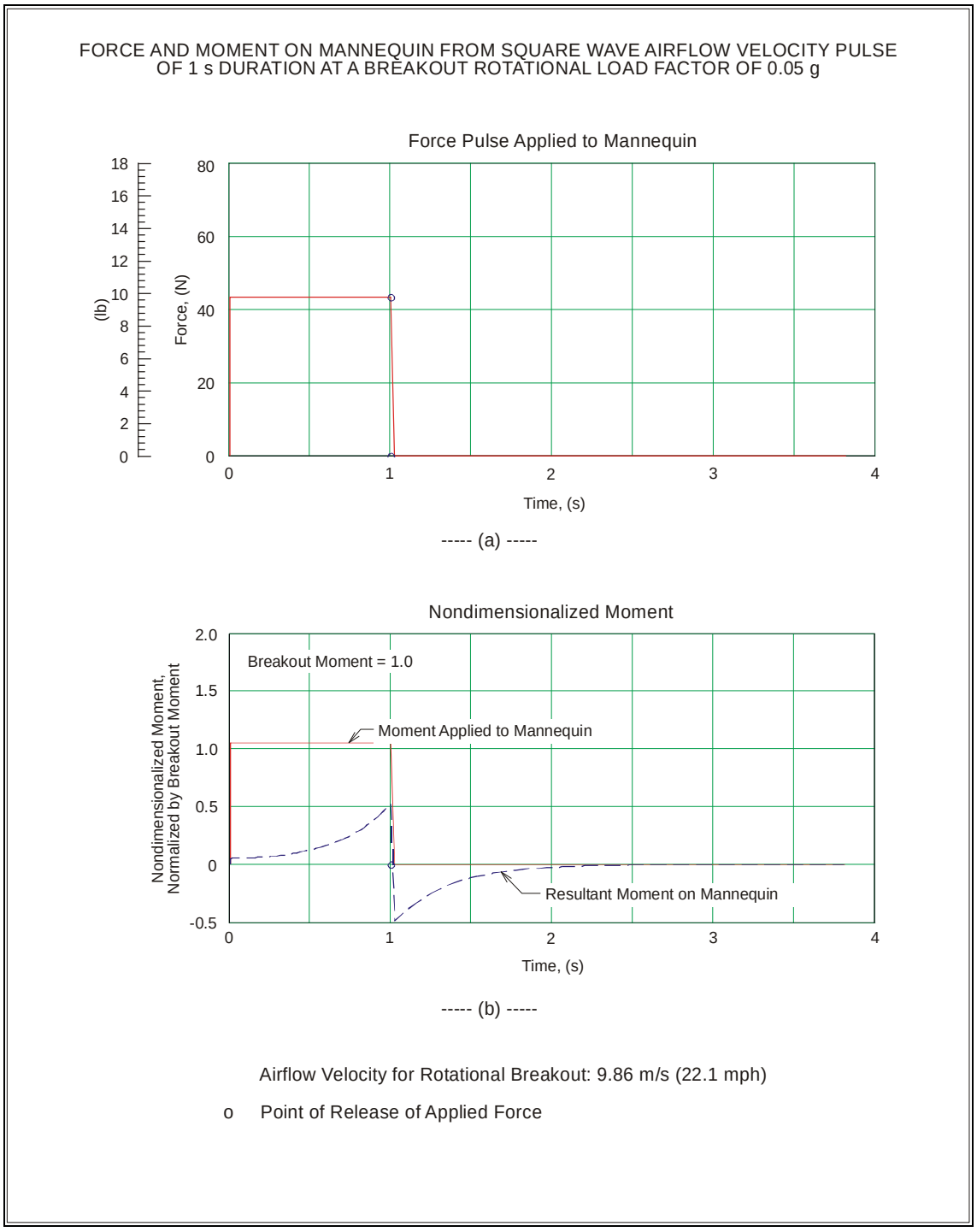

Figure 74. Time Histories of Force and Moment on a Mannequin from a Square Wave Airflow Velocity Pulse

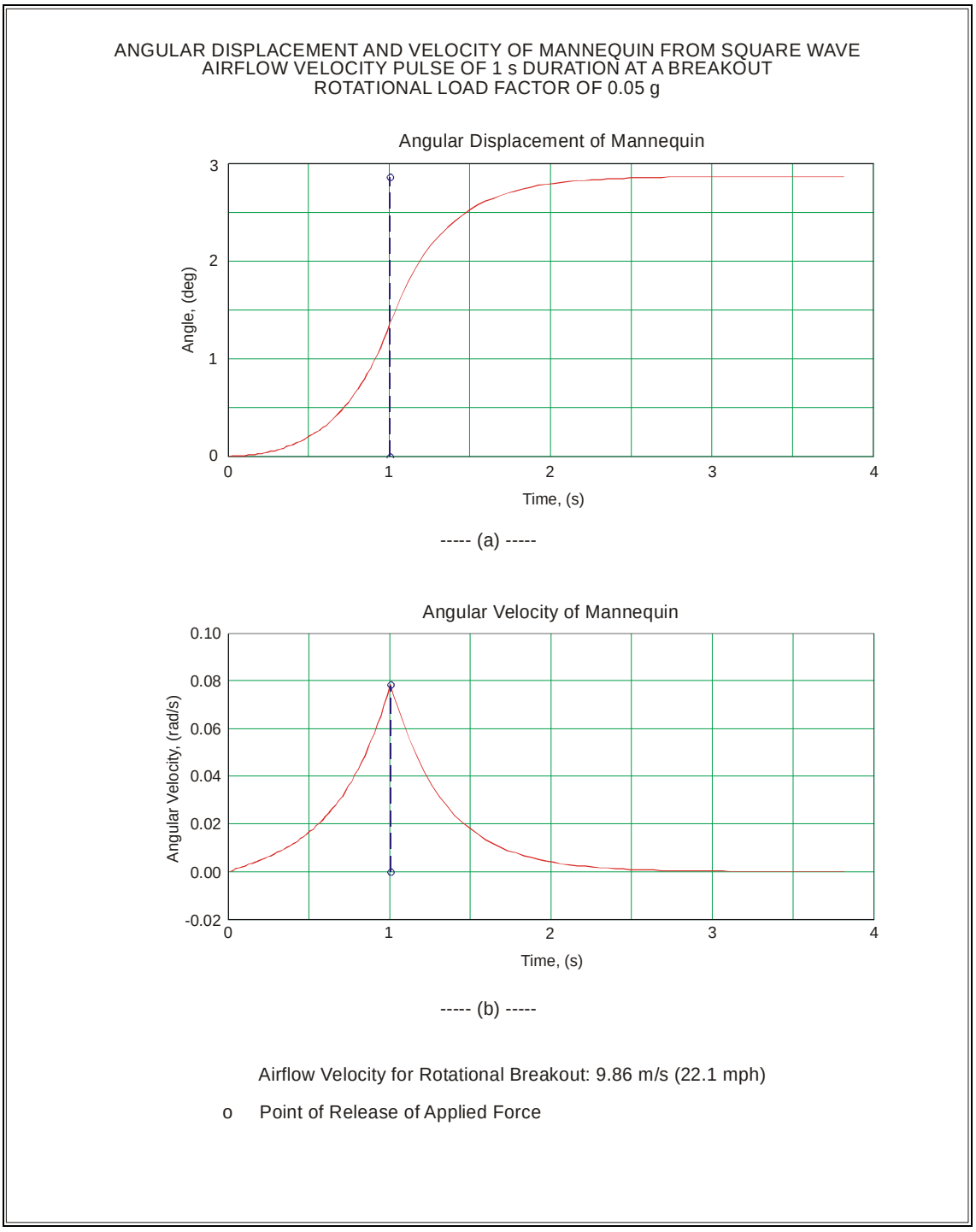

Figure 75. Time Histories of Angular Displacement and Velocity of a Mannequin from a Square Wave Airflow Velocity Pulse

Another case will be illustrated with a versine wave airflow velocity pulse applied to the mannequin with all other conditions being the same as in the previous case. The applied force and the corresponding moment are shown in Figure 76. In this case, the resultant moment on the mannequin remains at zero while the force is being applied until the breakout moment is reached. Once the resultant moment exceeds the breakout moment, the mannequin begins to rotate. This is further illustrated in Figure 77 where the angular displacement and velocity of the mannequin remains stationary until the applied moment is large enough to initiate rotation. The angular displacement approaches the SUE angle as the angular velocity approaches zero after the applied force is released.

These time history responses demonstrate the dynamics of the mannequin as it reaches the state of statically unstable equilibrium. For each time duration that an airflow velocity pulse is applied, there is a force amplitude of such magnitude that the mannequin will rotate and come to rest at the SUE point. The set of all points relating the force or velocity with time duration constitute the stability boundary.

The stability boundaries for the mannequin from the three airflow velocity pulses: the square wave, half sine wave, and versine wave, are illustrated for a breakout rotational load factor of 0.05 g. A plot of the stability boundary as amplitudes of rotational load factors for various durations of airflow velocity pulses is shown in Figure 78(a). For a 3 s duration, the amplitudes of all three wave shapes approach a rotational load factor of 0.05 g. As the duration of the pulse is reduced, the amplitude of the pulse required to reach the SUE point increases. At a pulse duration of 0.01 s, a load factor amplitude of over 1 g is required for all three pulses. The pulse amplitudes for the half sine and versine waves are higher than the square wave since for a portion of the time, the moments for half sine and versine waves are below the breakout moment. When the average rotational load factors are computed, the averages from the half sine and versine waves are higher than for the square wave at a short pulse duration, but lower than for the square wave at a long pulse duration as shown in Figure 78(b).

Instead of load factor limit, the stability boundary is also expressed as airflow velocity limit, which can be compared directly to airflow data. The limit on amplitude of airflow velocity shown in Figure 79(a) has the same trend and a similar characteristic as the limit on amplitude of rotational load factor. However, when the average is computed, both the averages from the half sine and versine waves are lower than for the square wave for all pulse durations as shown in Figure 79(b). Although the amplitude of airflow velocity forming the stability boundary is highest for the versine pulse, it is the lowest when expressed as an average airflow velocity.

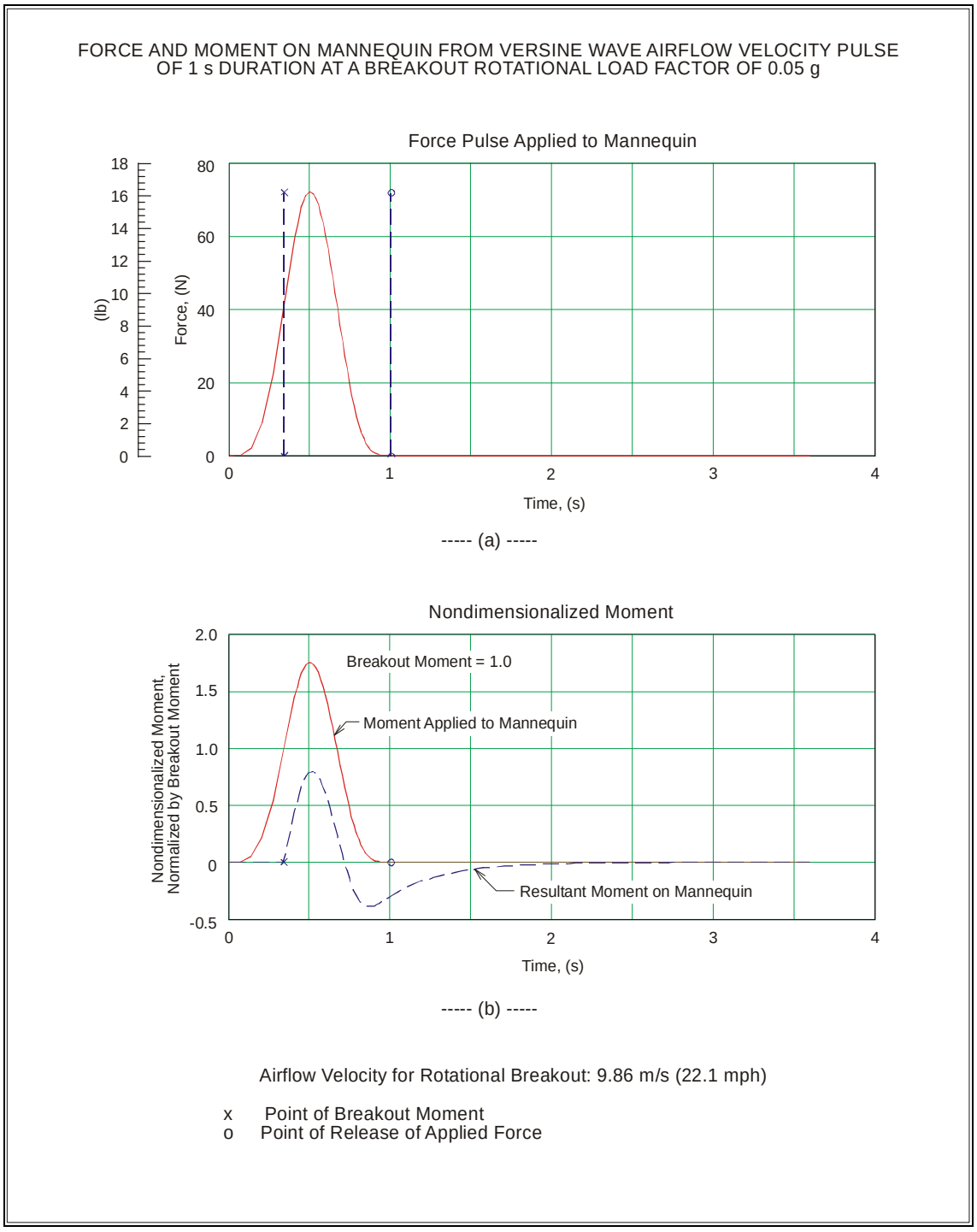

Figure 76. Time Histories of Force and Moment on a Mannequin from a Versine Wave Airflow Velocity Pulse

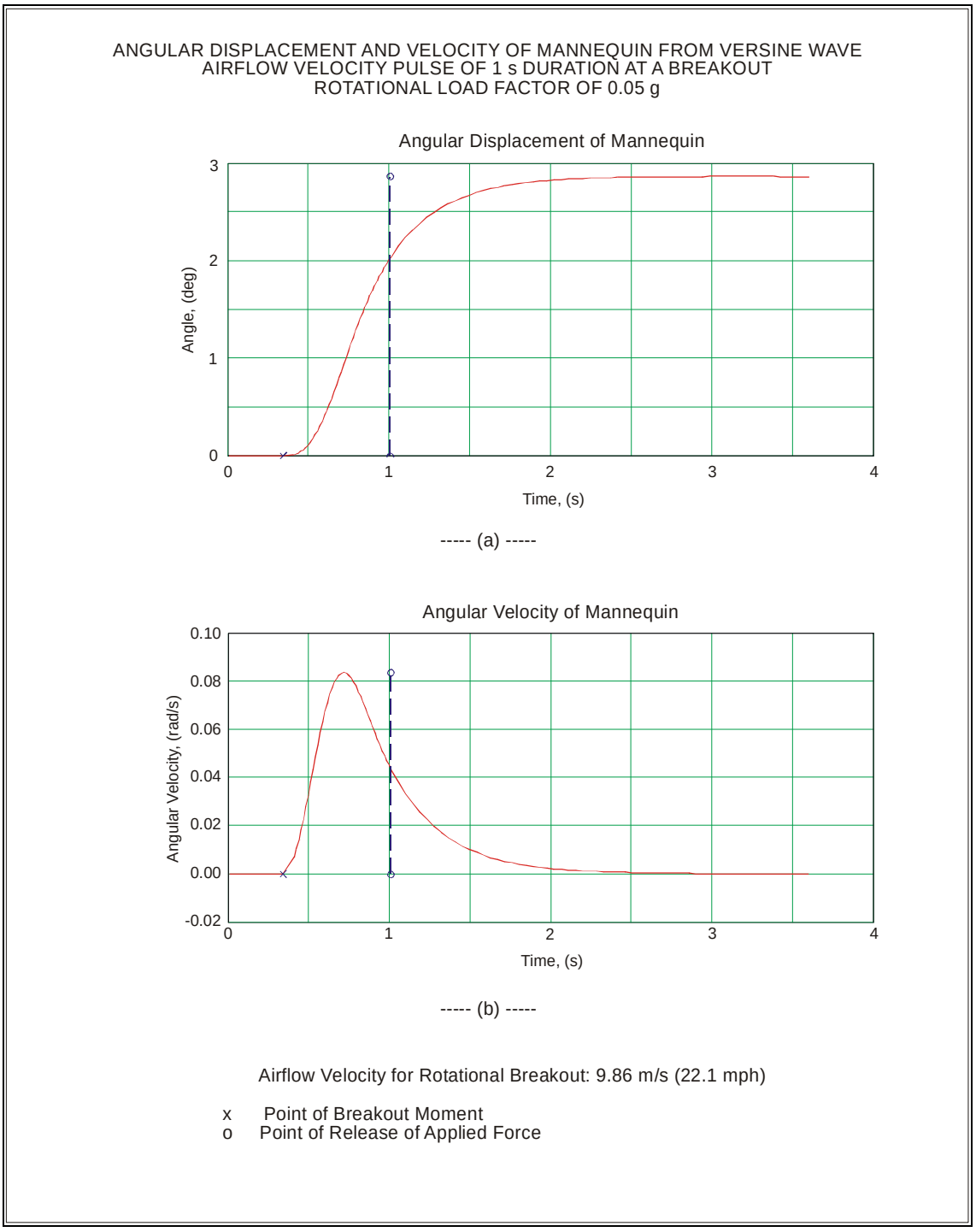

Figure 77. Time Histories of Angular Displacement and Velocity of a Mannequin from a Versine Wave Airflow Velocity Pulse

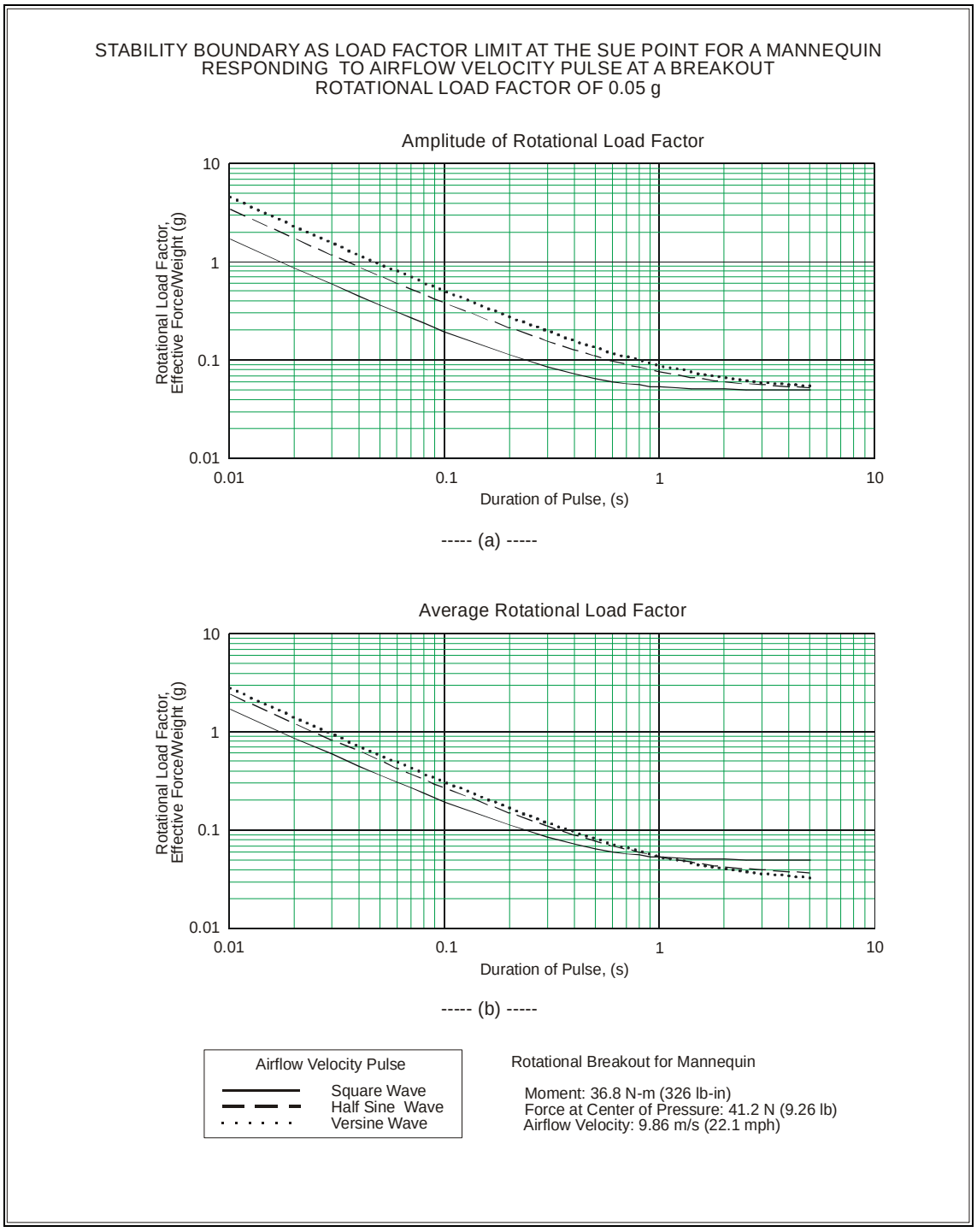

Figure 78. Stability Boundaries as Load Factor Limits for a Mannequin Responding to an Airflow Velocity Pulse

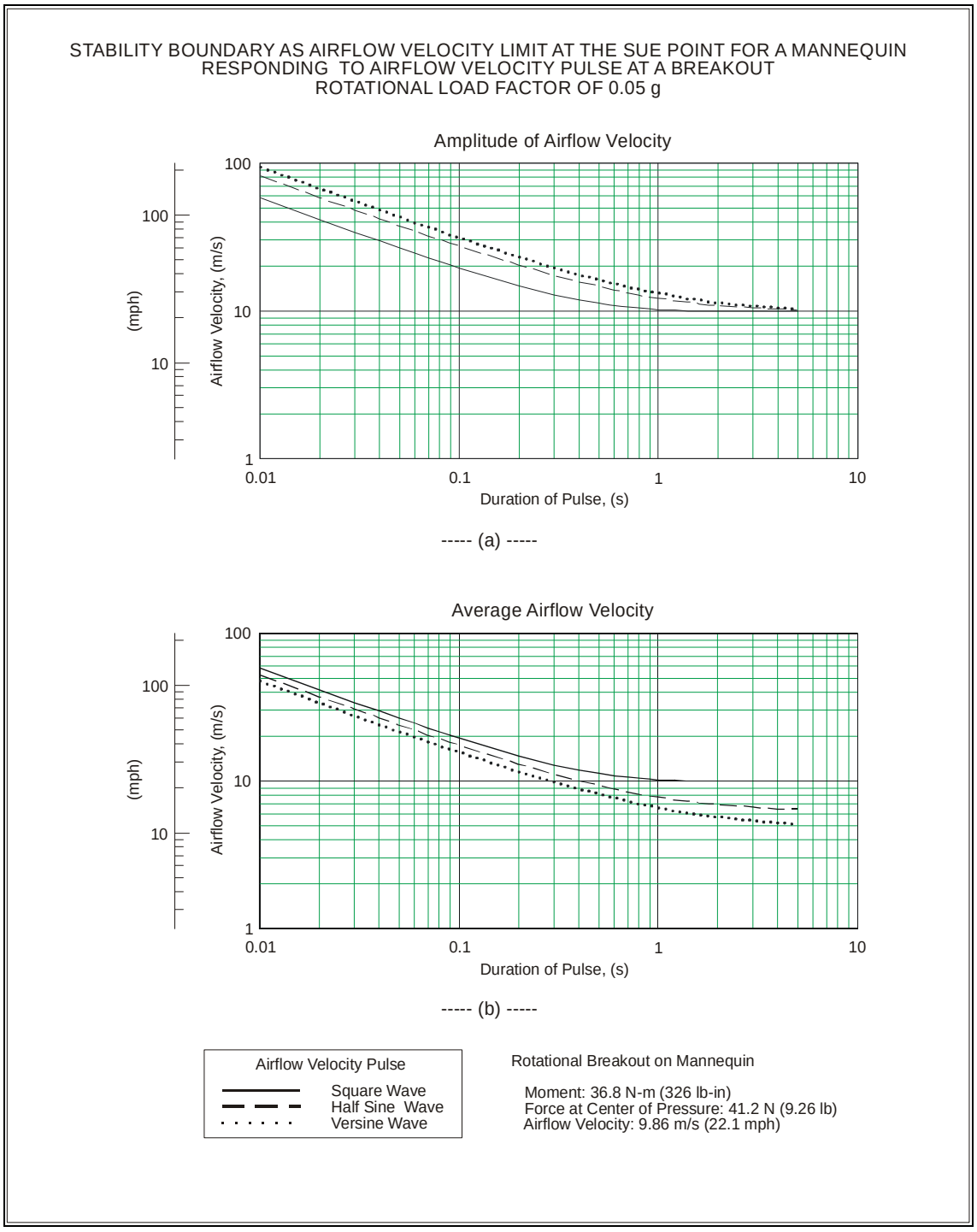

Figure 79. Stability Boundaries as Airflow Velocity Limits for a Mannequin Responding to an Airflow Velocity Pulse

Different stability boundaries exist for the different airflow velocity pulses. An examination of the airflow velocity data suggest that these three stability boundaries can be simplified to a single boundary based on the following assumptions:

- The airflow velocity data for averages of 1 s duration or longer is best represented by a square wave.

- The airflow velocity data for averages of 0.1 s duration or shorter is best represented by a vesine wave.

On the basis of these assumptions, a synthesized piecewise stability boundary from a versine and square wave velocity pulses for a breakout rotational load factor of 0.05 g were created as shown plotted in Figure 80. The synthesized boundary line is described by a power function of the form $u_{SUE} = \left(A_{syn} t_P^k\right) + U_{syn}$,

where,

u_{SUE}: synthesized piecewise stability boundary for the SUE point,
A_{syn}: coefficient that is a function of load factor,
U_{syn}: constant that is a function of load factor,
k: exponent, and
t_P: duration of velocity pulse.

A series of synthesized piecewise stability boundaries are shown plotted in Figure 81 with breakout rotational load factors of 0.05 g to 0.25 g as parameters of the curves. These curves can be closely fitted by the function u_{SUE} as follows,

$$u_{SUE} = \left[(0.80753) + (13.95173)n_\alpha - (16.90143)n_\alpha^2\right] t_P^{-0.71166} + \left[(4.96272) + (85.65632)n_\alpha - (103.55686)n_\alpha^2\right] \text{ m/s,}$$

Equation 16

within the range of,
$0.01\ s \le t_P \le 3\ s$ and,
$0.05\ g \le n_\alpha \le 0.25\ g$

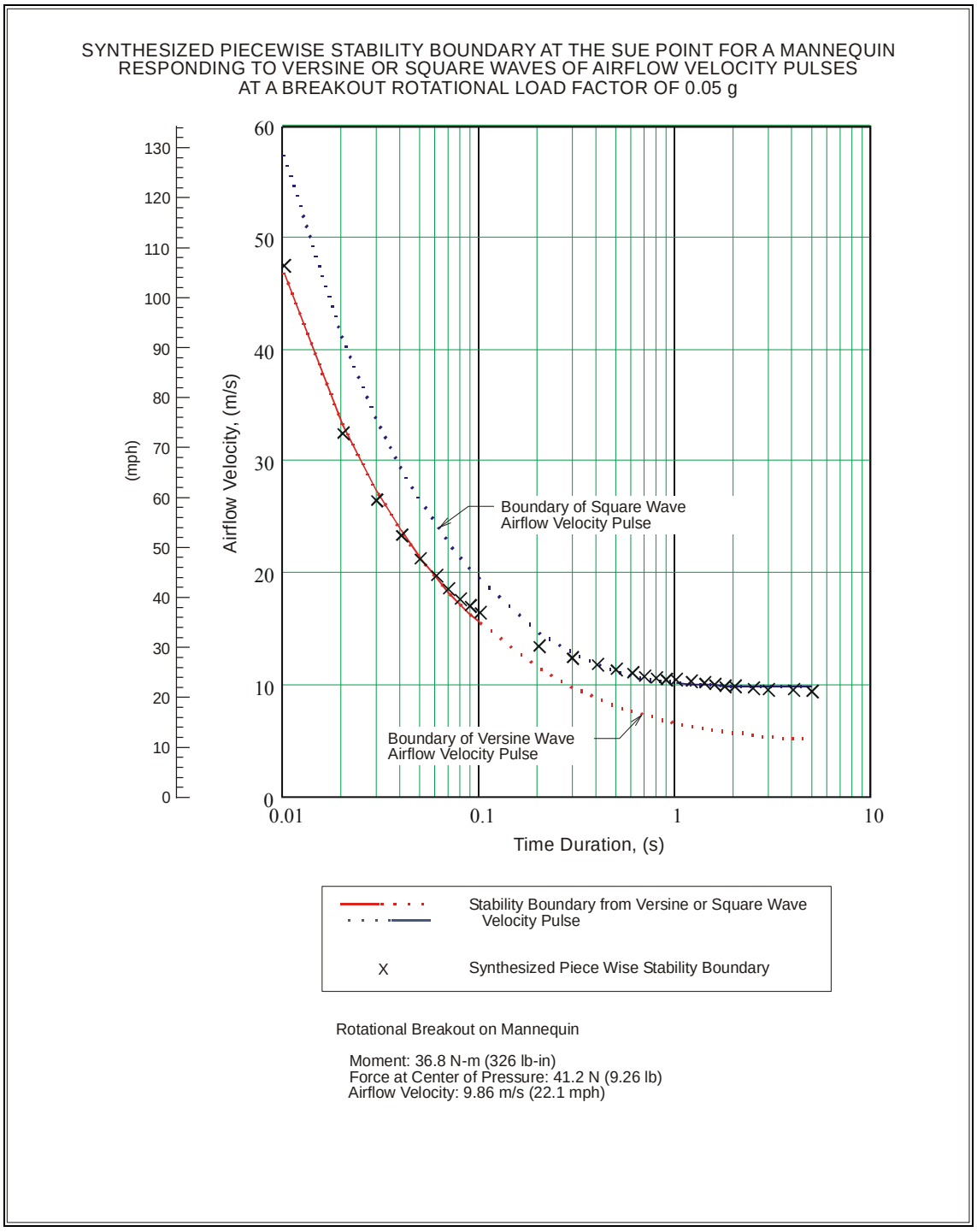

Figure 80. Synthesized Piecewise Stability Boundary for a Mannequin

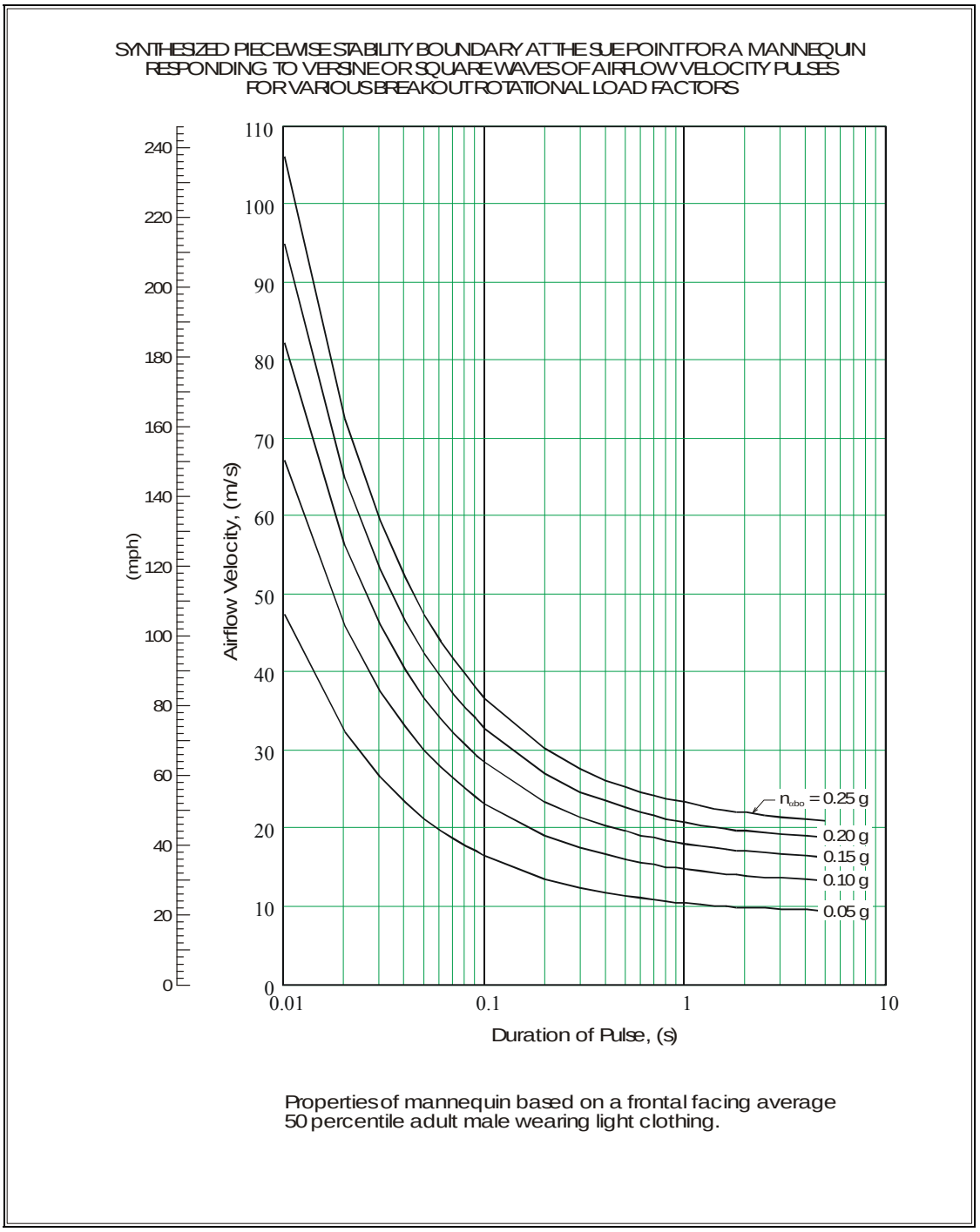

Figure 81. Synthesized Piecewise Stability Boundary for a Mannequin at Various Breakout Rotational Load Factors

10.5. Mannequin Stability to Train-Induced Airflow

In the previous chapter, the maximum airflow was determined at various lateral distances from the side of a passing train, and a minimum distance was established based on wind speed criteria. Another method to assess the airflow strength is to relate the airflow data relative to the stability boundary of the mathematical mannequin. The data for the assessment is from the resultant airflow velocity at quadrant 1 for nominal lateral distances of 1.17 m (46 in) and 1.43 m (56 in) from the side of the train. These two lateral distances correspond to the positions of the CIDs as referenced to their cylindrical axes. All the data were scaled so that the time and airflow velocity for the Acela Express train corresponded to a train speed of 241 km/h (150 mph), and the Amfleet train corresponded to a train speed 201 km/h (125 mph).

The first case analyzed was the airflow data measured from the bottom position at a nominal height of 0.97 m (38 in) from the top of the rail. At a nominal lateral distance of 1.17 m (46 in) from the side of the train (Figure 82(a)), the maximum airflow velocity reached a stability boundary of about 0.20 g. For the mathematical mannequin to remain stable, its stance distance must be wide enough to withstand a rotational load factor of 0.20 g when exposed to a steady uniform force applied to its center of mass. By increasing the nominal lateral distance to 1.43 m (56 in) from the side of the train (Figure 82(b)), the maximum airflow velocity reached a stability boundary of about 0.15 g. At this lateral distance, the mathematical mannequin can be stable at a narrower stance distance.

The next case is for airflow data measured from the top position at a nominal height of 1.73 m (68 in) from the top of the rail. At this greater height, the maximum airflow velocity reached a stability boundary of about 0.12 g at a nominal lateral distance of 1.17 m (46 in) from the side of the train (Figure 83(a)), and reduced slightly to 0.11 g when the nominal lateral distance is increased to 1.43 m (56 in) (Figure 83(b)).

Finally, the airflow velocity at a middle height was linearly interpolated from airflows measured at two other heights to estimate the value at a nominal height of 1.35 m (53 in) from the top of the rail. This intermediate height would be a better representation of the airflow at which an adult would be exposed. The interpolated maximum airflow velocity reached a stability boundary of about 0.15 g at a nominal lateral distance of 1.17 m (46 in) from the side of the train (Figure 84(a)), and reduced to 0.12 g when the nominal lateral distance is increased to 1.43 m (56 in) (Figure 84(b)).

These results lead to several observations. The maximum airflow velocity reaches a stability boundary with a lower rotational load factor when the height above the rail or the lateral distance from the train is increased, which is consistent with other observed trends (Table 31). Each of the cases analyzed was based only a single data point that reached the highest rotational load factor on the stability boundary. Other maximum airflow velocities are as much as 0.05 to 0.10 g below that single data point. Generally,

the maximum airflow velocity reaching the stability boundaries with the highest rotational load factor occurs between moving average windows of 0.1 to 1 s.

The effect on people from train-induced airflow velocity can be related to the dynamic response of a mathematical mannequin by interpreting the breakout load in terms of the Beaufort scale (Table 38). Now a relationship occurs between the airflow data relative to the stability boundary and its effect on people based on the Beaufort scale (Table 7). The strongest airflow was measured lowest to the ground at 0.97 m (38 in) above the top of the rail, and closest to the train at 1.17 m (46 in) from the side of the train. At this location, the mannequin remains statically stable up to a maximum airflow velocity of 19.7 m/s (44 mph), corresponding to a Beaufort number of 8. A Beaufort number of 8 will impede progress and cause great difficulty with balance in gusts. The remaining airflow corresponds to a Beaufort number of 7, which is described as "inconvenience felt when walking." The results are summarized in Table 39.

Table 39. Comparison between Maximum Airflow Velocities from a 3 s Moving Average and Uniform Airflow Velocities at Breakout from Stability Boundary on a Mathematical Mannequin

Nominal Height above Top of Rail	Nominal Distance from Side of Train	Maximum Airflow Velocity from 3 s Moving Average Window	Highest Breakout Load on Mannequin Stability Boundary relative to Airflow Velocity Data		
			Rotational Load Factor	Uniform Airflow Velocity	Beaufort Number
0.97 m (38 in)	1.17 m (46 in)	15.9 m/s (36 mph)	0.20 g	19.7 m/s (44 mph)	8
	1.43 m (56 in)	14.0 m/s (31 mph)	0.15 g	17.1 m/s (38 mph)	7
1.35 m (53 in)	1.17 m (46 in)	13.6 m/s (30 mph)	0.15 g	17.1 m/s (38 mph)	7
	1.43 m (56 in)	13.1 m/s (29 mph)	0.12 g	15.3 m/s (34 mph)	7
1.73 m (68 in)	1.17 m (46 in)	12.1 m/s (27 mph)	0.12 g	15.3 m/s (34 mph)	7
	1.43 m (56 in)	12.3 m/s (28 mph)	0.11 g	14.6 m/s (33 mph)	7

A comparison is made between the effects on people based on the dynamic response of a mathematical mannequin, and the wind speed criteria of Murakami and Deguchi, which is based on wind speed averaged over 3 s (Table 9). The maximum airflow velocities from a 3 s moving average window are shown in Table 39. The strongest airflow velocity is 15.9 m/s (36 mph), measured lowest to the ground at 0.97 m (38 in) above the top of the rail, and closest to the train at 1.17 m (46 in) from the side of the train. In the

Murakami and Deguchi criteria, the effect of this wind speed is described as “walking impossible to control with body blown sideways.” This is comparable to Beaufort number 8, which will impede progress and cause great difficulty with balance in gusts. The maximum airflow velocities for all the remaining locations are between 10 to 15 m/s (22 to 34 mph). The Murakami and Deguchi criteria describe the effect of this wind speed as “walking becomes irregular and difficult to control.” This is comparable to Beaufort number 7, which is described as “inconvenience felt when walking.” Since these effects on people are qualitative descriptions, the comparison is to some extent a subjective interpretation. Both methods predict similar effects on people amidst differences in phraseology between the two criteria.

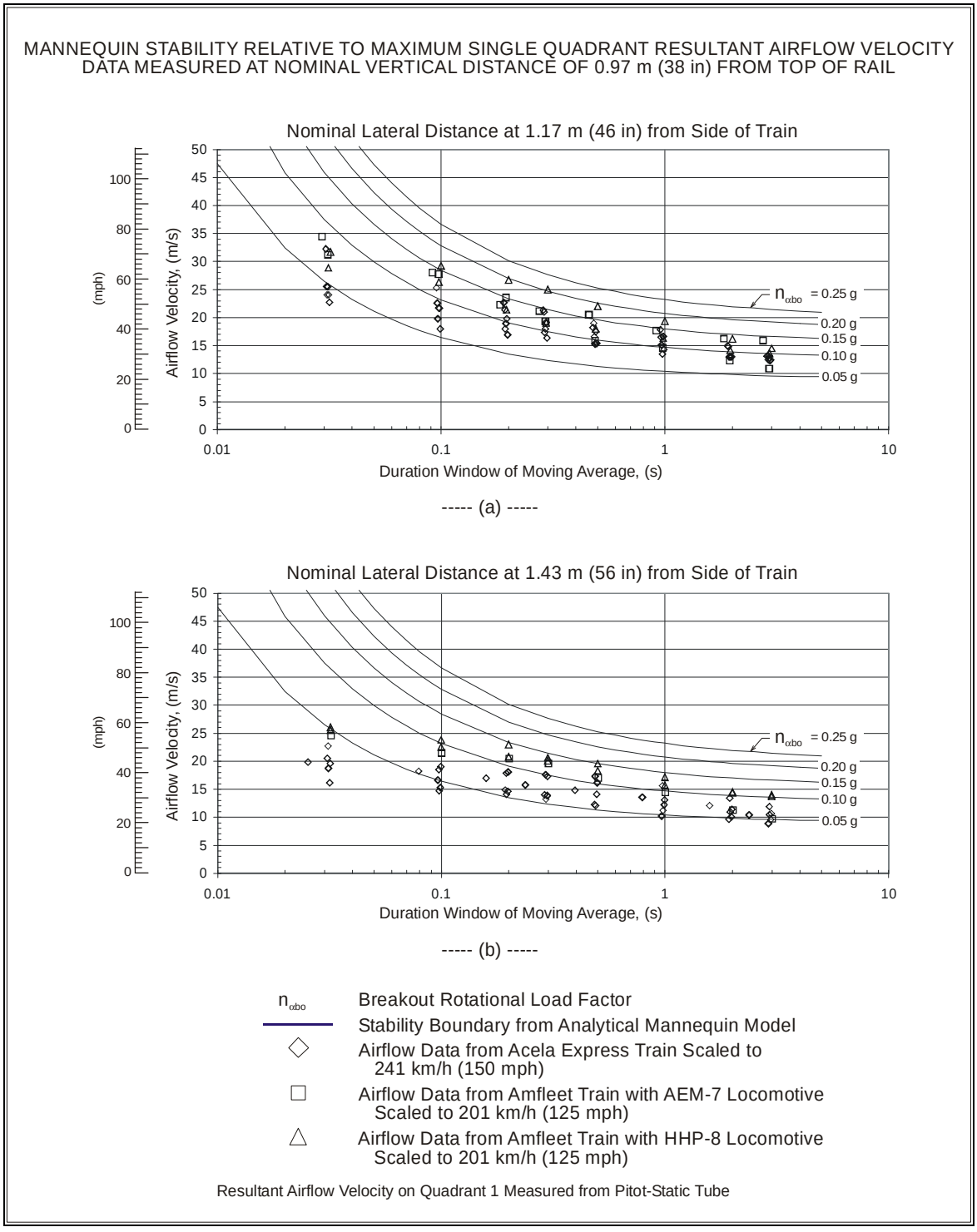

Figure 82. Mannequin Stability Relative to Airflow Velocity Data at 0.97 m (38 in) above Top of Rail

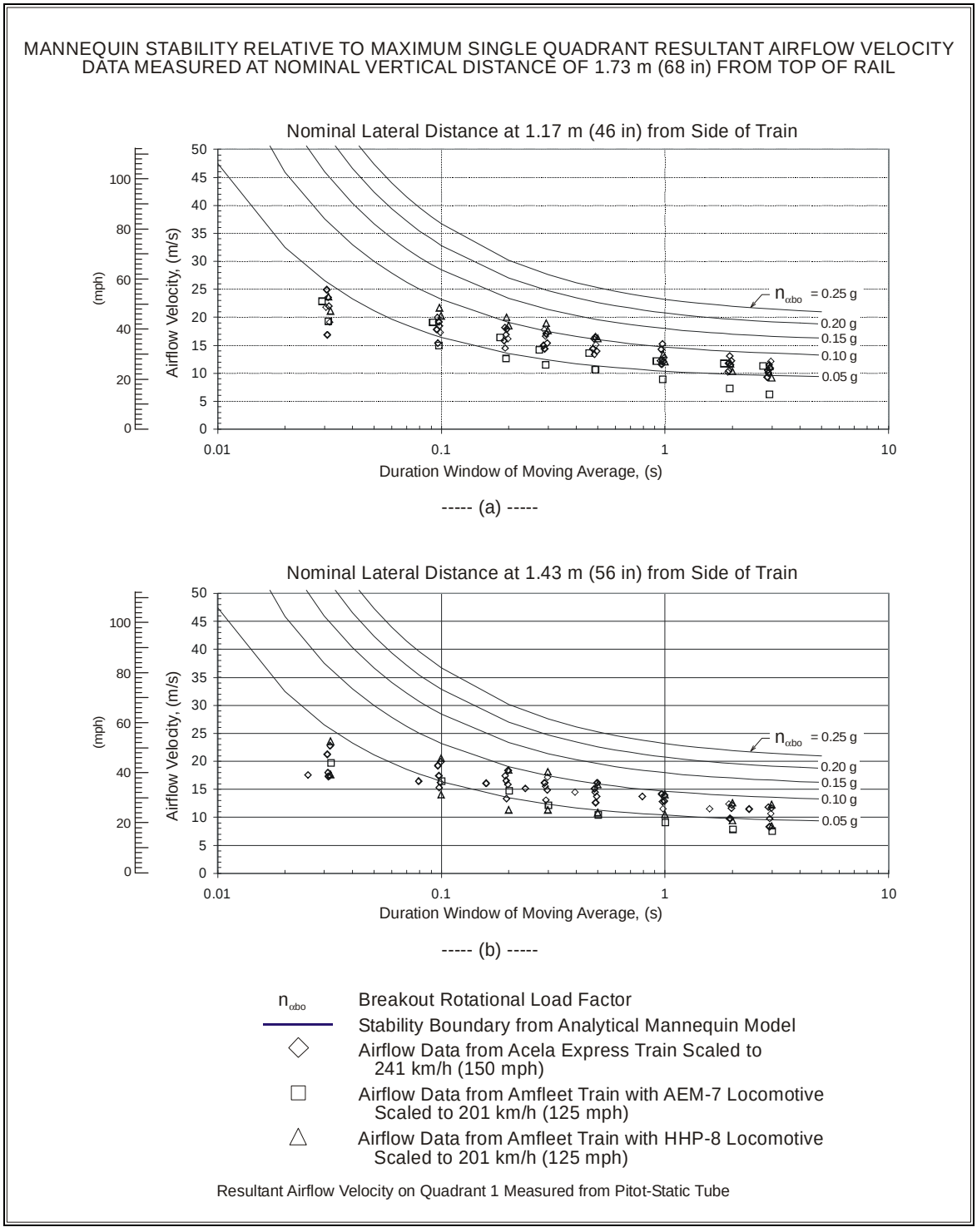

Figure 83. Mannequin Stability Relative to Airflow Velocity Data at 1.73 m (68 in) above Top of Rail

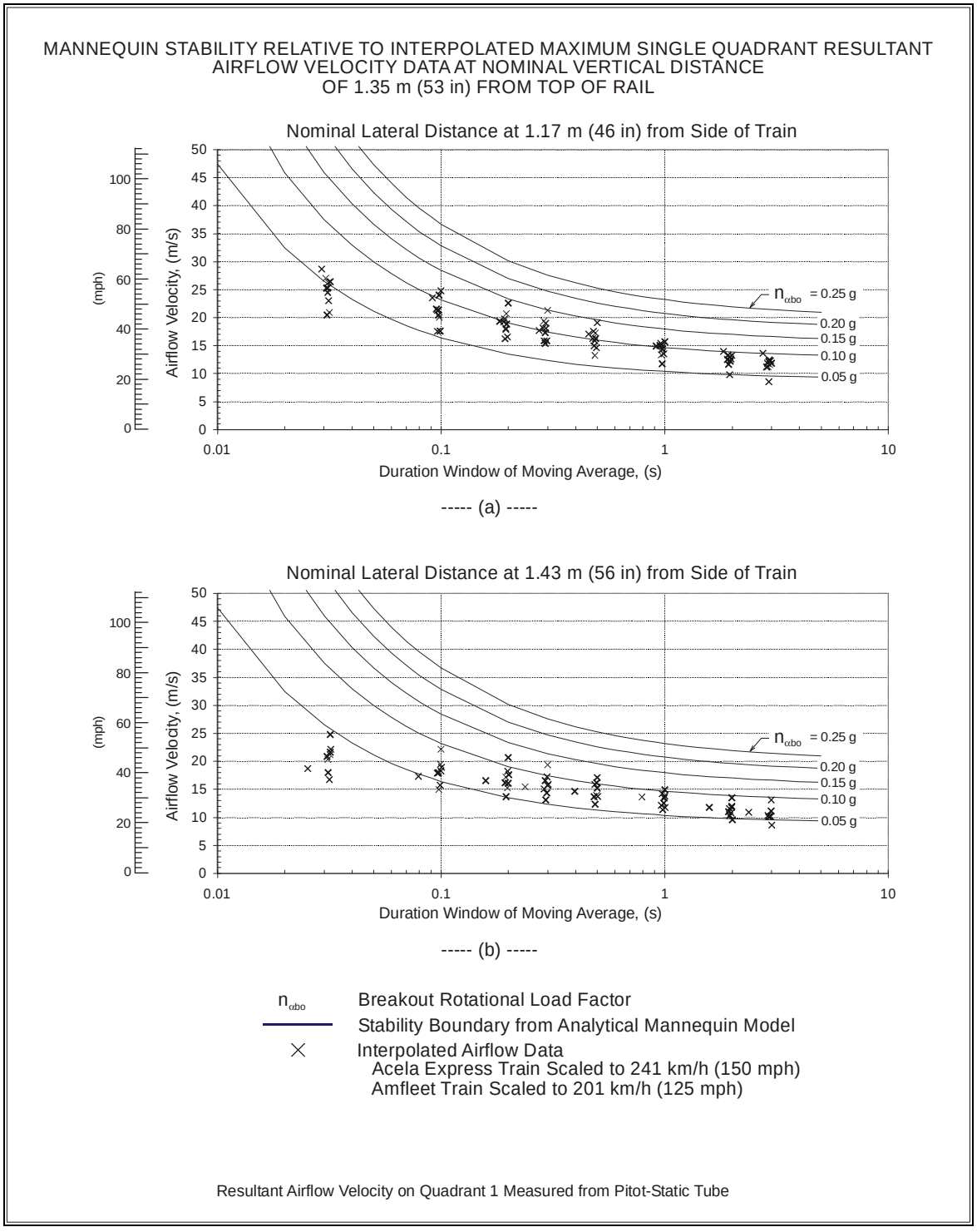

Figure 84. Mannequin Stability Relative to Interpolated Airflow Velocity Data at 1.35 m (53 in) above Top of Rail

10.6. Subjective Reaction to Passing Train

A train approaching at high speeds can evoke an emotional response in the form of anxiety or excitement from a person on a station platform. Although a person's subjective experience of being in proximity to a passing train is not a safety-related issue, a person's physical response can be influenced by psychological factors. There is value in their perception and sensation when it is included along with the quantitative data, where their perspective can portend a future problem, reveal a condition that is not easily measurable, or corroborate the finding from quantitative data.

10.6.1. Study by Swedish National Rail Administration

Lindberg (1994) described a study conducted in Sweden financed by the Swedish National Rail Administration on the perception and sensation experienced by travelers waiting on train station platforms where trains not scheduled to stop pass the platforms at speeds up to 200 km/h (124 mph). About 800 men and women, with ages up to 65 years, were interviewed while on the platforms at ten different stations. The platform edge had a yellow zigzag line to warn people from reaching too close to the edge of the platform, while some stations had either electronic signs or audio warnings of approaching trains that do not stop at the station. Forty to 70 percent of interviewees expressed discomfort from passing trains, but the proportions expressing discomfort varied with stations. Differences in stations that could affect people's response to passing trains included:

- Platform layout (platform width, whether trains pass on one or both sides, etc.),
- Access to shelters on the platform,
- Proportion of daily travelers (who have ample experience of passing trains) and,
- Speed of passing trains.

Table 40 shows the sources of discomfort and the frequency that was mentioned. A strong psychological factor appears to be associated with the passing train experience. "It may seem somewhat surprising that the most common reason for discomfort has nothing to do with the wind forces generated by the passing trains. Rather, the speed of the passing train seems to be the primary source of discomfort, or as one of the interviewees phrased it, 'the unpleasant feeling that something large and heavy is coming straight towards you at high speed'" according to Lindberg (1994). On the question of hazards, 18 percent of the interviewees expressed that passing trains were a hazard to people on the platform, while 10 percent did not think passing trains were dangerous to them, but might be a hazard to other people (mainly children) on the platform. Some respondents stating that this is particularly true in crowded or slippery conditions.

Table 40. Six Most Frequently Mentioned Sources of Discomfort from Passing Trains Listed in Order of Decreasing Frequency Mentioned (Lindberg 1994)

Common Source of Discomfort	Frequency Mentioned	
	Number	Percent
High Speed of the Train	140	37
Air Turbulence	108	29
Noise	61	16
Being Startled/Surprised	30	8
Concerns about the Safety of other People (mostly Children) on the Platform	27	7
Swirling Snow	11	3
Total	377	100

Views on the electronic advanced warning were mixed. There were positive responses to electronic warning signs and sound indications. However, some interviewed felt that they were insufficient. Audio advanced warning received less positive response and thought of as being unreliable. At stations with no advance warnings, about half said that it should be provided.

10.6.2. Observation from Test Crew

Many of the individuals that were involved with the test at the train station in Mansfield, Massachusetts, also had the opportunity to be on the platform as trains passed by the station at relatively high speeds. These members of the test crew were asked to express their views on their experiences of trains passing the station while they were on the platform. The views expressed were not a representative distribution of the population or a statistically significant sample. Their observations however, do provide a subjective perspective to the objective data.

The Mansfield train station has a low-level platform where commuter trains stop, but not intercity trains. The station had a warning area consisting of a yellow strip that was 0.965 m (38 in) wide along the edge of the platform. In addition, an electronic Train-Approach Monitoring System (TAMS) provided an audio announcement and a sign warning of an approaching train.

Nine people on the test crew provided their observations on their experience of being on the station platform while in proximity to trains passing by at high speeds. They were provided with specific questions with allowance for general comments. First, they were asked to express any concerns or discomfort of being on the station platform as a train passed. They were then asked on their perception of the force that was felt due to a passing train. The results of these observations are listed in Table 41. Two of the top three frequently mentioned sources of concern or discomfort relates to the size and speed of the passing train, whereas the other relates to the safety of other people on the platform. A small number expressed discomfort from noise, debris, and experience of instability that could lead to physical harm. The psychological factor is also a significant source of concern or discomfort. The test crew did not mention air turbulence as a source of discomfort or concern. Since the weather was mostly clear during the test, the effects of weather were not a factor on the test crew, but it was mentioned that rain or snow blown by a passing train could be an additional source of discomfort. When asked if they perceived the passing train as a source of concern or discomfort, seven out of the nine in the test crew felt that it was; and when asked if they perceived the passing train to be a hazard, four of the test crew responded positively.

Table 41. Observations from Test Participants on their Experiences in Proximity to Passing Trains Listed in Order of Decreasing Frequency Mentioned

Sources of Concern or Discomfort	Frequency Mentioned	
	Number	Percent
Size of the Train	4	22
Concerns about the Safety of other People (mostly Children) on the Platform	4	22
High Speed of the Train	3	17
Noise	2	11
Debris	2	11
Experienced Instability*	2	11
Being Startled/Surprised	1	6
Total	18	100

* The sense of instability was not expressed as a source of discomfort or concern, but was in specific response to the perception of force from a passing train.

The other observation from the test crew relates to the perception of force felt from the passing trains. The crew expressed general agreement from many that they perceived the strongest force produced by the Acela Express train at the tail end, while the Amfleet/AEM-7 train produced the strongest force at the head end. This is consistent with the quantitative data. In one case, the hard hats of two of the test crew were blown off by the passage of the Amfleet/AEM-7 train, but that did not occur for the passage of the Acela Express train. However, the sense of instability that was mentioned by two of the test crew was from the passage of the Acela Express train. A very interesting observation from three of the test crew was that not much sensation was perceived from the passage of the Amfleet/HHP-8 train. The quantitative data does show the level of aerodynamic forces on the CIDs from the Amfleet/HHP-8 train to be between the Acela Express train and the Amfleet/AEM-7 train.

A part of the subjective response to the passing train is the attentiveness of the person on the platform to an approaching train. The warning system that alerts people of an approaching train in some cases also produced the unintended effect in which a person's response places himself or herself in potential harm. Some of the test crew had claimed that people who are waiting on the platform had expected their commuter train to arrive at the activation of the warning system, and proceeded to moved toward the edge of the platform for boarding, but were not necessarily attentive to the type of train or its speed. In certain situations, perhaps due to a train not being on schedule, it was a high-speed nonstop train instead of a commuter train slowing to a stop. The person standing close to the edge of the platform may be caught unawares by the passage of an unexpected nonstop train. The test crew has suggested that the warning system should provide information on the type of train approaching.

As stated earlier, there was no mention by the test crew of air turbulence as a source of discomfort, although both air turbulence and swirling snow were mentioned with the Swedish study (Table 40). In the test at Mansfield, the weather was generally fair and mild with no snow present, and the test crew was asked about only their experience with passing trains during the test period. It is possible that in cold weather, as suggested by the presence of swirling snow in the Swedish study, that a wind chill factor due to air turbulence might be causing a discomfort that would otherwise not be sensed as uncomfortable.

The limited observations from the test crew at Mansfield and the specific questions that were asked of them cannot be compared directly with the study in Sweden described by Lindberg. It is notable that their subjective responses are so similar in both cases. The psychological factor appears to play a common role affecting a person's subjective response both in the Swedish study and Mansfield test crew observation. A natural anxiety expressed by many of being close to a large fast moving object exists. In neither of these cases were there reports of injuries or falls, but there was legitimate concern for the safety of others, particularly children on the platform. Small children, being shorter and closer to the ground, could be exposed to greater overall airflow velocity than an adult.

11. Conclusion

Numerical simulation and experimentation were conducted on the aerodynamic interaction between passing trains and the aerodynamic effects of trains passing people on station platforms. Numerical simulation included both simple single degree-of-freedom dynamics models and more complex CFD and multibody simulation models. Experimentation involved full-scale testing of a rail car passed by a high-speed train on an adjacent track, measurement of train-induced airflow velocities, and of forces on CIDs from its interaction with the flow field of a passing train.

11.1. Response of Double-Stack Well Car to Aerodynamic Load

A study was conducted to determine the response of a double-stack well car from aerodynamic interaction with a passing high-speed passenger train. Numerical simulation was performed to compute the response of a double-stack well car, and the results were examined for the potential of derailment and the stability of the containers. A full-scale test was performed to measure the aerodynamic pressure and roll response on a stationary double-stack well car when a train passes by on an adjacent track, and the test data was compared with modeling results. The possibility of window glazing being dislodged from its mount from the aerodynamic force of a passing train was investigated.

CFD simulation was performed to study the response of a five-unit articulated double-stack well car from the aerodynamic interaction with a passing Acela Express passenger train. The lateral aerodynamic loading applied to the double-stack well car did not produce significant carbody roll, but it did produce strong dynamic response leading to wheel unloading or high lateral wheel force. For the cases studied, the greatest potential for derailment on the five-unit articulated double-stack well car was when all containers were empty and with the presence of a strong headwind on the Acela Express train or a strong crosswind. The worst response occurred on the nonshared trucks of the first and last cars where each axle on those trucks is more lightly loaded than those on the shared trucks. The condition improved in a partially loaded configuration, when only the containers at the end units are loaded. With all the containers loaded, vertical wheel load increased and the wheel/rail L/V was much lower, therefore, meeting performance specifications. The only exception was when the Acela Express train passed in opposite direction to the loaded double-stack well car with a crosswind in which significant wheel unloading occurred.

Other results from the simulation are as follows:

- Highest lateral load on the double-stack well car occurs when the passing Acela Express train faces a headwind.

- Speed of the Acela Express train is more important than the speed of the double-stack well car for producing peak loads.

- The duration of the load on the double-stack well car, and therefore its response, depends on both the speed of the two passing trains and the directions in which they are traveling (passing in opposite directions or in the same direction). It is when the Acela Express train overtakes the double-stack well car that it was more likely to excite the natural frequency of the double-stack well car producing a strong dynamic response.

The stability of the containers is a factor to consider when another train passes a double-stack well car. Critical to stability is the top container, particularly when emptied. Results from this study found that the containers should not become dislodged.

A test was performed to measure the aerodynamic pressure and carbody roll angle of a double-stack well car as a high-speed TEL train passes it on an adjacent track. It was found that the measured and computed pressures agreed, except that the measured data exhibits a quicker pressure recovery past the negative pressure peak at the nose of the passing train. The roll angles on the double-stack well car are small, with the maximum zero-to-peak roll angle of 0.312° when the TEL train passed at 177 km/h (110 mph).

An analytical study was conducted using a single degree-of-freedom mathematical carbody roll model to extend the CFD results by including a broader range of train passing conditions. Excellent agreement occurs between the roll angles obtained from simulation and those measured from the test. The responses of carbody roll from the effects of altitude, ambient wind, passing train speed and closing speed, and unbalanced speed on curved track were studied.

Larger carbody roll response occurs on the observer car from the aerodynamic interaction with a passing train when any of these conditions exist:

- Reduced altitude,

- Presence of a headwind against the passing train,

- The relative speed between the passing train and observer car is such that the aerodynamic pressure variation sweeps past the observer car that corresponds to the natural roll frequency of the observer car, and

- The passing train is short in length and the relative speed between the passing train and observer car is such that the pressure variation from the tail pulse of the passing train is in phase with the roll motion of observer car.

The carbody roll response from the aerodynamic interaction with a passing train while the observe car is negotiating a curve below its balanced speed is as follows:

- Highest maximum roll angle is when the observer car rolls toward the inside of the curve.

- The observer car traveling at below balanced speed produces a greater maximum roll angle of oscillation when passed by a train on the inside than on the outside of the curve.

- When the carbody roll angle is measured as a deviation from its steady-state roll, a train passing the observer car on the inside curve produces the same maximum carbody roll angle as a train passing the observer car on tangent track.

11.2. Window Integrity from Aerodynamic Load

The aerodynamic force created by a passing train can exert a high force on the window of another train. An Acela Express train traveling at 241 km/h (150 mph) passing a Kawasaki passenger car traveling in the opposite direction at 129 km/h (80 mph) does not appear to have sufficient impulse to dislodge the window glazing on the passenger car, when compared with the impulse from an object striking and dislodging a window glazing. Sufficient data does not exist to arrive at a conclusion when the Acela Express train overtakes the Kawasaki car.

11.3. Aerodynamic Characterization of Passing Train

Numerical simulation and full-scale testing were conducted to determine the strength and characteristic of the aerodynamic effects from a train passing a station platform. The aerodynamic effects were examined from the train-induced airflow velocity and from the force on the CID during interaction with a passing train's flow field that included the following trains: Acela Express train, Amfleet/AEM-7 train, Amfleet/HH-8 train, and Amfleet/F40PH train.

A CFD simulation computed the airflow induced by an Acela Express and an Amfleet/AEM-7 train to provide a relative measure on the strength of airflow velocity between the two types of trains. The simulation revealed the following characteristics:

- The Acela Express train traveling at 241 km/h (150 mph) and an Amfleet train at 201 km/h (125 mph) induced about the same maximum longitudinal airflow velocities. At the furthest distance from the train, the wake from the Acela Express train produced a stronger airflow than the overall airflow from the Amfleet train.

- The Amfleet train produced the strongest airflow from the boundary layer, whereas the strongest airflow for the Acela Express train came from the wake.

- Induced airflow from the Acela Express train was lower on a high-level than on a low-level platform.

A full-scale test was conducted where train-induced airflow velocities were measured by using pitot-static tubes and forces were measured from CIDs' aerodynamic interaction with a passing train. Airflow velocities from CFD calculations were compared with test data, where the major features agree, particularly the relative levels of induced airflow characteristic between the different trains.

A passing train causes a disturbance to the surrounding air, which is very turbulent and chaotic, with airflow in various directions. However, the dominant airflow and load on the CID are primarily in the direction of the passing train. The strength of the airflow is derived mainly in the longitudinal component while the lateral component does not appear to contribute significantly to the resultant airflow, except in the case of a train with a bluff nose head where a strong lateral gust occurs. The force applied to the CID is similar for all the trains as follows:

- *Longitudinal Direction*: As the head of the train passes, the CID is pushed in the same direction as the passing train, immediately followed by a pull in the reverse direction. After the head of the train passes and for the remainder of the passing train, the CID is primarily being pushed in the same direction as the passing train.

- *Lateral Direction*: The CID is initially pushed away from the train immediately followed by a pull toward the train, as the head of the train passes by. Afterwards, the CID is being pushed and pulled oscillating about zero for the remaining train passage.

One of the characterizations of a passing train is the aerodynamic signature. The signature is the time or distance history variation in an aerodynamic variable that is caused by a passing train. A passing train produces an aerodynamic time history signature that depends on the geometry of the train. When all other factors are the same, the exterior geometry of a train and surface continuity play a significant role in its aerodynamic effect. An understanding of the relationship between the exterior surface geometry of a train, and the aerodynamic strength that it produces, can assist in body design to lessen the adverse effect to the surrounding.

The airflow velocity and the force on the CID are both examined from the perspective of its aerodynamic signature. Both exhibited similar time history signatures. The aerodynamic signatures for the trains with three different geometries are as follows:

- *Acela Express Train*: Both airflow velocity and load on the CID gradually increases from the tapered nose head end toward the tail and produces a persistent strong wake after the passage of the tapered tail base. The nose produces a minor airflow velocity but a relatively strong force on the CID. The airflow velocity at the wake retains a steady level with a gradual decrease, while a high initial load occurs on the CID from the wake, the load decreases more rapidly. The maximum load on the CID was largely from the wake of the train.

- *Amfleet/AEM-7 Train*: Both airflow velocity and load on the CID rises immediately from the bluff nose head end and remains at a high level until near the flat tail base where it rapidly drops, leading to a weak wake. The nose produces a relatively strong air gust but the CID has a much more prominent peak load. The airflow velocity at the wake is weak, but the CID load from the wake dropped to a negligible level. The maximum load on the CID was generally from the head of the train.

- *Amfleet/HHP-8 Train*: The slant nose and flat tail base share similar characteristics with the Acela Express and Amfleet/AEM-7 trains. Both airflow velocity and load on the CID produce a noticeable peak at the nose, increasing in strength and decreasing toward the tail end,. The airflow velocity at the wake remains relatively strong, while the CID load from the wake rapidly drops to a negligible level. The maximum load on the CID was somewhere between the head and tail ends of the train.

The airflow strength, either as a train-induced airflow velocity or as a force on the CID, is very much influenced by the geometry of the train. Trains with different geometries can pass by at different speeds but produce similar airflow strength because the airflow is very much dependent on its surface geometry of the train. In general, the head end of a train with a slender nose that gradually increases in cross section for a smooth transition to the body produces a weaker disturbance to the air than a bluff shape nose. For this reason, a tapered nose Acela Express train can travel at a greater speed than a bluff nose Amfleet/AEM-7 train without producing greater airflow. The disturbance to the air is even stronger for a freight train, which consists of freight cars of irregular geometric shapes, with sharp corners and protuberance.

The relative aerodynamic effects between different trains can be quantified by comparing the normalized forces on the CIDs as follows:

- With the cylindrical axes of the CIDs at 1.20 m (47.4 in) from the side of the train:

    - The Amfleet/AEM-7 train produced a force that is a factor of 2.4 higher than the Acela Express train.

    - The Amfleet/HHP-8 train is a factor of 1.8 higher than the Acela Express train.

- With the cylindrical axes of the CIDs at 1.46 m (57.7 in) from the side of the train, the Amfleet/AEM-7 train produced an aerodynamic force on the CIDs that is a factor of 1.9 higher than the Acela Express train

When the aerodynamic forces on the CIDs are scaled to the train's operating speed, the forces are as follows:

- The Amfleet/AEM-7 train passing at a speed of 201 km/h (125 mph) produced a force of 174 N (39 lb).

- The Acela Express train passing at a speed of 241 km/h (150 mph) produced a force of 106 N (24 lb).

Airflow strength varies with location relative to the passing train. Airflow velocity decreases with increased distance from the train and at increased height from the track. Airflow velocity is lower on a high-level than on a low-level platform. When the lateral distances of the CIDs are increased by 22 percent from the side of the train, the forces on the CIDs are:

- Reduced by 14 percent for the Acela Express train.

- Reduced by 32 percent for the Amfleet/AEM-7 train.

There is greater attenuation on the airflow with distance for Amfleet/AEM-7 train than for the Acela Express train. This is also the case in the CFD simulation where the wake from the Acela Express train produced a stronger airflow than the overall airflow from the Amfleet train when measured at the furthest distance from the train.

The drags on an isolated cylinder and on an isolated flat-body with constant drag coefficient were computed from airflow velocity and compared with the load on the CID. The force measured from the CID was higher in magnitude than from the drag computed from airflow velocity for an isolated cylinder. This is consistent with studies that suggest the CID is responding to the effects of static pressure variation from the flow field of the passing train. When the drag was computed for a flat-body, it is in general considerably higher than the drag computed for a circular cylinder, and is also generally higher than the force measured from the CID. This indicates the circular cylinder and the CID are not responding very strongly to the airflow velocity. Therefore, a circular cylindrical body is not an effective gauge of wind force in the range of airflow velocity induced by a passing train.

11.4. People on Trackside and Platform

A survey was conducted of railroad stations along the Northeast Corridor of the United States to provide the information necessary for assessing the impact of Acela Express trains passing the stations at high speeds. The survey of the selected stations involves observing the station surroundings, the general movement of people and trains, and station measurements. In addition to the on-site surveys, basic information was collected from Amtrak and other agencies on all 101 stations. The survey found that the conditions of the stations vary greatly from each other.

A common approach, practiced by railways in various countries to address the safety of people from the aerodynamic effects of a passing train, is to specify a minimum distance

from a passing train. Workers are to stay at a certain distance from the track when a train passes, meanwhile markings are used on station platforms to warn passengers from getting too close to the edge of the platform. Recommended distance from the passing train varies with railways in different countries, as does the maximum speed of the passing train. No safety requirements exist in the United States (as of 2005) for people on station platforms as it relates to the aerodynamic effects of passing trains. Amtrak has been installing yellow markings on the edge of station platforms in the Northeast Corridor that are 0.965 m (38 in) wide.

A passing train induces airflow that creates a destabilizing force on people in proximity to the train. The effects of wind on people have been studied with application to pedestrians in the vicinity of buildings and built-up environments. There are different wind speed criteria with one of the most common being the Beaufort scale. Various attempts have occurred to factor in the unsteady and turbulent airflow in the criteria based on experiments conducted in wind tunnel and from outdoor observation. The wind speed criteria of Murakami and Deguchi were applied in setting the minimum distance for people in proximity to a passing train.

The effects of wind on people from wind speed criteria were compared with the effects on people based on the dynamic response of a single degree-of-freedom mathematical mannequin model. The Murakami and Deguchi criteria are based on wind averages over a 3 s duration, while the mathematical mannequin provides a dynamic response to a transient force of an idealized pulse shape. The stability boundary from the mannequin was interpreted relative to the Beaufort scale from which the effects on a person from train-induced airflow velocity can be evaluated. Comparison of the effects on people from the mannequin stability boundary with the Murakami and Deguchi criteria indicates very similar results.

The criteria for airflow from a passing train were based in part on studies of pedestrian response to high wind in the vicinity of buildings. In addition to any differences between the dynamics of meteorological wind and the airflow induced by a passing train, differences occur between a pedestrian in a street setting, a worker on the trackside, or a waiting passenger on a station platform. These differences may affect their expectation of some disturbance, and thus their ability to counter any destabilizing effect.

In many of the studies on a person's response to wind force, the measure is for the stability of a person that is walking. Because of the kinematics of a walking person, their stability would presumably be less than that of a stationary person with both feet on the ground. Workers on the trackside would be expected to be standing still as a train approaches and passes. People on a station platform may be walking while many people are generally standing still or with little movement.

Another factor that enters into a person's response is their sensory input. A pedestrian in the street may be exposed to a strong wind gust without any warning. However, a worker on the trackside or a person on a station platform will have the benefit of perceiving an approaching train and preparing for its effect. From people's subjective response on the

passing train experience, the wind effect felt by a person is accompanied by an intimidation factor of seeing a train approaching at high speed. This factor is not applicable to a pedestrian walking on the street. If a person is alert to an approaching train, this additional visual sense and the anxiety that it produces could cause the person to move away from the approaching train for reasons that might or might not be related to the aerodynamic factor.

12. Recommendations

Recommendations are proposed to address safety issues relating to the aerodynamic interaction between passing trains, and the aerodynamic effects of trains passing people.

12.1. Aerodynamic Interaction Between Passing Trains

A train traveling at high speeds passing another train produces an aerodynamic force on the other train that can create the potential for structural damage, cargo being dislodged from the rail car, or derailment.

- Operating conditions and rail cars should be examined to determine if conditions exist to create a safety concern. In addition to the high speed of the passing train, other conditions that create the potential for adverse response on the observer car are:
    - Close track center spacing.
    - High ambient wind.
    - Confined environments such as steep embankments, overpasses, or tunnels.
    - Bluff nose on the high-speed passing train.
    - For the observer car:
        - Structural members susceptible to damage such as window glazing or flexible exterior surface material such as cloth.
        - Structural members that contain discontinuity such as attached panels, window frames, or doors.
        - Side surface with large vertical area such as double-stack well car.
        - A rail car that is light in weight.
- The integrity of structures susceptible to damage should be examined for potential failure from high aerodynamic loading, or fatigue failure from cyclic aerodynamic loading of frequent high-speed train passes. A more complete study should be conducted on the structural integrity of window mount and glazing to determine if cracking or dislodgement will occur. Further data required includes:
    - Pull out force on window glazing and mounting frame.

- Burst pressure for the window glazing.
- Window mounting design, dimensions, and structural properties.

- The effects of track geometry variation should be considered in rail vehicle response from aerodynamic interaction with a passing train.

- Maintain a source of aerodynamic data for mathematical modeling. The data should include pressure coefficients as it relates to: (1) geometry of the passing train, (2) configurations of the train being passed and surrounding structures, (3) lateral and vertical distances relative to the passing train, and (4) ambient wind.

12.2. Safety Limit for People from the Aerodynamic Effects of Passing Train

A person in proximity to a train passing at high speeds can experience destabilizing effects of the aerodynamic force created by the train. Debris can be blown and objects and equipment can be pushed onto the passing trains.

- Members of the public on a station platform and railroad workers on the trackside in open calm air should maintain a minimum distance from a passing train, as shown in Table 42.

Table 42. Recommended Minimum Distances for People Exposed to the Aerodynamic Effects of a Passing Train

	Minimum Lateral Distance		
	Distance from Centerline of Nearest Track	Distance from Outer Edge of Nearest Rail	Nominal Distance from Side of Train
Member of Public on Low-Level Passenger Platform	3.12 m (123 in)	2.33 m (92 in)	1.6 m (63 in)
Worker on Trackside at Low-Level Platform Height	2.72 m (107 in)	1.93 m (76 in)	1.2 m (47 in)

- Railroad worker is an adult that is of average size, physically fit, standing stationary on a stable surface, and alert to an approaching train and the sensation of aerodynamic force.

- The minimum distances apply to the following passenger trains and their passing speeds,
  - Amfleet/AEM-7 and Amfleet/HHP-8 trains passing at a speed no greater than 201 km/h (125 mph).
  - Acela Express train passing at a speed no greater than 241 km/h (150 mph).

  The minimum distances can also apply to other trains with similar geometry and corresponding passing speeds.

- The recommended distances from the passing train were based on data measured from a low-level platform at 203 mm (8 in) above the top of the rail. If the trackside or platform is at a height that is significantly different from this height, these distances may not apply.

- A warning strip on a low-level platform that is 1.57 m (62 in) wide as measured from the edge of the platform would correspond to the recommended minimum nominal distance from the side of the train of 1.6 m (63 in).

- Further study on the aerodynamic effects of passing trains should include: (1) the presence of ambient wind, (2) freight trains, and (3) locations that are more reflective of workers on the trackside or situations where pedestrians are on a public pathway adjacent to the track.

- The effects of people exposed to the aerodynamic force from a passing train were based on a person's physical ability to maintain stability. Human response is also influenced by psychological factors that can compromise safety.
  - Announcement of an approaching train should include information on the type of train service or whether the train is stopping at the station.
  - Further study should include the role that psychological factors play for people on station platforms.

- The applicability of the stability boundary derived from the mathematical mannequin should be confirmed with additional data and further analysis.

- Maintain a source of aerodynamic data for mathematical modeling. The data should include the normalized train-induced airflow velocity as it relates to: (1) train geometry, (2) configurations of surrounding structures, (3) lateral and vertical distances from the track of passing train, and (4) ambient wind.

- Platform safety limits were recommended based on the stability of an average adult male. Other factors that should be considered are as follows:

    - Train-induced airflow in itself is unlikely to be strong enough to propel a solid object such as a rock. However, any particles on the track agitated by the turbulent airflow and its buffeting effect, if struck by the train especially at the underside of a car, can cause the particle to become a fast moving projectile. This would propel it in the direction of the train unless it is deflected outward to the platform. A person on the trackside or low-level platform would be most vulnerable to this hazard.

    - Rolling objects put into motion by the aerodynamic drag of the train-induced airflow are a safety issue. A light cart can roll into and be struck by the train causing it to be propelled back onto the platform. The same risk would apply to a baby carriage with potential disastrous consequences if a baby should be in the carriage.

    - People on a station platform can be of different heights and different degrees of agility and strength. A small child could be exposed to greater airflow. People that are frail or the elderly would be less stable than the average adult.

Appendix A: Nomenclature and Glossary

A-1 Nomenclature

Symbol	Definition
A_F	fronted area
A_P	projected area
A_S	side area
A/D	analog-to-digital
ADC	analog-to-digital converter
Amtrak	National Railroad Passenger Corporation
AAR	Association of American Railroads
APTA	American Public Transit Association
ARA	Applied Research Associates, Inc.
AREMA	American Railway Engineering and Maintenance-of-Way Association
CARS	China Academy of Railway Sciences
CEN	European Committee for Standardization
CFD	computational fluid dynamics
CID	cylindrical instrumented dummy
C_D	drag coefficient
C_P	pressure coefficient
D_C	diameter of cylinder
DB AG	Deutsche Bahn A.G. (German Rail)
F_D	drag (force)
FRA	Federal Railroad Administration
FS	Trenitalia (Italian Railways)
ICE	Inter-City Express or Inter-City Experimental (German high-speed train)
ISO	International Organization for Standardization
L_C	length of cylinder
L/V	ratio of lateral to vertical forces

Symbol	Definition
MAS	Maximum Authorized Speeds
MIRA	Motor Industries Research Association
n_α	rotational load factor
NUCARS™	New and Untried Car Analytic Regime Simulation
PB	Parsons Brinckerhoff Quade and Douglas
q_∞	free stream dynamic pressure
Re	Reynolds number
RWT	rails-with-trails
RAPIDE	Railway Aerodynamics of Passing Interactions with Dynamic Effects
RSSB	Rail Safety and Standards Board
RTRI	Railway Technical Research Institute
SI	Système International d'Unités (International System of Units)
SNCF	Société Nationale des Chemins de Fer Français (French National Railways)
SUE	statically unstable equilibrium
TAMS	Train-Approach Monitoring System
TEL	turbine-electric locomotive
TGV	Train à Grande Vitesse (French high-speed train or the system)
TRANSAERO	Transient Aerodynamics for Railway System Optimisation
TTC	Transportation Technology Center
TTCI	Transportation Technology Center, Inc.
USDOT	United States Department of Transportation
Volpe	Volpe National Transportation Systems Center (VNTSC or Volpe Center)

Mathematical Symbol	
Symbol	Definition
u	velocity of fluid
v	velocity of solid body
x, y, z	x, y, z coordinate or translational displacement in the longitudinal, lateral, and vertical directions respectively, (length)
ϕ, θ, ψ	ϕ, θ, ψ rotation in roll, pitch, and yaw about the longitudinal, lateral, and vertical axes respectively, (angle)
ζ	damping ratio
Λ	excitation wavelength, (length)
λ	wavelength, (length)
λ_n	natural wavelength, (length)
ρ	fluid density
Ω	excitation frequency, (rad/time) or (rad/length)
σ	standard deviation
ω	frequency, (rad/time) or (rad/length)
ω_n	natural frequency, (rad/time) or (rad/length)
ω_d	frequency of damped oscillation, (rad/time) or (rad/length)

Subscript	
Symbol	Definition
1, 2, 3	longitudinal, lateral, and vertical directions respectively
bo	breakout
CM	center of mass
CP	center of pressure
cyl	cylinder
ef	effective

A-2 Glossary

Term	Definition
Acela Express	Bombardier/Alstom high-speed trainset for Amtrak passenger train service.
alongside the track	On the trackside or on a station platform.
Amfleet	Budd passenger rail car for Amtrak passenger train service.
Amfleet/AEM-7 Train	Train with Amfleet cars pulled by GM-ASEA AEM-7 electric locomotive.
Amfleet/HHP-8 Train	Train with Amfleet cars pulled by Bombardier/Alstom HHP-8 electric locomotive.
Amfleet/ F40PH Train	Train with Amfleet cars pulled by General Motors F40PH diesel-electric locomotive.
drag indicator	A force obtained by multiplying the normalized statistical force (mean plus 2 standard deviation) by the square of the desired train speed.
observer car	The observer car is the rail car that is responding to the force produced by the other passing train during aerodynamic interaction between passing trains.
rotational load factor	The ratio of the effective force acting at the center of mass to the weight of the body, with the effective force producing the same moment as the actual force acting at another location.
Shinkansen	New trunk line: the rail line of the Japanese high-speed passenger train.
slipstream	The boundary layer flow around the train, which may or may not include the wake.
swap body	A freight-carrying unit for intermodal transport and optimized to road vehicle dimensions, that was originally not strong enough to be top-lifted or stacked when loaded, but some can now be top-lifted or stacked.
trainset	A train whose cars are intended to be permanently coupled together.
turbine-electric locomotive	Locomotive using a gas turbine engine to generate power to an electric traction motor. Also refers to the prototype FRA/Bombardier turbine-electric locomotive.

Appendix B: Aerodynamic Quantity

B-1 Fluid Property

- u: Fluid velocity.
- ρ: Density.
- q: Dynamic pressure.
- μ: Coefficient of viscosity, for air at sea level.
- ν: kinematic viscosity,
- P: Static pressure.
- u_∞: Free stream flow velocity.
- ρ_∞: Free stream density.
- q_∞: Free stream dynamic pressure.
- μ_∞: Free stream coefficient of viscosity.
- ν_∞: Free stream kinematic viscosity,
- P_∞: Free stream static pressure.

Standard atmosphere at sea level:

- ρ_∞ = 1.225 kg/m^3 (0.0023769 slug/ft^3).
- μ_∞ = 1.7894x10^{-5} kg/m•s (3.738x10^{-7} slug/ft•s).
- ν_∞ = 1.4607x10^{-5} m^2/s (1.5723x10^{-4} in^2/s).
- P_∞ = 1.01325 x 10^5 N/m^2 (14.696 lb/in^2).

B-2 Quantitative Relation

Quantity	Definition
Dynamic Pressure (q)	$q = \frac{1}{2}\rho u^2$
Pressure Coefficient (C_P)	$C_p = \frac{P - P_\infty}{q_\infty}$
Peak-to-Peak Change in Pressure Coefficient (ΔC_P)	$\Delta C_p = \frac{P_2 - P_1}{q_\infty}$
Average Pressure Coefficient ($\overline{C}_P$)	$\overline{C}_P = \frac{1}{(X_2 - X_1)}\int_{X_1}^{X_2} C_P(s)ds$ Averaged over the range X_1 to X_2.
Center of Pressure (X_{CP}, Y_{CP})	$X_{CP} = \frac{\int_A p(x,y)xdA}{\int_A p(x,y)dA}$ $Y_{CP} = \frac{\int_A p(x,y)ydA}{\int_A p(x,y)dA}$ Distributed pressure p(x,y) over the surface area A.
Reynolds Number (Re)	$\mathrm{Re} = \frac{u_\infty \rho_\infty L}{\mu_\infty}$ Flow over surface length L.
Drag Coefficient (C_D)	$C_D = \frac{P - P_\infty}{q_\infty}$
Drag (F_D)	$F_D = q_\infty C_D A$
Turbulence Intensity	$\frac{\overline{u}'_{rms}}{\overline{u}}$ Mean flow velocity: $\overline{u} = \frac{1}{T}\int_0^T u(t)dt$ Fluctuation of the flow velocity from its average value: $u' = u - \overline{u}$ Root mean square (rms) of the fluctuation: $\overline{u}'_{rms} = \sqrt{\frac{1}{T}\int_0^T (\overline{u}')^2 dt}$

B-3 Circular Cylinder

B-3.1 Curve Fit for Drag Coefficient of a Circular Cylinder

The drag coefficient for a circular cylinder varies with Reynolds number (Figure 85). Empirical equations for the drag coefficient of a two-dimensional circular cylinder were derived by least square method of curve fit over a range of Reynolds numbers as follows:

Table 43. Empirical Equations for Drag Coefficients.

Reynolds number, Re	Drag Coefficient, C_D
$300 < \mathrm{Re} < 2.15\times10^5$	$C_D = 1.2$
$2.15x10^5 < \mathrm{Re} < 5.435\times10^5$	$C_D = \left(-2.728\times10^{-6}\times\mathrm{Re}\right)+1.787$
$5.435\times10^5 < \mathrm{Re} < 9.779\times10^5$	$C_D = \left(1.285\times10^{-7}\times\mathrm{Re}\right)+0.234$
$9.779\times10^5 < \mathrm{Re} < 3.5\times10^6$	$C_D = \left(1.6\times10^{-8}\times\mathrm{Re}\right)+0.344$
$3.5\times10^6 < \mathrm{Re} < 1.0\times10^7$	$C_D = 0.4$

Shown in Figure 86 and Figure 87 are comparisons of drag coefficients between data and curve fit.

B-3.2 Drag of a Circular Cylinder

When the dimensions of the circular cylinder and the fluid properties do not vary, the drag coefficient C_D is a function only of the flow velocity, and the drag F_D is, $F_D = \frac{1}{2}\rho_\infty u_\infty^2 D_C L_C C_D(u_\infty)$, where D_C is the cylinder diameter, and L_C is the cylinder length. The drag can also be expressed as,

$$F_D = \frac{1}{2}\rho_\infty u_\infty^2 D_C L_C C_{D2}(u_\infty)\left(\frac{C_D}{C_{D2}}\right),$$

where C_{D2} is the drag coefficient for a circular cylinder with long axial length, whose fluid flow over the cylinder can be approximated as two-dimensional flow (Figure 85).

B-3.3 Drag of CID

The circular cylinder of the CID has a diameter of D_C = 0.39 m (15.4 in) and a length of L_C = 0.92 m (36.2 in), with a Reynolds number of Re = (2.67×10^4 u_∞) for standard atmosphere at sea level. The aspect ratio is L_C/D_C = 2.36 (reciprocal is 0.42), and therefore the drag for the CID can be corrected for three-dimensional effects as approximately $\left(\frac{C_D}{C_{D2}}\right) = 0.56$. The drag for the CID can be expressed in terms of flow velocity as shown in Table 44.

Table 44. Drag on a CID as Function of Flow Velocity

Reynolds number (Re)	Drag (F_D) as Function of Flow Velocity (U)
$300 < Re < 2.15 \times 10^5$	$For \quad 0.011 < U < 8.1 \quad (m/s)$ $F_D = 0.2638 U^2 \left(\frac{C_d}{C_{d2}}\right) \quad (N)$ $For \quad 0.025 < U < 18 \quad (mph)$ $F_D = 0.01185 U^2 \left(\frac{C_d}{C_{d2}}\right) \quad (lb)$
$2.15 \times 10^5 < Re < 5.435 \times 10^5$	$For \quad 8.1 < U < 20 \quad (m/s)$ $F_D = \left[-(0.01601U) + 0.3928\right] U^2 \left(\frac{C_d}{C_{d2}}\right) \quad (N)$ $For \quad 18 < U < 46 \quad (mph)$ $F_D = \left[-(0.0003215U) + 0.01765\right] U^2 \left(\frac{C_d}{C_{d2}}\right) \quad (lb)$
$5.435 \times 10^5 < Re < 1.0 \times 10^6$	$For \quad 20 < U < 37 \quad (m/s)$ $F_D = \left[(0.0007541U) + 0.05143\right] U^2 \left(\frac{C_d}{C_{d2}}\right) \quad (N)$ $For \quad 46 < U < 84 \quad (mph)$ $F_D = \left[(0.00001514U) + 0.002310\right] U^2 \left(\frac{C_d}{C_{d2}}\right) \quad (lb)$

FLOW OVER A CIRCULAR CYLINDER

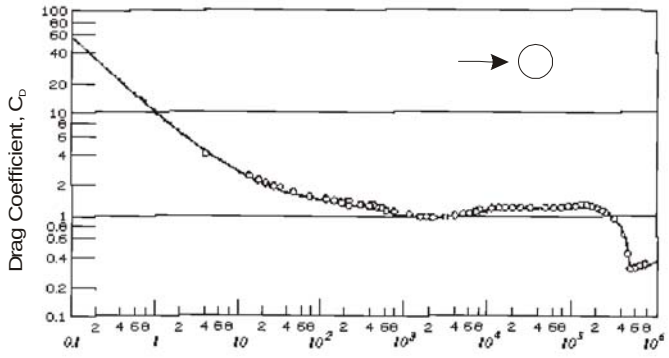

Source: Hermann Schlichting, *Boundary Layer Theory*, 2000

Drag Coefficients at Various Reynolds Numbers over a Cylinder in Two Dimensional Flow

----- (a) -----

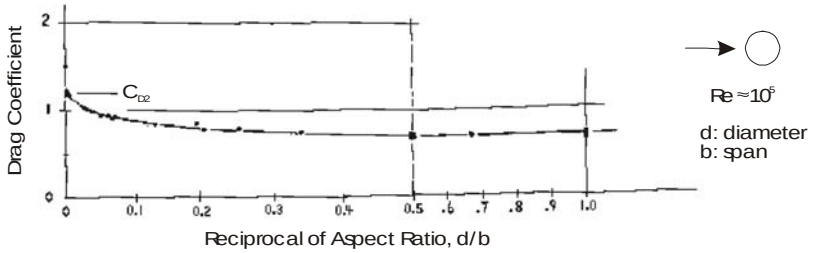

C_{D2}: drag coefficient in two-dimensional flow
b/d: aspect ratio

Source: S.F. Horner, *Fluid-Dynamic Drag*, 1958

Drag Coefficients for a Three Dimensional Cylinder at Various Aspect Ratios

----- (b) -----

Figure 85. Drag Coefficients for a Circular Cylinder with (a) Two Dimensional Flow (Schlichting and Gersten 2000) and (b) Different Aspect Ratios (Horner 1958)

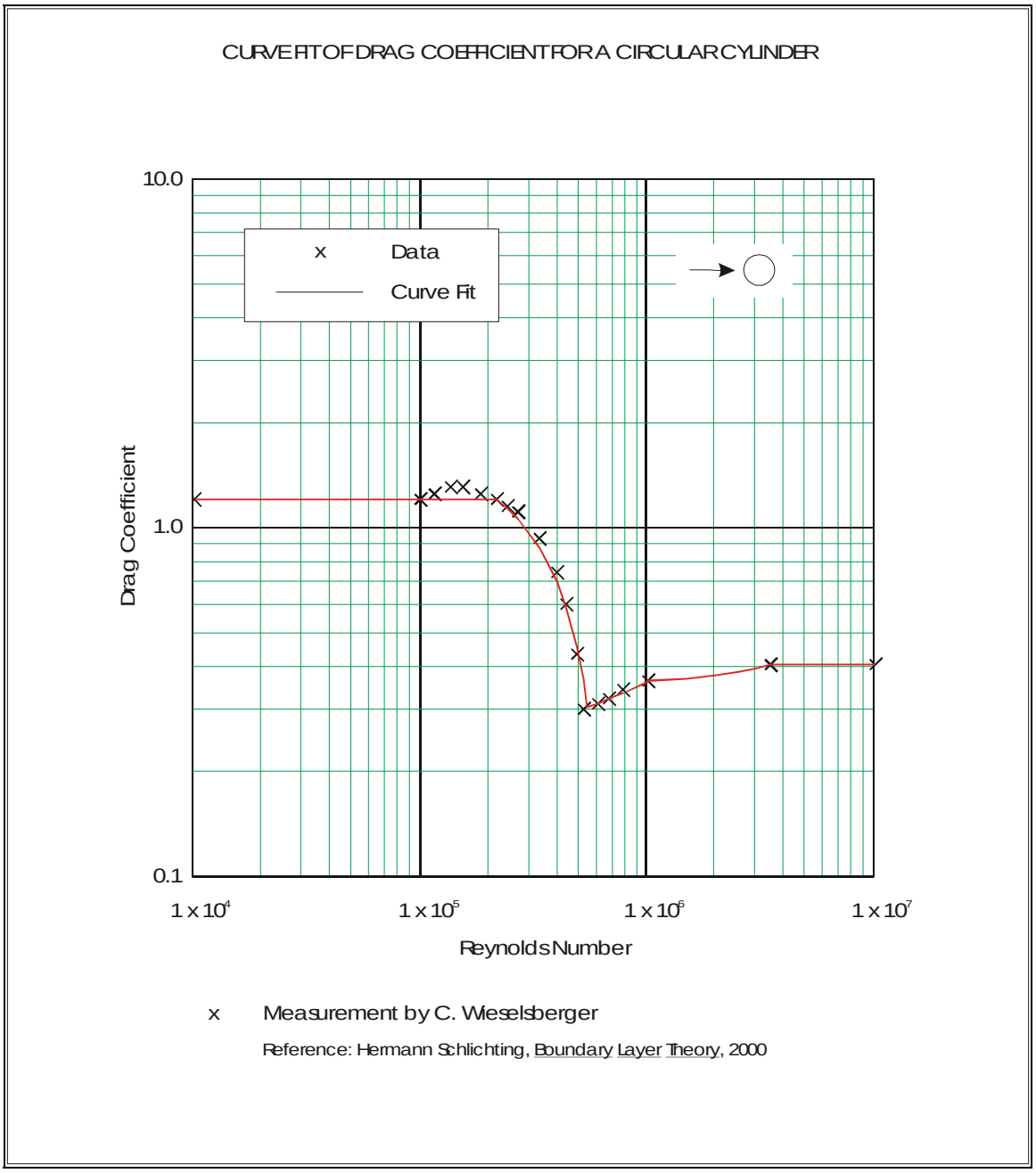

Figure 86. Comparison between Data and Curve Fit of Drag Coefficients for a Circular Cylinder

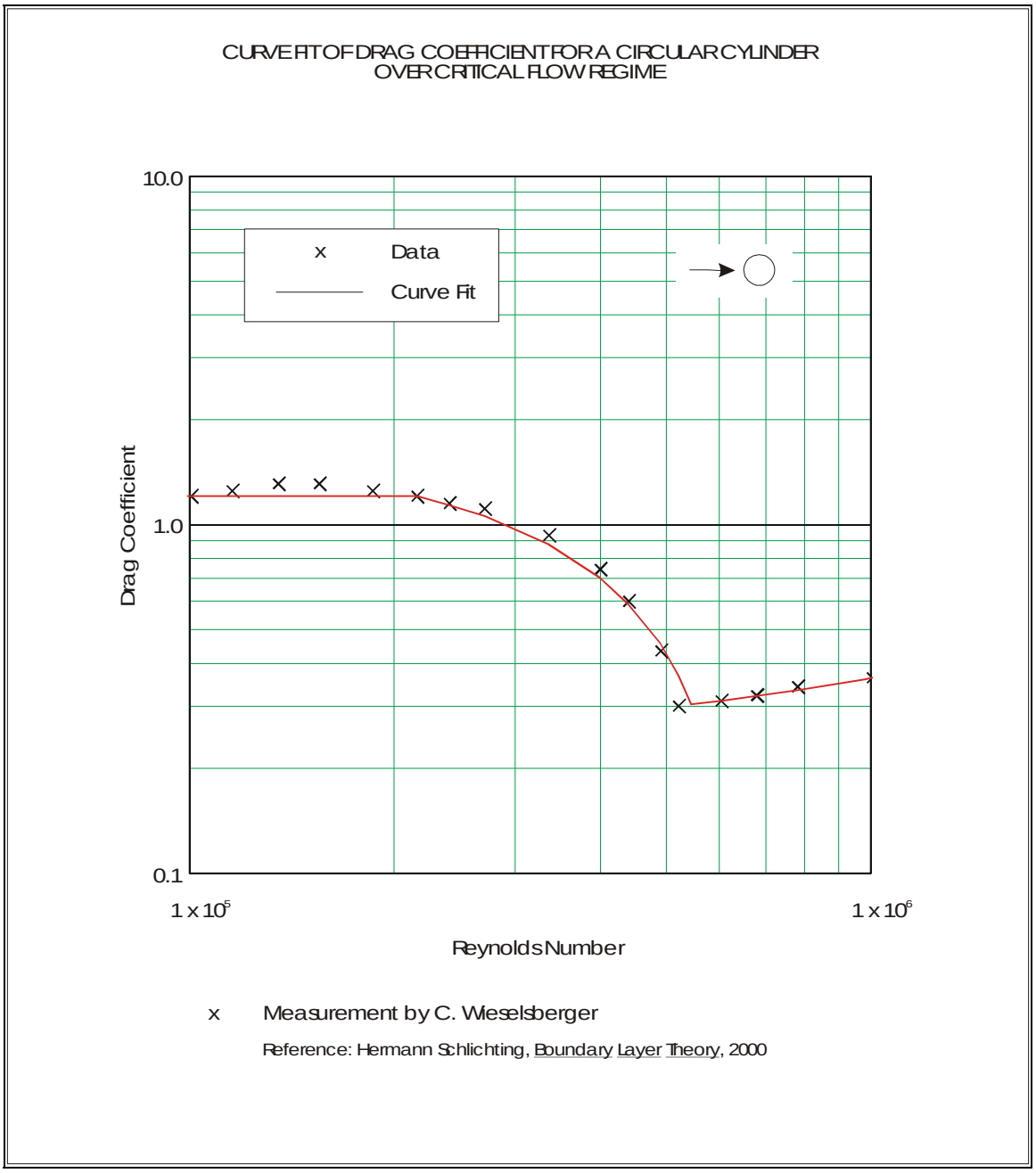

Figure 87. Comparison between Data and Curve Fit of Drag Coefficients for a Circular Cylinder over the Critical Flow Regime

Appendix C: Characterization of Locomotive and Rail Car

C-1 Dimension and Dynamic Property

The dimension and dynamic properties of rail cars and locomotives are shown in Table 45, and the dimension and dynamic properties for the double-stack well car is shown in Table 46.

Table 45. Dimensions of Rail Cars and Locomotives

Locomotive and Car	Length (Between Pulling Faces of Coupler)	Extreme Width	Rail to Extreme Height or to Roof
Well Car TTX 456013 (excluding containers)	21.8694 m (71’ 9”)	3.2004 m (10’ 6”)	1.9558 m (6’ 5”)
Acela Express Power Car	21.218525 m (69’ 7-3/8”)	3.175 m (10’ 5”)	4.318 m (14’ 2”)
TEL			
Acela Express Passenger Car	26.6446 m (87’ 5”)	3.1623 m (10’ 4-1/2”)	4.232275 m (13’ 10-5/8”)
Horizon Passenger Car	25.9842 m (85’ 3”)	3.2004 m (10’ 6”)	3.86715 m (12’ 8-1/4”)
TEL Train			
[TEL] + 2x[Horizon Passenger Car]	73.18 m (240’ 1”)		
Acela Express Trainset			
2x[Acela Express Power Car] + 6x[Acela Express Passenger Car]	202.34 m (663’ 8”)		

Table 46. Dimensions and Dynamic Properties One Unit of an Articulated Double-Stack Well Car

	Length Between Bolsters	Mass of Carbody (Excluding Trucks)	Height of Car Center of Mass from Top of Rail	Moment of Inertia		
				Roll	Pitch	Yaw
Empty	18 m (708 in)	21,420 kg (47,257 lbm)	1.81 m (71.1 in)	1.1×10^5 kg•m^2 (9.8×10^5 lbf•in•sec^2)	5.5×10^5 kg•m^2 (4.9×10^6 lbf•in•sec^2)	5.2×10^5 kg•m^2 (4.6×10^6 lbf•in•sec^2)
Loaded		61,243 kg (134,980 lbm)	1.75 m (68.8 in)	1.6×10^5 kg•m^2 (1.46×10^6 lbf•in•sec^2)	9.3×10^5 kg•m^2 (8.27×10^6 lbf•in•sec^2)	8.7×10^5 kg•m^2 (7.71×10^6 lbf•in•sec^2)

C-2 Roll Response of a Stationary Empty Double-Stack Well Car

The dynamic properties for the carbody of the empty double-stack well car were computed from the measured roll response shown in Figure 88, Table 47, and Table 48, as follows:

- Roll Natural Frequency: 1.6 Hz
- Damping Ratio: 0.03.

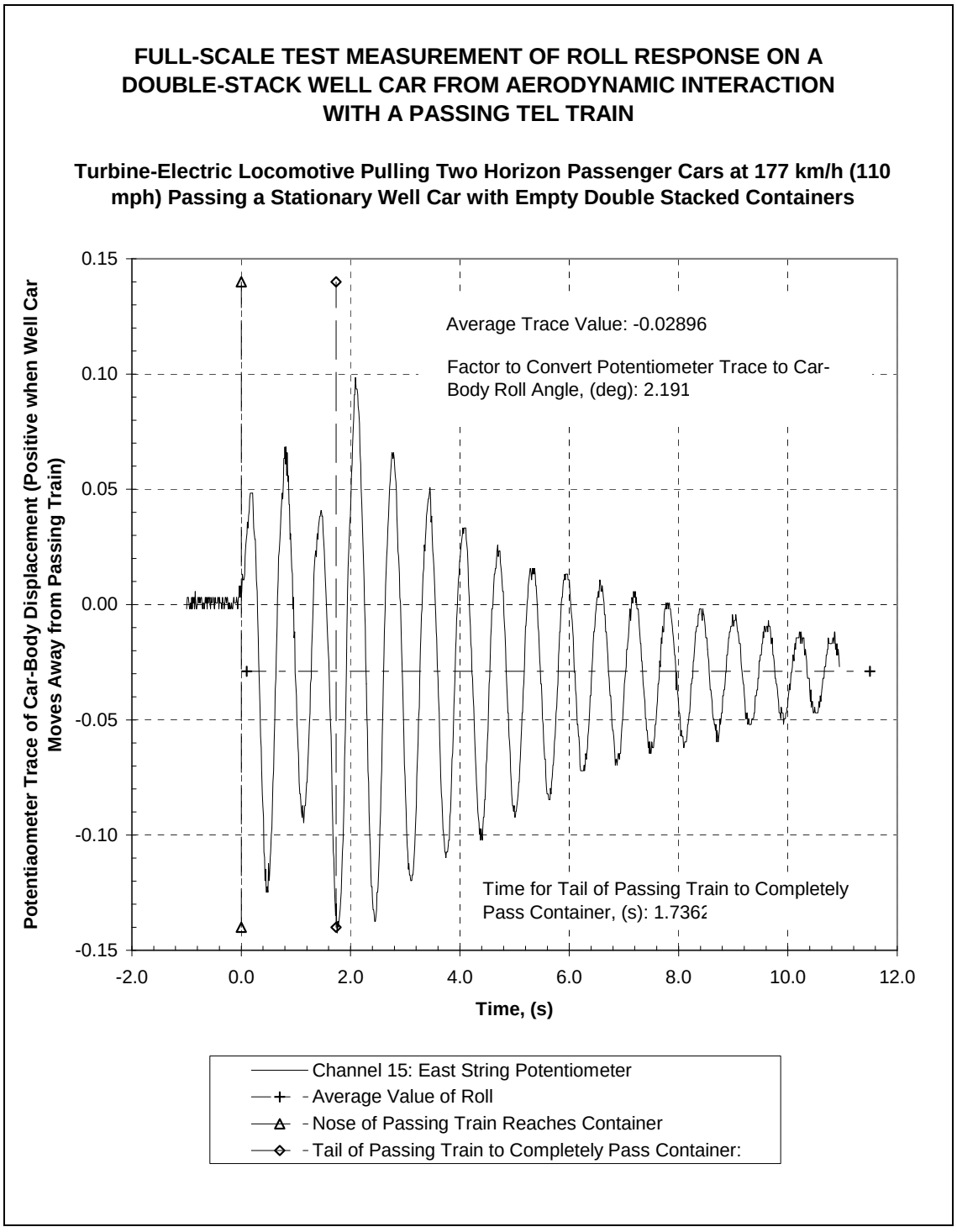

Figure 88. Roll Response of a Stationary Empty Double-Stack Well Car from Aerodynamic Interaction with a Passing TEL Train

Table 47. Periods and Logarithmic Decrements of Carbody Roll Decay of the Double-Stack Well Car after Tail Passage of a Passing Train

Time, (s)	Period, (s)		Logarithmic Decrement	
	Consecutive Maximum Peaks	Consecutive Minimum Peaks	Consecutive Maximum Peaks	Consecutive Minimum Peaks
2.0900	(+Peak 1)		(+Peak 1)	
2.4540		(-Peak 1)		(-Peak 1)
2.7660	0.6760		0.4022	
3.1090		0.6550		0.1371
3.4530	0.6870		0.2596	
3.7440		0.6350		0.0872
4.0870	0.6340		0.4234	
4.4090		0.6650		0.0717
4.6900	0.6030		0.2564	
5.0130		0.6040		0.1030

Table 48. Dynamic Properties of the Double-Stack Well Car from Measured Roll Response

	From Maximum Peak Value	From Minimum Peak Value	From Maximum and Minimum Peak Values
Average Damped Period, (s)	0.6500	0.6398	0.6449
Average Damped Frequency, (Hz)	1.5385	1.5631	1.5507
Average Damped Frequency, (rad/s)	9.6664	9.8213	9.7433
Average Logarithmic Decrement	0.3354	0.0997	0.2176
Average Damping Ratio	0.0533	0.0159	0.0346
Average Natural Frequency, (Hz)	1.5407	1.5633	1.5516
Average Natural Frequency, (rad/s)	9.6802	9.8226	9.7491

Appendix D: Instrumentation and Measurement

D-1 Measurement on Double-Stack Well Car

This instrumentation measures the time history of aerodynamic pressure and carbody roll motion for a double-stack well car.

D-1.1 Aerodynamic Pressure

Aerodynamic pressure on the near side of the container facing the passing train was measured by an Endevco 8510B-2 piezoresistive pressure transducer. Aerodynamic pressure on the far side of the container facing away from the passing train was measured by an PCB Piezotronics 103 A02 piezoelectric pressure transducer, modified for 10 s low frequency response.

D-1.2 Carbody Roll Response

Carbody roll motion was measured by two string potentiometers mounted between the carbody and truck frame on the left and right sides positioned at 0.930 m (36.625 in) from the car longitudinal centerline.

D-1.3 Data Acquisition and Processing

Train detection was provided by two methods. One method was by strain gages on the rail to detect of the axle of the passing train. A second method was by an optical beam directed across the track that detected the presence of a train when the beam is interrupted.

Data was collected by a 12-bit analog-to-digital converter (ADC) sampling at 100 μs intervals.

Data was processed by a 2 pole low-pass Bessel filter set a 1 kHz.

D-2 Airflow Velocity Measurement

D-2.1 Single Peak Value Airflow Velocity Measurement

This instrumentation provided a single peak airflow velocity measurement for each event using an Alnor Instrument velometer consisting of Alnor 6006AP meter, 6030CP range selector, and 6070P pitot tube.

D-2.2 Time History Airflow Velocity Measurement

This instrumentation measures the time history of airflow velocity.

Airflow velocity was measured by a Dwyer Instruments model 160-8 pitot-static tube with a hemispherical tip geometry which gives accurate reading for pitot tube misalignments up to 15 deg. The pitot-static tube is connected to a Setra Systems model 264 very low differential pressure transducer.

GEOLOG Data Acquisition system provided excitation voltage, signal conditioning, and analog to digital (A/D) conversion for four channels at an A/D rate of 250 Hz (4 ms per sample). A photoelectric beam directed across the track detected the presence of a train when the beam is interrupted.

A moving average low-pass filter was applied to the data with a minimum averaging duration of 0.032 s to remove high frequency noise.

D-2.3 Yaw Misalignment of Pitot-Static Tube

The pitot-static tube is designed to accurately measure airflow velocity when it is aligned with the direction of airflow, with increasing error as the misalignment increases. The effects of angular misalignment on pitot-static tube measurements of differential pressure and airflow velocity are shown in Figure 89.

Resultant airflow velocity computed from airflow velocity components measured from two pitot-static tubes perpendicular to each other requires the differential pressure on the pitot-static tubes to vary with a specific trigonometric relationship. For a differential pressure P_O at zero degree angular misalignment, and differential pressure P_ψ at ψ degree angular misalignment, the differential pressure must vary as $\frac{P_\psi}{P_o} = \cos^2 \psi$. An error is incurred in computing the resultant airflow velocity when the measurement with angular misalignment from the pitot-static tube deviates from this relationship.

D-3 Force Measurement on CID

This instrumentation measures the time history of force on the CID.

D-3.1 CID

The CID is an SNCF/VR Model 1993, which consists of a cylinder with a diameter of 0.39 m (15.4 in) and an axial length of 0.92 m (36.2 in). The cylinder is supported on a post with strain gauges attached to the post to measure the unbalanced force acting on the cylinder along a horizontal plane. Any bending to the post is related to the unbalanced force applied to the cylinder. Data from the CID was processed through a Bessel second order 15 Hz low-pass digital filter to account for the muscular reaction time of a human being. The natural frequency of the CID is slightly higher than 15 Hz. The criteria for dynamic behavior of CID are as follows:

- The peak value of the first oscillation following the release of load must not exceed 45 percent of initial value.
- The zero value with no load must be reached in less than 0.1 s.
- The peak value of residual oscillation after 0.5 s must not exceed 10 percent of initial value.

D-3.2 Weather Station

Weather data was measured from a Campbell Scientific weather station, which consists of:

- Barometer: 600 – 1060 mbar Vaisala.
- Wind captor: 05103 (wind direction and speed).
- Temperature and relative humidity: HMP45C.

D-3.3 Data Acquisition and Processing

Stain gages on the rail were used to detect of the axle of the passing train.

Data was acquired at a rate of 1200 samples per second.

Acquisition data was processed with the LabVIEW (National Instruments) software. "Univers Soufflé" created by SNCF performed the application data processing. Data from the CID was measured at 1200 samples per second and was processed through a Bessel second order 15 Hz low-pass digital filter to account for the muscular reaction time of a human being.

D-4 Moving Average

The moving average is computed as a continuous series of mean values over a domain t as follows:

$$\bar{y}(t_n)\Big|_{t_n=t_{n10}}^{t_n=t_{n20}} = \left(\frac{1}{2\alpha}\right)\int_{t_n-\alpha}^{t_n+\alpha} f(t)dt$$

where

- t_n is the midpoint of the averaging window, $t_n = \frac{t_{n1}+t_{n2}}{2}$,
- α is one half the averaging window duration, $\alpha = \frac{t_{n2}-t_{n1}}{2}$,
- t_{n1} and t_{n2} are the initial and final values respectively of the averaging window endpoints,
- and t_{n10} and t_{n20} are the initial and final midpoint values respectively over the domain from which the moving averages are computed.

The moving average for discrete values is computed as a series of mean values over a domain t as follows:

$$\bar{Y}(t_n)\Big|_{t_n=t_{n10}}^{t_n=t_{n20}} = \left(\frac{1}{N_t}\right)\sum_{t_n-\alpha}^{t_n+\alpha} f(t)$$

where N_t is the number of values, which for equal intervals Δt between values, $N_t = \left(\frac{t_2-t_1}{\Delta t}\right)+1$

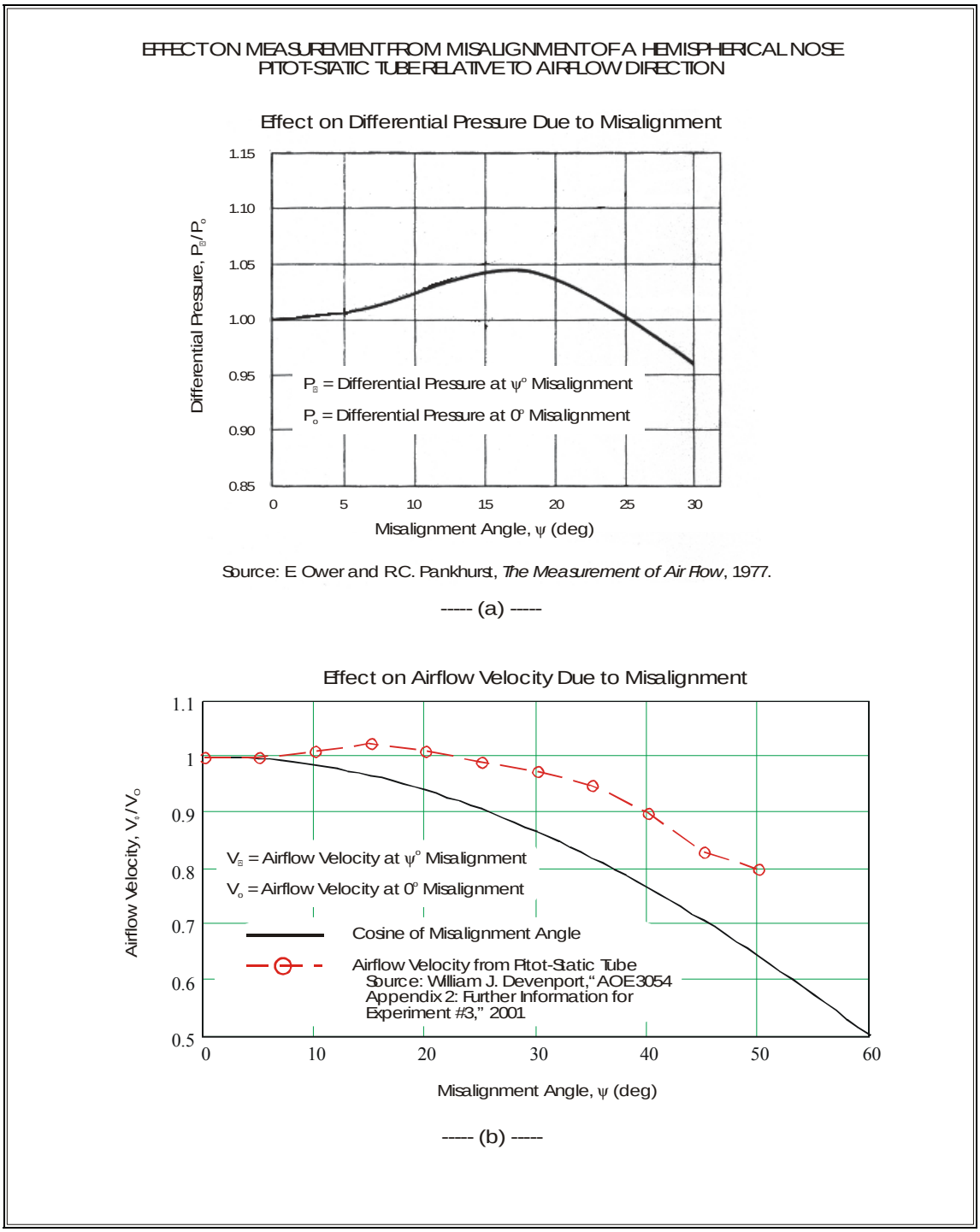

Figure 89. Effect of Angular Misalignment of a Pitot-Static Tube on (a) Differential Pressure (Ower and Pankhurst 1977) and (b) Airflow Measurement (Devenport 2001)

Appendix E: Modeling Computation

E-1 Impulse and Momentum in Shock Impact

In a shock impact where a mass is struck by an impulsive force of very short duration relative to the natural period of the system, the impulse can be related directly to the change in momentum. This relation can be derived by using a model of a single degree-of-freedom mass/spring/damper system,

$$m\frac{d^2y}{dt^2} + c\frac{dy}{dt} + ky = F(t)$$

where,

m: mass,
c: coefficient of viscous damping,
k: spring constant,
F(t): impulsive force.

The equation can be expressed as,

$$\frac{dv}{dt} + (\zeta)v + \left(\omega_n^2\right)y = \frac{F(t)}{m}$$

where,

ζ: damping ratio, $\zeta = \dfrac{c}{2m\omega_n}$

ω_n: natural frequency, $\omega_n = \sqrt{\dfrac{k}{m}}$

Integrating with respect to time,

$$[v(\xi) - v(0)] + (2\zeta\omega_n)\int_0^\xi v dt + \left(\omega_n^2\right)\int_0^\xi y dt = \frac{1}{m}\int_0^\xi F(t)dt$$

If it is assumed that:

- the mass is initially at rest, v(0)=0,
- the damping is small, $\zeta \approx 0$, and

- the pulse duration is short compared to the nature period of the system (pulse duration is about one tenth or less of the natural period) so that the displacement is small, $\int_0^{\xi} y dt \approx 0$,

then the initial velocity of the mass is approximately,

$$v(\xi) \approx \frac{1}{m}\int_0^{\xi} F(t)dt$$

Under these conditions, the initial velocity of the mass from the impulsive force is directly related to the mass and impulse.

E-2 Numerical Solution to Differential Equation by State Transition Method

State transition method is a numerical integration of differential equation where the excitation term is assumed constant over each incremental time or spatial interval, and an analytical solution is found for each increment. The case of a second order differential equation with a constant excitation is,

$$\frac{d^2 q}{ds^2} + 2\zeta\omega_n \frac{dq}{ds} + \omega_n^2 q = \omega_n^2 f_o,$$

where,

f_o: excitation (held constant at each discrete step),
q: response,
s: spatial variable,
ω_n: natural spatial frequency,
ζ: damping ratio.

The solution to this differential equation for an underdamped case (ζ<1.0) is,

$$for \quad \zeta < 1.0,$$
$$q = C_1 e^{-\zeta\omega_n s}\cos\omega_d s + C_2 e^{-\zeta\omega_n s}\sin\omega_d s + f_o,$$
$$\frac{dq}{ds} = -C_1\left(\zeta\omega_n \cos\omega_d s + \omega_d \sin\omega_d s\right)e^{-\zeta\omega_n s} - C_2\left(\zeta\omega_n \sin\omega_d s - \omega_d \cos\omega_d s\right)e^{-\zeta\omega_n s},$$

where, $\omega_d = \omega_n\sqrt{1-\zeta^2}$. Substituting initial conditions, $q(0) = q_o$ and $\frac{dq}{ds}(0) = \left(\frac{dq}{ds}\right)_o$, the arbitrary constants C_1 and C_2 can be expressed as, $C_1 = q_o - f_o$ and $C_2 = \left(\frac{1}{\omega_d}\right)\left(\frac{dq}{ds}\right)_o + \left(\frac{\zeta\omega_n}{\omega_d}\right)q_o - \left(\frac{\zeta\omega_n}{\omega_d}\right)f_o$. The numerical solution for the response (q) and the first derivative (dq/ds), are,

$$
\begin{aligned}
&for \quad \zeta < 1.0,\\
&q = e^{-\zeta\omega_n s}\left\{\cos\omega_d s + \left(\frac{\zeta\omega_n}{\omega_d}\right)\sin\omega_d s\right\}q_o\\
&+ e^{-\zeta\omega_n s}\left\{\left(\frac{1}{\omega_d}\right)\sin\omega_d s\right\}\left(\frac{dq}{ds}\right)_o\\
&- e^{-\zeta\omega_n s}\left\{\cos\omega_d s + \left(\frac{\zeta\omega_n}{\omega_d}\right)\sin\omega_d s\right\}f_o + f_o,
\end{aligned}
$$

and,

$$
\begin{aligned}
&for \quad \zeta < 1.0,\\
&\frac{dq}{ds} = -e^{-\zeta\omega_n s}\left\{\left(\frac{\omega_n^2}{\omega_d}\right)\sin\omega_d s\right\}q_o\\
&- e^{-\zeta\omega_n s}\left\{\left(\frac{\zeta\omega_n}{\omega_d}\right)\sin\omega_d s - \cos\omega_d s\right\}\left(\frac{dq}{ds}\right)_o\\
&+ e^{-\zeta\omega_n s}\left\{\left(\frac{\omega_n^2}{\omega_d}\right)\sin\omega_d s\right\}f_o.
\end{aligned}
$$

E-3 Single Degree-of-Freedom Carbody Roll Model

When a train passes by an observer car on an adjacent track, an aerodynamic pressure variation is swept across the observer car (Equation 1 and Equation 2). This produces a time varying force input to the car being passed (Equation 3 and Equation 4). The force depends on the position of the passing train relative to the observer car. Roll response to the single degree-of-freedom carbody roll model was computed from the equation of motion (Equation 5) by the numerical method of state transition using Mathcad software

E-4 Mannequin Stability Model

E-4.1 Geometric and Inertial Properties

The geometric and inertia properties for the mathematical mannequin are shown in Table 49, Figure 90, and Figure 91.

Table 49. Properties of a Human Body for an Average Adult Male

	Value	Source
Mass	78 kg (0.445 lb•s^2/in)	(Diffrient, Tilley, and Bardagjy 1974)
Pitch Moment of Inertia about Center of Mass	11.872 N•m•s^2 (105 lb•in•s^2)	Computed from Mannequin
Pitch Moment of Inertia about Bottom of Feet	84.2 N•m•s^2 (745 lb•in•s^2)	Computed from Mannequin* (Relative to Human Body Center of Mass)
	90.0 N•m•s^2 (796 lb•in•s^2)	Computed from Mannequin (Relative to Computed Center of Mass)
Height to Top of Head	1.748 m (68.8 in)	(Diffrient, Tilley, and Bardagjy 1974)
Height to Center of Mass	0.963 m (37.9 in)	(Diffrient, Tilley, and Bardagjy 1974)
	1.001 m (39.4 in)	Computed from Mannequin
Height to Center of Pressure	0.894 m (35.2 in)	Computed from Mannequin
Projected Frontal Area for Nude Body	0.577 m^2 (894 in^2)	Computed
Projected Frontal Area for Lightly Dressed Person	0.628 m^2 (973 in^2)	Computed from DuBois Formula

*Simulation was performed using a pitch moment of inertia about the bottom of the feet of 82.1 N•m•s^2 (727 lb•in•s^2) while the revised value is 84.2 N•m•s^2 (745 lb•in•s^2).

E-4.2 Gust Profile

The averages for each of the gust profiles for the airflow velocity can be found by $\frac{1}{t_2 - t_1}\int_{t_1}^{t_2} f_S(t)dt$, while the root mean square for the corresponding drag is

$\sqrt{\frac{1}{t_2 - t_1}\int_{t_1}^{t_2} f_S{}^2(t)dt}$, where $f_S(t)$ is a shape function which is a time varying waveform of unit amplitude that represents the gust profile and $(t_2 - t_1)$ is the time over which the waveform acts.

E-4.3 Statically Unstable Equilibrium Position

The stability boundary at the SUE position for the single degree-of-freedom mathematical mannequin was computed using Mathcad software. A set of simultaneous equations is formed from the general solution to the second order differential equation for the mannequin stability model (Equation 15 and Equation 15(a to c)). The amplitude of the force pulse is computed for each time duration satisfying the conditions at the following points in time:

- point of initial application of excitation force
- point at which the moment from excitation force balances the moment from the gravitational force of the mannequin (for half sine and versine wave pulses only)
- point of release of excitation force
- SUE point

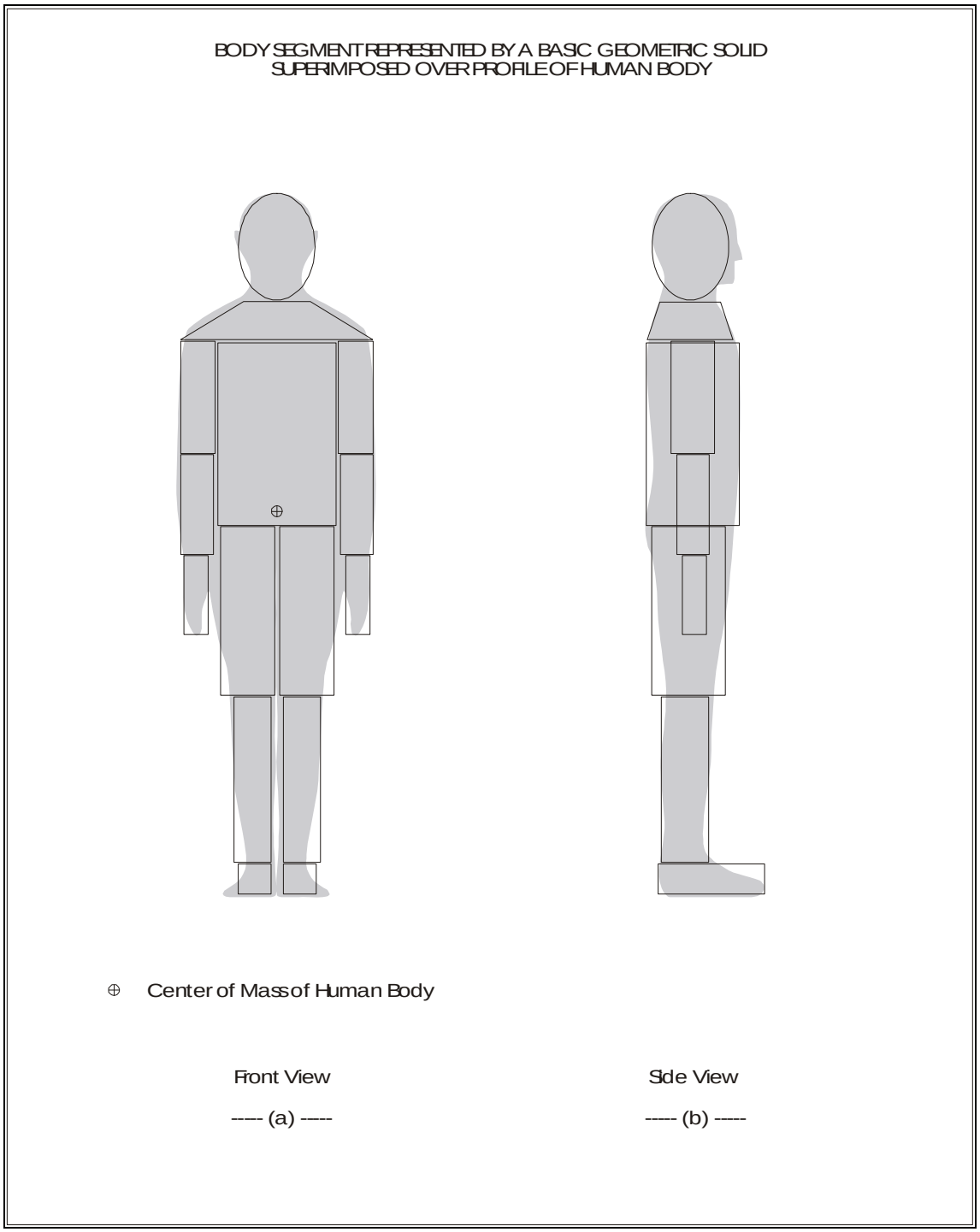

Figure 90. Geometric Solids Superimposed over the Profile of a Human Body

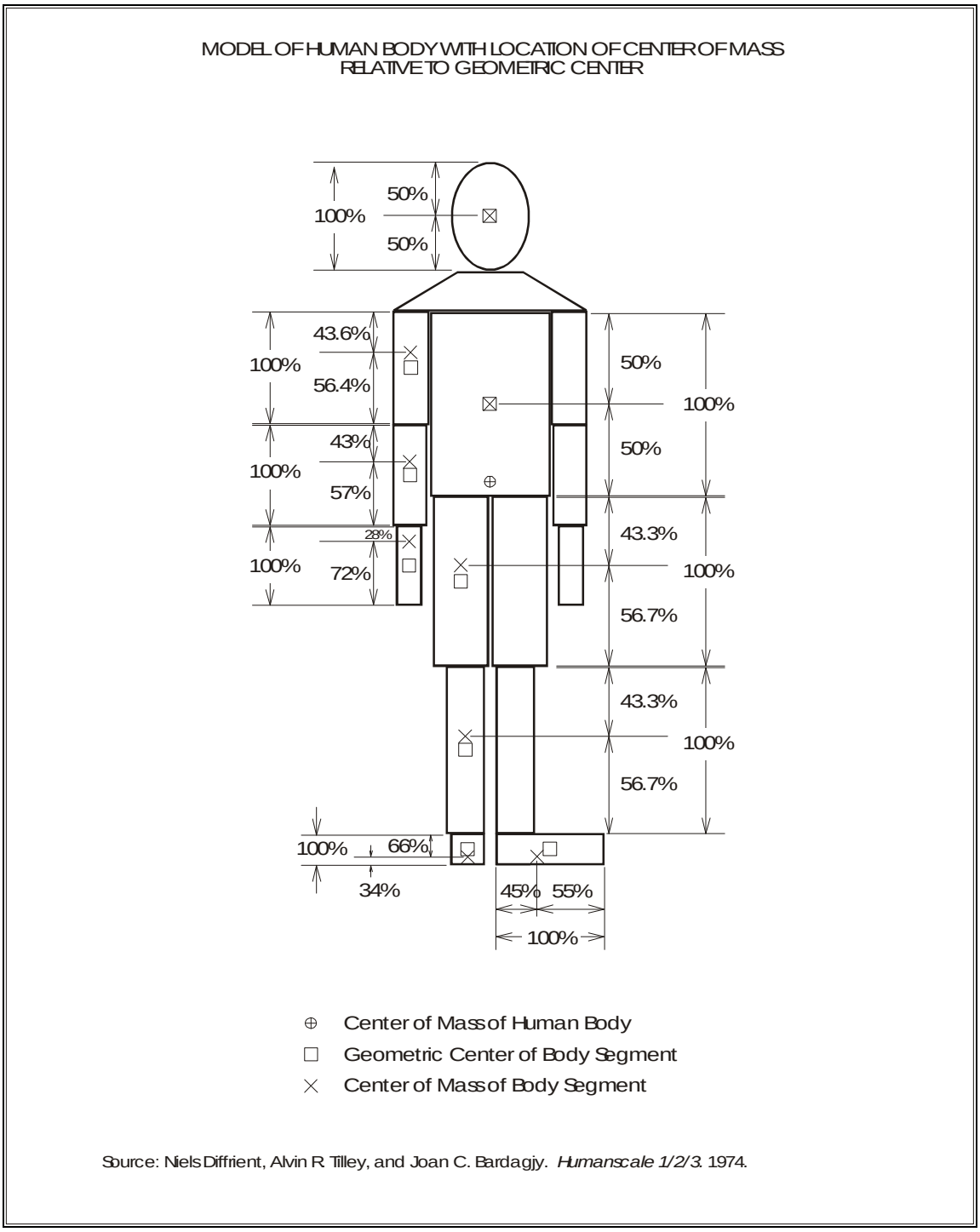

Figure 91 Locations of the Center of Masses for Segments of the Human Body (Diffrient, Tilley, and Bardagjy 1974)

References

Andersson, T.; Aronsson, L.; and Pettersson, B. (1994). *Train Wind Force Caused by Passing Trains*. Swedish National Testing and Research Institute. Report number: SP-RAPP-1994:23, ISBN-91-7848-482-0, NTIS No. PB95-131306 (Swedish).

AAR. (1984). "Passenger Car Requirements." *Manual of Standards and Recommended Practices: Section A: Part 3,* issue of 1980. Washington, DC: Association of American Railroads, revised.

AREMA. (1999). *AREMA Manual for Railway Engineering*. American Railway Engineering and Maintenance-of-Way Association.

Baker, C.J.; Dalley, S.J.; Johnson, T.; Quinn, A.; and Wright, N.G. (2001). "The Slipstream and Wake of a High-Speed Train." Proceedings of the Institution of Mechanical Engineers, Part F, *Journal of Rail and Rapid Transit*, 215, issue 2 (June 12) 83–99.

Baker, C.J., and Sterling, M. (2003). "Current and Recent International Work on Railway Aerodynamics." Report prepared for Rail Safety and Standards Board. http://www.rssb.co.uk/pdf/reports/research/ Current%20and%20recent%20international%20work% 20on%20railway%20aerodynamics.pdf.

Birk, M.L. (2003). "Trails and High-Speed Rail: Are They Compatible?" (NCBW Forum Article),. http://www.bikewalk.org/ncbw_forum/ highspeed.pdf.

Birk, M.L.; Ferster, A.; Jones, M.G.; Miller, P. K.; Hudson, G. M.; Abrams, J.; and Lerch, D. (2002). *Rails-with-Trails: Lessons Learned–Literature Review, Current Practices, Conclusions.*" Prepared at the direction of the U.S. DOT by Alta Planning and Design. Report number: DOT-VNTSC-FTA-04-05, FTA-MA-26-0052-04-1.

Devenport, W. J. (2001). "AOE 3054 Appendix 2: Further Information for Experiment #3." Aerospace & Ocean Engineering, Virginia Polytechnic Institute and State University. http://www.aoe.vt.edu/~devenpor/aoe3054/manual/app2/text.html.

Diffrient, N.; Tilley, A.R.; and Bardagjy, J.C. (1974). *Humanscale 1/2/3.* Cambridge, Massachusetts: The MIT Press.

DuBois, D,, and DuBois, E.F. (1916a). Clinical Calorimetry, Fifth paper: "The Measurement of the Surface Area Man." *Archives of Internal Medicine* 15:868–881.

———. (1916b). Clinical Calorimetry, 10th paper: "A Formula to Estimate the Approximate Surface Area if Height and Weight be Known." *Archives of Internal Medicine* 17: 863-871.

Duffell, T.J. (2000). "Project 18666F: Measurement of Train-Induced Air Velocity. Field measurement report, Parsons Brinckerhoff Quade & Douglas, Inc., 2000.

Freedenberg, M. (2003). "Train Rips Passengers' Items from Platform." *The Ventura County Star,* Ventura, CA, August 25, 2003.

Gandemer, J. (1977). "Wind Environment around Buildings: Aerodynamic Concepts." *Proceedings of the Fourth International Conference on Wind Effects on Buildings and Structures* (London, 1975), 423-432. K. J. Eaton, ed. New York: Cambridge University Press.

Gawthorpe, R.G. (1972). "Aerodynamic Problems of High-Speed Trains Running on Conventional Tracks." von Karman Institute for Fluid Dynamics, Lecture Series 48, High Speed Ground Vehicles, April 10–14, Rhode Saint-Genese, Belgium.

———. (1978). "Aerodynamics of Trains in the Open Air." *Railway Engineering International*, 3, no. 3 (May/June): 7–12.

Gawthorpe, R. (1994). "High Speed Aerodynamic Effects on Existing Railways." Proceedings from *WCRR'94 World Congress on Railway Research* (Paris, France, November 14–16, 1994) 1:787–795. Paris: SNCF.

GEOCOMP (2002). "Measurements of Train-Induced Airflow Using Pitot Tubes." Prepared for Parsons Brinckerhoff Quade & Douglas, Inc. by GEOCOMP Corporation.

Gregoire, R. (2001). "Trains Passing Each Other: Introduction and Methods." Presented at the RAPIDE Workshop in Cologne, Germany, November 29, 2001.

Gregoire, R.; Eckl, B; and Malfattti, A. (n.d.). "TRANSAERO: A Major European Research Programme on Transient Aerodynamics for Railway System Optimisation." http://www.bbw.admin.ch/html/pages/abstracts/abstr2001/html/fp/fp4/b95.0102.html.

Heshou, X.; Dezhao, H.; and Houxiong, W. (1996). "A Study on the Safe Clearance for Persons from Running Quasi-High-Speed Train." *China Railway Science.* China Academy of Railway Sciences, (Chinese).

Hill, A.V. (1928). "The Air-Resistance to a Runner." *Proceedings of the Royal Society of London, Series B, Containing Papers of a Biological Character* 102, no. 718 (February 1): 380–385.

Hirshfeld, C.F. (1932). "Disturbing Effects of Horizontal Acceleration." Bulletin No. 3. New York: Electric Railway Presidents' Conference Committee, September 27.

Hoblit, F. M. (1988). *Gust Loads on Aircraft: Concepts and Applications.* Washington, D.C.: American Institute of Aeronautics and Astronautics, Inc.

Holmes, S.; Schroeder, M.; and Toma, E. (2000). "High-Speed Passenger and Intercity Train Aerodynamic Computer Modeling." *Proceedings of the ASME International Mechanical Engineering Congress and Exposition* (Orlando, Florida, November 5-10, 2000), S.K. Punwani, ed. ASME RTD 19:153–160. New York: ASME.

Holmes, S., and Schroeder, M. P. (2002). *Aerodynamic Effects of High-Speed Passenger Trains on Other Trains.* Prepared for U.S. Department of Transportation by Applied Research Associates, Inc. Report number: DOT/FRA/ORD-01/12, DOT-VNTSC-FRA-01-05.

Horner, S.F. (1958). *Fluid-Dynamic Drag*. Library of Congress Catalog Card Number 57-13009. Midland Park, New Jersey: published and copyrighted by the author.

Hunt, J.C.R.; Poulton, E.C.; and Mumford, J.C. (1976). – "The Effects of Wind on People; New Criteria Based on Wind Tunnel Experiments." *Building and Environment* 11:15–28. Great Britain: Pergamon Press.

Johnson, T. (2001). "Risk to a Freight Wagon from a Passing High Speed Train." Presented at the RAPIDE Workshop in Cologne, Germany.

Johnson, T.; Dalley, S.; and Temple, J. (2002). "Recent Studies of Train Slipstreams" (The Aerodynamics of Heavy Vehicles: Trucks, Buses and Trains, Monterey-Pacific Grove, California, December 2–6).

Lawson, T.V., and Penwarden, A.D. (1977). "The Effects of Wind on People in the Vicinity of Buildings." *Proceedings of the Fourth International Conference on Wind Effects on Buildings and Structures* (London, 1975), Eaton K.J., ed., 605–622. New York: Cambridge University Press.

Lee, H.S. (1999). *Assessment of Potential Aerodynamic Effects on Personnel and Equipment in Proximity to High-Speed train Operations.* U.S.DOT, Volpe National Transportation Systems Center. Report number: DOT/FRA/ORD-99/11, DOT-VNTSC-FRA-98-3.

Liao, S.; Mosier, P.; Kennedy, W.; and Andrus, D. (1999). *The Aerodynamic Effects of High-speed Trains on People and Property at Stations in the Northeast Corridor.* Prepared for U.S. DOT by Parsons Brinckerhoff Quade & Douglas, Inc. Report number: DOT/FRA/ORD-99/12, DOT-VNTSC-FRA-99-11.

Lindberg, E. (1994). "A Look at the Platform Environment: Can Ambitions to Attract New Customers Cause Discomfort to Existing Ones?" Proceedings from *WCRR '94 World Congress on Railway Research* (Paris, France, November 14-16, 1994) 1:97–101. Paris: SNCF.

MacNeill, R.; Lynch, B.; and Schroeder, M. (2001). "High Speed Train Aerodynamic Pressure Measurement Program." Prepared for Volpe National Transportation Systems Center by Applied Research Associates, Inc.

MacNeill, R.; Holmes, S.; and Lee, H.S. (2002). "Measurement of the Aerodynamic Pressures Produced by Passing Trains." *Proceedings of the 2002 ASME/IEEE Joint Rail Conference* (Washington, DC, April 23-25, 2002), ASME RTD 22:1–8. New York: ASME.

Marty, P.; Coulmy, G.; and Luu, T.S. (1978). *Experimental Study on Aerodynamics of Trains Traveling at High Speeds*. Aeronautic and Astronautical Association of France, Report Number: AAAF-NT-78-21; ISBN-2-7170-0506-4; (N79-23036) (French).

McCormick, B. W. (1979). *Aerodynamics, Aeronautics, and Flight Mechanics*. New York: John Wiley & Sons.

Melbourne, W.H., and Joubert, P.N. 1971. "Problems of Wind Flow at the Base of Tall Buildings." *Proceedings of the Third International Conference on Wind Effects on Buildings and Structures* (Tokyo, 1971), Japanese Organizing Committee, ed.,105–114. Tokyo: Saikon.

Minnis, A., and Denti, M. (2001). "Influence of a Vehicle Passing Event on Vehicle Dynamics." Presented at the RAPIDE Workshop in Cologne, Germany. November 29, 2001.

Murakami, S., and Deguchi, K. (1981). "New Criteria for Wind Effects on Pedestrians." *Journal of Wind Engineering and Industrial Aerodynamics* 7:289–309. Amsterdam: Elsevier Scientific Publishing Company.

Ower, E., and Pankhurst, R.C. (1977). *The Measurement of Air Flow*, 5th edition. Oxford, England: Pergamon Press Ltd.

PB. 1999. "Railroad Vehicle Glazing Impact Strength Testing Program." Prepared for Volpe National Transportation Systems Center by Parsons Brinckerhoff Quade and Douglas, Inc., in association with ETC Laboratories. July 15.

———. 2000. "Measurements of Train-Induced Airflow Velocities Due to Passage of Trains at Non-Stop Stations in Rhode Island and Massachusetts." Prepared for Volpe

National Transportation Systems Center by Parsons Brinckerhoff Quade & Douglas, Inc. September 29, 2000.

Penwarden, A.D. (1973). "Acceptable Wind Speeds in Towns." *Build. Sci.* (Great Britain: Pergamon Press), 8: 259–267.

Penwarden, A.D., and Wise, A.F. (1975). *Wind Environment Around Buildings.* Building Research Establishment Report, Department of the Environment, Building Research Establishment. London: Her Majesty's Stationary Office.

Penwarden, A.D.; Grigg, P.F.; and Rayment, R. (1976). "Measurements of Wind Drag on People Standing in a Wind Tunnel." *Building and Environment* 13:75–84. Great Britain: Pergamon Press.

Phillips, P. (2000). "A 25-Year Rail Strategy: A Suggested Development Strategy for Britain's Railway System." Town & Country Strategies. United Kingdom, October. http://www.townandcountrystrategies.co.uk/Resources/25-Year%20Rail%20Strategy.pdf.

Prevezer, T. (2001). "Effects of Trains Passing People," Presented at the RAPIDE Workshop in Cologne, Germany, November 29, 2001.

Przybylinski, P.G., and Anderson, G.B. (1980). *Engineering Data Characterizing the Fleet of U.S. Railway Rolling Stock: Volume 2 Methodology and Data*, Appendix D-2. Prepared for U.S. Department of Transportation by Pullman Standard Company. April.

Railway Technical Research Institute (RTRI). (1998). Large-Scale Low-Noise Wind Tunnel. http://www.rtri.or.jp/rd/maibara-wt/wind-tunnel_EN.html.

"RAPIDE: Railway Aerodynamics of Passing Interactions with Dynamic Effects." 2001. Synthesis report from aerodynamics workshop held in Cologne, Germany. November 29, 2001.

R.E.R. (1997). *The Official Railway Equipment Register* 113, no..2: PC-542. Issued by R.E.R. Publishing Corporation, Publication of K-III Directory Corp., October.

Schlichting, H, and Gersten, K. with contributions from E. Krause and H. Oertel Jr. 2000. *Boundary-Layer Theory*, 8th revised and enlarged edition. New York: Springer.

SNCF. (2002). "Acela Aerodynamic Testing: A Test Report on the Aerodynamic Testing of Amtrak High Speed Trains." SYSTRA Consulting, Inc., in association with The SNCF. December.

Tanemoto, K., and Kajiyama, H. (2003). "Train Draft And Pressure Variation On A Platform." *RTRI Report* 17: 11;53–56 (Japanese).

Temple, J., and Johnson, T. (2003). "Review of Slipstream Effects on Platforms." Prepared for Rail Safety and Standards Board. Report number: AEATR-AER-2003-002, Issue 1. http://www.rssb.co.uk/pdf/reports/research/Review%20of%20train%20slipstream%20effects%20on%20platforms.pdf.

Thomson, W. T. (1988). *Theory of Vibration with Applications*, Third Edition. Englewood Cliffs, New Jersey: Prentice Hall.

Tsai, T.; Lamond, J.; and Lee, H. (2003). "The Aerodynamic Effects of High-Speed Trains on Surroundings, Train Operations, and People." Proceedings from *WCRR 2003: The World Congress on Railway Research* (Edinburgh, Scotland, September 28– October 1, 2003) 452–462. Online at www.wcrr2003.co.uk.

Whitaker, S. (1968). *Introduction to Fluid Mechanics*. Englewood Cliffs, N.J.: Prentice-Hall, Inc.